Experimental Study of a High Efficiency Step-Tunable MW Gyrotron Oscillator

by

David S. Tax

M.S. (EECS), Massachusetts Institute of Technology (2008)
B.Eng. (Electrical), Dalhousie University (2006)
C.A.S., Acadia University (2003)

Submitted to the
Department of Electrical Engineering and Computer Science
in partial fulfillment of the requirements for the degree of

Doctor of Philosophy

at the

MASSACHUSETTS INSTITUTE OF TECHNOLOGY

September 2013

Signature of Author . . . . . .
Department of Electrical Engineering and Computer Science
August 16, 2013

Certified by . . . . . .
Richard J. Temkin
Senior Research Scientist, Department of Physics
Thesis Supervisor

Accepted by . . . . . .
Professor Leslie A. Kolodziejski
Chairman, Committee on Graduate Students
Department of Electrical Engineering and Computer Science

Experimental Study of a High Efficiency Step-Tunable MW Gyrotron Oscillator

by
David S. Tax

Submitted to the Department of Electrical Engineering and Computer Science
on August xx, 2013, in partial fulfillment of the
requirements for the degree of
Doctor of Philosophy

Abstract

The gyrotron is a source capable of producing megawatt power levels at millimeter-wave frequencies for many important applications, including electron cyclotron heating and current drive in magnetic fusion devices. It is important that the gyrotron operates with high efficiency and provides a high quality output beam to minimize system size, maximize reliability and avoid additional losses in external systems. This thesis presents the experimental study of such a gyrotron designed to operate at MW power levels and whose initial 110 GHz operation was expanded to include operation at 124.5 GHz. To this end, a new set of components, including a cavity, mode converter, and output window were designed for operation at both frequencies. The cavity was designed using the code MAGY and the Q factors of 830 for the $TE_{22,6,1}$ mode at 110 GHz and 1060 for the $TE_{24,7,1}$ mode at 124.5 GHz would be suitable for CW operation in an industrial gyrotron. The mode converter consisting of a dimpled-wall launcher and 4 phase-correcting mirrors could theoretically produce an output beam with 99 % Gaussian beam content at each frequency while a single-disc window was implemented with over 99.5 % power transmission at both frequencies. The achieved output power in experiment was 1.1 MW at 110 GHz and 850 kW at 124.5 GHz for the design parameters of 96 kV and 40 A. At 98 kV and 42 A, the gyrotron achieved 1.25 MW and 1 MW at 110 and 124.5 GHz, respectively. Mode competition is typically a major limitation in such gyrotrons, and stable single-mode operation was demonstrated at both frequencies. At 110 GHz, the output beam had 98.8 % Gaussian beam content, while at 124.5 GHz, the output beam quality was 94.4 %. Another experiment within this thesis demonstrated the implementation of a mode converter with smooth mirrors that would be less susceptible to machining and misalignment errors. A Gaussian beam content of 96 % was measured in that experiment.

In addition, a thorough study of the gyrotron start-up scenario was performed, for which experimental work had been lacking in the literature. The start-up scenario is the sequence of modes that are excited during the rise of the voltage pulse and is essential for the gyrotron to operate in its most efficient regime known as the hard self-excitation regime. This gyrotron operates nominally in the $TE_{22,6,1}$ mode near the 110 GHz cutoff frequency with an axial field profile that is approximately Gaussian at the steady-state peak voltage. In experiments performed in the smooth mirror mode converter

configuration, lower frequency modes were observed at lower voltages as opposed to higher frequency modes as predicted by theory. Analysis of these modes showed that they are backward-wave modes far from their cutoff frequency which have higher order axial field profiles, i.e. $TE_{21,6,3}$ and $TE_{21,6,4}$ modes at frequencies of 108-109 GHz. The excitation of these modes was investigated and shown to be possible by using theory and single-mode simulations with the code MAGY. This discovery was important as these modes were not included in past code runs, and thus future improvements can be made to incorporate this effect.

Thesis Supervisor: Richard J. Temkin
Title: Senior Research Scientist, Department of Physics

Acknowledgements

The Ph. D. truly represents the culmination of a great journey. After many years, many tears (not really), and a whole lot of coffee, it is definitely an experience one could never forget. Like most experiences in life though, it's really the people that makes it what it is, and that is what makes the Waves and Beams division of the PSFC at MIT a special place.

First and foremost, I need to acknowledge Richard Temkin. I couldn't have asked for anything more from a research advisor. Rick was always encouraging. Whenever you encountered an unexpected challenge, he was always there to find a way to frame this new problem in a way that invigorated your enthusiasm. It truly was an honor to work with such a distinguished scientist, and a great person. I also owe thanks to Michael Shapiro, who was always there to help out with any theory troubles, or to discuss just about anything from hockey to the latest happenings in Russia. Ivan Mastovsky also played an integral role in helping to ensure everything worked in the lab, and there were definitely times where I would have been lost without his assistance.

Then, there are the students. The current group of graduate students has really made for a memorable experience. We had some great times sitting around discussing life, sports, and occasionally science over afternoon coffee. In particular, I want to acknowledge Emilio Nanni, who was probably the most dedicated, yet grounded, graduate student I have ever met, Jason Hummelt, whose travels consistently made me jealous, Brian Munroe, whose attention to detail was always of great help, Sam Schaub, whose assistance in the lab during the final push made a timely completion possible, and Elizabeth Kowalski, who could always humor us with an afternoon sigh, and was also gracious enough to step forward and read this thesis. And then there's Sasha Soane. What can I say? Sasha is truly one of the kindest, gentlest souls you'll meet. It was a great experience sharing an office with him for the past 2 years, and he definitely made sure that

there would never again be a dull moment in NW16-168. I also owe a lot to Nick Comfoltey, with whom I got to share an office for my first 2 years of grad school. I would also like to thank Sudheer Jawla, who was always happy to help out with analysis, Bill Guss for making sure the experiment was ready to go first thing in the morning and other Waves and Beams members past and present including: Antoine Cerfon, Antonio Torrezan, Colin Joye, Roark Marsh, Eunmi Choi, Sergey Arsenyev, Chiping Chen, Zhaoyun Duan, Xueying Lu, Paul Thomas, Paul Woskov, JieXi Zhang, and others. I wish everyone the best as they continue on in their careers.

I must also thank my other friends at MIT. I have to thank Dave Shirokoff, David Gosset and Mike Matejek for long nights out talking hockey, and Phillip Nadeau for good times on the curling ice and for taking over my leadership duties, in particular. I must also of course acknowledge Eva Polyzoeva, who made my final years at MIT quite special, and is the only person that I've met who could rival my passion for the Boston Bruins (2011 Stanley Cup Champions!!!). p.s. Thanks Bruins! And thanks to everyone else who has made my time at MIT so enjoyable.

Last, and definitely not least, I need to sincerely thank my family. I couldn't ask for more caring and supportive parents than Ted and Cara Tax. They have been with me every step of the way, and were always there to help in any way possible. Without them, this achievement would never have been possible. I also need to acknowledge my sisters, Jaimie and Dana, and of course my four-legged brother Cody. They have also stood by me every step of the way, and have taken great pride in my accomplishments here, and I want them to know too, how proud I am of them. I have no doubt that they will also accomplish great things, and I look forward to providing the same type of support that they provided me.

Table of Contents

List of Figures

List of Tables

Chapter 1

Vacuum Electron Devices: Applications and Development

As is often the case, the boundaries of science and engineering are pushed forward by a never ending supply of new and exciting challenges and ideas that require new, innovative solutions. The field of vacuum electronics is no different. Technological and scientific advancements in a variety of areas have consistently established a push for new concepts to extend the capabilities of the state-of-the-art devices of the day. This was true in the infancy of the field and remains true to this day; therefore, before exploring the modern day demand for these devices, the historical development of early vacuum electronics should be discussed.

1.1 History of Vacuum Electronics

1.1.1 Early Developments: Diodes, Triodes, and Gridded Tubes

This story begins in 1873 with the culmination of the work of James Clerk Maxwell as he laid out his famous series of equations linking electric, magnetic, and optical phenomena. Maxwell's equations predicted that electromagnetic fields propagate through space in the form of waves, a prediction which would be proven experimentally in 1888 by Heinrich Hertz. With these developments, the concept of wireless communication was born.

Early wireless communication was dominated by the spark-gap generator. The spark-gap transmitter is a simple and reliable device that charges a capacitor until the breakdown voltage of an air gap is reached and a current spark is discharged across the gap. The current spark excites a resonant circuit and generates a high frequency signal. Unfortunately, these devices also had their shortcomings, including power limitations and broad-band output signals that resulted in extensive interference with transmissions at neighboring frequencies. These shortcomings would lead to the eventual replacement of the spark-gap generator by alternative devices like Poulsen arc converters and high-frequency mechanical alternators. All of these devices, in turn, would eventually yield to vacuum tubes.

The first vacuum electron device actually preceded much of the aforementioned work and can be credited to Thomas Edison in 1893 when he observed, within an evacuated bulb, an electric current being drawn in between a heated filament and a conducting plate held at a positive voltage with respect to the filament. The current would eventually be identified as electrons being drawn from a cathode (the filament) towards an anode (the conducting plate). The "Edison effect," now simply referred to as thermionic emission, would be the basis for the world's first official vacuum tube developed in 1904 by Sir John Ambrose Fleming. The Fleming valve, or oscillation valve, employed a diode bulb, like that developed by Edison, to rectify high frequency oscillations, thus making the detection of transmitted signals much simpler. However, it would be Lee De Forest's audion which would aid in the development of sensitive heterodyne receiver circuits [1, 2] and set the stage for future work in radio communication. De Forest found that a modulation grid could be inserted between the cathode and anode to control the flow of electrons. By applying a weak radio signal to this grid, an amplified signal would appear between the cathode and anode. De Forest's device was not a true vacuum tube though, as he asserted (incorrectly) that a small amount of gas in the tube was essential to its operation. Nonetheless, it was through work to improve the audion that the first triode

vacuum tubes would be developed. These triodes were also the first demonstration of amplification of a radio signal, and they found a plethora of uses: from radio communications transmitters/receivers to consumer electronics.

As communication systems continued to evolve through the 1930s, the benefits of pushing for higher frequency operation were obvious. A higher frequency system would be capable of transmitting more information and would also provide a higher antenna gain, which would either yield larger transmitted signals or allow for the implementation of smaller antennae. As the development of gridded tubes for this application continued, the limitations of the devices also became apparent. Increases in both inductance in the wires and capacitance between the electrodes at higher frequencies limited the device's capabilities. However, the major limitation was the sharp degradation in performance that occurred when the electron transit time between the electrodes became longer than the period of the grid input signal [3]. While gridded tubes would continue to have a variety of uses for many years to come, the push for higher frequency devices would require some new concepts.

1.1.2 The Golden Age of Vacuum Tubes: Magnetrons, Klystrons, and Traveling-Wave Tubes

The new concepts to advance the field of vacuum electronics involved the replacement of the wires and electrode plates of the gridded devices with interaction structures like resonant cavities and waveguide. Cleverly designed structures facilitated the interaction between streaming electrons (an electron beam) and an electromagnetic wave within the structure and allowed for the power in the electromagnetic wave to be coupled out of the device.

One of the most important devices of our time, the magnetron, arose in this era. The first magnetron was developed in 1920 by Albert Hull as he experimented with the magnetic control of electrons in vacuum tubes. The simple two-pole Hull magnetron

consisted of a cylindrical heated cathode held at a large negative potential surrounded by a hollow cylindrical copper anode with a magnetic field along the axis generated by a permanent magnet [4]. Due to the orientation of the fields, magnetrons are classified as "crossed-field devices" and are an example of a crossed-field oscillator. While such magnetrons found their use, it wasn't until the invention of the cavity magnetron that the true power of the magnetron was unleashed.

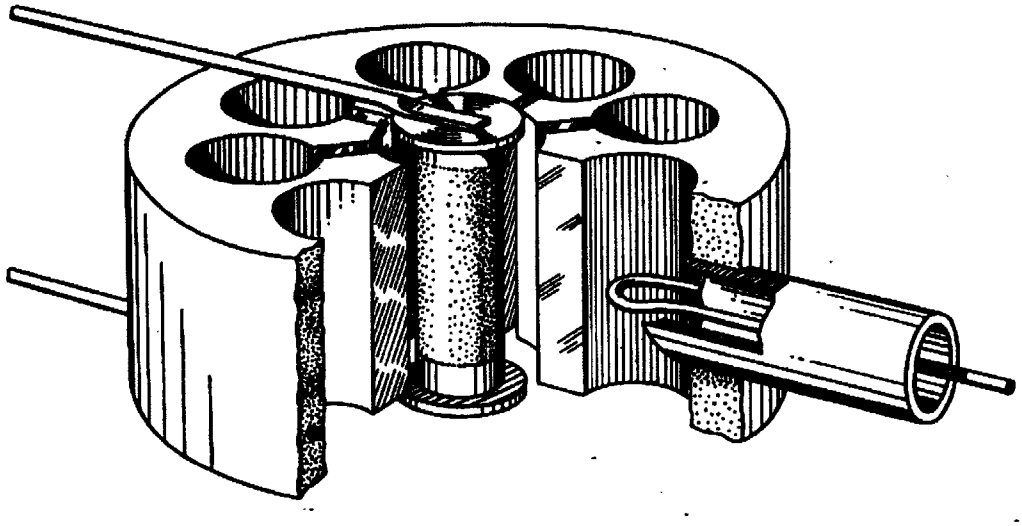

Figure 1-1: Model of a cavity magnetron. The cathode is located in the center of the device surrounded by the electron drift space, and 8 cylindrical cavities are built into the anode. A coaxial waveguide located in one of the cavities is used to couple the microwave power out of the device. Adapted from [5].

While many researchers worldwide had worked on the development of the cavity magnetron, some even filing patents, it was the work of Britons John Randall and Harry Boot in 1940 that truly demonstrated the device's capability. The modification introduced by Randall and Boot was to place several cylindrical resonating cavities in the form of cut-out "chambers" periodically along the inner surface of the anode [6]. A sample magnetron schematic is shown in Figure 1-1 where the anode cavities are visible as well as the central cylindrical cathode and a coaxial output waveguide to extract the microwave power from

one of the cavities. The poles of the permanent magnet are located at the top and bottom of this assembly to generate the axial magnetic field. Due to the applied voltage and magnetic field, the electrons are drawn from the cathode and spiral around the drift space, and, as they pass an opening, they excite electromagnetic fields in the cavity. The combined excitation of the cavities results in a traveling electromagnetic wave which will tend to bunch the drifting electrons in space, allowing for the generation of coherent microwave power. These magnetrons instantly surpassed the capabilities of other devices with their ability to generate upwards of 10 kW power at a 10 cm wavelength (3 GHz). While the benefits of pushing towards centimeter-wavelength radar systems had been obvious for some time, the lack of a suitable source had limited development, that is, until the invention of the cavity magnetron. In fact, many consider the cavity magnetron to be one of the most important technological achievements of our time due to its influence on the outcome of World War II [7].

One of the critical battlegrounds of World War II was not located on the ground at all, but in the skies above, and the key to victory in this arena was radar. Shortly after Randall and Boot's invention, the General Electric Company in Wembley, England was contracted to develop the tubes, however with Britain's industrial manpower and resources severely stretched thin, developing radar systems was a daunting task. Sir Henry Tizard, a British scientist and high ranking advisor to the Air Ministry, proposed a solution: share some of Britain's most guarded technological secrets in order to tap into the (then neutral) United States industrial complex. After acquiring Churchill's approval, the team for the "Tizard Mission" was assembled and the mission scheduled to proceed. The cargo would include a number of designs and reports relating to rocketry, submarine defense, and radar, however the most prized item would be "Magnetron Number 12". The team arrived in Halifax, Nova Scotia, Canada on September 6, 1940, one night before the Bombing of London began. Several meetings ensued with a variety of American and Canadian delegations as the secrets were divulged and the capabilities of the cavity

magnetron were demonstrated. The cavity magnetron was capable of producing several times the power of comparable technologies in the US, and thus Bell Telephone Laboratories was immediately contracted to produce copies of the device, while many manufacturers would also follow suit shortly thereafter.

Perhaps the most important immediate result of the Tizard Mission was the establishment of the Radiation Laboratory on MIT's campus. Many of the US's brightest microwave scientists converged on Cambridge, Massachusetts where the primary project for the "Rad Lab" would be a 10-cm radar detection system for fighter aircraft. Within six months, a radar system was developed and tested on aircraft. After some integration with parallel efforts by British scientists, a final radar system, the SCR-720, was ready for manufacturing and deployment. This radar system, far more advanced than anything developed previously and far more capable than any German or Japanese radar, would help ensure British and American air dominance in both Europe and the Pacific [8]. The Rad Lab would also be responsible for many more advances, including the development of ground-based anti-aircraft gunnery capable of detecting and tracking aircraft at distances up to 20 miles that further ensured Allied air supremacy. While the Rad Lab would close shortly after the war, its impact was lasting [9].

The cavity magnetron would have a lasting impact as well. The magnetron is, by far, the most ubiquitous vacuum electron device to this day, as one is at the heart of the millions of microwave ovens found in households around the world. These magnetrons typically operate at a moderate ~1 kW output power and at a frequency of 2.45 GHz (not far from the 10 kW, 3 GHz Randall and Boot tube developed over 70 years ago). Magnetron development continues to this day, as companies like Communications and Power Industries (CPI) manufacture magnetrons ranging from 915 MHz to 35 GHz in frequency and at power levels from 100 watts to 35 MW for a variety of applications, like air traffic control and weather radar [10]. Research in magnetrons is also ongoing as

scientists and engineers apply new, novel concepts to magnetron design and imagine new applications for their devices [11-14].

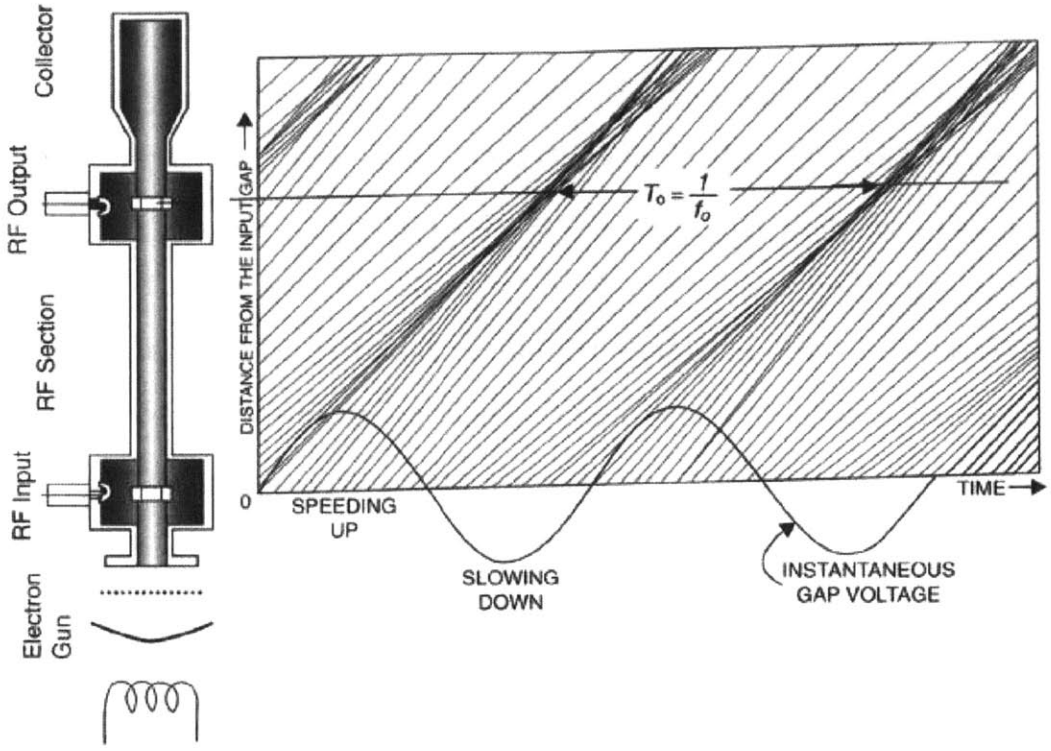

Figure 1-2: Schematic of a klystron and "Applegate" diagram showing the velocity modulation of electrons due to a voltage applied at the input gap. Adapted from [15].

Around the same time as magnetron development was underway, another device was emerging in the US. After completion of a prototype in 1937, the Varian brothers, Sigurd and Russell, working at Stanford University at the time, published the invention of the klystron in 1939 [16]. The simplest klystron is the two-cavity klystron amplifier. It functions by passing an emitted electron beam through a "buncher" cavity, where a weak radio frequency (rf) input field is present. The rf field will alter the electron velocities causing spatial bunching of the electrons as they propagate through a magnetically-confined drift space. When the modulated electrons arrive at the second "catcher" cavity, an electromagnetic wave is generated at the same frequency as the input signal resulting in a much larger rf output from this cavity. A schematic of this simple klystron configuration

is shown in Figure 1-2. The "Applegate" diagram shows the velocity modulation of electrons due to a voltage applied across the input gap [17]. For improved performance, a klystron may employ intermediate cavities to help bunch the beam or it may even operate as an oscillator by omitting the rf input signal and, instead, adding coupling between the cavities. It is no wonder that the klystron obtains its name from the Greek verb "klyzo," which expresses the breaking of waves on a beach, since the waves (bunches) of electrons crash when they reach the catcher cavity and give up their energy.

Klystron development through the 1940s would yield significant boosts in the device's capabilities, and by the latter part of the decade, a klystron producing over 20 MW of pulsed power at 2.857 GHz was achieved [18]. These klystrons would find an immediate use in linear accelerators. Linear accelerators are important tools in experimental particle physics research, work which continues to this day with ever-advancing accelerators; however, beginning in the 1950s, they would also find a use in the medical field, as scientists and doctors experimented with their use for cancer radiation therapy due to the large X-ray output of the device. The high power output of the klystron at cm wavelengths, far greater than the magnetron, also made them ideally suited for the radar community, and, thanks to its ability to utilize more complex waveforms and to operate multiple devices in parallel, the klystron allowed for significant advances in radar architectures throughout the 1950s [19]. Other more modern uses for the klystron include television signal transmission and many communication systems operating in the 1-12 GHz range. While work with high power klystrons continues, one of the modern directions in klystron research is in compact and efficient extended interaction klystrons (EIKs) designed to operate at much higher frequencies than a conventional klystron. EIKs have demonstrated the capability of producing kW peak power levels at 94 GHz [20] for uses which include airborne satellite communication uplinks and radar imaging systems.

There is one other device of note that arose in this era of vacuum electronics, and that is the traveling-wave tube (TWT). The TWT, like the klystron, is an amplifier,

meaning that the electron beam interacts with and gives up energy to a weak input rf field. In a typical TWT, the electron beam travels axially down the device, while the rf field travels through some sort of periodic circuit, often a spiraling helix or a series of cavities coupled along one side that snake along the axis. A schematic of a sample helix TWT is shown in Figure 1-3. The periodic circuits act to reduce the axial phase velocity of the rf field and match it to the velocity of the electron beam, allowing for spatial bunching of the beam and coherent amplification of the rf input. This results in a distributed interaction over the length of the device and allows the device to operate with a relatively large bandwidth, meaning that the device can yield excellent amplification for a wide range of input frequencies.

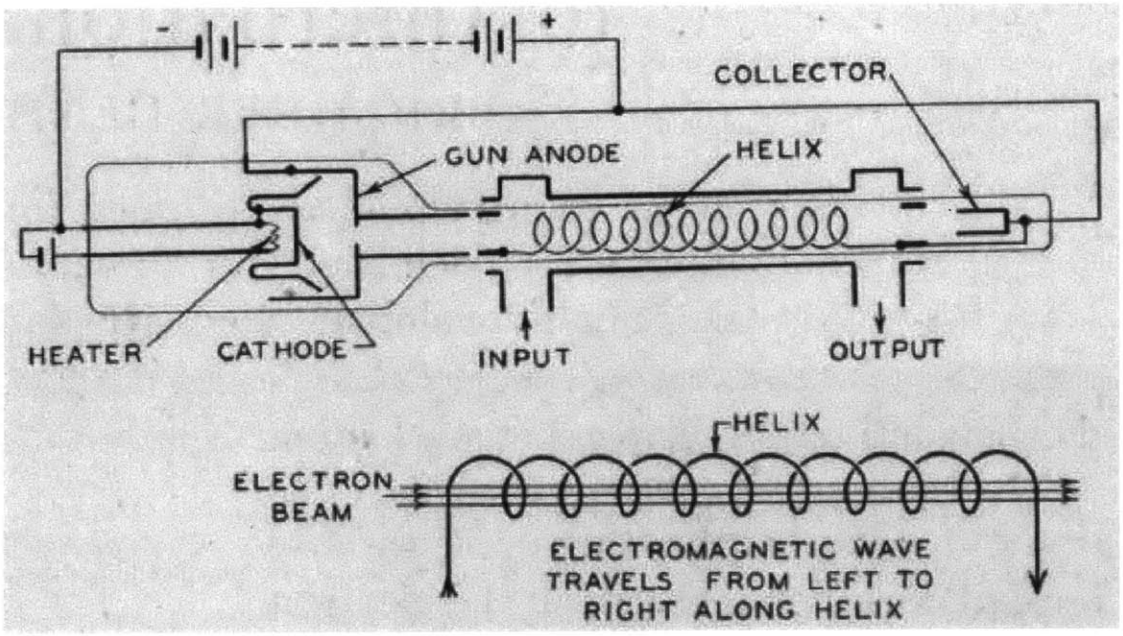

Figure 1-3: Schematic of a helical TWT. A Pierce gun consisting of an anode and a heated cathode emits an electron beam along the axis of the device. The electron beam interacts with rf power input into a helical circuit which amplifies the rf fields over the length of the device. The spent electron beam is then captured by a collector. Adapted from [21].

Early TWTs used a helical geometry, with the earliest work being attributed to Rudolf Kompfner during World War II [22]. Work on the TWT continued at Bell Labs

through the 1940s, and by the latter part of the decade, the helical TWT had demonstrated 23 dB of gain (200 mW output power) at 3.6 GHz with a bandwidth of 800 MHz [21]. While not necessarily capable of the power levels of the klystron, the TWT is a compact and robust device capable of moderate output powers with large bandwidths, and therefore these early TWTs would find a use as transponders on satellite communication systems as well as other airborne radar and communication systems [23].

The modern day helical TWT is generally limited to frequencies less than 100 GHz and kilowatt power levels due to the power handling capabilities of its components, however coupled-cavity TWTs are capable of MW power levels at S-band and C-band in pulsed operation, with similar average power capability to the klystron in this range. Nonetheless, the fact that the device's geometry must scale with the shrinking wavelength at higher frequencies further compounds issues with heat conduction as well as beam formation, and structure fabrication and assembly. Still, the attractive attributes of the TWT have continued to drive research in the field with hopes of compact, reliable devices at higher frequencies. One potential area for advancement is in the interaction structure. While a conventional coupled-cavity TWT producing over 100 W in the 80-100 GHz frequency range has been demonstrated [24], experiments are underway at MIT for the development of an overmoded coupled-cavity TWT to produce 300 W at 94 GHz [25]. By adding mode selectivity to the structure, some dimensions may be larger thus easing the fabrication of smaller features and also providing the opportunity to scale the device to higher frequencies before encountering limits imposed by machining capabilities and heat dissipation. Additionally, research into more advanced machining techniques can yield progress in the development of high frequency TWTs as researchers at the Naval Research Laboratory are currently in the midst of experiments on a 60 W, 220 GHz folded-waveguide TWT [26]. Another recent TWT-based device has even demonstrated the capability of generating 100 mW of power at 650 GHz [27].

Despite thriving in this "golden age", one final invention from the 1940s, the transistor, would spell the end to any dreams researchers might have had of a world whose technology was based solely on vacuum electronics. While the magnetron is aptly described as one of the most important devices arising in the 20th century, the transistor is oftentimes referred to as the single most important discovery of the 20th century.

1.1.3 The "Death" of Vacuum Tubes

Perhaps the term "death" is a bit excessive and misleading, but when John Bardeen and Walter Brattain experimentally observed the world's first functioning transistor in 1947, leading themselves and William Shockley to the 1956 Nobel Prize in Physics, the reverberations of the discovery were felt throughout the scientific world. By placing two gold point contacts on a small slab of semiconductor, in this case germanium with dimensions on the order of half an inch, Bardeen and Brattain were able to observe an amplification of a signal by a factor of several hundred. This tiny transistor would serve as the fundamental building block for a new generation of solid-state devices, providing complex switching and amplifier circuits in a substantially more compact package than could be accomplished using any vacuum electron device. By the mid-1950s, the transistor was taking over the world of consumer electronics. Gone were the large, bulky vacuum tube radios, as they were replaced by new, portable, transistor radios. Not only is the transistor much smaller and more reliable than many vacuum tubes, but it is also incredibly easy and cheap to make, paving the way for modern electronics and today's computing capabilities. Over time, feature sizes have shrunk from millimeters to microns and then to nanometers, with millions, and even billions, of transistors now being placed on a single chip.

A vacuum tube could never hope to match transistor technology for such applications, but solid state electronics are not limitless. In fact, there are two major limitations to solid-state devices. Even at modest frequencies, the power handling

capabilities of solid-state devices are limited; therefore, when very high powers are necessary, often times some sort of vacuum tube based technology is necessary. At the same time, as the wavelength gets smaller and smaller and approaches the feature size of some components, many fundamental approximations in the design and operation of solid-state circuits break down. This results in a sharp degradation in performance of these devices at higher frequencies. Therefore, while solid-state devices may have become the obvious technology of choice for the plethora of low frequency and relatively low power applications, some exciting research areas still exist that require high power and/or high frequency sources.

Thus, the invention of the transistor did not kill off the field of vacuum electronics at all. Rather, it encouraged a renewed focus on particular areas of the electromagnetic spectrum that would usher in a new generation of vacuum electron devices where exciting new applications awaited.

1.1.4 Modern Vacuum Electronics: The Electron Cyclotron Maser and Gyro-Devices

Through the 1950s, the groundwork for a new type of interaction was being laid out by the likes of Twiss [28], Schneider [29], and Gaponov [30]. These works described the possibility of negative absorption of electrons rotating (gyrating) around a magnetic field, i.e. the electrons could give up energy by exhibiting a bunching around their orbit of the magnetic field lines. Unlike a slow-wave device, such as the TWT, where the rf field has a phase velocity that is slowed to interact with the electrons, this interaction could take place between the electrons and fast waves (rf waves where the phase velocity is greater than c, the speed of light), like those that occur due to the excitation of a waveguide mode in a metallic cavity. While some early experiments may have witnessed this orbital phase bunching mechanism [31-33], it was the experiment by Hirshfield and Wachtel in 1964 that confirmed its existence and applied the moniker "electron cyclotron maser" to the device

[34]. In their experiment, the electron beam is first passed through a periodic corkscrew which acts to transfer some of the electrons axial kinetic energy into transverse motion. The electrons then encounter a large magnetic hill which compresses the beam adiabatically and increases the beam's transverse energy as it passes through a closed cylindrical interaction cavity in the center of this region of high magnetic field. Unfortunately, while this experiment did manage to demonstrate the implementation of this new type of interaction, a mere 10 mW of output power was achieved at a frequency of 5.8 GHz. This was hardly comparable to any conventional microwave tube and caused many laboratories to lose interest in this work [35]. A new configuration would be necessary to reach the goal of a practical cyclotron maser device.

The next big step would be taken under the Iron Curtain in the USSR in the 1960s. The configuration developed by the Russian scientists involved the formation of an annular electron beam using a magnetron injection gun (MIG) which propagates helically through an open cavity resonator located in a large axial magnetic field [36, 37]. The device that they invented is now known as the gyrotron or, more specifically, a gyrotron oscillator, and is also sometimes referred to as a gyromonotron. Given the status of foreign relations in this era, information did not necessarily flow freely from the Soviet Union, and much of the early work on gyrotrons stayed within its borders. Gyrotron development in Russia in the 1970s was largely successful as they investigated issues like cavity profiles and the effects of electron velocity dispersion and eventually realized devices capable of generating kilowatts of power up to 300 GHz [38-41]. In 1977, the Russian scientists would finally share their developments with the western world [42] and spark a renewed interest in the field, both in academia and in industry [43]. Research took off in a number of directions. The linear theory [44, 45] and non-linear theory [46] of gyrotron operation were revisited and the design potential was explored [47, 48]. At the same time, experiments were underway in a number of different laboratories. A number of gyrotrons quickly surpassed 100 kW of output power: a pulsed 140 GHz gyrotron at

MIT [49], and long-pulse gyrotrons like the 35 GHz tube at the Naval Research Laboratory [50], the 60 GHz tube at Varian Associates (now Communications and Power Industries) [51], and the 100 GHz tube at Thomson-CSF (now Thales) [11, 52].

Since the gyrotron is the basis of this thesis work, an in depth look at modern day gyrotrons and their applications will follow in the subsequent section, but even in the early days of gyrotron development, a niche had already been carved out that other devices could not match. It is also noted that a whole series of other gyro-devices exists similar to the different types of conventional tubes: devices like the gyro-klystron, gyro-TWT, and gyro-BWO (backward-wave oscillator) have all been realized and have demonstrated tremendous potential; however, discussions here will remain focused on the gyrotron oscillator.

1.2 Gyrotrons: Applications and Achievements

1.2.1 Microwave sources

In the previous section, the development of a number of different types of sources was outlined, and in many cases, development of these sources continues to this day. The ultimate decision on which source fits an application can be based on a number of factors. There are obvious constraints, such as the device's capability of providing the necessary output power at the required frequency, and more subtle issues, like bandwidth requirements or size and weight constraints. In most practical cases where a number of sources are available, the source that is the cheapest and easiest to fabricate will be selected. The capabilities of a number of solid-state and vacuum electron devices are shown in Figure 1-4. In this figure, it is clear that there is a distinct region in which the gyrotron is the only device capable of operation. Indeed there are numerous important and exciting applications that require sources in this region. For simplicity, gyrotrons can be broken down into two different classes: high-power megawatt class gyrotrons at frequencies from 10 to 200 GHz, and high-frequency gyrotrons with modest power outputs

(on the order of watts) and frequencies in the 100s of GHz and approaching 1 THz. The region between 300 GHz and 10 THz is often referred to as the "Terahertz Gap," due to the lack of available sources at these frequencies. In Figure 1-4, the lower end of the gap is apparent as solid-state and even gyro-devices see their power capabilities roll off at higher frequencies. The other side of the gap is lasers. Lasers can provide significant power at much higher frequencies, however their performance degrades sharply as the wavelength gets longer, and can only produce negligible power as the frequency approaches 1 THz. While gyrotrons may someday fill the need for terahertz sources for applications like detection of cancerous tissues, chemical identification, and imaging systems that can see through clothing and other non-metallic materials, these applications still remain largely undeveloped. It is important, now, to explore the applications that have pushed gyrotron development through the years, and continue to do so to this day.

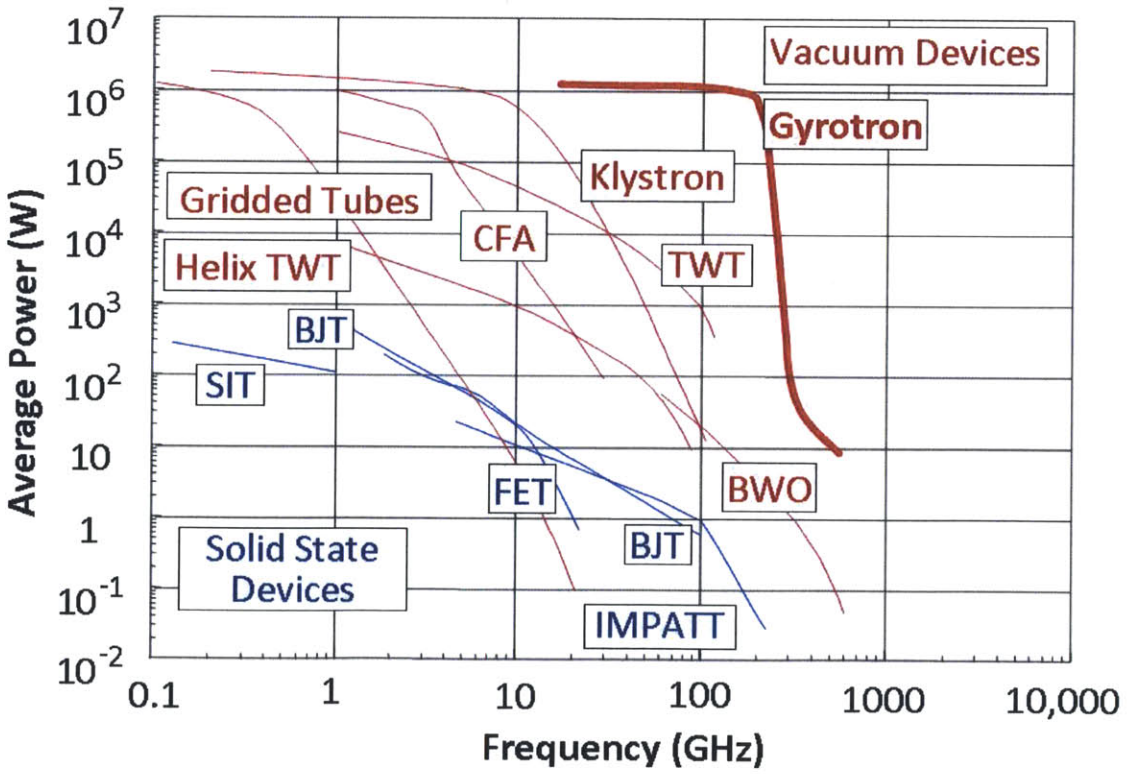

Figure 1-4: Comparison of the average output power vs. frequency for many solid-state and vacuum electron devices. Modified from [53].

1.2.2 Megawatt Gyrotrons for Fusion

From the earliest days of the gyrotron in Russia, one of the main driving forces behind the device was to fill the need for high power and high frequency sources for magnetic fusion experiments. As soon as gyrotron technology spread to the rest of the world, its value as a resource for fusion research was also apparent and continued to drive the technology forward to higher frequencies and powers [54, 55].

For the uninitiated, nuclear fusion is a promising renewable power source for the future based on the reaction where two hydrogen isotopes fuse together to form a helium atom and a neutron while emitting a relatively large amount of energy. Nuclear fusion could promise clean power free of environmentally harmful emissions, like those that occur in the burning of fossil fuels, and free of radioactive byproducts, like the spent fuel of a nuclear (fission) reactor. While the fusion reaction is naturally occurring, it is extremely rare at standard temperatures and pressures. Therefore, fusion scientists are exploring two main avenues of achieving the goal of a reactor that could produce practical amounts of energy. No matter which path is taken, in order to reach practical reaction rates, a large energy input into the system is required. The first obstacle towards fusion is reaching the "ignition" point, meaning that the fusion reactions are producing more energy than was put into the system and the reaction could be self-sustaining (given the right conditions, of course). One option is inertial confinement fusion, which attempts to generate significant fusion energy by heating and compressing a hydrogen fuel target with large amounts of laser energy. The National Ignition Facility (NIF), which strikes fuel targets with 192 laser beams, was recently built and experiments are ongoing to attempt to achieve ignition [56-60]. The other option to achieve ignition is magnetic confinement fusion. In this type of system, the fusion fuel is heated significantly and becomes a plasma, which is a state of matter where the atom breaks apart and exists as two distinct species: ions and electrons. Since both species are charged, the heated fuel can be confined by magnetic fields and behaves much like a fluid. A variety of ways exist to heat the plasma,

all coming with their own technical challenges and limitations. Some examples include Ohmic heating, ion cyclotron heating, and lower hybrid heating. However, it is electron cyclotron heating (ECH), also called electron cyclotron resonance heating (ECRH), which is made possible by gyrotron technology.

Electron cyclotron heating involves the transfer of energy from electromagnetic waves to the fuel's electrons by means of a cyclotron damping, or collisionless damping, mechanism. This energy transfer can take place when the frequency of the wave is approximately equal to the cyclotron resonance frequency of the electrons and is proportional to the strength of the magnetic field. ECH presents several advantages over other types of plasma heating. First, due to the variation in magnetic field strength throughout the plasma, ECH allows for localized heating since the resonant frequency will only match the electromagnetic waves in a specific region. A second benefit of ECH technology is that the ECH power is easy to transmit to the fusion reactor and can be launched into the plasma from a safe distance, in contrast to other heating mechanisms which may require launching antennae to be placed directly adjacent to the plasma [35].

Development of fusion gyrotrons, though, is no easy task. These experiments demand high power, ideally at or above 1 MW, to minimize the required number of gyrotrons and long pulse lengths, on the order of seconds. Such operating conditions place a tremendous heat load on the device. In addition, the magnetic fields in the fusion experiments are quite powerful, typically 4 T or larger, meaning that the ECH frequency is over 100 GHz. Some examples of active ECH systems include the DIII-D tokamak at General Atomics in San Diego, CA which has six 1 MW gyrotrons operating at 110 GHz, a 1.2 MW gyrotron at 110 GHz and a 1.5 MW, 117 GHz gyrotron under development [61], the ASDEX Upgrade tokamak in Germany which has four 0.7 MW gyrotrons operating at 140 GHz [62], and the LHD stellarator in Japan which has four 0.4 MW gyrotrons operating at 168 GHz [63]. The requirements for future ECH systems will be even more challenging for the gyrotron community. The upcoming international ITER tokamak, for which

construction has recently begun in France, will have a 170 GHz ECH system with twenty-four 1 MW gyrotrons capable of continuous-wave (CW) operation for up to 100 s [64, 65]. Another project, the W7-X stellarator in Germany, is also placing a heavy demand for gyrotrons, as it plans to implement 10 1 MW gyrotrons capable of CW operation for up to 1800 s for its 140 GHz ECH system [66].

Research and development for the next generation of fusion gyrotrons is well underway in the United States, Europe, Russia, and Japan. The latest results reported by the various groups are shown in Table 1-1. ITER gyrotrons built in Japan and Russia have already met the specifications, and the outputs produced by these state-of-the-art gyrotrons are constantly improving due to the current feverish pace of research with production deadlines for ITER looming near. However, it should be noted that this has been no easy task and a great number of technological hurdles have been overcome to improve the efficiency and stability of these devices. Optimism is high as gyrotron research puts an eye towards the next generation of fusion gyrotrons.

Table 1-1: Reported results for long pulse, MW power level gyrotrons.

Institution	Frequency	Power	Pulse Length
JAEA (Japan) [67]	170 GHz	1.0 MW	800 s
CPI (USA) [68]	110 GHz	1.2 MW	10 s
CPI (USA) [69]	140 GHz	0.9 MW	1800 s
GYCOM (Russia) [70]	170 GHz	1.0 MW	500 s
	170 GHz	0.9 MW	1000 s
KIT (Germany) [71]	140 GHz	1.0 MW	350 s
KIT (Germany) [72]	170 GHz	2.2 MW	1 ms (prototype)

In addition to simply heating the plasma, the ECH power has also been shown to provide some other beneficial effects in fusion experiments. For example, when a resonant electron absorbs rf power from the ECH system, its velocity increases only along

one axis. By selectively heating electrons moving in one direction, a net current can be achieved and this process is known as electron cyclotron current drive (ECCD) [73]. Fusion scientists have discovered a number of phenomena through experiments that have highlighted the challenges of controlling and sustaining a plasma for a viable fusion reactor. Many performance degrading instabilities have been observed, like the neoclassical tearing modes (NTMs) that may break up the magnetic surfaces that confine the plasma [74]. Thankfully, it has been shown that ECH/ECCD can be used to suppress these NTMs and other undesirable instabilities that arise, and may also provide assistance to plasma initiation and control [75-80].

Developing an ECH/ECCD system for a project like ITER is no simple task. Figure 1-5 shows the conceptual design of the reactor as well as a schematic of the ECH/ECCD delivery system, which includes equatorial launchers for plasma heating and upper launchers for mode stabilization. The progress of the gyrotron development has already been discussed, but there have also been large research efforts in other areas, like the design of a large scale efficient, low-loss transmission line system to bring the gyrotron power to the tokamak [81] and the design of smaller components like the steerable upper launchers [82]. Though rife with technical challenges, the ITER team expects the project to be operational by the end of the decade.

1.2.3 High Power Gyro-Devices for Radar and Industry

While the fusion application drove much of the high-power gyrotron development, scientists began to explore other uses for these gyrotrons. Various materials processing applications have emerged including the sintering of ceramics, the application of coatings, and the joining of materials [83]. The gyrotrons used for this application typically have output powers in the 10s or 100s of kilowatts and frequencies in the 10s of GHz [84]. The advantage of using millimeter-waves for these purposes relates to their ability to couple strongly to the ceramic materials as well their ability to penetrate deeper into the material

for localized heating and to heat it evenly [35]. A number of more compact gyrotron systems have been developed for these applications and research is ongoing to make the technology as easy to use and cost effective as possible.

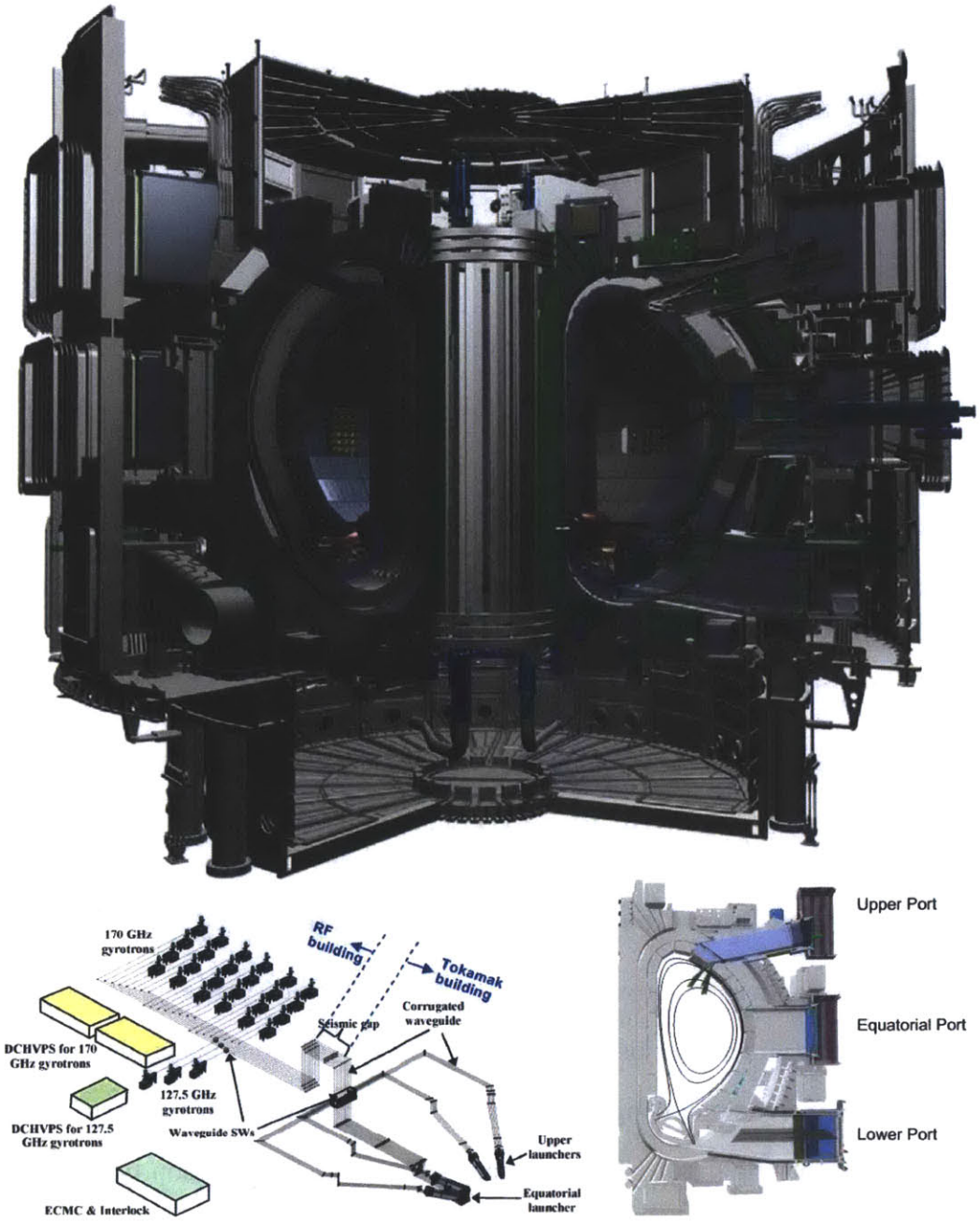

Figure 1-5: Conceptual design of the ITER reactor and its electron cyclotron heating and current drive (ECH/ECCD) system. Adapted from [85] (ITER reactor), [86] (ECH/ECCD system), and [82] (launchers).

For radar applications, it is the gyro-amplifier that is the source of choice due to its large bandwidth capabilities and capacity for a phase-stable output [87]. The millimeter-wave frequency range is attractive for radar not just for the ability to generate higher resolution radar systems due to the shorter wavelength, but also for atmospheric "windows" that exist at 35 GHz and 94 GHz. At these frequencies, the frequency dependent energy absorption by molecules in air, like water, is at a minimum, which allows for better transmission of radar power. Such gyro-devices definitely have the potential to match and exceed the average power capabilities of TWT or EIK technology at these frequencies, though this comes at the expense of size, weight, and cost. Nonetheless, it makes for an attractive option for ground-based or ship-based radar systems where high power is desired. Gyro-amplifiers may also find a place as sources for future linear collider experiments as physicists set their sights towards higher energy systems [88].

1.2.4 Terahertz Gyrotrons

Previously, a number of terahertz applications were presented, and while researchers have kept an eye towards these goals, the development of high frequency gyrotrons that push towards the terahertz gap has been largely driven by a different application: nuclear magnetic resonance (NMR) spectroscopy. NMR is a popular spectroscopic tool for mapping proteins and chemicals and has applications in a number of other areas as well. NMR is based on the resonant radiation of an isotope's nuclei due to their quantum spin when placed within a magnetic field. One of the major challenges in this type of spectroscopy arises from the fact that the resultant NMR signal is fairly weak, and presents a rather poor signal to noise ratio (SNR). However, techniques do exist to improve this issue, one such example being dynamic nuclear polarization (DNP). DNP typically enhances the NMR signal by a factor of ~100 by irradiating the sample with high-frequency waves which transfers the large polarization of electronic spins to the nuclear spins [89]. This enhancement may reduce the acquisition time in an NMR experiment by a

factor of 10,000 [90]. Typical NMR systems operate at frequencies in the 100s of MHz with strong magnetic fields, greater than 5 T, which require DNP frequencies of over 100 GHz. The gyrotron is, thus, ideally suited to satisfy the needs for such systems as there is a dearth of other sources capable of supplying the watts of power needed for these experiments.

Table 1-2: Reported results for THz gyrotrons

Institution	Year	Frequency	Power
MIT (USA) [91]	2012	250 GHz	35 W
MIT (USA) [92]	2011	330 GHz	18 W
CPI (USA) [93]	2010	263 GHz	80 W
Fukui (Japan) [94, 95]	2010	395 GHz	40 W
MIT (USA) [95]	2010	460 GHz	16 W
IAP (Russia) [96]	2009	260 GHz	100 W
MIT (USA) [97]	2000	250 GHz	30 W
Fukui (Japan) [98]	1998	301 GHz	17 W
IAP (Russia) [99]	2008	1.022 THz	1500 W (pulsed solenoid)

Just as in other areas, NMR scientists aim to push their experiments to higher fields and, thus, higher frequencies. This push has led to the development of a number of gyrotrons capable of over 10 W of CW output power at frequencies determined by the NMR systems. The achievements of several THz DNP gyrotrons are shown in Table 1-2. The 460 GHz gyrotron developed at MIT was used in a 700 MHz DNP/NMR system, making it the highest frequency operational system at the time of its completion [100]; however, the push to higher frequencies has continued, and DNP/NMR at 527 GHz / 800 MHz has since been demonstrated [101].

1.3 This Work

In this chapter, the motivations for and the historical development of microwave sources have been presented, with an emphasis on the gyrotron. This thesis will summarize experimental and theoretical work on a pulsed megawatt class gyrotron. The results presented in this thesis were obtained using two different configurations of the gyrotron: a high efficiency 110 GHz design which was previously developed and was tested for efficiency and mode competition as part of this thesis work, and a dual frequency 110/124.5 GHz gyrotron configuration whose components were designed, fabricated, and tested as part of this thesis work.

In Chapter 2, the principles of operation of gyrotrons will be discussed, including a description of the theory behind the gyrotron interaction. Chapter 3 will describe the experimental setup and diagnostic equipment and detail experimental results for the original high efficiency configuration. Chapter 4 will present further experimental results using this original configuration with a special focus on the start-up scenario of the gyrotron, i.e. the sequence of mode excitation that occurs during the rise of the voltage pulse. Chapter 5 will discuss the design of new components for the dual frequency configuration and the experimental results that were achieved. Finally, conclusions and future recommendations will be presented in Chapter 6.

Chapter 2

Principles of Gyrotron Operation

This chapter describes the gyrotron and how it functions. The discussion begins with an overview of the gyrotron and its components from a more general perspective, allowing for a basic understanding of the device for readers of broader backgrounds. This general description of the device will then be complemented with the specific theory behind gyrotron operation, including the theory of the electron cyclotron maser interaction and a non-linear gyrotron theory that allows for the full determination of device efficiency.

2.1 Gyrotron Overview

The gyrotron was briefly introduced in Chapter 1. To understand how the gyrotron operates, it is best to first consult a schematic of a gyrotron, like the one shown in Figure 2-1. Conceptually, the gyrotron can be broken up into three processes: electron beam formation/propagation, wave-beam interaction, and microwave extraction/beam collection. In the following subsections, these processes will be explored, along with the governing laws and equations that describe them.

2.1.1 Electron Beam Formation and Propagation

The principal component of electron beam formation is an electron gun, or specifically a magnetron injection gun (MIG) in gyrotrons. A diode configuration, as shown in Figure 2-1, is used in the experiments detailed in this work, meaning that the gun is comprised

simply of a cathode and a single anode. Many different types of cathodes exist, like the M-type cathode consisting of a porous tungsten pellet impregnated by a mixture of BaO, CaO, and Al_2O_3 and coated with osmium. While the materials science behind cathodes is quite complex, the overall goal is a metal with a low work function, which is the minimum amount of energy needed to break the atomic bonds and draw an electron to the surface of the metal.

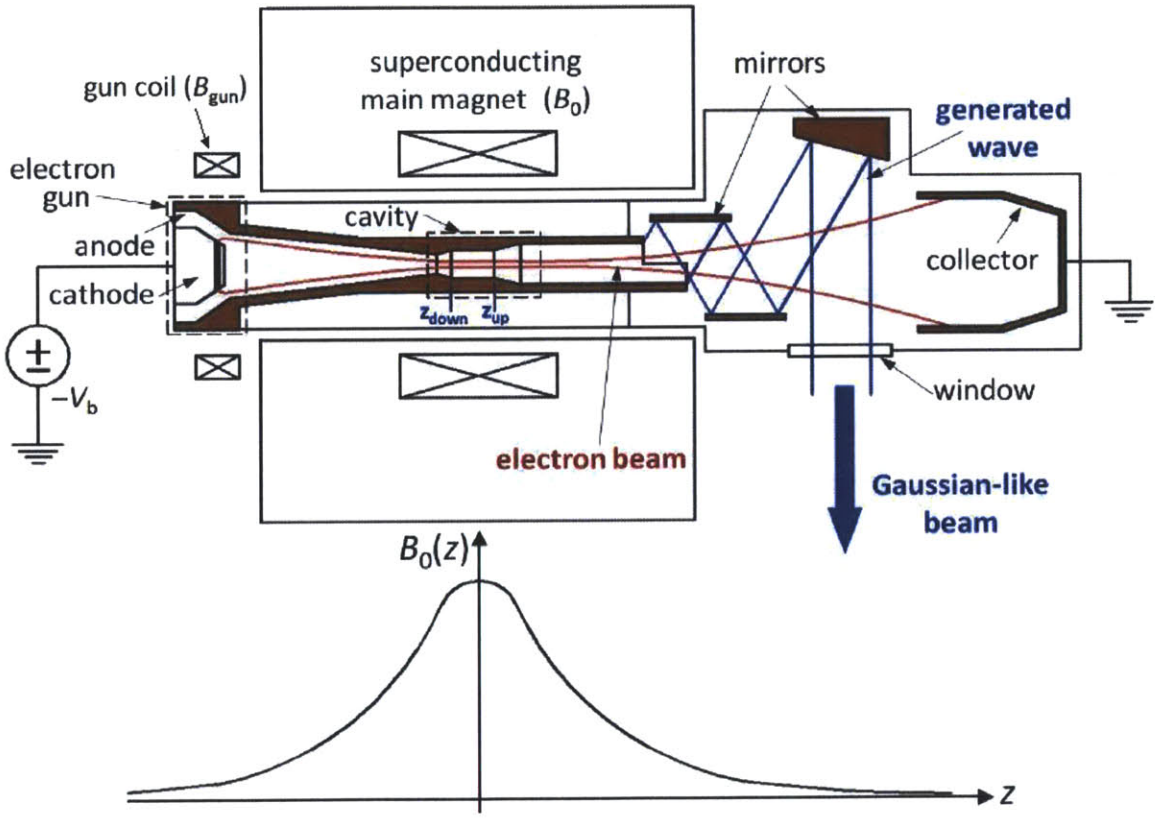

Figure 2-1: Schematic of a gyrotron oscillator. An electron beam is drawn towards a grounded anode from the surface of a heated thermionic cathode held at a high negative potential. The electron beam is compressed by a powerful magnetic field, B_0, where it interacts with an electromagnetic mode of a cavity located at the center of the solenoidal superconducting magnet. The wave power is extracted through a quartz window by means of a mode converter and a set of copper mirrors. The electron beam terminates on a grounded copper collector. Modified from [102].

In a MIG, the annular cathode ring is placed on a solid stock with a heating filament. Electrons are drawn to the surface of the cathode by means of thermionic emission as the cathode is heated to temperatures of ~1000°C. They are then accelerated towards the anode when a large negative DC voltage is applied at the cathode while the anode is maintained at ground potential. Two regions of operation exist for such a gun: a space-charge-limited regime and a temperature-limited regime. In the space-charge limited regime, the electron population at the surface saturates and prevents further electrons from being drawn to the surface without increasing the applied voltage and accelerating more electrons towards the anode. In the temperature-limited regime, the population of electrons at the surface is wholly accelerated towards the anode, and the emitted current can only be increased by raising the cathode temperature and thus the amount of electrons being drawn to the surface. There is also an additional element in the temperature-limited regime from the Schottky effect, in which the electric field at the cathode surface causes an effective lowering of the metal's work function and enhances emission. The emitted current density for the space-charge-limited regime is given by the Child-Langmuir law:

$$J_{SCL} = \frac{4\varepsilon_0\sqrt{2e/m_e}}{9d^2}V^{3/2} \tag{2.1}$$

where e is the charge of an electron, m_e is its mass, ε_0 is the permittivity of free space, d is the spacing between the cathode and anode, and $-V$ is the cathode voltage. The combination of the terms that relate the scaling of current to the voltage to the 3/2 power is known as the gun's perveance, κ. This law applies only up to some threshold voltage at which point the current emission will be described by the Richardson-Dushman equation for the temperature-limited regime:

$$J_{TL} = \lambda_R A_0 T^2 \exp\left[\frac{-e}{kT}\left(\varphi - \sqrt{\frac{eE}{4\pi\varepsilon_0}}\right)\right] \tag{2.2}$$

where A_0 = 120 A/cm^{2}K^2 is a constant, λ_R is a material-specific correction factor (~0.5) [103], T is the cathode temperature, e is the elementary charge, k is the Boltzmann constant, φ is the cathode work function, and E is the electric field at the cathode surface [104]. A sample I-V curve is shown in Figure 2-2, where the transition between the two operational regions of the electron gun is easily observed around 15-20 kV. The exact transition point is ill-defined due to a finite spread in the value of the work function throughout the cathode [105].

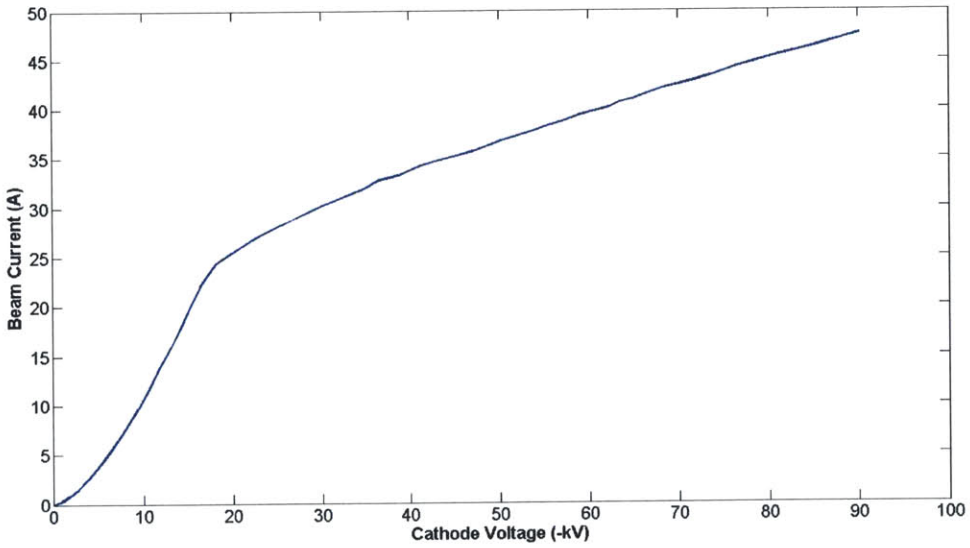

Figure 2-2: Sample I-V curve for the electron gun used in the MIT 1.5 MW, 110 GHz gyrotron experiment. At higher voltages the gun operates in the temperature-limited regime. Below 15-20 kV, it operates in the space-charge-limited regime.

Electron guns for megawatt class gyrotrons require high beam power and operate at high voltages (50-100 kV), therefore they must operate in the temperature-limited regime. This is convenient for gyrotron operation due to the fact that the beam current depends only weakly on any perturbation to the voltage, and stable beam current is essential for high efficiency operation. For beams of this energy, it is also necessary to recognize that

relativistic effects must be taken into account. Therefore, the mass of the electrons is given by $m = \gamma m_e$ where m_e is the electron rest mass and γ is the relativistic factor defined as:

$$\gamma = \frac{1}{\sqrt{1 - v^2/c^2}} = 1 + \frac{eV}{m_e c^2} \approx 1 + \frac{V(kV)}{511} \tag{2.3}$$

for electrons of velocity v and where c is the speed of light and V is the accelerating potential.

While the potential difference between the cathode and anode accelerates the electrons off the surface of the cathode, the geometry of the gun determines the directionality of the electrons. The MIG, which is located in the tail of the superconducting magnetic field, employs a slanted cathode. This results in crossed electric and magnetic fields at the emitter surface, which imparts an initial transverse velocity, $v_\perp$, into the electrons in addition to their axial velocity, v_z (note that the axis of the superconducting magnetic field is denoted as the **z** axis).

The electrons then propagate through a region of increasing magnetic field as they approach the gyrotron cavity (and the center of the superconducting solenoid). In this region, the beam undergoes an adiabatic compression according to the invariant magnetic moment:

$$\mu = \frac{0.5 m v_\perp^2}{B} = const. \tag{2.4}$$

where m is the particle's mass, or simply:

$$\frac{p_\perp^2}{B} = const. \tag{2.5}$$

for momentum p. The transverse energy of the electron beam thus grows significantly as the beam enters the high-field region. The physical compression of the annular beam

follows from Busch's theorem, where the beam radius, also referred to as the guiding center radius, at position z is defined by:

$$r(z) = r_{cathode}\sqrt{\frac{B_{cathode}}{B_0(z)}} \tag{2.6}$$

where $r_{cathode}$ is the radius of the cathode ring and $B_{cathode}$ is the magnetic field at the gun location [106].

There is also one other element to electron beam formation and that is the role of the gun coil, as seen in Figure 2-1. In this experiment, the gun coil is centered at the axial location of the cathode and takes the form of a water-cooled short solenoid magnet which provides a small variable magnetic field, on the order of 1 % of the peak main magnetic field. The magnetic field at the cathode is thus a superposition of these two fields such that $B_{cathode} = B_{gun} + B_0(z_{cathode})$. The compression ratio (the ratio of the magnetic field at the cavity to the field at the gun) is typically in the 20 to 25 range for a MW gyrotron. By tuning the gun coil field, the beam radius in the cavity may therefore be adjusted as in Eq. (2.6).

As the beam now approaches the cavity located in a region of constant magnetic field, there is an important characteristic of the beam to consider. Recall that, in gyro-devices, the power is extracted from the transverse energy of the electrons, $v_\perp$, for which the interaction will be discussed in detail later in this chapter. It is therefore convenient to define a velocity ratio, known as the pitch factor α, such that:

$$\alpha = \frac{v_\perp}{v_z} \tag{2.7}$$

for electrons with transverse velocity $v_\perp$ and axial velocity v_z. Due to the adiabatic compression of the beam, as described by Eq. (2.4), the normalized transverse velocity, where it's noted that $\beta = v/c$, at the cavity is given by:

$$\beta_{\perp} = \left(\frac{E_{cathode}}{cB_{cathode}}\right)\sqrt{\frac{B_0}{B_{cathode}}} \tag{2.8}$$

where $E_{cathode}$ and $B_{cathode}$ are the electric and magnetic fields at the cathode location, respectively, and B_0 is the cavity magnetic field. It follows that the pitch factor for a beam accelerated by a given voltage is:

$$\alpha = \frac{1}{\sqrt{\frac{\gamma^2 - 1}{\gamma^2 \beta_{\perp}^2} - 1}}. \tag{2.9}$$

The pitch factor may, therefore, also be controlled by tuning the gun coil field, B_{gun}, and altering the magnetic field at the cathode. A high α beam is naturally desirable in a gyrotron, as it means that more transverse energy is available for the interaction, but there are limitations. If α is made too large for a given beam voltage, then the electrons will have insufficient axial energy to climb the magnetic hill of the main magnetic field and will be mirrored back towards the gun. Reflected electrons, of course, are not conducive to stable device operation, and must be avoided.

2.1.2 Wave-Beam Interaction

The annular electron beam, with defined beam energy, pitch factor α, and beam radius, now arrives at the interaction region of the gyrotron. In this region, the magnetic field may be considered constant and aligned purely along the axis of the solenoid, therefore $\mathbf{B} = B_0 \mathbf{z}$. The electrons gyrate around the magnetic field lines at their relativistic cyclotron frequency given by:

$$\omega_c = \frac{eB_0}{\gamma m_e} \tag{2.10}$$

for the relativistic factor γ defined in Eq. (2.3). In order for any transfer of energy to take place, the electron beam and an electromagnetic wave must be synchronous. In the case of

the gyrotron, this synchronism relates to the gyration of the electrons and yields the Doppler shifted resonance:

$$\omega = n\omega_c + k_z v_z \tag{2.11}$$

where ω is the wave frequency, n is an integer harmonic number, k_z is the axial wavenumber of the electromagnetic wave, and v_z is the axial velocity of the electrons. A gyrotron typically operates close to the cutoff frequency of a waveguide mode, meaning that k_z is small, and therefore the final term in Eq. (2.11) may be considered negligible in some analyses. To understand the nature of this interaction, a discussion on the nature of these electromagnetic waves is warranted.

The interaction structure of the gyrotron is quite simple, taking the form of a round, azimuthally symmetric pipe. A gyrotron cavity will include two elements that are crucial to the design: a section of fixed length and constant radius, the true "cavity" region where the interaction takes place, and shallow tapers on either end of the cavity where the wall radius will increase or decrease slightly. To determine the nature of the waves excited in the cavity, first consider a cylindrical metallic waveguide, e.g. a round pipe of infinite extent. The electromagnetic fields in the waveguide result from Maxwell's equations in a cylindrical coordinate system, defined by an axial vector along the direction of propagation, **z**, a radial vector, **ρ**, and an azimuthal vector, **φ**. In vacuum, the constitutive relations are given by $\mathbf{B} = \mu_0\mathbf{H}$ and $\mathbf{D} = \varepsilon_0\mathbf{E}$. A straightforward derivation yields the wave equation for the axial electric and magnetic fields [107]:

$$\left[\frac{1}{\rho}\frac{\partial}{\partial\rho}\left(\rho\frac{\partial}{\partial\rho}\right)+\frac{1}{\rho^2}\frac{\partial^2}{\partial\varphi^2}+k_\perp^2\right]\begin{Bmatrix}E_z\\H_z\end{Bmatrix}=0 \tag{2.12}$$

for a wave propagating in **z** as $\exp(-jk_z z)$ and where the wavenumber, k, is:

$$k^2 = \omega^2 \mu_0 \varepsilon_0 = k_z^2 + k_\perp^2. \tag{2.13}$$

A complete basis set of solutions to this wave equation is obtained and split into two groups: Transverse Electric (TE) waveguide modes, for which the electric field is perpendicular to the direction of propagation and $E_z = 0$, and Transverse Magnetic (TM) modes, for which the magnetic field is purely transverse to the direction of propagation and $H_z = 0$. Although they can be theoretically excited, the group of TM modes may be neglected in gyrotron analyses because their threshold for oscillations is $\sim 1/(\beta_z)^2$ higher than that of TE modes and they have a weaker beam-wave interaction due to a scaling factor of k_z/k in their transverse electric field [108]. The TE solution to this wave equation is of the form:

$$H_z = J_m(k_\perp \rho) \begin{Bmatrix} \sin(m\varphi) \\ \cos(m\varphi) \end{Bmatrix} \exp(jk_z z) \tag{2.14}$$

where J_m is a Bessel function of the mth order and any combination of sinusoidal function may be used to define the azimuthal variation. The electric fields are thus:

$$E_\rho = E_0 \frac{j\omega\mu_0}{\omega^2 \mu_0 \varepsilon_0 - k_z^2} \frac{m}{\rho} J_m(k_\perp \rho) \begin{Bmatrix} \cos(m\varphi) \\ -\sin(m\varphi) \end{Bmatrix} \exp(jk_z z) \tag{2.15}$$

$$E_\varphi = E_0 \frac{-j\omega\mu_0 k_\perp}{\omega^2 \mu_0 \varepsilon_0 - k_z^2} J'_m(k_\perp \rho) \begin{Bmatrix} \sin(m\varphi) \\ \cos(m\varphi) \end{Bmatrix} \exp(jk_z z). \tag{2.16}$$

For a waveguide of radius a, in order to satisfy the boundary condition, E_φ must vanish at $\rho = a$, therefore:

$$J'_m(k_\perp a) = 0 \tag{2.17}$$

and

$$k_\perp = \frac{\nu_{m,n}}{a} \tag{2.18}$$

where $\nu_{m,n}$ denotes the nth zero of the derivative of the J_m Bessel function. Therefore, by noting that $c^2 = 1/(\mu_0 \varepsilon_0)$, the waveguide dispersion relation can be formulated:

$$\omega^2 = c^2\left[k_z^2 + \left(\frac{v_{m,n}}{a}\right)^2\right]. \tag{2.19}$$

The $TE_{m,n}$ mode will thus have m variations around the azimuth and n variations in the radial direction. The value $v_{m,n}$ for the mode can be looked up in a table. In such a waveguide, the values of k_z are continuous, however, unlike this waveguide, the gyrotron cavity is not infinite in extent.

To reconcile the finite gyrotron cavity, consider a cylindrical metallic box, in essence a round waveguide with end plates located at $z = 0$ and $z = L$. The field solution for this closed cavity requires applying additional boundary conditions at the axial limits and defining the axial field profile $f(z)$. This problem yields a solution of the form $f(z) = \sin(k_z z)$, which must vanish at $z = L$, therefore:

$$k_z = \frac{q\pi}{L} \tag{2.20}$$

where q is the axial mode number and can be any positive integer. The cavity mode $TE_{m,n,q}$ will therefore have the transverse field structure of the $TE_{m,n}$ waveguide mode and q variations in the axial direction. The values of k_z are no longer continuous and, instead, solutions only exist for a discrete set of "axial modes".

Finally, consider the case of a gyrotron cavity. The resonator is no longer closed and instead an open resonator is employed with a downtaper to smaller radius on the gun side and an uptaper to larger radius on the collector side, as shown in Figure 2-1. A sinusoidal profile still yields a reasonable approximation to the field profile and can be useful in many analyses; however, in the non-linear theory that follows later in this chapter, a Gaussian field profile is used and provides a much better approximation to the actual field profile for the $q = 1$ modes, which are the modes of interest for high efficiency operation. The Gaussian field profile is given by:

$$f(z) = exp\left(-\left(\frac{2z}{L} \right)^2 \right) \tag{2.21}$$

for a cavity length L. To fully solve for the real axial field profile, computer simulations are required, including both cold cavity codes to approximate the field profile in the absence of the electron beam and self-consistent codes to account for beam effects [109]. While the axial field profile is not as strictly discretized in the case of an open resonator as it is for a closed resonator, the axial mode number q is still attributed to the mode having q variations in the axial direction.

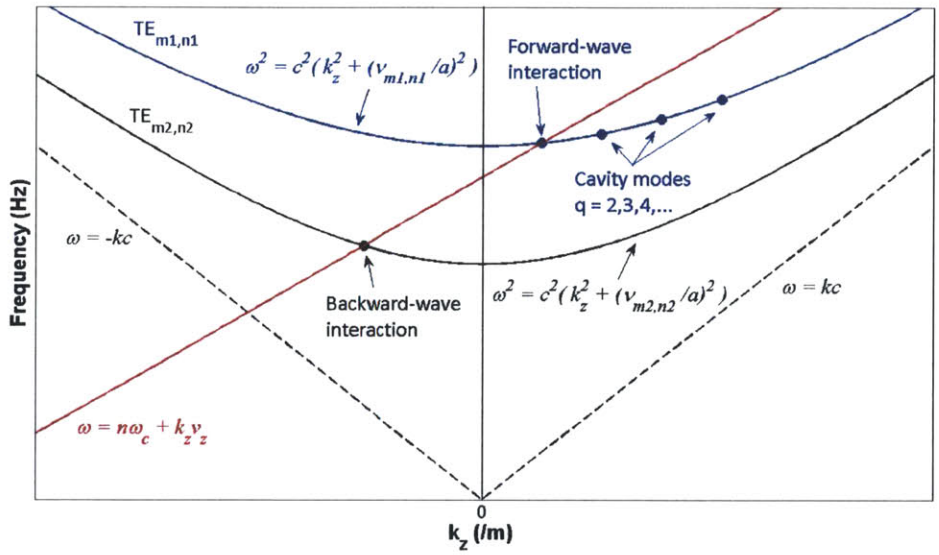

Figure 2-3: Uncoupled dispersion diagram example. Waveguide dispersion curves are plotted along with a beam resonance condition. The diagram shows a possible forward-wave interaction with the $TE_{m1,n1,1}$ cavity mode and a possible backward-wave interaction with the $TE_{m2,n2,2}$ cavity mode.

The beam-wave interaction is better understood by considering the uncoupled dispersion relation obtained by combining the results of the Doppler shifted beam resonance of Eq. (2.11) and the waveguide dispersion of Eq. (2.19). The dispersion diagram is plotted in Figure 2-3. In Figure 2-3, the beam resonance line, which depends on the magnetic field, the beam energy, and the pitch factor, intersects the waveguide dispersion

curves of two different modes. These intersections denote possible beam-wave interactions that, of course, depend on many other factors and may be either forward waves, where $k_z > 0$, or backward waves, where $k_z < 0$. The forward-wave interaction with the $TE_{m1,n1,1}$ mode, which is close to cut-off and thus has small k_z, is the desired excitation for a high power, high efficiency gyrotron [110]. However, there is also a possible backward-wave interaction with the $TE_{m2,n2,2}$ mode, which may be excited instead if there is strong coupling to the mode. This simple example highlights a major challenge in the design of MW gyrotrons as they must operate with large overmoded cavities in very high order modes, like the $TE_{22,6,1}$ mode used in this work. Mode competition is a serious issue when operating with such a dense concentration of modes and it is essential to select a fitting design mode and suitable operating parameters that minimize the effects of parasitic mode excitations.

While this dispersion diagram covers the basis of which modes may be excited, it does not explain why. A detailed explanation follows in the subsequent sections; however, in short form, this interaction begins with the spontaneous radiation by the electrons that excites electromagnetic fields in the cavity. Next, an azimuthal bunching process takes place, which is shown illustratively in Figure 2-4. In Figure 2-4, an annular electron beam with radius R_e gyrates around the field lines of axial magnetic field B_0 in Larmor orbits of radius r_L. In Figure 2-4(a), the phase of the electrons is random. The net energy transfer to or from the beam for such a configuration would be zero, as there are just as many electrons in the decelerating phase (traveling with the electric field and giving up their energy) as there are in the accelerating phase. However, due to the relativistic dependence of the cyclotron frequency as detailed in Eq. (2.10), decelerating electrons that lost energy to the electric field will see an increase in their cyclotron frequency while the converse will occur to electrons that gained energy from the electric field. The resulting effect is that the electrons will bunch in phase. This instability allows the electrons to act

coherently in giving up their energy to the rf fields at the cyclotron resonance. In addition, there is a mismatch at each end of the cavity caused by the tapers that results in a reflection. If these mechanisms are strong enough, the energy gain in the system can overcome the Ohmic and diffractive cavity losses and the fields will grow significantly. Then, the powerful electromagnetic fields can diffract out from the shallow uptaper towards the microwave extraction region.

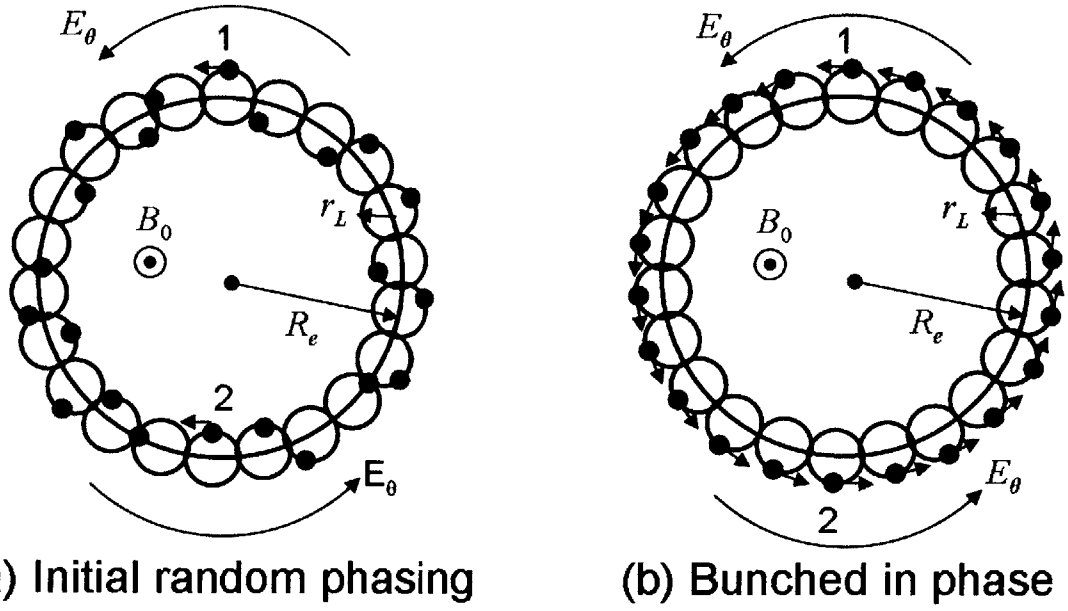

Figure 2-4: Diagram of the gyrotron's azimuthal bunching process. An annular electron beam, of radius R_e, enters a region with an axial magnetic field, B_0, and gyrates around the field lines in Larmor orbits, of radius r_L. While the electrons are randomly distributed in phase initially, the effect of the electric field speeds up some electrons while it slows down others, causing the electrons to bunch in phase. Modified from [111].

2.1.3 Microwave extraction and beam collection

The output taper of the cavity is, essentially, a weakly tapered cylindrical waveguide that allows the high-order TE mode to propagate further down the axis. In the same region, the electron beam, after losing a significant portion of its energy, continues to traverse towards a collector located at the far end of the vacuum tube.

The simplest method of power extraction is to continue propagating the electromagnetic waves axially to a window located at the end of the tube. Early gyrotrons used this approach, and it is still employed occasionally as an experimental configuration; however, it is not particularly practical in a real gyrotron system where the output power is to be used since the spatial intensity pattern of the output radiation is quite complex.

Instead, gyrotrons implement internal mode converters which aim to convert the TE mode into a more practical output for transmission, like a Gaussian beam. An internal mode converter can be seen in Figure 2-1 and consists of a quasi-optical "launcher", i.e. a section of waveguide following the cavity, and a set of copper mirrors. The launcher can be best understood by considering the propagating waveguide mode as a set of rays bouncing around the inside of the waveguide at an angle. By implementing a step-cut at the end of this waveguide, these rays are "launched" out of the waveguide and may be collected on the surface of a copper mirror which directs the power towards a window [112]. In the case of a mode that rotates with the electron beam, such a cut should be helical. By adding perturbations to the surface of the launcher, these rays may become grouped and a Gaussian intensity profile is generated on the surface of the waveguide [113]. Proper design of this launcher allows for this Gaussian profile to be launched from a cut onto the surface of the first mirror. As codes to design these launchers have become more sophisticated, the efficiency of these converters has increased. Output beams with as high as 98 or 99 % Gaussian beam content are now achievable.

Dealing with the spent electron beam is simultaneously a remarkably simple process and a challenging one. In the case of a pulsed gyrotron, even for high beam power, like the ~4 MW of a 96 kV and 40 A beam, at microsecond pulse lengths, this only yields a maximum of a few joules of energy deposited on the collector. Therefore, in such an experiment, the collector may simply be a grounded copper cylinder without any cooling required. In a CW tube, the energy deposition is significant. Not only do these tubes require massive water cooling systems, but they also often implement a sweeping coil,

which is a small variable magnetic field that ensures the beam does not constantly impact the same location on the collector.

An additional element that can be introduced is a "depressed collector." The depressed collector allows for improvement of the gyrotron's overall efficiency by holding the collector at an intermediate potential while maintaining the same potential difference between the cathode and the anode, which is part of the tube's "body". This can be accomplished by either adding a resistive load between the collector and body or using two separate power supplies. Implementation of a depressed collector was part of previous doctoral work on the experiment in this thesis [111], though it was not used as part of this work.

The final component to consider is the window. First and foremost, it must be strong enough to maintain high vacuum in the tube. An additional concern in CW gyrotrons is the heat loading. Diamond windows are thus a necessity in a CW megawatt gyrotron, while a simple fused quartz window will suffice for pulsed operation or for lower power gyrotrons. For a single frequency gyrotron, a single disc window whose thickness is designed for full transmission at that frequency is employed. In instances where frequency transmission over a wider frequency band is desired, then alternatives like a double disc window or a Brewster window must be considered. In experiments like those contained in this work where full transmission is desired at two distinct frequencies, a single disc window may still be employed with more stringent constraints on the thickness. The design and operation of such a window is discussed in the later chapters of this thesis.

2.2 Non-Linear Gyrotron Theory and the Interaction Efficiency

The basis for the gyrotron interaction is the energy dependence of the cyclotron frequency of the weakly relativistic electrons in the gyrotron's annular beam. The non-linear theory

discussed here follows the formalism of Danly and Temkin [46] using a set of normalized parameters and is derived in cgs units.

Begin by considering an electron, whose energy and momentum are given by:

$$\xi = \gamma m_e c^2 \tag{2.22}$$

$$|\vec{p}| = \gamma\beta m_e c \tag{2.23}$$

where the relativistic factor γ was defined in Eq. (2.3). The equations of motion under the effects of electric and magnetic fields are given by:

$$\frac{d\xi}{dt} = -e\vec{v}\cdot\vec{E} \tag{2.24}$$

$$\frac{d\vec{p}}{dt} = -e\vec{E} - \frac{e}{c}\vec{v}\times\vec{B}\,. \tag{2.25}$$

As discussed previously, the electric field is a TE cavity mode with a fixed axial field profile and the magnetic field has amplitude B_0 and is aligned axially. The contribution of the rf magnetic field is small and may be ignored in this analysis.

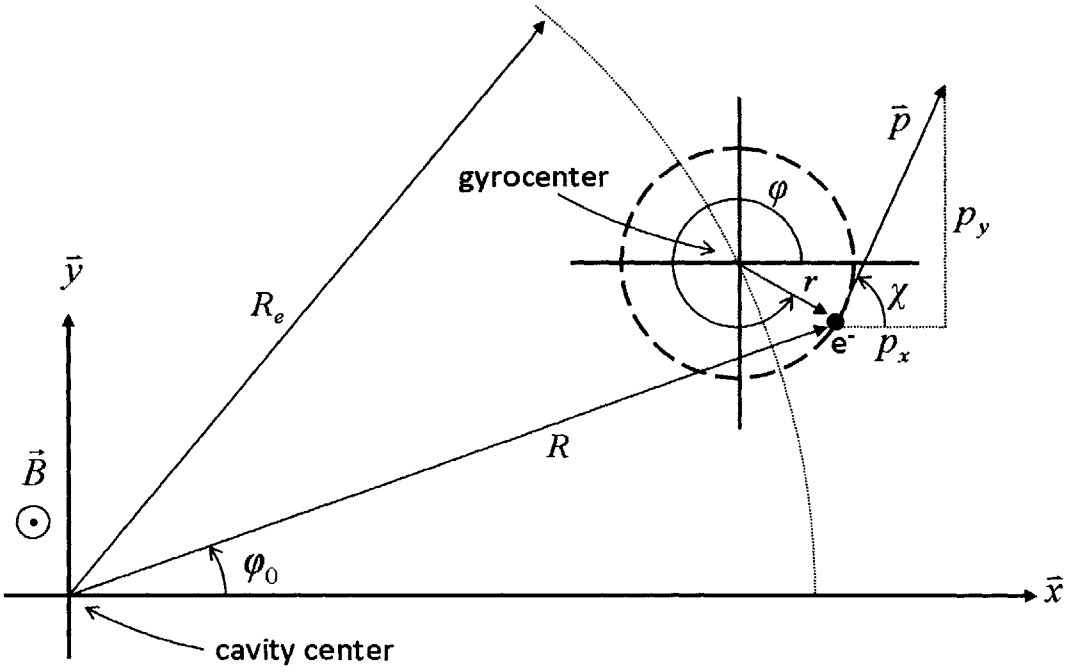

Figure 2-5: Coordinate system of a gyrating electron in a cylindrical cavity.

To track changes in electron energy and velocity, initial values at the entrance of the cavity will be differentiated by adding the subscript zero, i.e. β_0 and γ_0, and a relative energy variable is introduced:

$$w = 1 - \gamma/\gamma_0 \tag{2.26}$$

such that $w = 0$ for electrons having the same energy, $w > 0$ for electrons that have lost energy, and $w < 0$ for electrons that have gained energy. By normalizing the axial position as $Z = (\omega/\beta_{z0}c)z$, the energy of a single electron is:

$$\frac{dw}{dZ} = \frac{e}{(m_e c)^2 \omega} \frac{\beta_{z0}}{\gamma_0 \gamma \beta_z} \vec{p} \cdot \vec{E} \,. \tag{2.27}$$

To visualize this process, it helps to diagram the electron's position in this coordinate system as shown in Figure 2-5. The electron orbits have radius r equal to the Larmor radius. Each electron orbits around its gyrocenter, which is located along the guiding center of the annular beam at a distance R_e from the cavity center. The electron momentum can be expressed in complex notation to describe the transverse plane:

$$\vec{p} = p_x + jp_y = p_+ = |p_+| \exp(j\chi) \tag{2.28}$$

where χ is the angle of the momentum vector about the gyrocenter, and leads the electron phase angle φ by $\pi/2$. The electric field can be expressed similarly such that:

$$\vec{E} = E_x + jE_y = E_+ = |E_+| \exp\big(j(\omega t + \psi)\big) \tag{2.29}$$

where ψ represents an arbitrary initial phase. An equation for the phase of the electron momentum may then be obtained:

$$\frac{d\chi}{dZ} = \frac{\beta_{z0}\omega_c}{\beta_z \omega} - \frac{e\beta_{z0}}{\omega \beta_z |p_+|} \mathrm{Im}(p_+^* E_+) \tag{2.30}$$

where * denotes the complex conjugate and ω_c is the cyclotron frequency given by adding an additional factor of c to the denominator in Eq. (2.10) to account for cgs units. Also,

note that the dot product in Eq. (2.27) is equivalent to the real part of the product between the electric field and the complex conjugate of the momentum.

The electric field for the $TE_{m,p}$ mode near cutoff, $k_z \approx 0$, can be formulated in this coordinate system, shown in Figure 2-5, by referring to Eqs. (2.15), (2.16) and (2.18) and converting from SI to cgs units:

$$\vec{E} = (E_R \vec{R} + E_{\varphi_0} \vec{\varphi}_0) \exp\left(j(\omega t + \psi)\right) \tag{2.31}$$

$$E_R = jE_0 \left(\frac{m}{k_\perp R}\right) f(z) J_m(k_\perp R) \exp(jm\varphi_0) \tag{2.32}$$

$$E_{\varphi_0} = E_0 f(z) J_m'(k_\perp R) \exp(jm\varphi_0) \tag{2.33}$$

for an axial field profile $f(z)$ whose peak value has been normalized to unity. However, in order to determine the effect of the electric field on the electrons, both must be represented in the same reference frame, which is, logically, that of the electron about its gyrocenter. To perform this transformation, Graf's addition theorem is used. The electric field about the electron gyrocenter is thus:

$$\vec{E} = (E_r \vec{r} + E_\varphi \vec{\varphi}) \exp\left(j(\omega t + \psi)\right) \tag{2.34}$$

$$E_r = jE_0 \left(\frac{1}{k_\perp r}\right) f(z) J_{m\pm1}(k_\perp R_e) J_1(k_\perp r) \exp\left(-j(\varphi + (m-1)\varphi_0)\right) \tag{2.35}$$

$$E_\varphi = E_0 f(z) J_{m\pm1}(k_\perp R_e) J_1'(k_\perp r) \exp\left(-j(\varphi + (m-1)\varphi_0)\right). \tag{2.36}$$

The above electric field expressions have been simplified to consider only the first harmonic since that is the relevant operating condition for a megawatt class gyrotron, though the theory is generalized for any harmonic [46]. A slow time scale phase variable may be introduced such that $\theta = \omega t - \varphi$ and the electric field may again be expressed in complex notation:

$$E_+ = -|E_r|\sin[\theta+\psi-(m-1)\varphi_0]e^{j\varphi} + |E_\varphi|\cos[\theta+\psi-(m-1)\varphi_0]je^{j\varphi}. \tag{2.37}$$

Now that both the momentum and electric fields are expressed in complex notation in the electron reference frame, the real and imaginary parts of their product may be computed to obtain real expressions for the equations of motion:

$$\frac{dw}{dZ} = \frac{e}{\gamma_0 m_e c\omega} p'_\perp |E_\varphi| \cos[\theta+\psi-(m-1)\varphi_0] \tag{2.38}$$

$$\frac{d\theta}{dZ} = \delta_0 - w - \frac{e}{\gamma_0 m_e c\omega}\frac{1-w}{p'_\perp}|E_r|\sin[\theta+\psi-(m-1)\varphi_0] \tag{2.39}$$

where

$$p'_\perp = \frac{|p_+|}{\gamma_0 m_e c} = \sqrt{\beta_{\perp 0}^2 - 2w + w^2} \tag{2.40}$$

and an important parameter known as the magnetic field detuning, δ_0, is introduced such that $\delta_0 = 1 - \omega_{c0}/\omega$ for $\omega_{c0} = (eB_0)/(m_e\gamma_0 c)$. To simplify the argument in the sinusoidal terms, recognize that the initial phase of the electric field, ψ, is arbitrary since there is no bunching of the beam at the cavity entrance. This allows for a convenient choice of ψ such that $\psi - (m-1)\,\varphi_0 = -\pi/2$. By additionally taking note that $\omega \approx \omega_{c0}$ for such a first harmonic gyrotron interaction near cutoff, the equations of motion reduce to:

$$\frac{dw}{dZ} = \frac{|E_\varphi|}{B_0} p'_\perp \sin\theta \tag{2.41}$$

$$\frac{d\theta}{dZ} = \delta_0 - w + \frac{|E_r|}{B_0}\frac{(1-w)}{p'_\perp}\cos\theta. \tag{2.42}$$

Examination of these equations points to two bunching mechanisms. According to Eq. (2.41), there is an inertial bunching caused by the electrons' interaction with the azimuthal electric field, E_φ, which directly affects the electron energy w. This is the dominant phase bunching mechanism of the gyrotron. There is also a force bunching mechanism, demonstrated by Eq. (2.42), that contributes to the phase bunching through the radial electric field E_r.

While the dependence of the cyclotron frequency on electron energy has been discussed, recall that the Larmor radius is defined as:

$$r_L = \frac{v_\perp}{\omega_c} = \frac{\gamma m_e c v_\perp}{eB_0} \tag{2.43}$$

and thus also has an energy dependence. Therefore, the term within the Bessel function of the electric fields can be expressed in terms of the energy variable:

$$k_\perp r \approx \frac{\gamma\beta_\perp}{\gamma_0} = \beta_{\perp 0}\sqrt{1-\frac{1}{\beta_{\perp 0}^2}(2w-w^2)} = p'_\perp . \tag{2.44}$$

At this point, it is convenient to redefine the variables of the equations of motion one last time as follows:

$$u = \frac{2}{\beta_{\perp 0}^2} w = \frac{2}{\beta_{\perp 0}^2}\left(1-\frac{\gamma}{\gamma_0}\right) \tag{2.45}$$

$$\zeta = \frac{\beta_{\perp 0}^2}{2} Z = \pi \frac{\beta_{\perp 0}^2}{\beta_{z0}} \frac{z}{\lambda} . \tag{2.46}$$

A new set of normalized parameters may now be introduced such that:

$$\mu \equiv \pi \frac{\beta_{\perp 0}^2}{\beta_{z0}} \frac{L}{\lambda} \tag{2.47}$$

is the normalized length for a cavity of physical length L and:

$$F \equiv \frac{E_0}{B_0} \beta_{\perp 0}^{-3} J_{m\pm 1}(k_\perp R_e) \tag{2.48}$$

is the normalized field parameter where the sign within the Bessel function depends on whether the TE cavity mode rotates with the electron beam (m-1) or whether it is counter-rotating (m+1). A detuning parameter can also be defined:

$$\Delta \equiv \frac{2\delta_0}{\beta_{\perp 0}^2} = \frac{2}{\beta_{\perp 0}^2}\left(1-\frac{\omega_{c0}}{\omega}\right). \tag{2.49}$$

Even in the case of MW gyrotrons, which operate at relatively high voltages of ~70-100 kV, the electron beam is considered weakly relativistic since:

$$\beta_{\perp 0}^2 / 2 << 1 \tag{2.50}$$

is satisfied and allows for the approximation:

$$p'_\perp \approx \sqrt{\beta_{\perp 0}^2 - 2w} = \beta_{\perp 0}\sqrt{1-u}\,. \tag{2.51}$$

This leads to the the final set of simplified equations of motion in terms of the normalized variables from Eqs. (2.45) and (2.46):

$$\frac{du}{d\zeta} = 2Ff(\zeta)\sqrt{1-u}\sin\theta \tag{2.52}$$

$$\frac{d\theta}{d\zeta} = \Delta - u - Ff(\zeta)(1-u)^{-1/2}\cos\theta\,. \tag{2.53}$$

where the small argument expansion of the Bessel functions was used in the case of a weakly relativistic gyrotron.

The efficiency of this interaction may now be determined. The monoenergetic electron beam at the cavity entrance is assumed to have electrons evenly distributed in phase with a relative energy that is naturally 0. The efficiency is defined as:

$$\eta \equiv \frac{\gamma_0 - \gamma}{\gamma_0 - 1} = \frac{\beta_{\perp 0}^2}{2(1-1/\gamma_0)}\eta_\perp = \eta_{el}\eta_\perp \tag{2.54}$$

where the transverse efficiency, $\eta_\perp$, is obtained by averaging the relative energy at the output of the cavity over all initial electron phases such that:

$$\eta_\perp = \langle u(\zeta_{out})\rangle_{\theta_0} \tag{2.55}$$

and the electron efficiency, η_{el}, indicates the amount of transverse energy available for the interaction and may also be expressed as:

$$\frac{v_\perp^2}{v^2} = \frac{\alpha_0^2}{1+\alpha_0^2}\,. \tag{2.56}$$

This system of equations allows for a calculation of the transverse efficiency that depends only on the three normalized parameters F, μ and Δ defined by Eqs. (2.47)-(2.49).

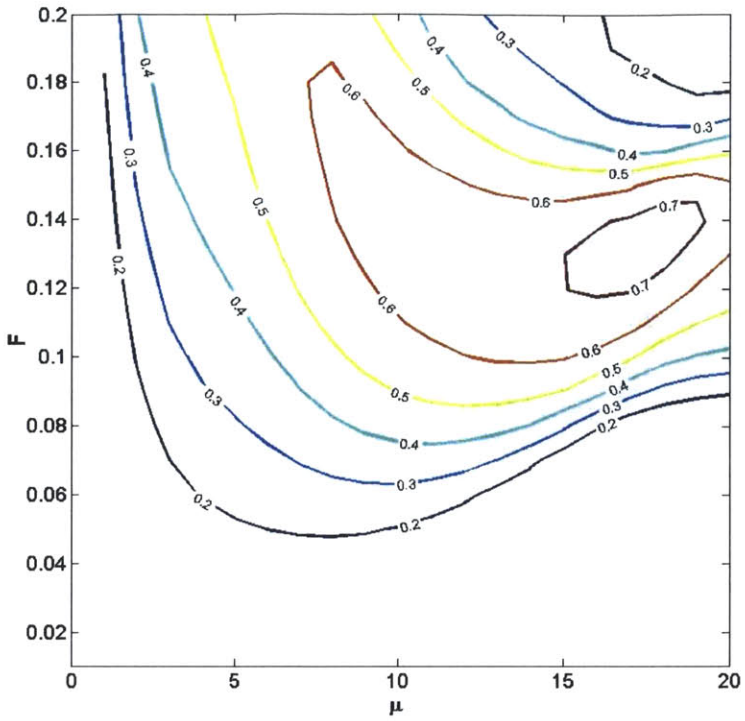

Figure 2-6: Contour plot of the transverse efficiency as a function of the normalized parameters F and.

To calculate the efficiency, a numerical integration using a fourth-order Runge-Kutta algorithm may be employed where the axial field profile is assumed to have a Gaussian distribution. To approximate the rf fields of an open resonator, the limits $\zeta = \pm \sqrt{3}/2$ are chosen [114]. While this yields an efficiency with respect to the three normalized parameters, interpretation of the results is complicated in such a vast parameter space. This problem is rectified by considering that the detuning parameter is controlled by the magnetic field, which is a relatively easy parameter to change. Therefore, the efficiency can be viewed as dependent on the other two parameters, F and μ, with the detuning parameter set to the optimal value, Δ_{opt}, leading to highest efficiency. An example of such a plot is shown in Figure 2-6, which is calculated by averaging the efficiency of a fixed number of particles (32 in this case) that were evenly spaced across all phases at the input. While it appears that there is a single region of optimum efficiency at F = 0.12-0.14 and μ = 16-18 corresponding to a transverse efficiency of a little more than

70 %, there are also other local maxima at higher values of F and μ (not shown). In fact, there exist regions of even higher efficiency. However, operation at these other maxima would present a stiffer challenge, both technologically and theoretically, and thus the gyrotron should be designed around the first optimum region.

2.3 Cavity Losses and the Starting Current

The non-linear theory in the previous section presented a relatively simple solution to a complex problem using a set of normalized parameters; however, for practicality, these parameters must be extended to the real physical parameters of the gyrotron.

Begin by considering the efficiency shown in Eq. (2.54). The power input into the system is given by the electron beam power:

$$P_{in} = I_{beam} V . \tag{2.57}$$

This input power enters the cavity and can either be extracted from the electrons or remains with the electrons such that $P_{in} = P_{cavity} + P_{outputelectrons} = \eta P_{in} + (1-\eta)P_{in}$. As previously discussed, the cavity is an open resonator, meaning that it is a structure capable of storing energy that is introduced into the system before it then dissipates out through a loss mechanism. In such a resonator, there are two loss mechanisms: a resistive loss at the resonator walls due to the finite conductivity of the metallic structure and a diffractive loss due to power radiating out of the resonator ends. The power balance is then $P_{cavity} = \eta P_{in} = P_{ohmic} + P_{diffractive}$. In resonator analysis, an important parameter known as the Q factor is employed which is frequency dependent and relates the energy stored in the system, U, to the power loss, P, such that:

$$Q = \frac{\omega U}{P} . \tag{2.58}$$

Q factors may therefore be defined for each loss mechanism where $P_{cavity} = \omega U/Q_{total}$, $P_{ohmic} = \omega U/Q_o$, and $P_{diffractive} = \omega U/Q_D$, and the Q factors are related such that:

$$\frac{1}{Q_T}=\frac{1}{Q_o}+\frac{1}{Q_D}. \tag{2.59}$$

These parameters may be computed beginning with the stored energy which is evaluated by integrating the electric field over the volume of the resonator:

$$U=\frac{\varepsilon_0}{2}\int_V\left|\vec{E}\right|^2 dV \tag{2.60}$$

where an additional factor of $4\pi\varepsilon_0$ would be present in the denominator for cgs units. For the $TE_{m,p}$ mode in a cylindrical cavity, the stored energy is:

$$U=E_0^2\varepsilon_0\frac{\pi}{2k_\perp^2}(v_{mp}^2-m^2)J_m^2(v_{mp})\int_0^L f(z)dz. \tag{2.61}$$

Next, the ohmic loss may be calculated by integrating the tangential magnetic field at the surface of the resonator:

$$P_{ohmic}=\frac{1}{2\sigma\delta}\int_S\left|\vec{H}_t\right|^2 dS \tag{2.62}$$

where σ is the conductivity of the metal, typically copper, and the skin depth is given by:

$$\delta=\sqrt{\frac{2}{\omega\mu_0\sigma}}. \tag{2.63}$$

The ohmic Q may therefore be calculated:

$$Q_o=\frac{r_{wall}}{\delta}\left(1-\frac{m^2}{v_{mp}^2}\right) \tag{2.64}$$

Ohmic loss is of particular concern in MW gyrotrons due to the intense electron beams that generate powerful electromagnetic fields in the cavity. Cooling such a copper structure can be quite challenging, and there are, of course, limitations. This includes both difficulties in implementing a water cooling system within a vacuum vessel and the limits on how much heat dissipation the cooling system can handle. It is for this reason that MW gyrotrons must employ large overmoded cavities, as explained by the ohmic Q's dependence on cavity radius, r_{wall}, in Eq. (2.64) which is then inversely proportional to the ohmic power dissipation.

For practical gyrotron cavities that may include complex tapers, the diffractive Q is typically computed using a cold-cavity code; however, the basic geometry may be examined here. Recall that the gyrotron's open cavity resonator includes a straight section of length L with a fixed radius, a downtaper to smaller radius towards the gun and an uptaper to larger radius towards the output. At each end of the straight cavity section, the mismatch results in a reflection, with reflection coefficients R_{down} and R_{up}, respectively. The diffractive Q can then be expressed as:

$$Q_D = \frac{Q_{D,\min}}{1-|R_{down}||R_{up}|} \tag{2.65}$$

where the minimum diffractive Q is given by:

$$Q_{D,min} \approx 4\pi\left(\frac{L}{\lambda}\right)^2. \tag{2.66}$$

Since power diffracting towards the gun is undesirable, the cavity is designed such that $R_{down} \approx 1$. This provides a general guideline to the effects of varying cavity parameters like the length and uptaper angle.

These parameters may now be referred back to the result given by the non-linear theory of the previous section. An energy balance equation is introduced relating the normalized field amplitude, F, to a new normalized current parameter, I, by:

$$F^2 = \eta_\perp I. \tag{2.67}$$

By applying Eq. (2.3), (2.58), and (2.61), and assuming a Gaussian axial field profile as given by Eq. (2.21), the normalized current may be defined:

$$I = \frac{e}{4\pi m_e \varepsilon_0 c^3}\frac{Q_T I_{beam}}{\gamma_0}\beta_{\perp 0}^{-4}\frac{\lambda}{L}C_{mp} \tag{2.68}$$

for the actual beam current I_{beam} and assuming first harmonic operation. The C_{mp} term is known as the coupling coefficient and is a geometric factor representing the field intensity of the $TE_{m,p}$ mode at the electron beam location:

$$C_{mp} = \frac{J_{m\pm1}^2(k_\perp R_e)}{(v_{mp}^2 - m^2)J_m^2(v_{mp})} \tag{2.69}$$

where the +/- sign of the Bessel function applies to the counter-rotating or co-rotating mode, respectively. Ideally, the electron beam should be placed along a field maximum of the mode for strongest coupling. Similar to the previous section, efficiency contours can be plotted in the I-μ parameter space. Efficiency contours for several harmonics are plotted in [46].

Another crucial parameter for gyrotron operation is the starting current, a term common to many resonant devices. The starting current indicates the minimum current required to overcome the losses in the cavity, beyond which the fields may grow within the resonant cavity. The starting current may be derived using a linear theory [44] about the energy balance equation given in Eq. (2.67). This analysis will yield an expression for the normalized start current such that:

$$I_{start\_norm} = \left(\left(1 + \frac{\partial}{\partial \Delta} \right) \left| \int_0^\mu f(\zeta) \exp(j \int_0^\zeta \Delta d\zeta') d\zeta \right|^2 \right)^{-1}. \tag{2.70}$$

This expression may be evaluated by assuming a Gaussian axial field profile which yields:

$$I_{start\_norm} = \frac{4}{\pi \mu^2} \frac{\exp(\mu^2 \Delta^2 / 8)}{(\mu^2 \Delta / 4) - 1} \tag{2.71}$$

where both expressions are evaluated at the first harmonic. To determine the minimum start current, Eq. (2.71) must be minimized with respect to Δ where Δ_{min} is given by:

$$\Delta_{min} = \frac{2}{\mu} \left(\sqrt{1 + \frac{1}{\mu^2}} + \frac{1}{\mu} \right) \tag{2.72}$$

To determine the actual starting current, the normalized start current can be related to a corresponding beam current by Eq. (2.68).

The start current is an interesting parameter in MW gyrotrons. In order to operate at the necessary efficiency to produce the highest possible power, the gyrotron must operate in a regime where the beam current is actually smaller than the start current. This

is known as the hard-excitation regime. This means that if the sources were true step functions and the gyrotron cavity was absent of any fields at turn-on then the gyrotron would simply not be capable providing any output power at all. Thankfully, a true step function is non-physical and the gyrotron must progress through some time period where the voltage and current rise from 0. As it happens, during the voltage rise, modes are excited in the soft-excitation regime, that is, where the beam current exceeds the start current. This is known as the start-up scenario. Once these fields attain a certain strength, the hard-excitation regime may be accessed. While a strong seed field is required to enter this regime, it does allow for stable operation. A discussion of theory and experiments relating to the start-up scenario follows in Chapter 4.

2.4 Ohmic Losses and Overall Device Efficiency

Thus far, two terms from the overall device efficiency have been discussed: the transverse efficiency of the gyrotron interaction and the portion of the electron beam's total energy which is in the transverse direction and available for the interaction. Multiplying this efficiency by the total input power from Eq. (2.57) yields the dissipated power in the device. By considering the loss mechanisms described in the previous section, ohmic and diffractive, it is the diffractive loss that constitutes the output power of the device, particularly for a downtaper that is perfectly reflecting where all of the power diffracts out from one end of the cavity. The derivation for $\eta_{rf} = P_{diffractive} / P_{cavity}$ follows from Eqs. (2.58) and (2.59) to yield:

$$\eta_{rf} = \frac{Q_o}{Q_o + Q_D}. \tag{2.73}$$

It is here where gyrotrons may be split into a couple of different groups.

First, consider a gyrotron where the highest possible power is desired. Such a gyrotron would have a very powerful electron beam, and it would be crucial to keep ohmic loss to a minimum. First, this means that a high ohmic Q is desirable, which is achieved

by a cavity that is large in radius compared to the wavelength of operation. Additionally, a low diffractive Q is beneficial to ensure that all of the rf power is diffracted out rather than dissipated in the cavity through ohmic heating, though it must be still large enough to enable the interaction. In successful MW gyrotron designs, η_{rf} of over 98 % can be achieved and wall losses are limited to about 2 kW/cm^2 [47]. These designs operate with large, overmoded cavities in high-order TE modes where the diffractive Q is ~800-1000.

A second type of gyrotron may desire tunability in the output frequency, which may be accomplished by operating in different axial modes through tuning of the voltage or magnetic field [115]. The diffractive Q of modes with q variations in their axial field profile scales by $\sim 1/q^2$, thus in order for the higher order modes to be excited, the diffractive Q must be large. This may be accomplished by implementing a cavity that is quite long compared to the wavelength ($L >> \lambda$). These gyrotrons will have limited output power and generally use cavities with smaller radii operating in lower order modes than would a MW gyrotron. Their beam power is also substantially lower.

There is one final efficiency component to consider. Thus far, the efficiency of the rf power output from the cavity has been obtained, but this energy must somehow be extracted. As discussed previously, most gyrotrons include an internal mode converter (IMC) that generates a Gaussian beam from the high order rotating TE mode. The quasi-optical IMC will have ohmic and diffractive losses as the electric fields propagate through the launcher and reflect off the surface of copper mirrors. The IMC efficiency, η_{IMC}, is then given by the ratio of power extracted from the device to the power output from the cavity. The complex IMCs implemented in gyrotrons have wide varying geometries and may have any number of mirrors. Therefore, there is no analytical expression for this efficiency, and it should be calculated numerically for a specific design. Losses on a well-designed mode converter, however, should be limited to ~2 %. Another metric associated with the IMC is the Gaussian beam content of the output beam. While it technically does

not affect the efficiency, a poor output beam quality will result in additional losses in the external systems making use of the gyrotron output power. Therefore, while the Gaussian beam content of the output beam is not included in the official device efficiency, it is nevertheless an important metric of a gyrotron and will be discussed in the results in this work.

Additionally, a depressed collector may be used to improve the efficiency of the gyrotron, as described previously. A depressed collector is capable of doing so by reducing the required wall plug power rather than improving the efficiency of the device physics. By implementing a depressed collector, the input power may be reduced from $I_{beam}V$ to $I_{beam}(V - V_{DC})$. The first expression is the effective input power for the interaction, while the second term is the actual input power. An efficiency for a simple single-stage depressed collector could be defined as:

$$\eta_{SSDC} = \frac{P_{effective}}{P_{in}} = \frac{I_{beam}V}{I_{beam}(V - V_{DC})} = \frac{1}{\left(1 - V_{SSDC}/V\right)}. \tag{2.74}$$

which is greater than unity for a non-zero depressed collector voltage.

The total device efficiency may now be summarized as follows:

$$\eta_{TOT} = \frac{P_{out}}{P_{in}} = \frac{\eta_{el}\eta_{\perp}\eta_{rf}\eta_{IMC}P_{eff}}{P_{eff}/\eta_{SSDC}} = \eta_{el}\eta_{\perp}\eta_{rf}\eta_{IMC}\eta_{SSDC}. \tag{2.75}$$

where all the efficiencies have been defined in this chapter.

2.5 Space Charge Effects: Voltage Depression and the Limiting Current

While briefly introduced in discussing operation of the electron gun, space charge effects have largely been neglected in the treatment thus far of the interaction region. However, it turns out that they can play an important role.

An annular electron beam propagating through a hollow pipe, like the cavity of a gyrotron, will experience a voltage depression where a portion of the beam's kinetic

energy is converted into potential energy [116, 117]. The voltage depression may be derived by solving Poisson's equation in cylindrical coordinates and is given by:

$$\Delta V = \frac{I_{beam}}{2\pi\varepsilon_0 v_z} \ln\left(\frac{R_{wall}}{R_{beam}}\right). \tag{2.76}$$

In a MW gyrotron, given the high intensity beams with large α values, this quantity is not negligible. In this experiment, where the 96 kV, 40 A beam with α = 1.4 passes through an approximately 2 cm radius cavity with a beam radius of about 1 cm, the voltage depression value is around 5 kV. This value represents a significant energy deviation, and should be taken into account in analyses, like dispersion diagrams, in order to accurately predict and analyze gyrotron operation. In addition, voltage depression also has the effect of increasing the spread in the beam's axial velocity and presents a major design limitation. From Eq. (2.76), it is clear that the voltage depression scales with the beam current, and it should also be noted that the perpendicular component of the momentum remains unaffected by voltage depression. As a result, there exists a current at which point the voltage depression becomes too large, such that $v_z \rightarrow 0$, and reflection of the beam may occur. This limiting current can be expressed as:

$$I_L = \frac{0.4V^{3/2}}{(1+\alpha)^2 \ln(R_{wall}/R_{beam})} \tag{2.77}$$

for a voltage V given in kV. For the above parameters, this gives a limiting current of about 94 A. In CW operation, the space charge will be neutralized by the background gas after operation for several milliseconds; however, the effects of increased velocity spread persist, and the beam's effective velocity ratio will be reduced. It is thought that for successful CW operation, the limiting current should be at least a factor of two larger than the operating current, and the voltage depression should be kept to less than 10% of the accelerating potential [118].

2.6 Gyrotron Codes

While the theory covered in this chapter can provide a guideline to a successful gyrotron design, there are a number of assumptions and omissions that are required to generate a simplified set of solvable equations. A few of these issues include:

- *Self-consistency*: A fixed Gaussian axial field profile was used in the non-linear theory presented here. In reality, the presence of the electron beam perturbs the "cold cavity" field profile, which is not truly Gaussian, either. Thus, a more elaborate set of self-consistent equations that fully encompass all of the mutual effects between the rf fields and the electrons should be employed. Gyrotron theory has been evaluated using a self-consistent approach [109].
- *Mode interaction*: The non-linear theory also assumed a single mode excitation in the interaction region. In reality, many modes may be excited and additionally will interact with one another. In some cases, the excitation of one mode may suppress other mode excitations, while, in other cases, competing modes may drive the device into unstable operation. Especially in MW gyrotrons where the spectrum of modes is quite dense, the interaction between modes is an important issue and has been examined extensively in the literature [119, 120].
- *Time dependence*: A fixed set of parameters is assumed in theory, but, in reality, a device must progress from zero to its steady-state operating parameters. As the voltage rises for example, the beam current and pitch factor will also evolve and the mode excitation may not be as straightforward. The sequence of mode excitations during the voltage rise is referred to as the start-up scenario. It has been shown that a variation of the parameters for this start-

up can affect the final steady-state operating mode [121]. A full discussion of the start-up scenario will accompany experimental results later in this work.

- *Experimental deviations*: In theory, it is easiest to assume fixed parameters like a monoenergetic electron beam and a constant magnetic field. In reality, the parameters in an experiment will have some imperfections. Even the best electron beam will have a velocity spread on the order of a few percent, which can have a major effect on efficiency. Additionally, it is convenient to be able to use real parameters whenever possible, like the exact profile of the cavity and tapers and the real magnetic field profile, which may have some small amount of tapering even in the interaction region.

Encompassing all of these effects requires the development of a code that is much more involved. While a full particle-in-cell (PIC) simulation of the gyrotron is still beyond the capabilities of current codes and computing resources, other approaches can be taken to reduce the computing demands. For example, instead of solving the full set of equations for the fields within the volume of the cavity, the fields can instead be represented by a superposition of modes in the interaction region. The University of Maryland and Naval Research Laboratory (NRL) developed such a code known as MAGY [122]. MAGY takes into account a number of the aforementioned issues as its inputs including: full circuit geometry, real magnetic field profile, and velocity spread of the electron beam. MAGY can also consider the interaction between modes, in particular the "triplet" case where a strong coupling between a mode and its two sideband modes with identical radial mode index but differing by one in the azimuthal mode index has been observed. MAGY has been an important tool in the design and analysis of the MIT gyrotrons, and is again employed within this work.

Chapter 3

High Efficiency 110 GHz Gyrotron Experiment

The MIT 110 GHz MW gyrotron is part of an ongoing research program into high power gyrotrons for fusion applications. Following a 170 GHz gyrotron program [123], a 110 GHz gyrotron was developed by former graduate student James Anderson [124]. This initial design was later improved upon by another graduate student, Eunmi Choi, who was tasked with reducing the mode competition in the gyrotron and improving its efficiency [125]. Initial experiments in this work utilize this improved gyrotron design.

In this section, the design and operation of the gyrotron components, including those specific to the high efficiency configuration, will be reported. The experimental diagnostic tools that allow for measurements of gyrotron performance will then be described, and some recent experimental results for this initial configuration will be presented.

3.1 High Efficiency 110 GHz Gyrotron Configuration

In the previous chapter, the layout of a gyrotron was introduced, including its primary components: an electron gun, a superconducting magnet, an interaction cavity, a mode converter, and a collector. Many of the components, like the magnet and electron gun, are common to all of the different configurations of the MIT gyrotron, where typically it is

only the cavity and IMC that is redesigned and interchanged. A description of all components, including those specific to the high efficiency design follows.

3.1.1 Electron Gun

The magnetron injection gun (MIG) implemented in this experiment was designed as part of the initial implementation of the 110 GHz MW gyrotron. A gyrotron MIG should be designed to have a large perpendicular velocity, $v_\perp$, and a suitable beam radius at the cavity for the operating mode, given the nominal operating voltage and the magnetic field intensity that yields a cyclotron resonance at the desired operating frequency. At the same time, the design must also attempt to minimize the beam velocity spread, defined by $\Delta v_\perp / v_\perp$, which arises due to a number of factors like beam optics, surface roughness, non-uniform cathode emission, and mechanical machining and misalignment errors. A large velocity spread has been shown to have a major effect on reducing the achievable efficiency [126].

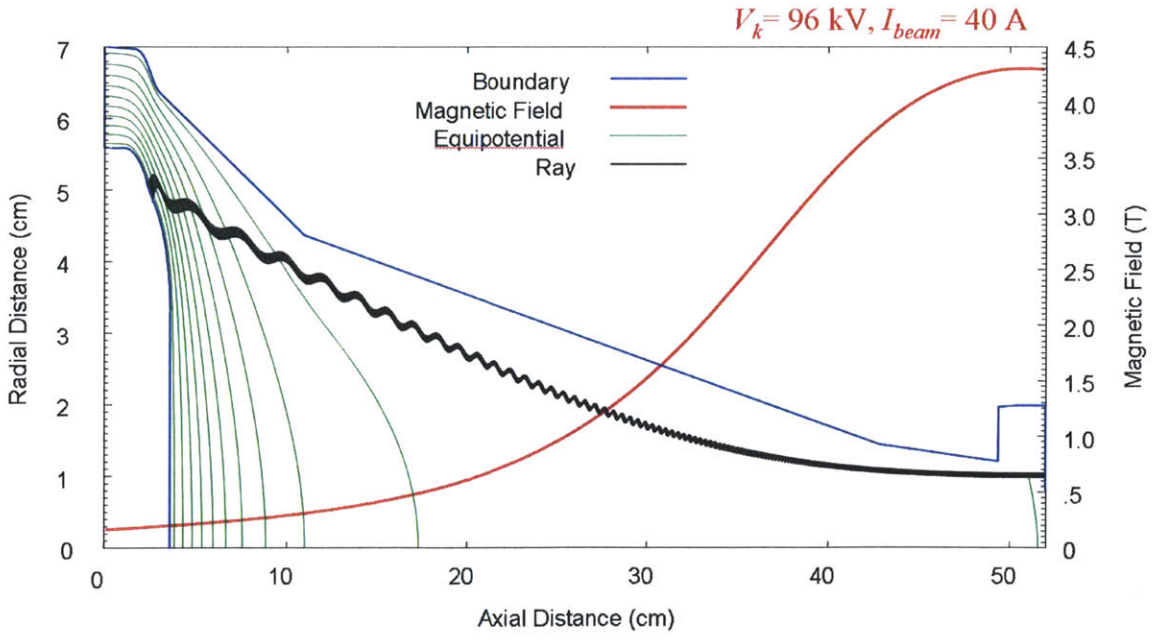

Figure 3-1: Geometry of the MIT diode magnetron injection gun (MIG). Electric and magnetic fields are shown along with the beam trajectory. Adapted from [127].

The MIT gyrotron implements a MIG with a diode configuration that was designed as a collaboration between CPI and MIT [128]. The same electron gun design was used by CPI in their 110 GHz 1 MW CW gyrotron. Figure 3-1 shows the gun's geometry and the beam trajectory, while a table of operating parameters for the 110 GHz MIG is shown in Table 3-1. The gun utilizes an M-type cathode manufactured by SpectraMat. It contains a 5:3:2 impregnate ratio of $BaO:CaO:Al_2O_3$ which has been shown to have a reduced susceptibility to cathode poisoning [129] and was selected after the previous 4:1:1 ratio cathode failed to activate with cathode poisoning being the suspected cause. The current output versus voltage (IV curves) for several values of the cathode heater is shown in Figure 3-2. The gun is designed to operate in the temperature limited regime where the current dependence is slowly increasing due to the Schottky effect as described in the previous chapter. Over the course of experiments for each gyrotron configuration, the gun has proven to be quite reliable, providing the required current, beam radius, and pitch factor to achieve the desired results. However, it is not necessarily perfect, as a variation in the emission around the azimuth has been measured, which may contribute to a decrease in the achievable device efficiency [105].

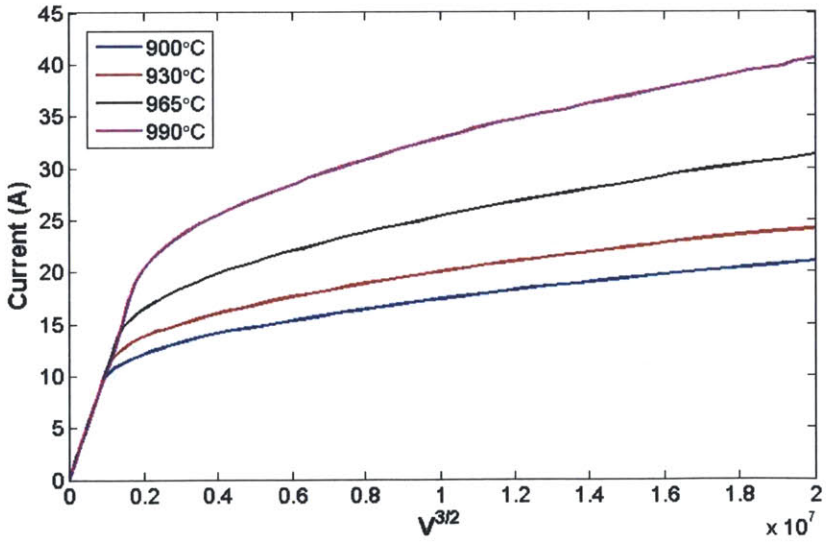

Figure 3-2: I-V curves for the MIT electron gun. Output current is plotted as a function of voltage for a variety of cathode temperatures.

Table 3-1: Design parameters for the 1.5 MW, 110 GHz gun

Voltage	96 kV
Current	40 A
Cathode angle	36°
Cathode width	0.36 cm
Cathode radius	4.8 cm
Cathode work function	1.88 eV
Cathode temperature	965°C
Emission current density	4 A/cm^2
Cathode-anode distance	1.5 cm
Cavity beam radius	1.024 cm
Beam thickness	0.09 cm
Cavity pitch factor ($v_\perp/v_z$)	1.4
Velocity Spread	2.5 %
Magnetic compression	22.13

3.1.2 Magnetic Fields

The two sources of magnetic fields in the MW gyrotron experiment include a superconducting magnet to generate the main magnetic field and a room temperature "gun coil" that generates the small field at the cathode location to tune parameters like the pitch factor and beam radius. The superconducting magnet was manufactured by Cryomagnetics Inc. and was capable of a peak field of 7.5 T because it was initially implemented on the 170 GHz gyrotron experiment. However, past events limited the current handling capabilities of this magnet, though it is still more than capable of producing the required 4.4 T for operation at 110 GHz or 5.0 T for operation at 125 GHz. The conversion factor for the magnet's coil is 0.095276 T/A and it has a field homogeneity of 0.7% over a 2.5 cm length at its center, which is longer than the cavity straight section lengths implemented in each configuration. The gun field is generated by a water-cooled

room-temperature solenoid magnet. It generates a small magnetic field using a 0 to 55 A supply with a conversion factor of 0.000676 T/A and is centered at the cathode. The maximum intensity of the gun field represents about 25% of the superconducting magnet's magnetic field intensity at that axial location, allowing for the compression ratio to range from 20 to 25 for typical operating values. Figure 3-3 shows the axial magnetic field profile for the superposition of the two fields where the small red shaded region indicates the possible range of gun coil fields.

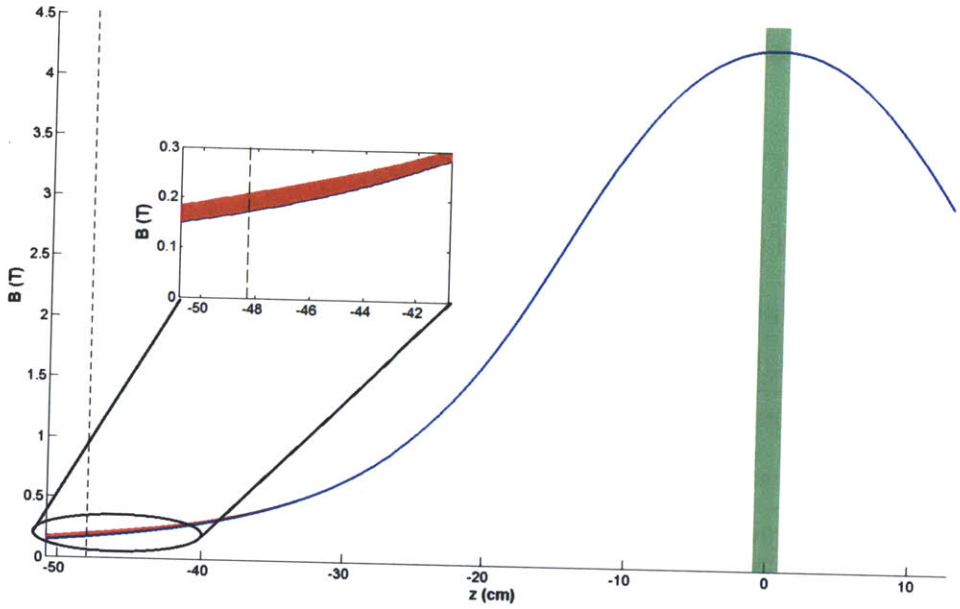

Figure 3-3: Axial magnetic field profile for the MIT gyrotron. The superconducting magnetic field is given for a peak field of 4.3 T. The cavity is indicated by the green shaded region with its center located at z = 0 cm. The small red shaded region approximates the possible range of field values for the room temperature gun coil located around the cathode at z = -48.3 cm, marked by the dotted line.

3.1.3 Cavity

The design of the high efficiency cavity was part of previous doctoral work [111]. The goal for this gyrotron has been operation at 110 GHz with 1.5 MW of output power. The initial cavity, internally referred to as the V-2003 cavity, showed good promise as it

provided over 1 MW of output power, however it failed to reach the 1.5 MW operating point due to severe mode competition with the $TE_{-19,7}$ mode, where the minus sign indicates that the mode rotates opposite to the electron beam. This counter-rotating mode is very close in frequency to the $TE_{22,6}$ operating mode, with a difference of only 400 MHz, and such modes are very common competitors when attempting to operate at maximum efficiency. Other concerns in the design of such a cavity included the ohmic heating, which should be limited in MW gyrotron designs. Even if excessive Ohmic heating may not be problematic in a pulsed device, the cavity design should still be suitable for CW operation.

Table 3-2: Design parameters for the V-2005 cavity

Input taper angle	2.5°
Straight section length	1.8 cm
Straight section radius	1.98 cm
Output taper angle	0.7°
Operating mode	$TE_{22,6}$
Frequency	110.07 GHz
Q factor	837
Normalized length (μ)	16.1
Peak ohmic loss	0.8 kW/cm^2
Simulated power (triplet)	1.62 MW
Simulated power (triplet w/ 5 % velocity spread)	1.4 MW

The design parameters of this high efficiency cavity, internally referred to as the V-2005 cavity, are summarized in Table 3-2. The design was based on the previous cavity and optimized using the self-consistent MAGY code, where a similar output power was predicted with lower ohmic loss. The basic cavity geometry is the same as that described in the previous chapter with a straight section of fixed length and input/output tapers.

Additionally, the cavity section includes a non-linear uptaper to a 2.0955 cm radius at which point the IMC section begins. This non-linear taper is designed to maximize the mode purity to ensure successful IMC operation.

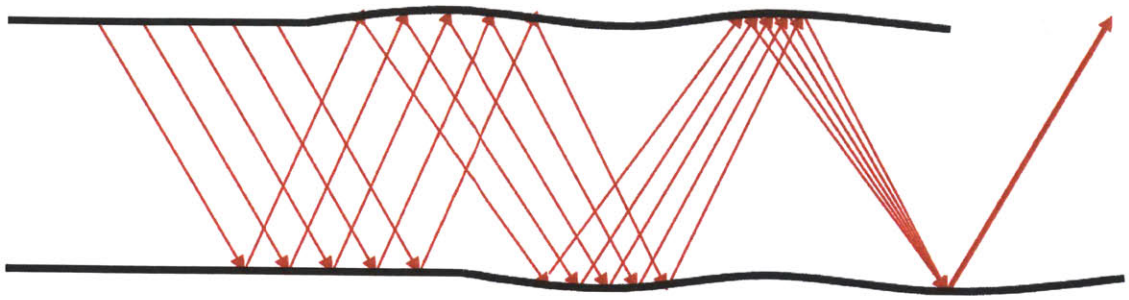

Figure 3-4: Conceptual diagram of ray bunching due to a perturbed waveguide surface profile. Initial fields with uniform spatial distribution become bunched in the axial direction resulting in the launching of a focused Gaussian field pattern.

3.1.4 Internal Mode Converter (IMC)

The high-efficiency gyrotron configuration used two different IMCs over the course of experiments. In each case, the IMC consisted of a quasi-optical launcher with a helical cut that converts the $TE_{22,6}$ operating mode into a Gaussian beam and a set of 4 copper mirrors that directs the power to the window.

The launcher is best understood with a geometrical optics approach. The waveguide modes may be represented as a series of rays that bounce along the waveguide with a particular bounce angle. In the case of a rotating mode, they bounce around the surface of the waveguide and tangential to a caustic, where, in the geometrical optics approximation, the field intensity is infinite. Between each successive bounce, the rays will travel a given axial length along the launcher and subsequent reflections will be separated by a particular azimuthal angle. The expressions for these terms will be discussed in Section 3.4 where the IMC design is discussed in detail. A Brillouin region can then be defined as a section of waveguide wall which is intercepted by the complete bundle of rays. The axial length of such a region is naturally the axial distance travelled

for a bouncing ray to complete a full revolution around the azimuth. The elimination of such a Brillouin region from the end of the waveguide will cause the full microwave power to be launched from the cut section. In the case of a smooth wall Vlasov launcher, the power is evenly distributed and even though the full microwave power is launched, considerable power is lost due to diffraction [112]. Since large amounts of diffracted power could be quite troublesome in a MW gyrotron, a solution to this problem is to introduce some perturbations to the waveguide radius that will act to focus the power along the surface of the waveguide. This process is shown conceptually in Figure 3-4, where rays that are initially evenly spaced become bunched as they reflect at different angles from the curved surface. While a sinusoidal profiling of the wall radius could yield a reasonably bunched beam, more advanced profiles are required to truly optimize the output of the launcher, which requires a numerical solver. One such code that is specialized for the design of gyrotron IMC launchers is known as LOT (Launcher Optimization Tool) and was developed by Dr. Jeff Neilson of Lexam Research and Calabazas Creek Research, Inc [130]. Best results are obtaining by allowing the launcher to taper slowly to a larger radius and by optimizing the coefficients of cubic spline functions. There are two optimization metrics: maximization of the Gaussian content on the aperture for a high quality output beam and minimization of the fields along the spiral cut for reduced diffractive loss. LOT uses a coupled mode theory to solve for the fields in the waveguide and a Stratton-Chu formulation to calculate the radiated field at the aperture.

Once the launcher is finalized, the set of mirrors may be designed. While calculations based on Gaussian optics can be used, it is best to refer to computer codes designed to calculate the fields scattered from an arbitrary metal surface. Some examples of these codes are Surf3D which solves the electric field integral equation and SCATTER, developed by former graduate student Dr. Monica Blank, which uses the Stratton-Chu formula. With the use of these codes, a set of phase-correcting mirrors could be designed,

meaning that the mirror surface is not smooth and is designed to offset the phase error of the incident beam. In the previous work that will be described, a mode converter using a set of such mirrors was implemented, however the results obtained as part of this work using the high efficiency configuration had a mode converter with a set of smooth, curved mirrors. A detailed description of this mode converter design can be found in Section 3.4.2.

3.1.5 Collector

The basic collector design for such a gyrotron is a simple copper can. While the beam is quite powerful, the pulses are short and, therefore, given the low energy, no additional cooling systems are required. One can, however, introduce a depressed collector to improve device efficiency. The depressed collector was not used as part of this work, but one was implemented for the previous results obtained in the high efficiency configuration. For simplicity, the depressed collector did not use a second power supply and instead installed a resistive network between the collector and ground. Thus, a potential difference was placed between the body of the tube and the collector, due to the voltage drop across the resistor. While such a configuration does not technically change the wall-plug efficiency of the device, the dissipated energy in the resistor represents the power that could be recovered. The depression voltage may be varied by interchanging different resistors. An upper limit on the depression voltage is given by the minimum energy of the spent electron beam since that is the level at which electrons would be reflected.

3.2 Experimental Diagnostic Tools

To obtain experimental results, a number of diagnostics are necessary to measure the important input and output parameters of the gyrotron. The tools that allow for the important measurements of the output power and frequency, as well as those that track the operating parameters of the gyrotron will be discussed in this section.

3.2.1 Power Measurement

In order to measure the output power of the gyrotron, a calibrated time-domain measurement is required, and, given the frequency and power levels, this is no easy task. In the experimental setup, two pieces of equipment are necessary. The first component is a dry calorimeter which measures the total energy of the gyrotron pulse. The Scientech 378 calorimeter uses a 20 cm diameter plate which has been modified for better absorption of microwave frequencies and demonstrates excellent uniformity across its surface [131]. The corresponding temperature rise on the calorimeter plate is measured as a voltage which can be read on an accompanying analog signal meter. Through cold test measurements taken with a vector network analyzer (VNA), it was found that the absorption was measured to be 85% of the total power. The second component should measure the time dependence of the microwave power. To accomplish this, the power reflected from the calorimeter is received by a small WR-10 cut waveguide antenna. After passing through an attenuator stage, an F-band rf diode measures the power. Using the pulse shape obtained by the broadband video detector and knowing the total energy from the calorimeter, the peak output power can be determined.

Since the gyrotron quickly reaches steady-state operation as the voltage reaches its peak value, the pulse shape is approximately trapezoidal and a full-width half-max (FWHM) approximation of the pulse width may be used. The output power during the flat-top of the voltage pulse is therefore:

$$P_{out} = \frac{E_{out}}{0.85 \cdot PW \cdot Rate} \tag{3.1}$$

where the power is calculated in MW when the pulse width PW is given in μs and the total energy E_{out} is given in J. The repetition rate typically used for experiments was 1 Hz, though, for more accurate power readings, the experiment could be run at 2 Hz or even 4 Hz. Additionally, for accurately measured power, the rf diode should be calibrated and the real pulse shaped used to determine the steady-state power level.

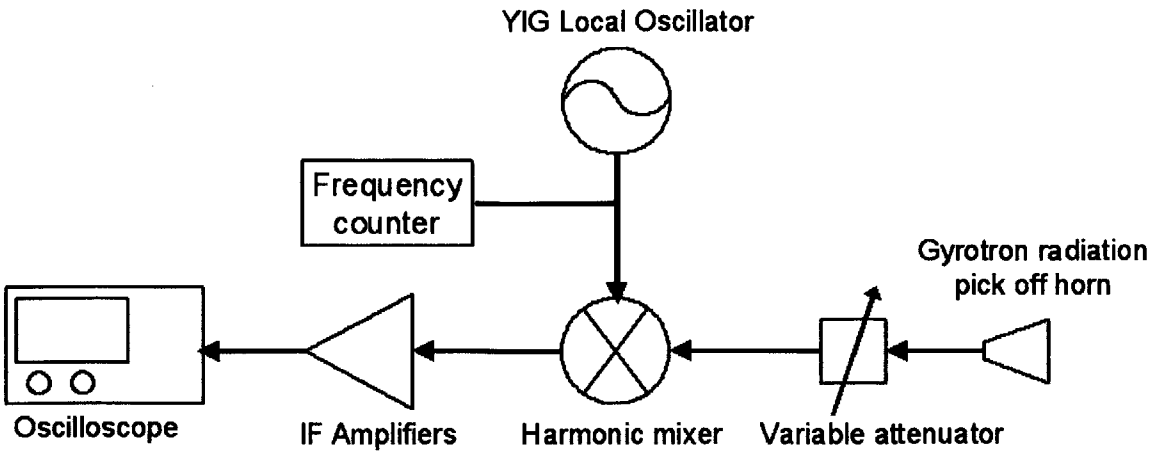

Figure 3-5: Schematic of the heterodyne receiver system for measuring the frequency of the gyrotron output power. Adapted from [111].

3.2.2 Frequency Measurement

Several different measurement techniques are available for frequency measurements. Unfortunately, direct frequency measurement equipment is not readily available (at least at a reasonable cost), therefore other methods must be used. The primary means of frequency measurement is through the use of a heterodyne receiver system. A schematic of the frequency system is shown in Figure 3-5. A waveguide horn picks off a small amount of the gyrotron radiation, which is transmitted across to an F-band harmonic mixer diode. At the same time, an 8-18 GHz tunable YIG oscillator generates a local oscillator (LO) signal that is connected to a diplexer where its harmonics can be mixed with the gyrotron signal. The LO frequency is measured using a microwave frequency counter and has an accuracy of ± 1 MHz. The resulting intermediate frequency (IF) signal, equal to the difference between the two frequencies, is band limited to 150-500 MHz by filters and amplified significantly using a series of solid-state amplifiers. This amplified IF signal then passes to a LeCroy LT372 4 GS/s digital oscilloscope with a 500 MHz bandwidth where a fast Fourier transform (FFT) is applied to the signal. The frequency of the gyrotron rf signal is therefore given by:

$$f_{rf} = nf_{LO} \pm f_{IF} \tag{3.2}$$

where n is the harmonic number and must be determined. The + or – sign can be determined visually by seeing how the IF frequency varies as the LO frequency is tuned. If an increase in the LO frequency causes the IF frequency to increase, then it is indicative of an upper sideband where the LO harmonic frequency is greater than the rf frequency and a – sign should be used in Eq. (3.2). The converse applies when the IF frequency varies inversely to the LO frequency for the lower sideband. The harmonic number may be derived from two pairs of LO and IF frequencies. While it is convenient to measure an upper sideband and a lower sideband at the same IF frequency (usually 300 MHz since it is right in the middle of the bandpass region), it is not necessary. Alternatively, two similar sidebands could be used. Though, for all frequency measurements performed here, upper and lower sidebands are used. In this case, the general equation to determine the harmonic number is:

$$n = \frac{f_{LO,upper} - f_{LO,lower}}{f_{IF,lower} + f_{IF,upper}}. \tag{3.3}$$

Once the harmonic number is determined ($n \approx 10$), the gyrotron radiation frequency can be calculated using Eq. (3.2) and one pair of LO and IF frequencies. The frequency can therefore be measured with an accuracy of about ± 10 MHz. The FFT performed on the oscilloscope may also be gated over a very narrow time window of the pulse, as low as 20 ns, meaning that the frequency may be measured only over a very specific time during the microwave pulse.

Another means of measuring frequency is by using a wavemeter. A wavemeter may be used in conjunction with the broadband video detector employed in the power measurement system and is, essentially, a tunable frequency-dependent attenuator. By tuning a dial, the dimensions of a narrowband resonant cavity within the wavemeter are altered. When off-resonance, power simply transmits straight through the waveguide

connections at either end of the wavemeter. However, power at the resonant frequency will be partially coupled out of the waveguide and into the resonant cavity. Two wavemeters were used in the experimental setup: a W-band wavemeter which can provide about 2 dB of attenuation and a D-band wavemeter that can provide around 5 dB of attenuation. In each case, the bandwidth of the attenuation is < 100 MHz. While not as accurate as the heterodyne frequency system, once calibrated, wavemeter measurements can yield frequencies with an accuracy of approximately ± 50 MHz. This enables rapid frequency measurements when measurement equipment obstructs the pickoff horn of the heterodyne receiver system. The wavemeter is also capable of detecting the frequency dependence of the rf pulse with time as the attenuation will only be seen at times during the pulse where the resonant frequency is excited.

3.2.3 Alpha Probe (Pitch Factor Measurement)

In the previous chapter, the role of the pitch factor, $\alpha = v_\perp/v_z$, was discussed. Since it is an important part of the gyrotron efficiency, it would be helpful to be able to measure this parameter. The pitch factor may be measured through the use of a capacitive probe located at the entrance to the cavity. The alpha probe consists of a metallic ring isolated from the grounded tube by a ceramic. As the beam passes through the center of this ring, a voltage is induced which is related to the capacitance of the probe [132]. The α value may be determined with an accuracy of about ±10% by this method. However, for many of the results in this work, the alpha probe signal became too noisy to detect values with reasonable precision, possibly due to grounding problems, and thus was not employed as part of the analysis.

Even when α values are not recorded though, the probe can still prove useful as it does provide a source of "in-situ" measurement within the tube. A previous study took the output traces of the probe and analyzed the frequency content to discover low frequency

oscillations [133]. For this work, the alpha probe traces were typically used to diagnose problems with the gyrotron. When the beam is partially intercepted by the tube or when undesirable modes were excited that caused rf power to radiate within the tube resulting in a pressure rise, the alpha probe trace became quite distorted. This is of particular help during the alignment process and when taking measurements, like a mode map, where the tube is operated far away from its design point and it may no longer be possible to measure the rf output power.

3.2.4 Voltage and Current Measurement

For the voltage measurement, it is worth mentioning that the high voltage modulator implements a parallel load, which is necessitated by the variation in the impedance of the gyrotron. If the parallel resistance is selected to be large enough, then the impedance seen by the pulse forming network should be insensitive to small changes in the gyrotron impedance. Changes to the load impedance would de-tune the pulse forming network and result in a system that would no longer be matched, distorting the voltage waveform.

For current measurements, the beam current is not measured directly. Rather, the current is measured at the collector and on the body of the tube with the beam current determined by the sum of these two currents. The collector is isolated from the tube and the current is simply measured by a Rogowski coil as it passes through a grounding cable. The body current is the current intercepted by other internal components of the tube. To avoid damaging components, a beam scraper is used at the end of the beam tunnel region, and before the cavity. The radius of the beam scraper should ensure be small enough to ensure that the beam could not impact the surface of other components, like the cavity or launcher, though should also be sufficiently large to avoid interfering with the beam. A Rogowski coil around the grounding cable connected to the body of the tube therefore allows for measurement of the body current.

3.3 Previous Experimental Results

The experimental study of the high efficiency 110 GHz configuration using the V-2005 cavity and an IMC with phase-correcting mirrors was completed as part of the doctoral work of previous graduate student Dr. Eunmi Choi [111]. It is helpful to summarize some of the primary results of this study in order to provide some background on the experiments that are part of this work.

The goal of the upgraded design was to improve the efficiency of the gyrotron. It was thought that one of the limitations in the inaugural version of the tube was the heavy mode competition around the high power operating point. Thus, the design of this new cavity focused on the reduction of the counter-rotating $TE_{-19,7}$ mode excitation. A type of measurement that investigates mode competition is known as a "mode map." The mode map explores the parameter space of the gyrotron at a fixed beam current and voltage, while varying the main magnetic field and the gun field, which tunes the beam radius and α value. Outside from the source limitations of the gun magnetic field, there are two physics limitations as well. First, if the gun coil field is too large, the beam radius becomes too large and will be intercepted by the tube. Second, if the gun coil field is too small, then α is too large, and the electrons will have insufficient longitudinal energy to reach the cavity and are reflected back towards the cathode. A comparison of the mode map between the V-2003 and the V-2005 cavity is shown in Figure 3-6. In each case, the mode map was taken in the axial configuration, meaning that no IMC is used at all and was instead replaced by an uptaper which allows the output power to propagate axially down the device to a window located at the center of the collector (recall that the beam expands in the region of decreasing field and thus would strike the sidewall of the collector). Power measurements in the axial configuration also showed an improvement in the V-2005 configuration, and thus the new design did successfully improve on the original.

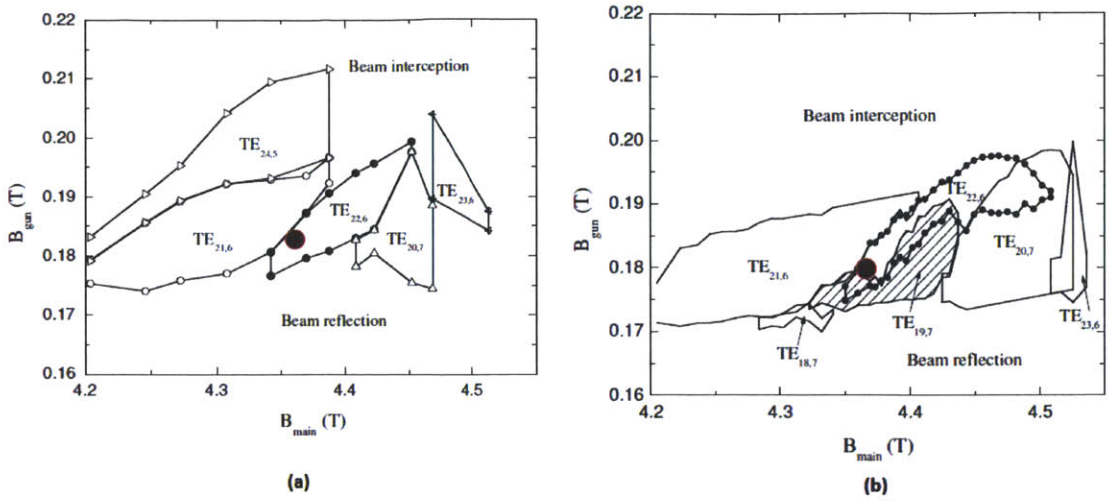

Figure 3-6: Comparison of mode maps for old cavity configurations. Data are taken in the axial configuration using **(a)** the V-2005 cavity and **(b)** the V-2003 cavity. Both mode maps are taken at 97 kV and 40 A and, in each case, the maximum efficiency point is marked by a large dot.

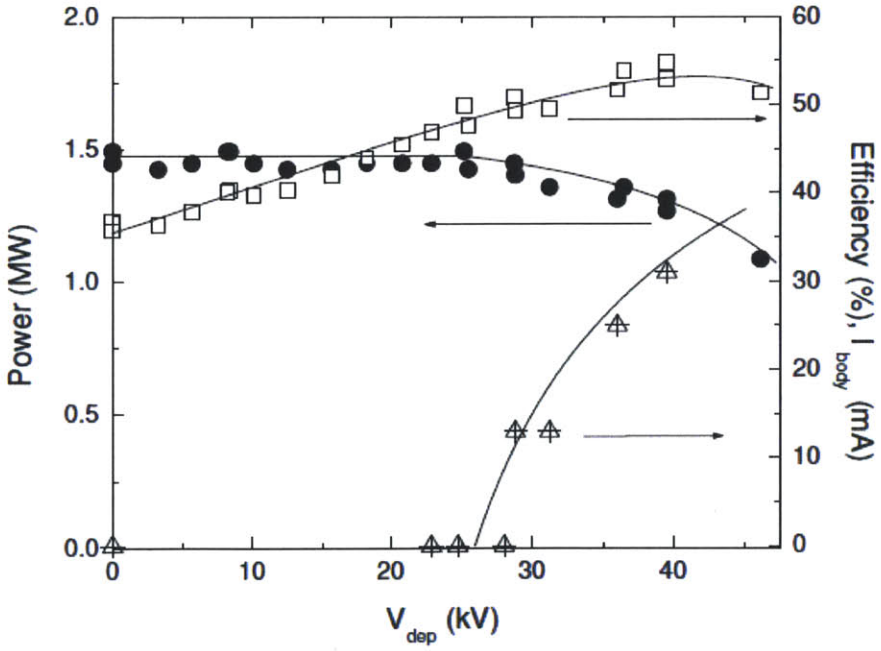

Figure 3-7: Operational achievements of the V-2005 depressed collector experiment. Power (solid circles), efficiency (hollow squares) and body current (hollow triangles) are measured as a function of depressed collector voltage for the V2005 cavity using an internal mode converter with phase-correcting mirrors. Adapted from [111].

The next question in that work was how high the efficiency could be pushed. In this case, it was important to operate in an IMC configuration to obtain real, useful output power, and with a depressed collector to maximize efficiency. The IMC with phase-correcting mirrors and the resistor based depressed collector implemented in this experiment were briefly described previously in this chapter. The results of this experiment were quite successful and are summarized in Figure 3-7. It was found that the gyrotron was capable of generating 1.5 MW of power and, using the depressed collector, an efficiency of over 50% could be achieved at depression voltages of up to 30 kV. Once the depression voltage was made too large, even though the efficiency continued to improve, electrons would begin to reflect, and though the pulsed device is capable of continued operation, this is not a valid operating condition for CW gyrotrons. In addition to the achievement of the gyrotron, some important device physics was also discovered as part of this study. It was found that, as the beam and microwave power propagated through the launcher of the IMC, the gyrotron synchronism condition was once again met, a phenomenon which is referred to as the after-cavity interaction (ACI). However, in this case, the beam and wave interacted in the accelerating phase, meaning that the microwave power would lose energy to the beam, causing a reduction in output power. Not only that, but it was also discovered that the spread of the beam energy was increased as a result of this interaction, which would have a secondary effect of limiting the maximum depression voltage before the onset of reflected electrons.

3.4 Smooth-Mirror Mode Converter Design and Test

Following the success of the previous experimental work, the experiments as part of this thesis work began with an investigation in how to make gyrotron operation more reliable. One perceived weakness of the previous design was the mode converter. Despite the excellent result, as always, the theory and simulations predicted a higher output power and efficiency. One source of efficiency degradation is the physical principles that govern the

device, like the ACI effect which was discovered and was shown to reduce the output power [134, 135]. However, one must always be aware when constructing a real, physical system that there will always be experimental imperfections whether they stem from machining tolerances or alignment errors.

The role of the internal mode converter (IMC) is particularly important. Poor IMC design may lead to both direct and indirect losses. Direct losses may also be classified in two ways. First, there are Ohmic losses within the launcher and on the surface of mirrors, which are typically small. The second and larger source of loss is diffractive losses which may come from reflected power due to tapering and waveguide mismatches or stray radiation in the tube resulting from the launcher output power not being fully intercepted by the surfaces of the mirrors and thus not propagating towards the vacuum window. Indirect losses include the losses that occur outside of the gyrotron system itself, in the systems that make use of the gyrotron's output power. These losses will typically be proportional to the output beam quality generated by the IMC, where the ideal output is defined by a fundamental Gaussian beam with a flat phase front at the window. In a typical fusion heating application, the Gaussian beam output of the gyrotron is coupled into a large cylindrical corrugated waveguide. While large, overmoded waveguide has low loss, the transmission distances are often quite large and, in addition, many lossier passive components must be incorporated into the transmission line design. The transmission efficiency of both the passive components and straight sections of waveguide are dependent on the Gaussian beam content of the gyrotron output beam. In large waveguide systems, Ohmic losses may remain low, however poor beam quality will result in mode conversion losses as higher order modes will be excited in the waveguide components [136, 137]. While other equipment, like a matching optics unit (MOU), may be implemented to help reduce the additional loss caused by a tilt or offset from misalignments between the beam and transmission line, it still can't fix the problems of poor Gaussian beam content. Analysis of the prototype transmission line for ITER's ECH

system showed that the gyrotrons should produce output beams with 95% Gaussian beam content in order to meet the specification for transmission efficiency [81].

The discussion and results in the remainder of this chapter were published by the author in the paper: "Experimental Results on a 1.5 MW, 110 GHz Gyrotron with a Smooth Mirror Mode Converter" in the *International Journal of Infrared, Millimeter and Terahertz Waves*, vol. 32, pp. 358-370, 2011 [138].

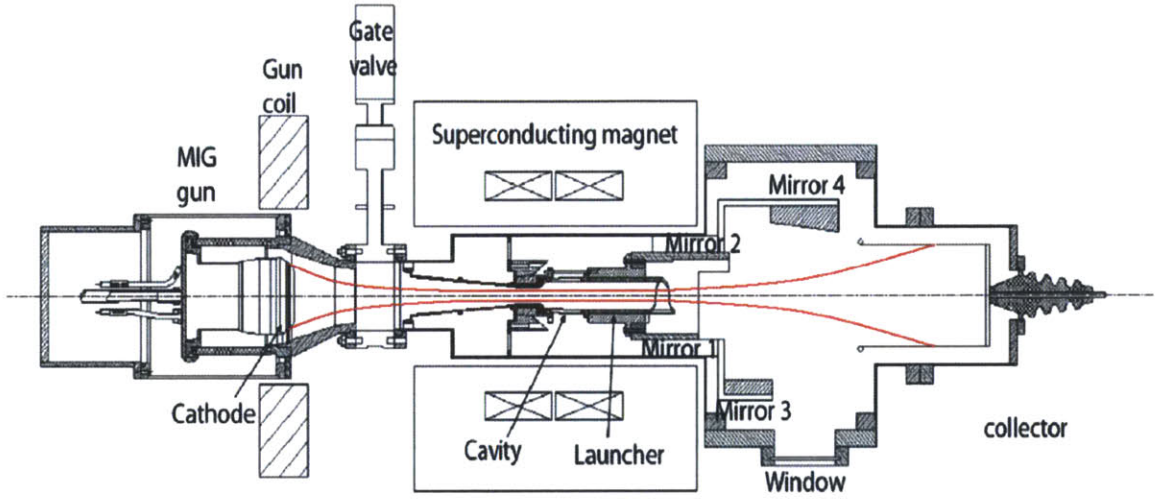

Figure 3-8: Schematic of the 1.5 MW, 110 GHz gyrotron with a 4 mirror internal mode converter (IMC). Annular electron beam is shown in red.

3.4.1 Generalized IMC Launcher Design Theory

This design is based on the standard MW gyrotron IMC configuration which uses a launcher section, with wall perturbations to convert the cavity's TE mode and emit a highly Gaussian beam, and a set of metallic mirrors, which shape the fields and focus the beam with an appropriate waist at the window. The previous IMC used a set of mirrors with phase correcting surfaces, meaning that a finely calculated perturbation was machined into the surface of the mirrors and allowed for improvement of the Gaussian beam content. However, in this case, we explore the use of simple, smooth, curved mirrors which may alter the beam waist and focal point but do not correct any imperfections in the Gaussian profile of the beam coming from the launcher. The layout

of the gyrotron is shown in Figure 3-8. In order to accommodate the tube geometry and transmit the power through the window, a 4 mirror system is employed. However, only 3 mirrors are used to shape the beam, so the system will be designed with 3 smooth, curved mirrors and one flat mirror, in this case, mirror 3.

The basics of the helical cut launcher were described previously. In the case where smooth mirrors are used, it is even more imperative that the launcher be designed to have the maximum achievable Gaussian content. Luckily, refinements to the design codes have improved them to the point where this is possible. The Launcher Optimization Tool (LOT) which was briefly introduced was employed in the design of this launcher. The general form of the wall deformation in LOT is given by:

$$r(\varphi, z) = r_0 + \kappa z + \sum_l \sum_m a_{lm}(z) \cos\left(H_{lm}(z) - l\varphi\right) \tag{3.4}$$

where r_0 is the average wall radius, κ is the tapered slope and the spline points of cubic splines $a_{lm}(z)$ and $H_{lm}(z)$ are the free parameters for optimization. As previously discussed, LOT uses a coupled mode theory to calculate the field intensities; therefore, before providing the specifics of this design, a discussion of these concepts is warranted.

In the geometrical optics representation, the rays of a rotating TE_{mp} mode bounce around the inside of the waveguide tangential to the caustic, whose radius is given by:

$$r_c = a\frac{m}{\nu_{mp}} \tag{3.5}$$

where a is the radius of the waveguide, m is the azimuthal mode index and ν_{mp} is the p^{th} zero for the derivative of the m^{th} order Bessel function. The ray travels at an angle with respect to the axis known as the bounce angle given by:

$$\theta_B = \arcsin\left(\frac{v_{mp}}{ka}\right) \tag{3.6}$$

for a propagation constant $k = \omega/c$. The divergence angle, that is the azimuthal rotation between subsequent bounces, and not to be confused with the previous use of α as the velocity ratio, is:

$$2\alpha = 2\arccos\left(\frac{m}{v_{mp}}\right) \tag{3.7}$$

and the axial pitch angle can then be determined as:

$$\beta = 2\arctan\left(\frac{\alpha \tan\theta_B}{\sin\alpha}\right). \tag{3.8}$$

The parameter known as the launcher cut can be determined as the axial length travelled while a ray completes a full revolution around the azimuth:

$$L_c = \frac{2\pi a \sin\alpha}{\alpha \tan\theta_B} \tag{3.9}$$

which defines the length of the Brillouin region at the end of the launcher which contains the complete bundle of rays and, thus, the full power of the microwave beam.

For a single mode, the distribution of rays is uniform. However, when wall perturbations are introduced, the distribution of rays becomes distorted and the field solution within the launcher must be defined by a superposition of different modes. Using the above equations, the desired set of modes may be broken down into 2 groups: axial bunching modes and azimuthal bunching modes. For axial bunching, a set of modes whose interference length with the operating mode is equal to the launcher cut length of Eq. (3.9) is desirable. This means that the modes may interfere destructively at the ends of the cut while interfering constructively at the center. For azimuthal bunching, the same principles apply, but the desired interference length is related to the divergence angle given in Eq. (3.7). For the $TE_{22,6}$ mode where $m = 22$ and $v_{mp} = 45.6243$, the divergence angle α is approximately $\pi/3$. In addition, the bunching modes should have similar caustic

radii and mode indexes. Azimuthal bunching modes should thus be of the form m +/- 3 with p -/+ 1, i.e. $TE_{19,7}$ and $TE_{25,5}$, and axial bunching modes will have the form $TE_{22 \pm 1,6}$, i.e. $TE_{21,6}$ and $TE_{23,6}$. Coupled mode theory was also part of previous doctoral thesis work at MIT [139]. A general form for the theory is provided for the case of forward propagating TE modes in vacuum at a frequency ω:

$$\frac{dA_a^+}{dz} = jk_{z,a}A_a^+ + \sum_b c_{ab}A_b^+ \tag{3.10}$$

where the coupling coefficient c_{ab} between mode a, defined as $TE_{m1,p1}$, and mode b, defined as $TE_{m2,p2}$, is given by:

$$c_{ab} = \frac{1}{2}\left[Q_{ab}\frac{\omega\mu_0}{\sqrt{k_{z,a}k_{z,b}}} + R_{ab}\sqrt{\frac{k_{z,b}}{k_{z,a}}}\right] \tag{3.11}$$

where:

$$Q_{ab} = \frac{j\left(\frac{v_{m2,p2}}{a}\right)^2}{a\pi\omega\mu_0\sqrt{v_{m2,p2}^2 - m_2^2}} \times \int_0^{2\pi}\left[\frac{jm_1}{\sqrt{v_{m1,p1}^2 - m_1^2}}\frac{\partial\delta(\varphi,z)}{\partial\varphi} + \delta(\varphi,z)\sqrt{v_{m1,p1}^2 - m_1^2}\right]\exp[j(m_1 - m_2)\varphi]d\varphi \tag{3.12}$$

$$R_{ab} = \frac{m_1 m_2}{a\pi\sqrt{v_{m1,p1}^2 - m_1^2}\sqrt{v_{m2,p2}^2 - m_2^2}}\int_0^{2\pi}\exp[j(m_1 - m_2)\varphi]\frac{\partial\delta(\varphi,z)}{\partial z}d\varphi, \tag{3.13}$$

and $\delta(\varphi,z)$ is a small amplitude perturbation to the waveguide wall such that:

$$r_{wall}(\varphi,z) = a + \delta(\varphi,z). \tag{3.14}$$

The theory described here had been applied to the design of a previous mode converter [140], while codes like LOT have since refined the technique and improved the accuracy and speed of the similar calculations. LOT therefore takes a pre-defined list of modes, applies this coupled mode theory by introducing small perturbations, and runs an

optimization metric. As previously mentioned, the optimization looks to minimize the field along the helical cut and maximize the complex Gaussian content at the aperture.

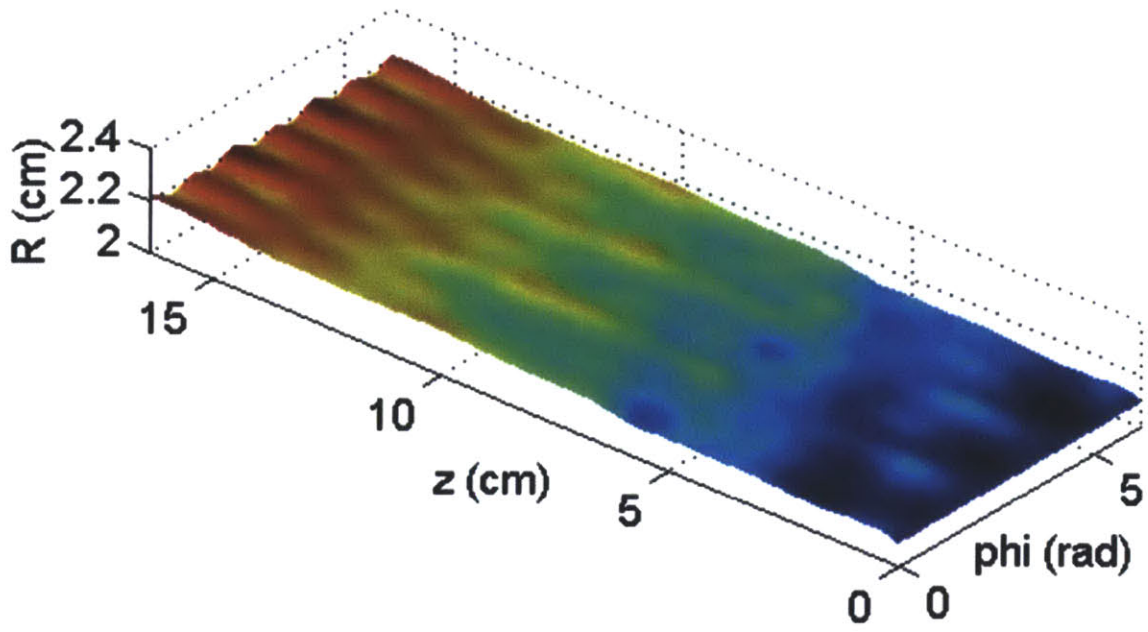

Figure 3-9: Wall radius profile for the dimpled wall IMC launcher.

3.4.2 Smooth-Mirror IMC Design

We now look to the launcher design using LOT for this IMC. The IMC design constraints are given by the input to the launcher, which is the field of a $TE_{22,6}$ mode within a waveguide of radius 2.0955 cm as defined by the terminus of the cavity's uptaper, and the physical dimensions of the system. The design should, of course, fit the tube, transmit the microwave power to the window, and must not allow for any IMC surface to intercept the electron beam, which is expanding rather quickly in this region. The basic mode mixture that LOT must consider includes the operating mode and the four bunching modes that were previously described. However, four additional modes to complete the set must also be included, such that each of the primary bunching modes forms a bunching triplet in the opposite direction. The set of nine modes for this design includes $TE_{21/22/23,6}$, $TE_{18/19/20,7}$, and $TE_{24/25/26,5}$. Additional satellite modes may also be included for improved accuracy. The designed launcher has a length of 16.4 cm and a slight uptaper of 0.35°. The

unwrapped profile of the wall radius is shown in Figure 3-9 where ripples in both the axial and azimuthal direction are apparent, though small. The process of mode conversion can be seen by examining Figure 3-10 which shows the mode content of the launcher averaged around the azimuth as a function of axial position. As expected, the pure $TE_{22,6}$ mode at the input is slowly converted to the satellite modes that bunch the field. The $TE_{22,6}$ center mode remains the strongest component throughout, however there is significant power in each of the primary bunching modes by the end of the launcher. The effect of this mode conversion is best seen by calculating the field intensity along the walls of the launcher. Recall that the goal was to form a Gaussian intensity distribution centered in a Brillouin zone that could then be launched from the helical cut. Examination of Figure 3-11 shows that this design appears to be quite successful, as the final Brillouin region of the launcher appears to contain a highly Gaussian beam with nearly no field along the launcher cut.

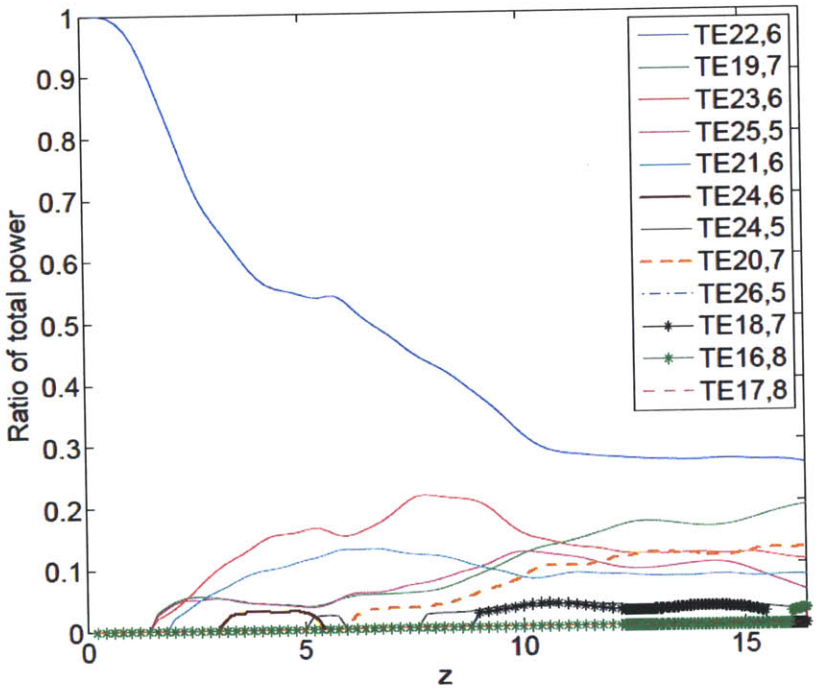

Figure 3-10: Modal composition of the launcher field as a function of axial distance. The wall perturbations convert the $TE_{22,6}$ mode power at the input into a mixture of satellite modes to bunch the fields along the surface.

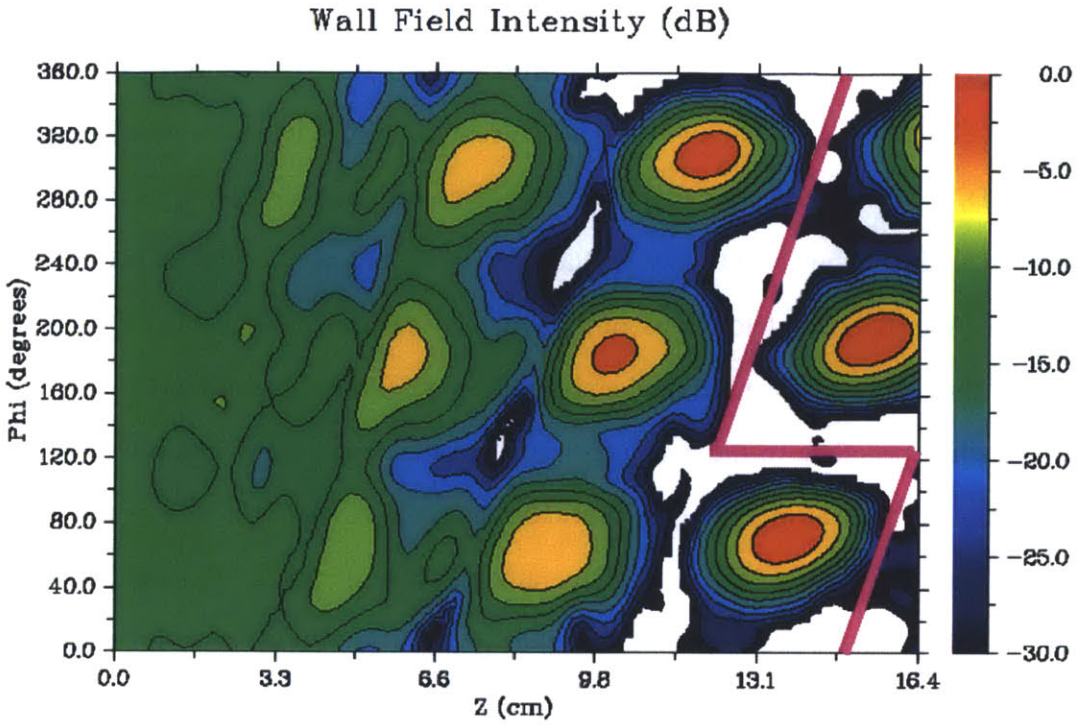

Figure 3-11: Field intensity along the wall of the launcher. The input at $z = 0$ shows a uniform field distribution for the $TE_{22,6}$ input mode and unperturbed surface, while the helical launcher cut is shown on the right, in magenta, enclosing the final Brillouin region.

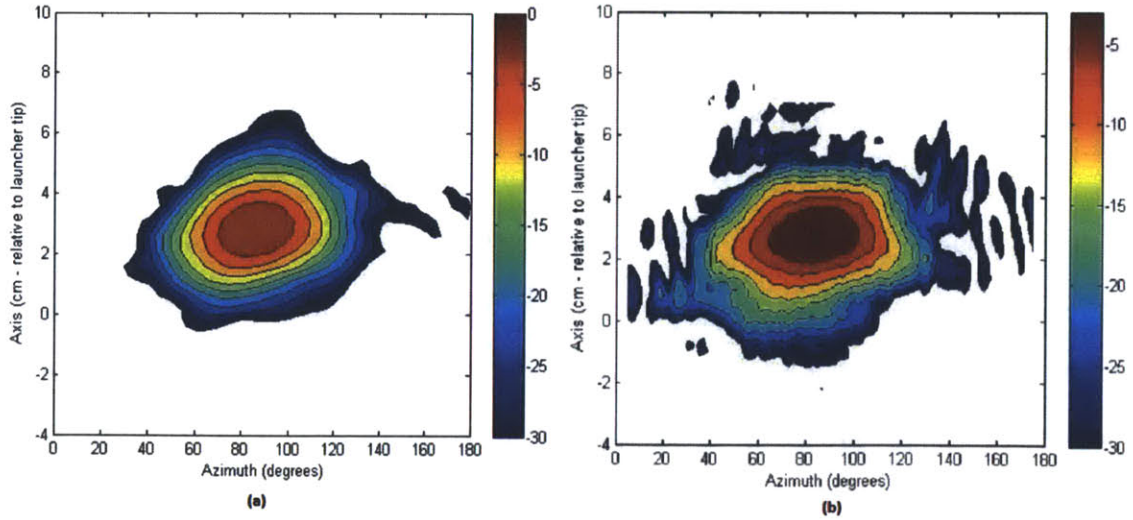

Figure 3-12: Output radiation pattern of the launcher. Patterns measured along a cylindrical surface located at the launcher tip with 5 cm radius: (a) Surf3D calculation and (b) cold test scanner measurement using a $TE_{22,6}$ mode generator.

Next, the launcher design is validated using a more rigorous calculation within Surf3D which calculates the rf field scattered from a metal surface by solving the electric field integral equation for an unknown surface current using the method of moments [141]. Using Surf3D, the fields along a cylindrical surface at the launcher tip with a radius of 5 cm are calculated and shown in Figure 3-12(a). The beam has high Gaussian content, and there are no significant sidelobes at or above the -30 dB power level. For further verification, the launcher was machined and sent to our collaborators at the University of Wisconsin, who specialize in the design of such launchers and have a readily available scanner capable of measuring along cylindrical planes for a cold test. The result of the cold test measured by R. Vernon and D. Minerath of UW is shown in Figure 3-12(b). The agreement between theory and experiment is quite good. The 9 dB beam width along each axis is quite similar in both cases, with a 2.95 cm axial width and 60° azimuthal width measured in the Surf3D calculation and a 2.9 cm axial width and 70° azimuthal width measured in cold test. We do note however that the magnitudes of the sidelobes in the measured case are somewhat larger, reaching the -20 dB level, which is still quite small. There are a several reasonable explanations for this discrepancy. First, the cold test measurement requires the use of a TE22,6 mode generator [142]. Such a mode generator is a very complex piece of equipment, and while it is tremendously useful, we acknowledge that the output mode is not a pure TE22,6 mode. Any spurious mode content at the input will therefore result in less efficient mode conversion within the launcher. Additionally, a dimpled wall launcher is no simple task for the machinists, and additional loss should be expected due to the required tolerances. Finally, there will also be experimental errors resulting from the alignment of the measurement system [143].

With the launcher successfully designed, attention can now be directed towards the mirror system. Previously, in order to get output beams with very high Gaussian beam content, many IMCs employed phase correcting surfaces on the mirrors [143]. Using simulation codes, the field distribution at the first mirror is calculated. Then, knowing that

a Gaussian beam with flat phase and appropriate beam waist is desired at the window, a phase retrieval code would be employed [144] to calculate the required mirror surfaces to satisfy such a transition [145]. While this method, in theory, can yield a nearly perfect Gaussian beam output, there are some caveats. First, it should be acknowledged that the theoretical output at the first mirror is likely to differ somewhat from the actual fields in experiment. While the simulated pattern could be replaced with a measured pattern, this approach would also be accompanied by small sources of experimental error. Therefore, the phase corrections would always be based on a close approximation to the actual fields. Additionally, the phase corrections require that the mirrors have the exact theoretical profile and be located in the exact position as defined by their design. In reality, machining tolerances will lead to small errors in the perturbations on the mirror surface and even a perfect mechanical design should expect some tiny misalignments. While these sources of error are not catastrophic, they still play a role in limiting the achievable IMC efficiency. One alternative is to introduce a set of smooth, curved mirrors instead, which would be less sensitive to alignment errors. Given that the output beam quality of the launcher has continued to improve in recent years, high quality output beams can be achieved by designing an IMC with smooth mirrors which presents both a simpler design process as well as looser mechanical tolerances in the overall assembly.

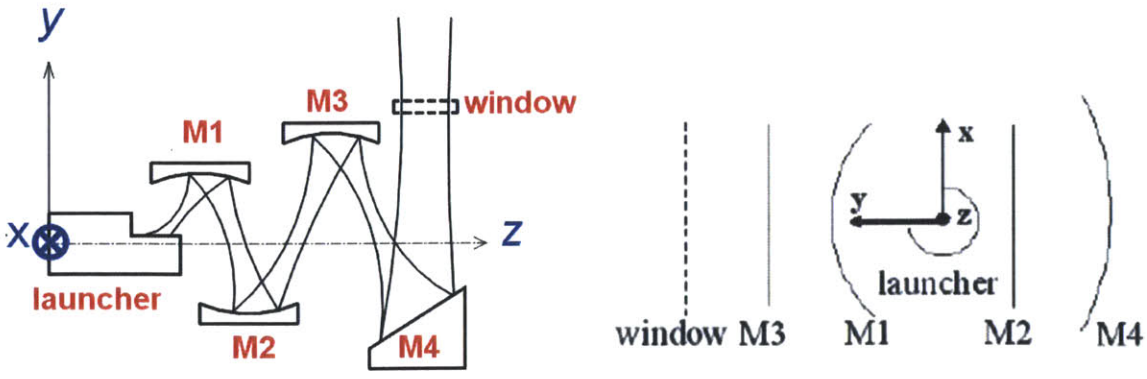

Figure 3-13: Layout of the IMC's system of 4 mirrors. Left: top view, Right: view along axis.

The mirror system in this latest design is comprised of 4 smooth mirrors. The rf power will propagate along a horizontal plane with the mirror system providing shaping in the vertical plane (x) and the axial plane (z). The first two mirrors shape the beam along one axis each, with mirror 1 shaping the beam along x while mirror 2 shapes the beam along z. Mirror 3 is perfectly flat and is only necessary to ensure the beam arrives at the window, while mirror 4 is the only mirror that has curvature along both axes. The layout of the system of mirrors of the IMC is shown in Figure 3-13. The mirror system design begins with the calculated fields from the launcher obtained in Surf3D. It is the launcher design that defines the characteristics of this first mirror which should be a parabolic cylinder with a focal length of 5 cm and whose position must be offset from the vertical axis by the caustic radius of 1.06 cm. Beyond the first mirror, simpler codes, or even Gaussian beam optics as a close approximation, may be used. The code we used is known as SCATTER which computes the radiated field at an arbitrary metal surface using the Stratton-Chu formula [140]. Based on the results, mirror 2 is determined to have a regular cylindrical surface with a curvature radius of 62 cm. Finally, the fields are propagated to the flat third mirror and onto the surface of mirror 4. Mirror 4 is oriented such that its center is located at the same axial and vertical position as the window and is tilted so that the microwave power reflects off its surface and propagates normal to the window. The curvature radii for mirror 4 are found to be 104 cm in the axial plane, and 209 cm in the vertical plane. The size, shape, position, and calculated beam size on the surface of each mirror are summarized in Table 3-3. With the design completed, the theoretical output at the window may be determined using SCATTER. The calculated field amplitude and phase distributions along each axis are shown in Figure 3-14. A circular beam with high Gaussian beam content is predicted. The predicted beam waist at the window is $w_x = w_z \approx$ 2.9 cm with a flat phase. The Gaussian beam content, which will be discussed later, is 98 %.

Table 3-3: Smooth mirror IMC mirror system specifications

	Beam size (cm)		Mirror Center (cm)			Mirror Size (cm)		Curvature (cm)	
	w_x	w_z	x_0	y_0	z_0	D_x	D_z	R_x	R_z
M1	2.20	1.13	1.06	5.00	0	10.0	5.0	10	---
M2	2.53	1.69	0	-5.00	5.04	10.2	6.8	---	62
M3	2.71	2.47	0	11.00	12.50	10.9	10.0	---	---
M4	3.11	3.11	0	-10.00	22.55	14.0	14.0	209	104
Window	2.93	2.93	0	25.40	22.55	9.75	9.75	---	---

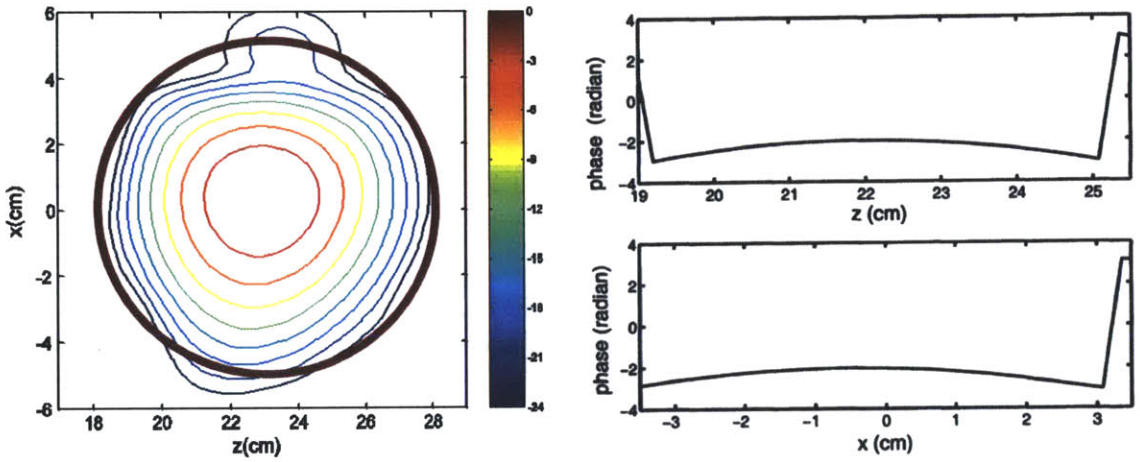

Figure 3-14: Theoretical output beam amplitude and phase distribution at the window. Fields are calculated using SCATTER. Amplitude data is shown on a logarithmic scale with 3 dB contours plotted and the phase plots, showing a cross-section along each axis, are wrapped between $-\pi$ and π.

3.4.3 Cold Test Measurement

To verify IMC operation, it is important to first measure it in cold test before installing it on the gyrotron. This is not only to validate the theoretical design of the IMC, but it also serves to ensure that the mechanical design is sound. In the first version of the 110 GHz tube, it was found that one of the mirrors was located in the wrong position, and a distorted

beam with less than half the expected power was coming out of the gyrotron, meaning that the majority of the power was bouncing around inside the tube [127].

To perform the cold test, a $TE_{22,6}$ mode generator, like the one used for the launcher measurement, was obtained [142]. The mode generator converts the fundamental mode of rectangular WR-8 waveguide into the $TE_{22,6}$ mode in a cylindrical waveguide with dimensions equal to the launcher input radius. For measuring the beam pattern, we use a 3-axis scanner along with a vector network analyzer (VNA), specifically the Agilent E8363B PNA with F band (90-140 GHz, WR-8) Oleson millimeter-wave extension heads. The VNA provides for very accurate and repeatable results, and, provided the system has reasonable transmission, excellent dynamic range with high signal to noise ratio (SNR). In order to measure the beam pattern, the fields must be sampled at an array of points, so the VNA receiver is mounted to the 3-axis scanner and a cut waveguide antenna is connected to sample the fields over a very small region. Using a Labview control system which communicates with the VNA and the scanner's motor controllers, large grids of data can be measured quite quickly. The general limitation is the sweep time of the VNA. While larger IF bandwidths on the VNA could be used to speed up measurements, the standard deviation of each data point would go up substantially, and thus low IF bandwidths, < 100 Hz, are used with a small number of sampling points. Data can still be collected at a rate of about 1 Hz, meaning that a single plane of data, with a 50 x 50 grid, can be measured in under an hour.

The VNA is capable of measuring both the amplitude and the phase of the radiated fields, however for these measurements we focus on the amplitude data only. The phase measurement is particularly sensitive to slight misalignments between the scanner and IMC and is quite noisy towards the edges of the beam. Though, it should be noted that in a measurement system that is more stable and where precision alignment can be performed, the phase measurements are extremely reliable and compare well with any calculated phase [146]. In the case where only amplitude measurements are considered, the phase

may be calculated via a phase retrieval code using amplitude measurements in several planes.

The formulation of the iterative phase retrieval procedure involves the measurement of amplitude A_1(x,y) at plane $z = z_1$ and amplitude A_2(x,y) at plane $z = z_2$. The full, complex field distribution at each plane is also a function of the phase, φ_1(x,y) and φ_2(x,y), respectively. The total field at plane z_n is therefore:

$$\psi(x,y,z_n) = \psi_n(x,y) = A_n(x,y)\exp(j\varphi_n(x,y)). \tag{3.15}$$

The important part of the phase retrieval process is relating the field at both planes. This can be done by defining a propagation operator based on the plane wave expansion as follows [147]:

$$\psi_2(x,y) = \mathcal{P}_{12}\{\psi_1(x,y)\} = \mathcal{F}^{-1}\left\{\mathcal{F}\{\psi_1(x,y)\}\cdot\exp\left(j(z_2 - z_1)\sqrt{k^2 - k_x^2 - k_y^2}\right)\right\} \tag{3.16}$$

where $k^2 = k_x^2 + k_y^2 + k_z^2$ and $\mathcal{F}$ represents the Fourier transform.

To begin the process, an initial guess must be supplied, which could be as simple as a constant zero phase at the first plane. The initial field guess at plane 1 is:

$$\psi_1^{(0)}(x,y) = A_1(x,y)\exp\left(j\varphi_1^{(0)}(x,y)\right) \tag{3.17}$$

and the amplitude and phase at plane 2 may be obtained via the propagation operator:

$$\psi_2^{(0)}(x,y) = \mathcal{P}_{12}\left\{\psi_1^{(0)}(x,y)\right\} = A_2^{(0)}(x,y)\exp\left(j\varphi_2^{(0)}(x,y)\right). \tag{3.18}$$

Since the fields at plane 2 are already known, a better approximation of the real case can be given by combining the measured fields and calculated phase, such that:

$$\psi_2'^{(0)}(x,y)) = A_2(x,y)\exp\left(j\varphi_2^{(0)}(x,y)\right). \tag{3.19}$$

This field may then be propagated back to the first plane:

$$\psi_1'^{(0)}(x,y) = \mathcal{P}_{21}\left\{\psi_2'^{(0)}(x,y)\right\} = A_1'^{(0)}(x,y)\exp\left(j\varphi_1'^{(0)}(x,y)\right) \tag{3.20}$$

and similarly the measured amplitudes may replace the calculated ones:

$$\psi_1^{(1)}(x,y) = A_1(x,y)\exp\left(j\varphi_0'^{(0)}(x,y)\right) = A_1(x,y)\exp\left(j\varphi_1^{(1)}(x,y)\right) \tag{3.21}$$

where $\varphi^{(m)}(x,y)$ represents the improved phase guess after m iterations. A mathematical proof shows that such an algorithm converges [147]. Therefore, after each iteration, as the calculated phase approaches the real phase, so too will the calculated amplitudes approach the measured ones. This allows for a convergence parameter to be defined by the normalized error between the calculated amplitudes and the measured amplitudes, which for a discrete set of data is given by:

$$Error^{(m)} = \frac{\sum_{x,y}\left[A_1(x,y) - A_1'^{(m)}(x,y)\right]^2}{\sum_{x,y} A_1^2(x,y)}. \tag{3.22}$$

Once this error becomes small enough, the phase has converged and the propagation of the complex fields back and forth would yield the measured amplitude.

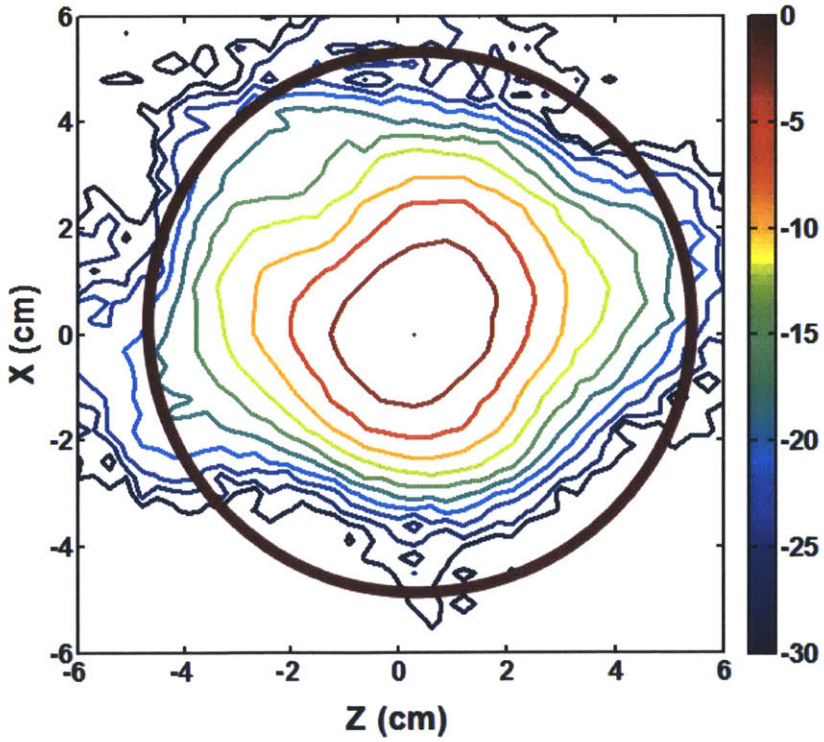

Figure 3-15: Cold test measurement of the output beam at the location of the window. 3 dB contours are plotted.

Returning to the IMC cold test measurement, the experimental setup allows for measurements of the amplitude directly at the location of the window. Such a measurement is shown in Figure 3-15 where the position of the window is also illustrated. The output beam is of high quality with only a slight ellipticity as the measured beam waists of w_x = 2.7 cm and w_z = 2.9 cm agree quite well with the theoretical output beam of Figure 3-14 where $w_x = w_z$ = 2.9 cm. A dynamic range of over 30 dB was achieved in the measurement. The important metric to consider is the output beam quality which can be defined by the Gaussian beam content. To perform such a calculation, the phase must be known as well. The phase was obtained by measuring the amplitude in several planes and applying the iterative phase retrieval procedure detailed above. The Gaussian beam content can then be determined as:

$$GB\% = 100\frac{\left|\int A_{Gaussian}(\alpha_x,\alpha_z,w,x,z)\cdot A^{*}_{Measured}(x,z)dxdz\right|^2}{\int\left|A_{Gaussian}(\alpha_x,\alpha_z,w,x,z)\right|^2 dxdz\cdot\int\left|A_{Measured}(x,z)\right|^2 dxdz} \tag{3.23}$$

where the circular Gaussian beam propagates in the y direction and has beam waist w and tilt angles with respect to the propagation axis of α_x and α_z. A small tilt is allowed to account for any misalignment between the measurement axis and the propagation axis so that the mode content may be determined more accurately. Without any fixed mechanical alignment, it is difficult to align the system to better than 1° and, therefore, the Gaussian beam content should be optimized over a small range of tilt angles. The equation for the field of a fundamental Gaussian beam traveling along the y axis is given by:

$$A_G(x,y,z) = A_0\sqrt{\frac{2}{\pi w^2(y)}}\exp\left(\frac{-\left(x^2+z^2\right)}{w^2(y)}\right)\exp(j\zeta)\exp\left(j\frac{k\left(x^2+z^2\right)}{2R}\right)\exp(jky) \quad (3.24)$$

$$w^2(y) = w_0^2\left(1+\left(\frac{\lambda y}{\pi w_0^2}\right)^2\right) \quad (3.25)$$

$$\frac{1}{R} = \frac{y}{y^2+\left(\pi w_0^2/\lambda\right)^2} \quad (3.26)$$

$$\zeta = \arctan\left(\frac{y}{\pi w_0^2/\lambda}\right) \quad (3.27)$$

where w_0 is the minimum waist size at the beam focus, which is ideally the window location, R represents the radius of curvature of the phase front, and ζ is the Gouy phase shift.

Using the measured amplitude at the window and retrieved phase, a Gaussian beam content of 95.3 % was calculated with beam waist w = 2.8 cm.

3.5 Smooth Mirror Mode Converter Gyrotron Experiment

The IMC whose design was detailed in the previous section was then installed in the gyrotron where the V2005 cavity was used and the collector was grounded.

The primary goal of this experiment was to validate the operation of the new mode converter, though some other interesting work would arise as well. Once the new components were installed and the tube was brought back to high vacuum, an alignment was performed: first by finding the physical center by recording the extreme positions where beam interception occurs and then by refining the alignment to maximize the output power. Eventually stable operation at MW power levels was achieved and the beam pattern was measured. The parameters of the operating point were: B_0 = 4.40 T, V_k = 96 kV, and I_{beam} = 43 A where 1.2 MW of output power was measured.

Just as in cold test, an accurate, high resolution beam pattern is desired. For such measurements, we require a larger scanning system since measurements must be taken

well beyond the window due to the fact that the microwave beam intensity is too focused close to the window and the magnetic field is too large for the scanner components. This larger scanning system is only a 2-axis scanner, meaning that alignment between planes cannot be preserved and misalignment between planes must be handled in post-processing. Again, we use a cut waveguide antenna to measure the fields over a small region which feeds a setup comprised of a programmable variable attenuator and an rf diode. Since the high power from the gyrotron could easily damage the rf diode if the attenuation is insufficient, instead of measuring a variable signal level, we vary the attenuation required to yield the same reference signal from the diode. At each point, the programmable attenuator's attenuation level is slowly dropped until the diode reads the defined reference value. As long as caution is taken to limit the spacing between points, the entire pattern can be safely measured. The downside of this approach is that scanning takes significantly longer than it did in cold test, especially with the gyrotron pulsing at only 1-4 Hz. Not only that, but such measurements cannot be left unattended as the beam current will tend to drop as the pressure rises from constant operation. Therefore, the size of the data grid must be limited. For these measurements, we used a 25 x 25 point array and kept the spacing between points to 1 or 2 cm.

Since measurement is impossible at the location of the window, beam patterns must be measured far away and a phase retrieval algorithm will be applied to obtain both the amplitude and phase of the beam at the window. The measurement planes we used were located 80, 100, and 120 cm from the window. The measured beam pattern at 100 cm is shown in Figure 3-16. This measurement technique is quite robust. While the specification of the programmable attenuator is 0-60 dB, we found that the attenuation saturates around 40 dB, though this still provides an excellent dynamic range. In addition, the programmable attenuator was calibrated using the VNA thus limiting any error introduced by the attenuator to $< \pm 0.1$ dB. We found that the measurements are very repeatable and have an error of approximately ± 0.3 dB at each point. This error is a

combination of error due to experimental effects, since there is some shot-to-shot variation in intensity, and effects from the measurement system. The measurement error arises from the variation in the rf diode output voltage during the flat-top of the pulse and the need to assign a range of acceptance values rather than a single value that the measurement system tries to reach by varying the attenuation. By having a small acceptance range for the reference voltage, which is on the order of the measurement error of the rf diode voltage on the oscilloscope, measurement time can be optimized without significantly increasing any measurement error.

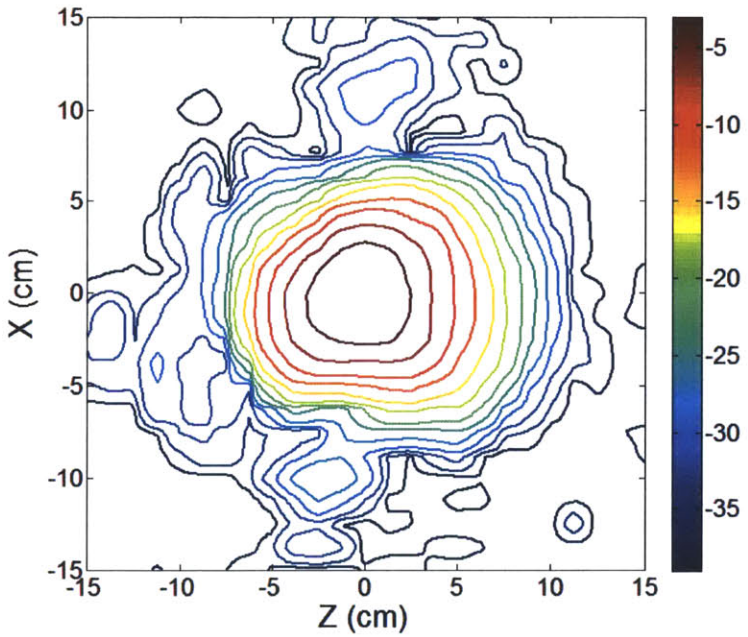

Figure 3-16: Beam pattern measured 1 m from the gyrotron window in hot test. 3 dB contours are plotted.

The phase retrieval algorithm that has been described was applied to this data set and the retrieved amplitude distribution at the window was obtained and is shown in Figure 3-17. The beam waists of the phase retrieved beam pattern are $w_x = 2.9$ cm and $w_z = 3.0$ cm, which agrees well with both the cold test measurement and the theoretical prediction. The Gaussian beam content of this beam was then analyzed using Eq. (3.23) and was found to be 96.3% for a beam with $w = 2.9$ cm, which is identical in size to the

theory calculation. This also agrees quite well with the cold test measurement since slightly higher Gaussian beam content would be expected in hot test due to the improved mode purity at the input of the launcher.

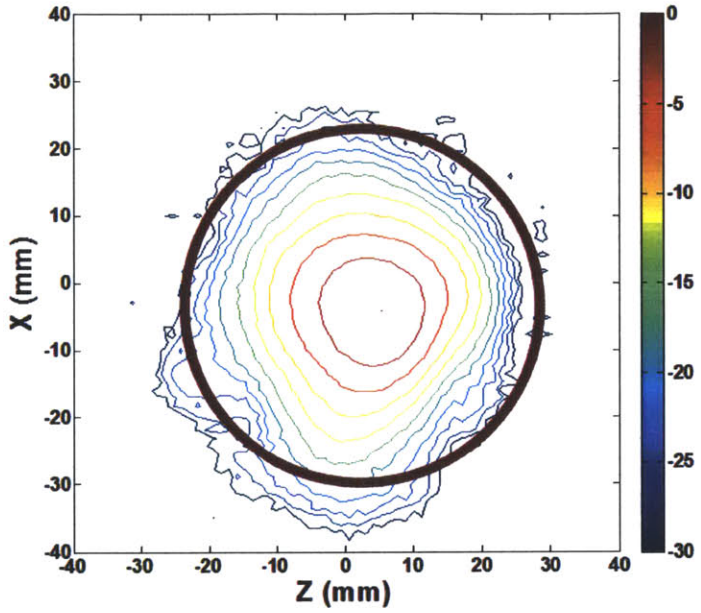

Figure 3-17: Output beam at the gyrotron window calculated by a phase retrieval algorithm. Phase retrieved from amplitude data in planes 80, 100, and 120 cm from the gyrotron window. 3 dB contours are plotted.

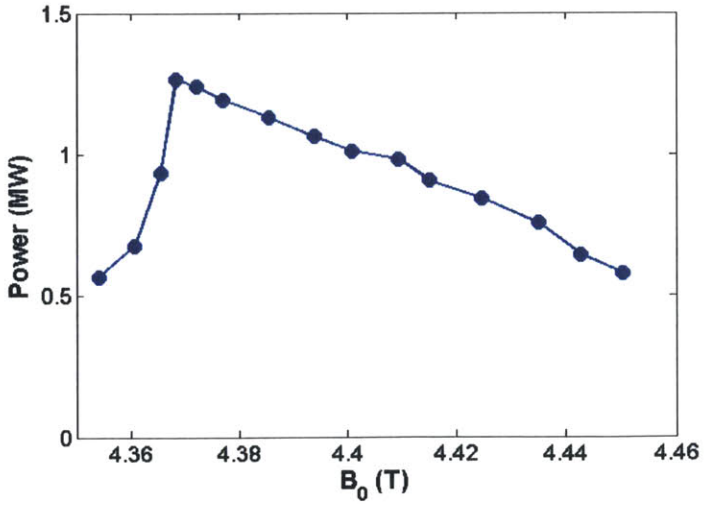

Figure 3-18: Measured output power vs main magnetic field (B_0) at 98 kV and 42 A.

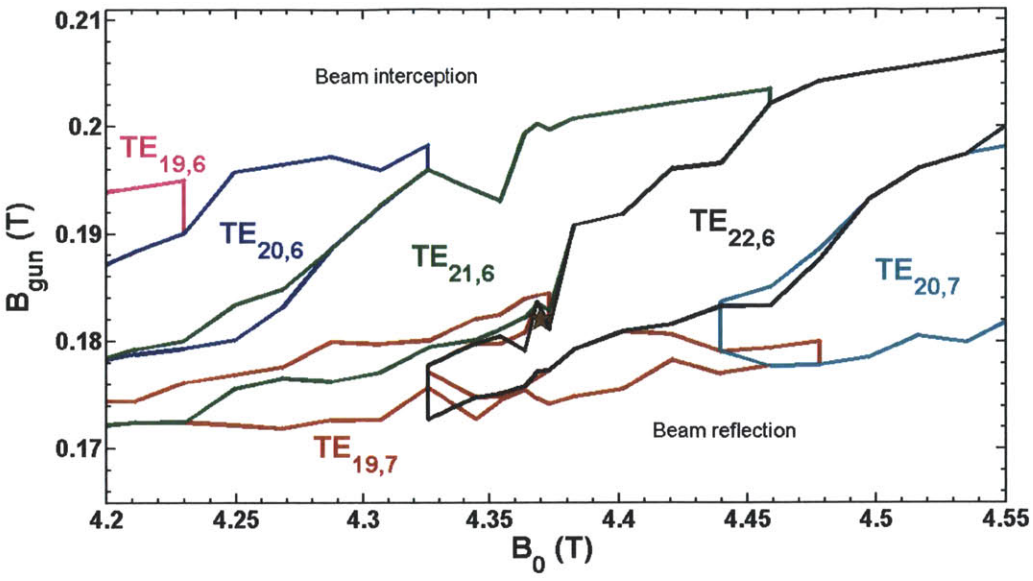

Figure 3-19: Mode map measured at 98 kV and 42 A. High power operating point is marked by the gold star.

Experiments continued as operation with this new mode converter was thoroughly investigated. While 1.5 MW was anticipated, as hard previously been demonstrated with the V-2005 cavity, operation was now limited to only 1.3 MW, which was found in operation at 98 kV and 42 A. The dependence of the output power on the magnetic field for the above operating condition is shown in Figure 3-18. The next step was to investigate the mode competition by measuring the mode map with this new mode converter. The mode map shown in Figure 3-19 indicates that there is, indeed, additional mode competition as the $TE_{19,7}$ mode is excited around the high efficiency operating point marked by the gold star. Frequency measurements at main magnetic field values that are slightly lower than that of the high efficiency operating point showed a 400 MHz signal which is explained as the beat frequency between the $TE_{22,6}$ and $TE_{-19,7}$ modes. This suggests that the mode could be simultaneously excited and competing, thus limiting higher power operation in the $TE_{22,6}$ mode at that operating point.

A number of possible explanations for the decreased output power and increased mode competition were explored. The performance of the electron gun was revisited to determine if, perhaps, there was any performance degradation after years of operation. However, the measured performance, shown previously in Figure 3-2, agreed well with initial studies of the electron gun [105], though a full study of the emission uniformity was not conducted. While it is also possible that the new launcher may generate some additional microwave field reflection that could alter the cavity performance, such effects should have been predicted in a code like MAGY, which did not predict any appreciable change in performance.

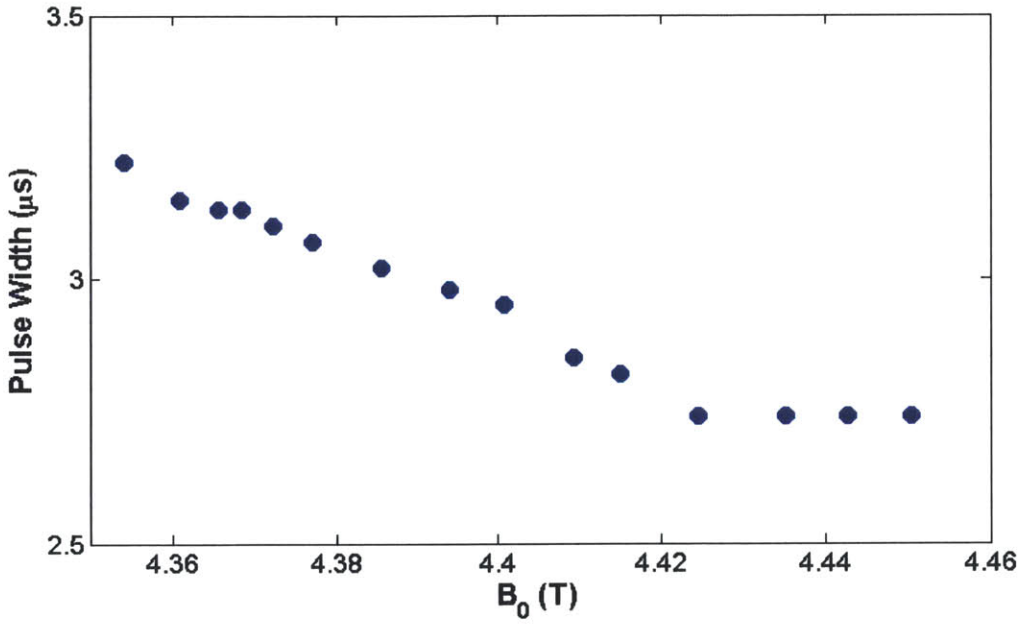

Figure 3-20: Pulse width measured as a function of main magnetic field.

However, there is one noticeable difference between these measurements and those taken previously. In past measurements, the measured microwave pulse showed a very steep rise with a pulse width of about 2.6 μs. In current experiments, we actually found that the maximum average power measured by the calorimeter is quite similar to that measured previously during 1.5 MW operation; however, in this case, the pulse width

has grown much longer. The measured pulse width for different main magnetic field values is shown in Figure 3-20. At lower magnetic field where the output power is larger, we observe significant broadening of the rf pulse, while at higher magnetic field where the output power is more modest, the pulse width is quite similar to previous experiments. Figure 3-21 shows two representative rf traces, one from the V-2005 depressed collector and one from this work. It is quite clear that the behavior on the leading edge of the pulse, during the rise of the voltage pulse, is different in each case. In the diode trace for the smooth mirror experiment, shown in Figure 3-21(b), the power begins to rise around 1.7 μs, while the rise did not occur until after 2 μs in the depressed collector experiment, shown in Figure 3-21(a). Since the voltage triggering is identical in each case, we must conclude that the recent experiment is showing significant power in the modes excited before the voltage has reached its flat-top level, which occurs at ~2.8 μs. This result sparked an interest to investigate the mode excitation sequence as the voltage rises and a discussion of such experiments follows in the next chapter.

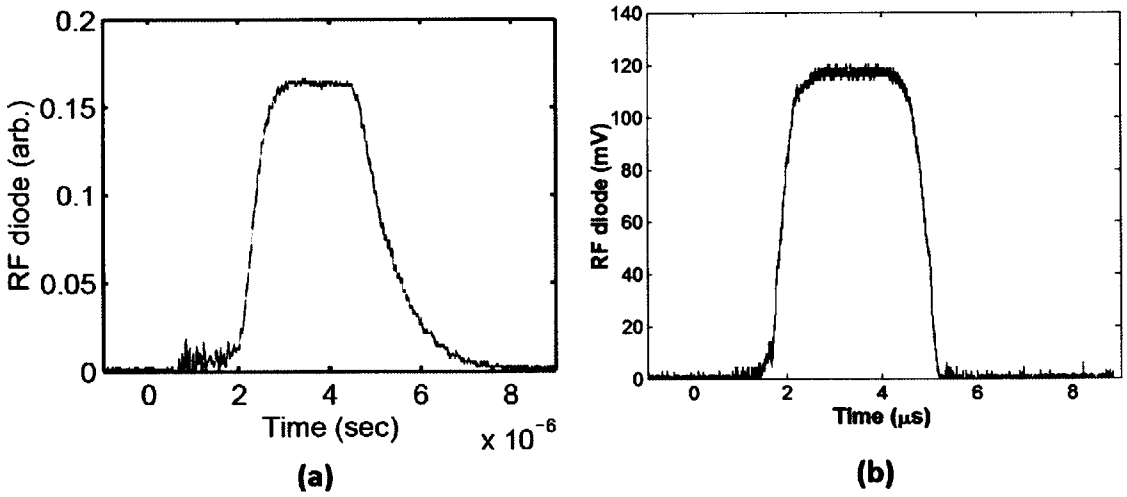

Figure 3-21: Comparison of measured rf diode (power) traces. (a) the previous 1.5 MW experiment and (b) the smooth mirror experiment where the maximum measured output power was 1.3 MW.

3.6 Summary

The experimental configuration of the gyrotron has been introduced. Operation of the principal components of the gyrotron, namely the electron gun, the magnets, the cavity, the mode converter, and the collector, were presented along with the design and performance characteristics of each. The gyrotron has a set of diagnostic tools to quantify performance, including power measurement using calorimetry and a broadband video detector, frequency measurement using wavemeters and a heterodyne receiver system, and a capacitive probe to measure the pitch factor.

The theory and design of a new internal mode converter that implements smooth, curved mirrors was described in detail. A high quality beam with 98 % Gaussian beam content is predicted by theory. The IMC design was then validated in cold test using a $TE_{22,6}$ mode generator. While slightly elliptical, the results agreed well with theory and a Gaussian beam content of 95.3% was calculated. The IMC was installed on the gyrotron and operated at MW power levels. After measuring the beam pattern, the calculated Gaussian beam content of 96.3% was expectedly a little higher than cold test, and the beam waist of 2.9 cm matched theoretical predictions. The results were obtained by using a phase retrieval algorithm to calculate an amplitude and phase at the window from amplitude data measured in several planes further away.

After lengthy attempts to further align the tube, it was found that the output power peaked at around 1.3 MW, falling short of the 1.5 MW that had been measured in the previous depressed collector experiment. While the gyrotron average power output is approximately the same, the microwave power pulse had broadened, resulting in a reduction of the measured peak power. The broadening of the rf pulse is the result of more power being excited while the voltage is still rising to its flat-top level and warrants further investigation, which follows in Chapter 4.

Chapter 4

Study of the Start-Up Scenario for a MW Gyrotron

When studying gyrotron operation, extensive work goes into mapping the power and frequency over a wide parameter space of magnetic field, velocity ratio and current. While it is true that the steady-state operation of the gyrotron is what matters, oftentimes device performance falls well short of theoretical predictions, and the reasons are usually not obvious. Many factors, like the velocity spread of the electron beam, are known to degrade the efficiency. While it is possible to set up an experiment to measure the spread, it is not a practical measurement to be done as part of the development of every system. Instead, researchers can assume a possible range of values based on simulations and past experience. At the same time, there are other possible explanations for efficiency shortcomings that have remained largely overlooked. One such area is the examination of the gyrotron's start-up scenario, which is the sequence of modes that is excited during the rise of the voltage pulse. While previously investigated theoretically via simulation, experimental treatments remained lacking. In this section, a discussion of the mode excitation process in high power gyrotrons will be discussed and the results of recent experimental work in this area will be presented. The author has published these results in a paper, from which some portions of this chapter have been adapted: "Experimental Study of the Start-Up Scenario of a 1.5-MW, 110-GHz Gyrotron", *IEEE Transactions on Plasma Science*, Vol. 41 (4), pp. 862-871, April 2003 [148].

4.1 Mode Competition in MW Gyrotrons

The issue of mode competition has been touched upon in previous chapters. It was discussed that MW gyrotrons must operate with large, overmoded cavities to maintain acceptable Ohmic cavity losses, thus requiring operation in a mode with large axial and azimuthal indexes within a dense spectrum of modes. This means that exciting the correct mode over the desired range of operating parameters can be quite challenging.

In Section 2.3, the discussion of cavity losses introduced some metrics to help evaluate which mode may be excited. We now explore these metrics in more detail in this chapter for the particular case of the cavity design presented in Chapter 3.

4.1.1 Coupling Coefficient Analysis

The derivation for the coupling coefficient emerged through the study of the non-linear theory of the gyrotron. It represents a geometric coupling factor between the mode and the beam and its definition, previously shown in Eq. (2.69), is reproduced here for convenience:

$$C_{mp} = \frac{J_{m\pm1}^2(k_\perp R_e)}{(\nu_{mp}^2 - m^2)J_m^2(\nu_{mp})} \tag{4.1}$$

where the – sign in the term indicating the order of the Bessel function is used for a co-rotating electric field. The coupling coefficient is an important parameter to consider in the design stage as an operating mode, cavity radius and corresponding optimal beam radius must be selected. Figure 4-1 shows the coupling coefficient for the 1.98 cm cavity radius and the $TE_{22,6}$ design mode as well as the modes that present the greatest mode competition, namely $TE_{21,6}$, $TE_{23,6}$ and the counter-rotating $TE_{19,7}$ mode, hereby denoted $TE_{-19,7}$. In this case, the coupling coefficient of the competitor modes is quite significant, even at the optimal beam radius, and their excitation could not be discounted. It is worth noting that this is partially explained by the fact that there exists a finite spread in the beam radius. The spread in beam radius is equal to 2 times the Larmor radius plus an additional contribution from the radial spread of the electron gyrocenters [47]. At the same time, the

$TE_{25,5}$ mode could theoretically be a risk for mode competition since it is close in frequency to the $TE_{22,6}$ mode but it may be discounted since its coupling coefficient at the design beam radius is far smaller. It is no surprise then that $TE_{25,5}$ excitations are not encountered during experimental operation. One may also gain some intuition for the interpretation of the coupling coefficient as it essentially represents the magnitude of the mode's electric field as a function of radial position. Thus, when the beam radius is at the location of one of the electric field peaks of the cavity mode, there is strong coupling for an ECM interaction, while there would be no coupling at a field null.

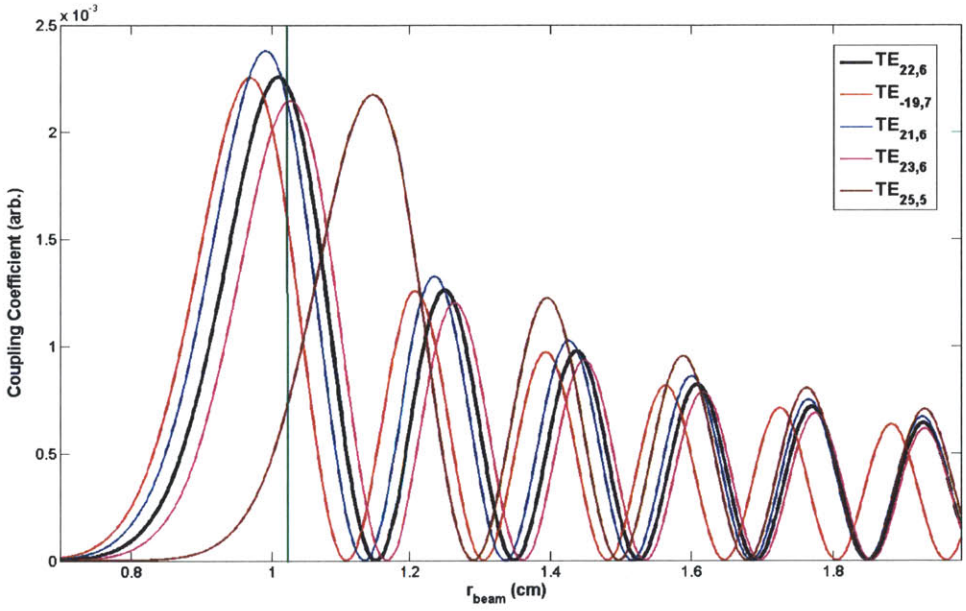

Figure 4-1: Coupling coefficient vs. beam radius of the $TE_{22,6}$ operating mode and its main competitors. The cavity radius is 1.98 cm and the optimal design beam radius, r_{beam} = 1.024 cm, is shown with the vertical line.

The coupling coefficient may also be used to aid in further analyses. While much can be explained by only analyzing the straight section of the cavity, additional effects like mode excitation in the tapers can be investigated. These occur due to the adiabatic expansion of the beam outside of the region of flat, peak magnetic field and a broadening of the electric field distribution as the wall radius increases, which varies the coupling and

potentially favors another mode. In Figure 4-2, the mode competition is explored for the V-2005 cavity geometry along with the launcher of the IMC where the beam radius is 1.024 cm in the straight cavity section. The issue of mode competition however is incomplete without also considering the synchronism condition, given by Eq. (2.11) and reproduced here for convenience:

$$\omega = n\omega_c + k_z v_z . \tag{4.2}$$

While Figure 4-2 would seem to indicate the possibility of major mode competition throughout the tapers and launcher, evaluation of Eq. (4.2) would show that one need not be concerned in most cases. However, it turns out that Eq. (4.2) is indeed satisfied for the $TE_{22,6}$ mode at z = 11 cm, where Figure 4-2 shows that there is still strong coupling. This is the ACI effect that was observed during the previous high efficiency gyrotron experiments in which the beam regained some power from the microwaves [134]. Analysis of coupling and synchronism can therefore be a helpful tool to diagnose gyrotron operation.

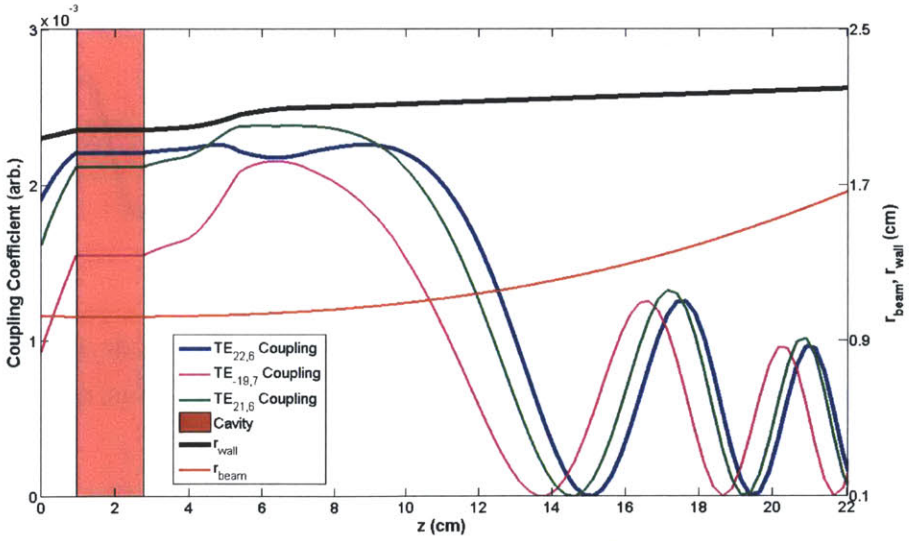

Figure 4-2: Coupling coefficient for the $TE_{22,6}$ operating mode and competing modes shown as a function of axial position. Thick black line indicates the wall radius while the beam radius is shown in red. The shaded region represents the cavity.

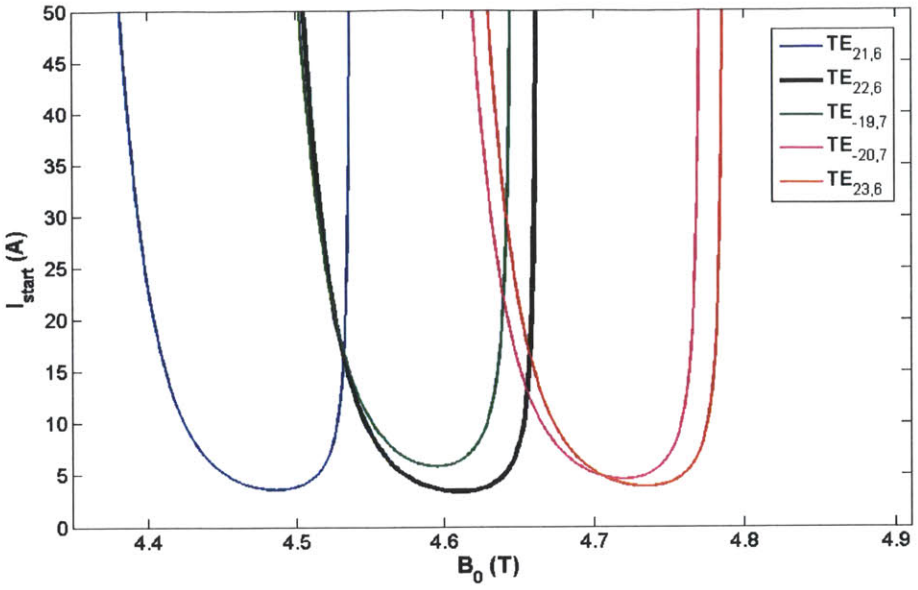

Figure 4-3: Starting current of the $TE_{22,6}$ operating mode and competing modes as a function of main magnetic field, B_0. Calculation is done at 96 kV, 40 A, α = 1.4 and r_{beam} = 1.024 cm. The Q factor of each mode was determined via cold cavity simulations.

4.1.2 Starting Current Curves

While the coupling coefficient does provide some information, it develops as part of the derivation for the starting current, which is inversely proportional to the coupling. The starting current, i.e. the necessary current to overcome cavity losses and sustain or grow the oscillation, was described in Section 2.3. Naturally, if the coupling between the fields and the beam is weaker, then more beam energy would be required to provide similar power to the oscillations to overcome the losses.

The starting current for the excitation of a mode can be calculated from Eqs. (2.68) and (2.71) where the axial field profile is assumed to be Gaussian. This assumption is sufficient in the majority of analyses since the starting current itself only yields an approximate, yet quite useful, result. The only caveat with this assumption is that it limits consideration to forward wave modes with axial mode index of 1, therefore other field profiles, like a sinusoidal distribution, must be implemented in theoretical calculations

involving modes with multiple maxima/minima in their axial field profile. In Figure 4-3, the starting current for the $TE_{22,6}$ mode and nearby competing modes is plotted as a function of main magnetic field at 96 kV and 40 A with the optimal beam radius of 1.024 cm and α of 1.4. The diffractive Q factor for each mode is determined via cold cavity simulations using the real cavity profile. In terms of mode competition, the general interpretation of such a diagram is that the mode with the lowest starting current should experience higher gain and therefore should be able to suppress other mode excitations, even when their starting current is lower than the beam current. We also see in Figure 4-3 that lower order modes are excited at lower magnetic field and higher order modes are excited at higher magnetic field. The minimum start current occurs where the detuning parameter is at its optimum value. The evolution of the starting current during the rise of the voltage pulse will be considered in the next section exploring gyrotron start-up scenarios.

4.2 The Start-Up Scenario

Thus far, the discussion of mode excitation has assumed a set of steady-state parameters, which, in the case of a pulsed device, means during the flat-top portion of the pulse. While this is, of course, the area of interest for operation, it is necessary to recognize that the gyrotron must pass through a range of parameter space before arriving at steady-state operation. Even in a CW device, the device parameters must still ramp up from zero. However, since the device is capable of running for long periods of time, the operator can develop a well-defined starting procedure on a slower timescale. In the case of pulsed operation, especially using a diode-type gun, the start-up scenario is well-defined by the input parameters and may not be altered. A better understanding of the start-up process would nonetheless be very helpful in the development of both types of gyrotrons. It is of particular importance in MW gyrotrons.

4.2.1 High-Efficiency Operation: The Hard Self-Excitation Regime

The state at which the gyrotron resonator oscillates due to the effects of the electron beam is known as self-excitation. Self-excitation regimes are typically defined by a region of parameter space where the beam current exceeds the starting current, allowing a noise-level oscillation to grow. Within the gyrotron, such a regime is referred to as soft self-excitation, where the additional distinction is required since there exists a second regime of self-excitation. This second regime, known as hard self-excitation, is actually where the peak efficiency of the device lies for the efficiency contour plot shown in Chapter 2. The region of hard excitation is characterized by the fact that the starting current is greater than the beam current. One would therefore be correct in asserting that stable operation in this regime could not be achieved without satisfying additional conditions, which in this case involves an initial field amplitude that exceeds a certain threshold. One way that this is achieved in gyrotrons, and the only way in a pulsed device, is via the start-up scenario, meaning the sequence of mode excitation during the temporal evolution of the input parameters. As the operating voltage and current grow, the soft self-excitation condition for a mode can be met, allowing the fields to grow from noise level. As the parameters continue to rise, the gyrotron may enter a regime where hard excitation is possible, and, should the fields have achieved sufficient amplitude from the initial mode excitation, it may access this regime. To aid in this discussion, a conceptual diagram may be shown, analogous to other theoretical treatments of the gyrotron start-up [149]. In Figure 4-4, the possible excitations of two modes are displayed. Mode M_1 is excited in the soft self-excitation regime as it begins to grow once the beam current surpasses its starting current $I_{start,1}$. When the beam current reaches a particular value at a given time, a bifurcation in the possible outcomes of the excitation is observed. If the conditions are right, given the strong fields generated by the mode M_1 excitation, mode M_2 may be excited in the hard excitation regime, pushing the efficiency to much higher levels. It is noted of course that

when this excitation of M_2 occurs, the beam current is still well short of $I_{start,2}$, the starting current for mode M_2. However, should mode M_2 not be excited, then the excitation of mode M_1 in the less efficient soft excitation regime would continue. If mode M_1 were not excited at all, then mode M_2 may be excited at lower efficiency in the soft self-excitation regime once $I_{beam} > I_{start,2}$ as well.

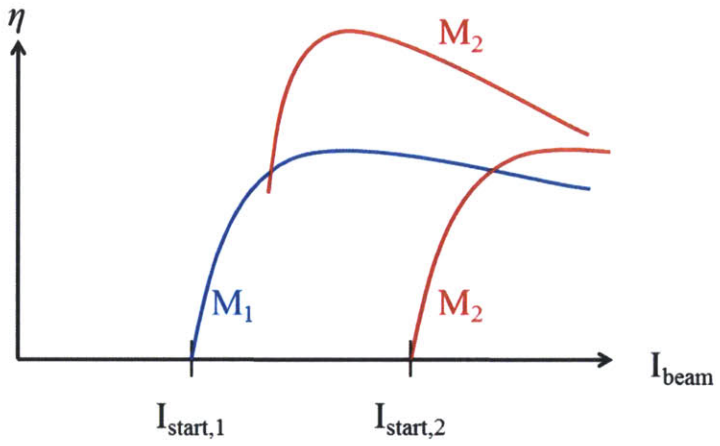

Figure 4-4: Conceptual diagram showing the possible mode excitation in a gyrotron for two different modes. The starting currents for mode M_1 and M_2 are $I_{start,1}$ and $I_{start,2}$ respectively. If the conditions are right, then the mode M_1 excitation may provide enough field intensity to allow mode M_2 to be excited in the hard excitation regime, pushing the efficiency higher than the efficiency for an excitation in the soft self-excitation regime.

In simulation studies of the gyrotron, the hard excitation regime is difficult to model. While results will be shown in the following sections of simulations using time-varying parameters, such simulations are significantly more demanding on both computing resources and necessary simulation time for convergence. Ideally, one would like to simply be able to simulate steady-state operation, particularly when large amounts of simulations must be run for design studies or other analyses. Luckily, the MAGY code provides the means of doing so by including an input rf pulse. Therefore, to simulate a possible operation in the hard self-excitation regime, a "kick" is provided in the form of a

very intense but short-lived pulse for the desired operating mode. Following this brief pulse, the mode must still be capable of sustaining its self-excitation condition for steady-state output power to continue. While such an approach is practical, it does however neglect the issue of the start-up scenario, essentially assuming that the desired sequence of modes for optimal performance would be excited. Thus one must take caution in interpreting results obtained by this method and should be aware of the issues related to start-up.

4.2.2 Starting Currents during Gyrotron Start-Up

As discussed previously, the starting current provides a good indication of which mode excitation may be favored. In the previous section, a starting current calculation was shown for the case of steady-state operation to explore the parameter space. The same analysis may be used to examine how the starting current changes during the rise of the voltage pulse to get an idea of which modes may be excited during start-up.

Such a study was performed in the design of the V-2005 cavity. For that study, a more elaborate starting current calculation was used which takes into account additional factors like the real magnetic field and simulated axial electric field profiles [150]. One possible factor in determining whether a mode is preferentially excited at steady-state is whether that mode is excited first during start-up. In order to determine which mode, the $TE_{22,6}$ or $TE_{-19,7}$, might be excited first, iso-starting current plots may be generated in a parameter space analogous to the rise of the voltage pulse [121]. This means that a curve may be plotted such that all points on the line have an identical starting current, and the area enclosed by the curve indicates the region where the starting current is even smaller. When such a curve is plotted in a voltage-alpha parameter space, the beam may also be shown rising from low voltage and alpha to the designed operating point of 96 kV and α = 1.4. A sample of these iso-starting current plots is shown in Figure 4-5 which compares

results for the V-2005 cavity, which saw reduced competition from the $TE_{-19,7}$ mode, and the V-2003 cavity at different beam radii.

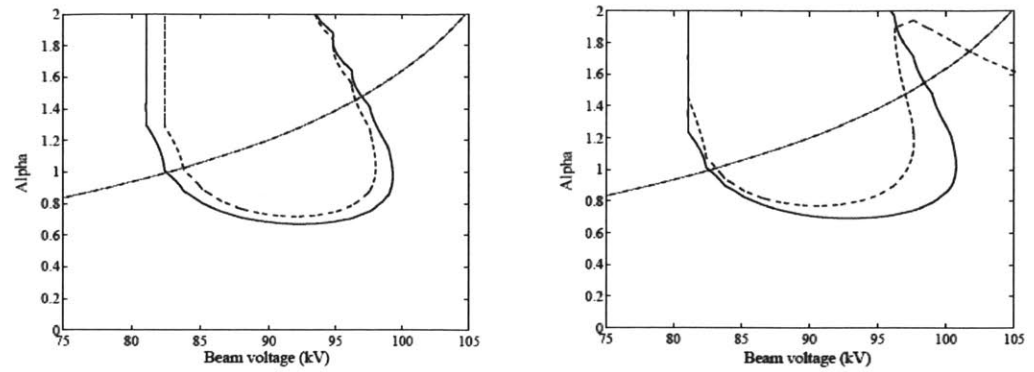

(a) $r_b = 0.52a$ (b) $r_b = 0.52a$

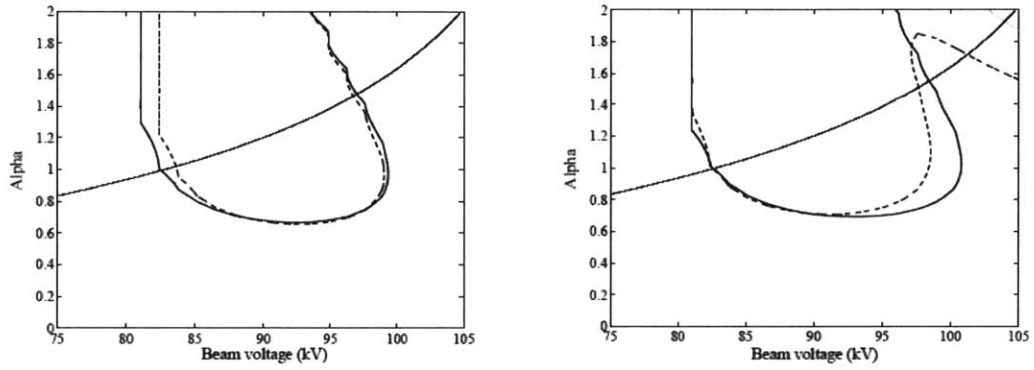

(c) $r_b = 0.505a$ (d) $r_b = 0.505a$

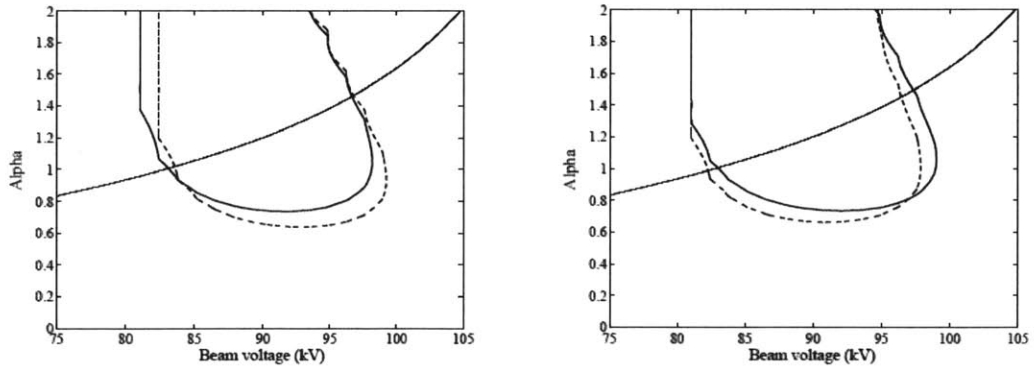

(e) $r_b = 0.48a$ (f) $r_b = 0.48a$

Figure 4-5: Iso-starting current plots for I_{start} = 40 A as a function of voltage and alpha at different beam radii. The evolution of the beam is shown along with curves for the $TE_{22,6}$ mode, given by the solid line, and the $TE_{-19,7}$ mode, given by the dashed line. (a,c,e) are for the V-2005 cavity which saw reduced mode competition from the $TE_{-19,7}$ mode as compared with the V-2003 cavity (b,d,f). Adapted from [111].

The interpretation of such plots is that the curve which is first intersected by the beam line, i.e. at lower voltage, could be excited first to help it suppress the excitation of the other mode. At each normalized beam radius plotted, the V-2005 cavity should excite the $TE_{22,6}$ mode first as seen in Figure 4-5(a,c,e). In Figure 4-5(b,d,f), the plots for the V-2003 cavity show that the $TE_{-19,7}$ mode may be excited first for smaller beam radii, therefore this can help explain the experimental results that were previously obtained. While such analysis is helpful, it neglects to consider that other modes can be excited at lower voltage, which may play a role in determining the eventual outcome at steady-state operation.

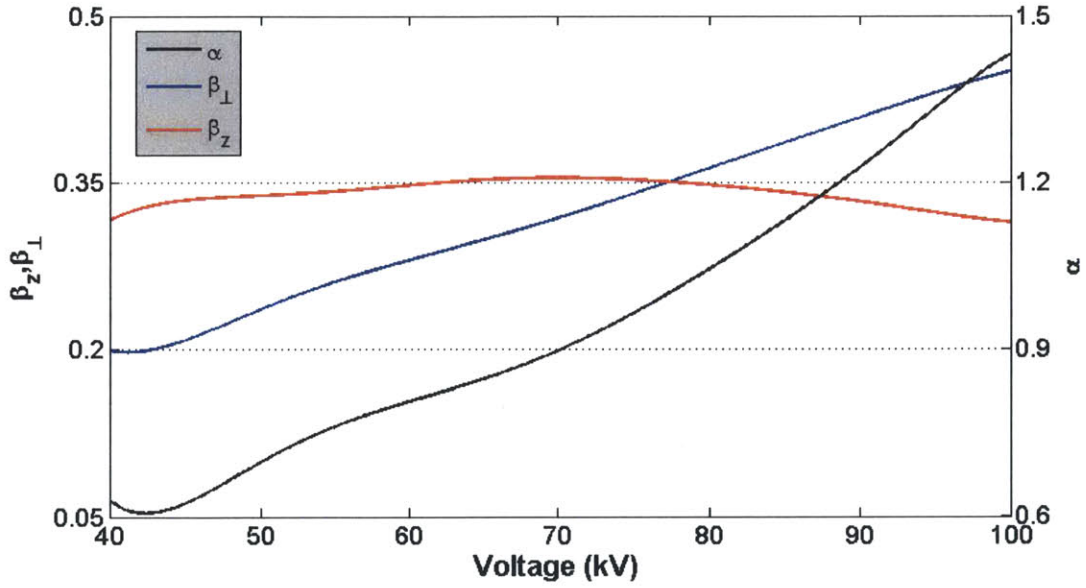

Figure 4-6: Evolution of the beam parameters, including normalized velocities, β_z and $\beta_\perp$, and α, during the voltage rise.

To investigate the full extent of modes excited during the voltage rise, the starting currents for various modes may be calculated as a function of the temporal evolution of the gyrotron parameters. For this purpose, a code was developed that incorporated effects like voltage depression to compute starting current values during start-up for a fixed magnetic field. Parameters like the beam's axial and transverse velocities were calculated

theoretically, while the beam current was calculated via a fit to experimental data. The evolution of these parameters is shown in Figure 4-6 where it is noted that alpha does indeed vary approximately adiabatically, and β_z varies only slightly and could be assumed to be constant.

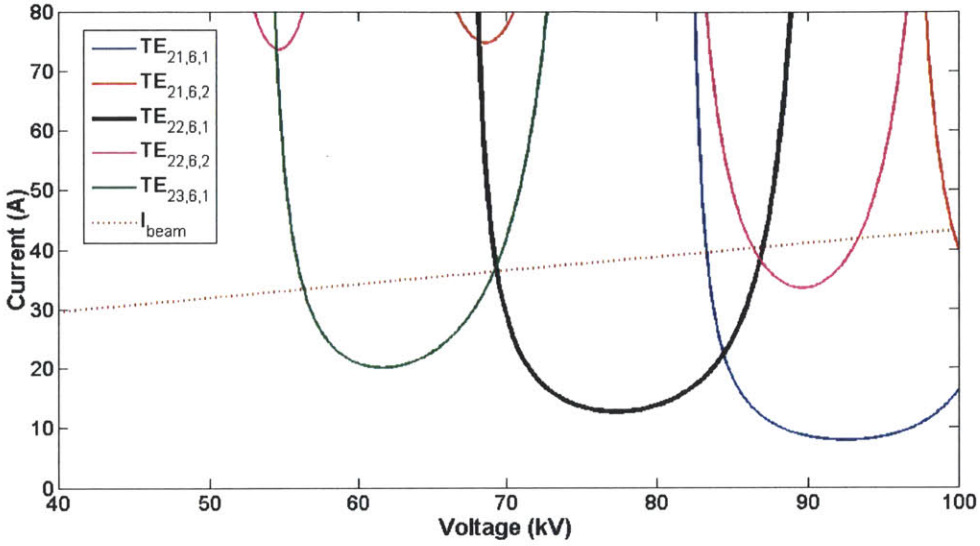

Figure 4-7: Starting current curves at $B_0 = 4.42$ T during the voltage rise for various modes, including those with high order axial field profiles. Beam current is shown by the dotted line. At 96 kV, the $TE_{22,6,1}$ mode may still be excited due to operation in the hard self-excitation regime.

For this analysis, we would like to examine the starting current of $TE_{m,p,q}$ modes with axial mode number $q > 1$, therefore a sinusoidal axial field profile is used. Figure 4-7 shows starting current curves as a function of voltage for the triplet of modes with identical radial mode number, including those with higher order axial field profiles. Note that such curves are consistent with Figure 4-3 since a higher voltage results in a higher relativistic factor which reduces the relativistic cyclotron frequency, and would be equivalent to lowering the magnetic field at a fixed voltage. There are a number of takeaways from this figure. First, we observe that the linear theory predicts the excitation of higher order modes, and thus higher frequency modes, as the $TE_{23,6,1}$ mode is the only

one with sufficiently low starting current at voltages as low as 60 kV. Second, we observe that there are two separate starting current curves visible for the modes with axial mode index $q = 2$. Early linear theory work had predicted this outcome [44], with the result being that higher order axial modes may exist at either lower or higher voltages, or conversely magnetic field. Therefore while lower frequency modes may also be excited at lower voltages, their start currents are generally higher since the diffractive Q of the mode, which is inversely proportional to the starting current, scales approximately by $1/q^2$. Finally, we note that Figure 4-7 is generated for operating parameters where the $TE_{22,6,1}$ mode is excited at 96 kV, however it would seem by observation that the mode should not be excited at that voltage. This is a result of operating in the hard self-excitation regime in which the start current is not lower than the beam current, and a region of stable operation extends up to higher voltages thanks to the electric fields generated by exciting the start-up modes. While such curves provide a useful guide, the linear theory does not take all physical, or experimental, effects into account, and therefore a nonlinear, time-dependent code like MAGY should be employed to better predict and analyze experimental behavior.

4.2.3 Simulation of the Start-Up Scenario

A number of studies have been done to investigate the start-up scenario by simulation. While we have explored some aspects of start-up mode excitation using MAGY, the full study of such phenomena is better left to those with extensive experience with the code. Earlier work on the start-up scenario focused on establishing the physics and developing a methodology to perform these complicated studies using MAGY [149, 151]. Once this was complete, more elaborate investigations of the start-up scenario could be performed. One such study modeled the start-up sequence for different rates of rise of the voltage pulse [152]. It was found that there existed a range of short voltage rise times where a single-mode start-up was achievable without any significant excitation of other modes. However, it was also shown that for rise times that are too short, the desired mode may not be excited

during steady-state operation. These simulations also showed the possibility of exciting both higher and lower frequency modes during the voltage rise.

A particularly relevant study to this work was also done in MAGY where the operating parameters and geometry for the high efficiency configuration were used [153]. The main figure from this paper is reproduced here in Figure 4-8. In this study, it was found that the higher frequency $TE_{23,6,1}$ mode was excited during the voltage rise from 62-74 kV before the eventual $TE_{22,6,1}$ mode was excited and rose to MW power levels. At even lower voltage, brief excitations were observed with an axial field pattern containing multiple peaks. However, we note that while this study used the parameters of the voltage rise in the MIT experiment, it did not use the same timescale.

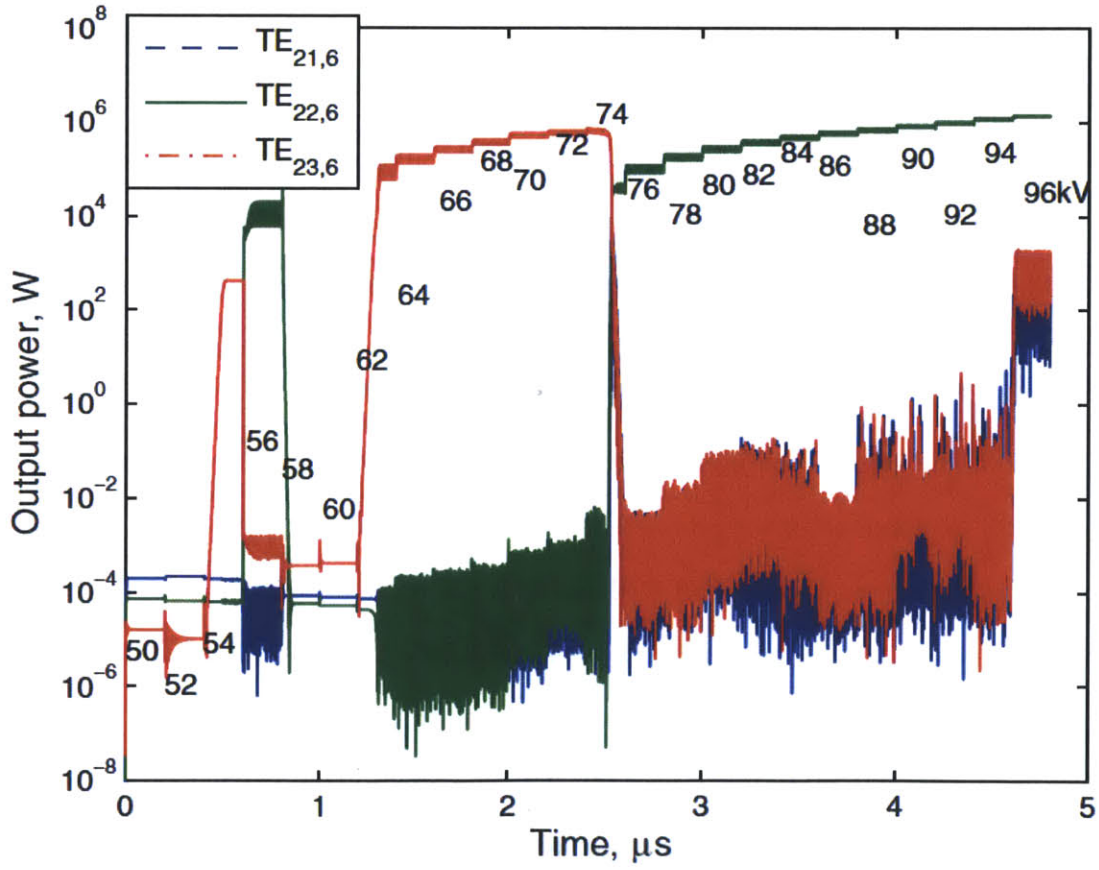

Figure 4-8: Simulation of the start-up scenario for the MIT 1.5 MW, 110 GHz gyrotron in MAGY. The voltage rise was simulated by increasing the voltage in 2 kV steps every 200 ns. Adapted from [153].

4.2.4 Consequences of Mode Excitation during Start-Up

There are a number of reasons why it is important to study the phenomenon of mode excitation during the voltage rise. First, and most obvious, the steady-state operation of the device is naturally a function of the start-up. For the case of operation in the hard self-excitation regime, the existence of mode excitations at lower voltage is a necessity to allow for operation in the regime. Even in soft excitation regimes, an incorrect start-up sequence may lead to the excitation of an incorrect mode at steady-state, or even the simultaneous excitation of the desired mode along with spurious modes that are detrimental to the gyrotron's output power and efficiency [154, 155].

Not only is it important to understand the gyrotron start-up scenario in order to improve the design of future gyrotrons, it is also necessary to consider that such megawatt class gyrotrons are incorporated as parts of a much larger system. One such example is the magnetic fusion devices that were discussed in Chapter 1. These experiments utilize gyrotron power for discharge initiation, plasma heating, as well as current drive. However, this represents only one small part of a large system which incorporates a variety of plasma diagnostics. These include sensitive equipment like electron cyclotron emission radiometers and infrared cameras, which are commonly protected from the ECH power only over a narrow band of frequencies centered at the nominal operating frequency of the gyrotron. It is therefore important to carefully understand the gyrotron's start-up scenario to ensure that spurious modes are not excited with significant power levels outside of the protected stop band.

Another concern is that some applications for the gyrotron may desire modulation of the output power which is achieved by modulating the voltage [156]. Such a modulation may result in the excitation of unwanted modes during both the voltage rise and fall of the modulation pulse meaning that the full spectrum of modes that could be excited should be well understood.

It is these issues, among others, which have motivated this work since experimental studies of this topic had been lacking in the literature.

4.3 Start-Up Scenario Experiments

The experimental setup for measuring the start-up scenario is the same as the one described in the previous chapter for the high efficiency configuration using the V-2005 cavity and the smooth-mirror IMC. As the simulation studies have shown, a number of different possibilities exist for the start-up scenario. In this experiment, given a diode-type MIG and a fixed voltage rise, the start-up sequence for operation at a nominal voltage and current could depend only on the two magnetic field inputs into the system, B_0 and B_{gun}. Therefore, each steady-state excitation on the mode map corresponds to a single start-up sequence. Recall as well that that the highest output power for a mode is found at approximately the minimum magnetic field for which that mode may be excited. This generally requires operation right on the stability limit for that mode where it is only excited for a very narrow range of parameters, and small deviations from those values may result in the excitation of other modes or an unstable oscillation where the excited mode varies from shot-to-shot. Meanwhile, at higher magnetic fields, there exists a wide range of parameters suitable for stable excitation of the desired mode, though at lower power levels as shown previously. While a nearly infinite number of possibilities may exist for the start-up scenario, where many should be quite similar, we would like to examine two characteristic cases in detail to simplify analysis. Figure 4-9 shows the measured mode map for the smooth-mirror IMC configuration where we note that the boundaries between modes are often ill-defined and unstable. This is particularly the case in the region of parameter space where the $TE_{19,7,1}$ mode may be excited. Two points have been marked on this figure indicating the two representative cases that we would like to examine: a high power operating point (⊕) at B_0 = 4.38 T and B_{gun} = 0.184 T where 1.2 MW of output power is observed at a frequency of 110.08 GHz, and a highly stable operating point (⊗) at

B_0 = 4.45 T and B_{gun} = 0.193 T where a more modest 600 kW of output power is observed at a frequency of 110.12 GHz.

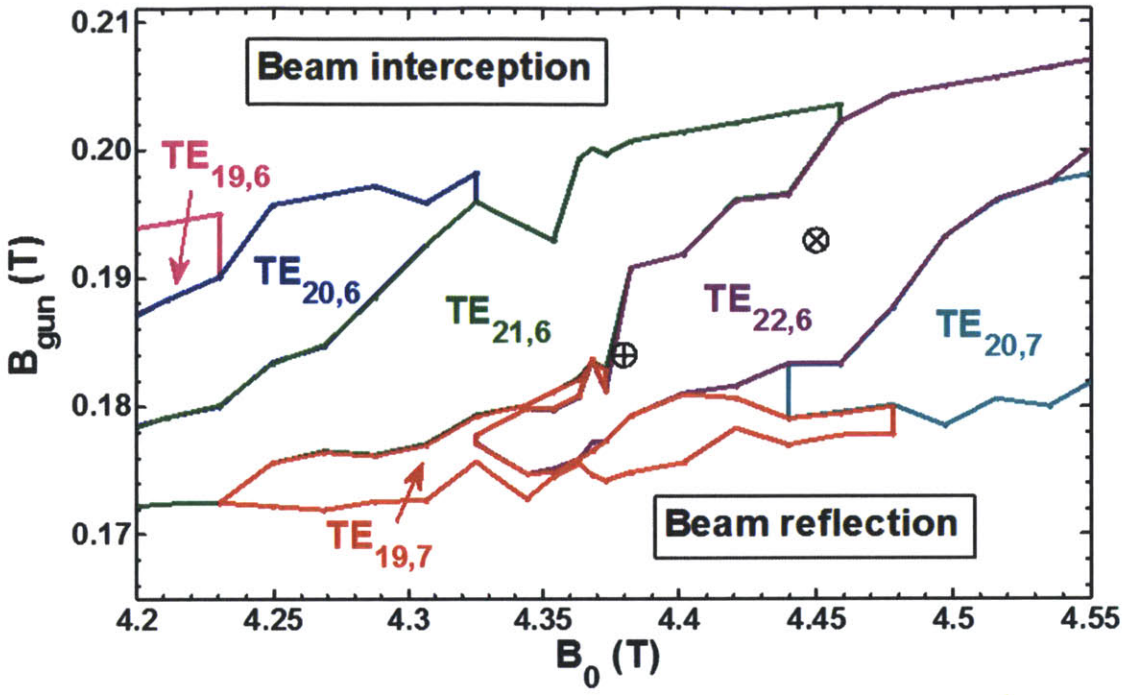

Figure 4-9: Mode map for the MIT gyrotron showing mode excitation with various magnetic field parameters with V_k = 96.7 kV and I_{beam} = 42 A. High power operating point shown by ⊕ and highly stable operating point shown by ⊗. All observed modes have a single field maximum in the axial direction (q = 1). Beam reflection at low gun field results from magnetic mirroring. Beam interception, presumed to be at the scraper just before the cavity, at high gun field results from insufficient compression of the beam.

4.3.1 Power and Frequency Measurements

In order to measure the mode excitation versus time during start-up, i.e. during the rise of the voltage pulse, different methods of frequency measurement may be used. Direct frequency measurements, i.e. measurement of the instantaneous frequency at various times during the voltage rise, were made by adjusting the time delay of the aforementioned gated heterodyne frequency receiver system. However, the signal to noise ratio (SNR), defined by the amplitude of the sideband signals relative to the noise

background in the frequency domain, of this dynamic measurement technique decreases significantly at earlier times during the voltage rise. This decrease in SNR is a result of rapidly changing voltages and lower instantaneous power levels and makes the identification of frequencies impossible below a certain threshold. For this reason, many results presented herein will also be obtained with the heterodyne frequency receiver system gated only over the steady-state portion of the pulse, i.e. during the voltage flat-top, where the SNR is largest. For such measurements, the voltage pulse amplitude was adjusted to obtain the power and frequency at each data point. In this manner, modes and frequencies could be identified right down to the onset of oscillations. The results obtained by these two methods are in very good agreement. We first present data taken by the voltage flat-top method, then present data from the dynamic measurement technique.

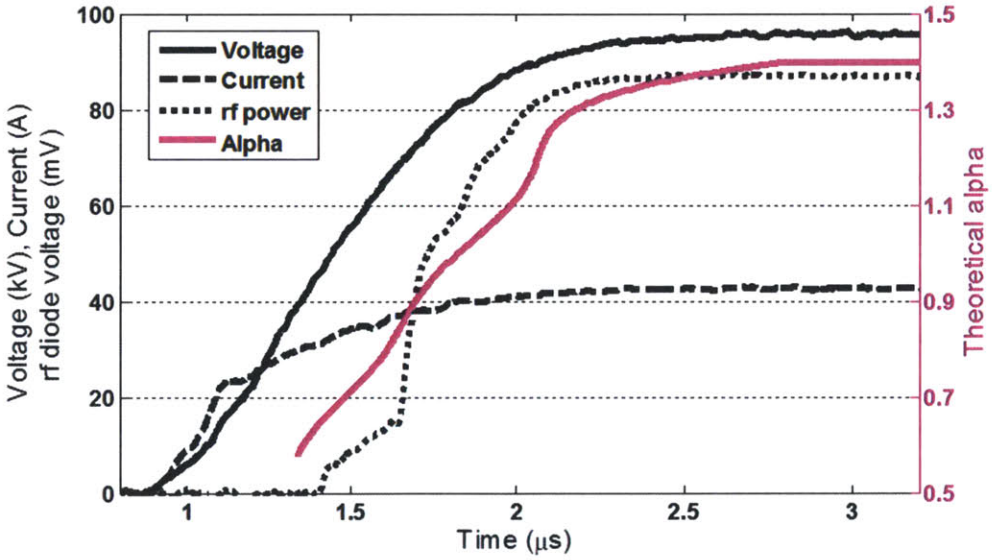

Figure 4-10: Experimental traces of parameters during the voltage rise. The voltage (solid black), beam current (long dash), rf power as measured by a rf diode (short dash), and a theoretical alpha curve for voltages of 40-96 kV (solid magenta) are all shown as a function of time.

As previously mentioned, we would like to record the frequency and the peak power, during the flat-top of each pulse. To ensure that this method of measurement was consistent with the full dynamic scenario, we varied only the voltage while maintaining a

fixed gun field across all data points. Since our cathode operates in the temperature-limited regime, the beam current varies approximately linearly from 31 A at 50 kV to 42 A at 96 kV due to the Schottky effect in the Richardson-Dushman equation. Meanwhile, theoretical calculations indicate that the beam alpha ($v_\perp/v_z$ ratio) varies adiabatically from a value of 0.7 at 50 kV to the desired 1.4 at 96 kV, which is in agreement with gun simulations. Figure 4-10 shows experimental traces of the voltage, beam current, and rf power as well as a theoretical curve showing the variation of alpha during the voltage rise.

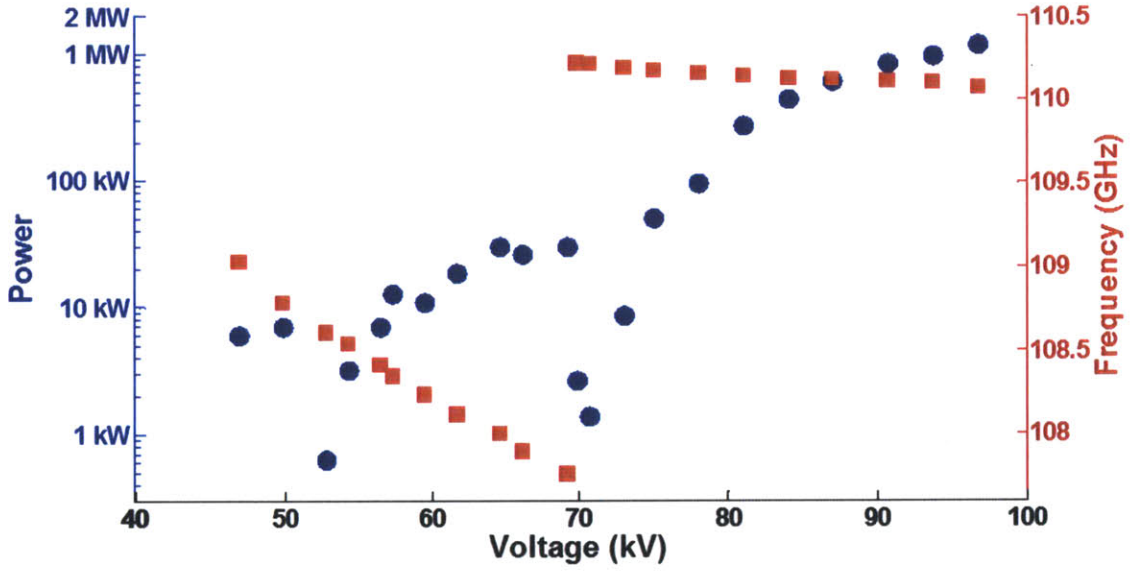

Figure 4-11: Flat-top measurements for the high power operating point ($B_0 = 4.38$ T, $B_{gun} = 0.184$ T). Power (●) and frequency (■) are shown.

The measured power and frequencies as a function of voltage at the high power operating point with $B_0 = 4.38$ T are shown in Figure 4-11. The data were taken by changing the voltage in a sequence of shots and analyzing the power and frequency during the flat-top of the voltage pulse. Oscillations were observed starting at 47 kV where ~5 kW was detected in a mode at 109.03 GHz. At 53 kV, we observed an interesting local minimum in the output power, which dropped to 600 W and then grew to 30 kW at 69 kV, while the frequency rapidly tuned down by over 1 GHz from the initial oscillation frequency. At 71 kV, there was another local minimum in power however in this case it

coincided with a sudden jump in frequency from 107.76 GHz to 110.22 GHz. As the voltage increased, the power eventually reached a peak of 1.2 MW at 96 kV and a small amount of frequency tuning was observed over this voltage range, on the order of 100 MHz, which agreed with the well-known frequency pulling effect seen in gyrotrons [157, 158].

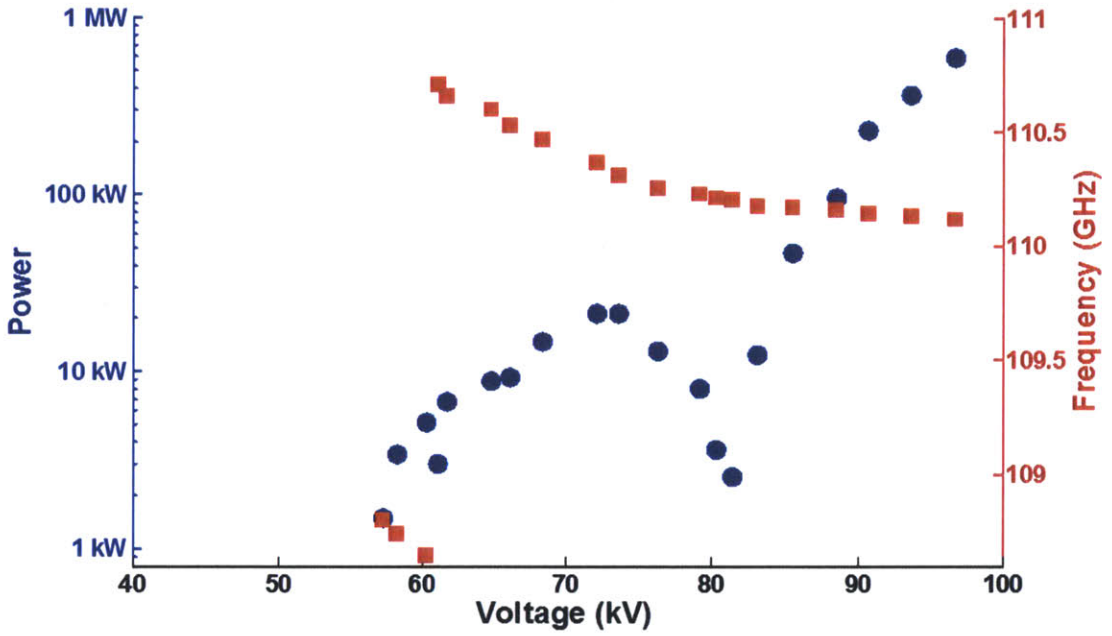

Figure 4-12: Flat-top measurements for the highly stable operating point (B_0 = 4.45 T, B_{gun} = 0.193 T). Power (●) and frequency (■) are shown.

The recorded powers and frequencies at the B_0 = 4.45 T highly stable operating point are shown in Figure 4-12. Here, the first oscillations were observed at 57 kV where 1.5 kW was measured at 108.80 GHz. At 61 kV, there was a local minimum in power and the frequency increased abruptly from 108.65 GHz to 110.71 GHz. The power then reached a peak of 21 kW at 73 kV before approaching another local minimum at 81 kV. Over this region, the frequency showed a modest level of tuning from 110.71 GHz down to 110.18 GHz. Finally, as the voltage approached 96 kV, the power increased rapidly to 600 kW and a small amount of frequency pulling was observed as the frequency approached its final value of 110.12 GHz.

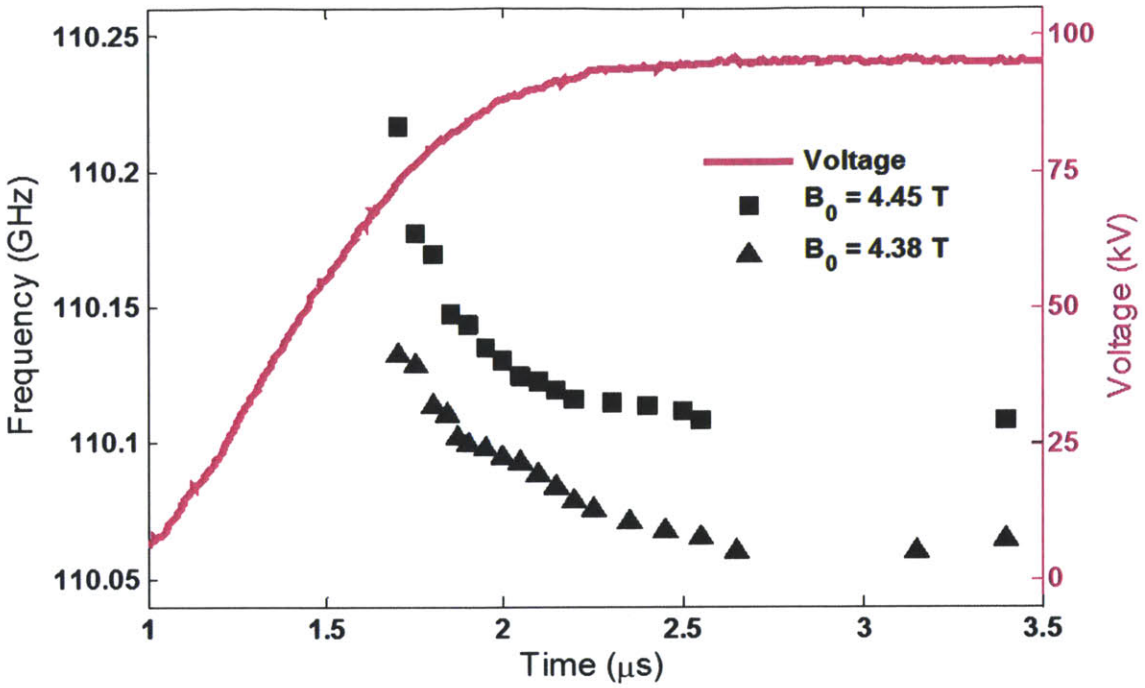

Figure 4-13: Start-up scenario measured as a function of time. Measurements are shown for the high power operating point, $B_0 = 4.38$ T (▲), and the highly stable operating point, $B_0 = 4.45$ T (■), by measuring the frequency over differing time intervals of a 96 kV pulse.

While the flat-top measurements demonstrated an interesting sequence of mode excitation, the particular case of interest was the mode excitation during the voltage rise of a 96 kV pulse. As previously mentioned, the frequency system can be gated over various short time intervals during the voltage rise to measure the instantaneous frequency. Figure 4-13 shows this dynamic result where the frequencies were measured at various times during a 96 kV pulse by gating the time window of the heterodyne frequency measurement system. Due to the SNR limitations at lower voltages, frequencies cannot be distinguished below 70 kV. However, over the measurable range, the frequency pulling witnessed is in good agreement with the flat-top results of Figure 4-11 and Figure 4-12.

In order to ensure that the flat-top behavior of the gyrotron is fully consistent with the dynamic behavior, a further check was carried out using a wavemeter and detector. A wavemeter is a frequency tunable attenuator allowing for narrowband attenuation of the rf

signal. Sample measurements for this wavemeter analysis are shown in Figure 4-14 and Figure 4-15. Figure 4-14 shows the output power trace for the high power operating point with V_k = 75 kV and I_{beam} = 38 A, while Figure 4-15 shows the output power trace for the highly stable operating point with V_k = 85 kV and I_{beam} = 39 A. The flat-top frequency in both cases was 110.2 GHz. In each case, we observed secondary local maxima in the output power that were not attenuated when the wavemeter was tuned to 110.2 GHz, indicating the presence of power at a frequency other than 110.2 GHz. These secondary peaks correspond to the power excited at earlier times/lower voltages in modes of differing frequencies. In Figure 4-14, the secondary peak was attenuated by setting the wavemeter to 108.0 GHz, which agrees with the result shown in Figure 4-11, while in Figure 4-15, the secondary peak was attenuated by setting the wavemeter to 110.4 GHz, which agrees with the result of Figure 4-12. We can therefore conclude that the flat-top results are indeed representative of the dynamic results for a 96 kV pulse.

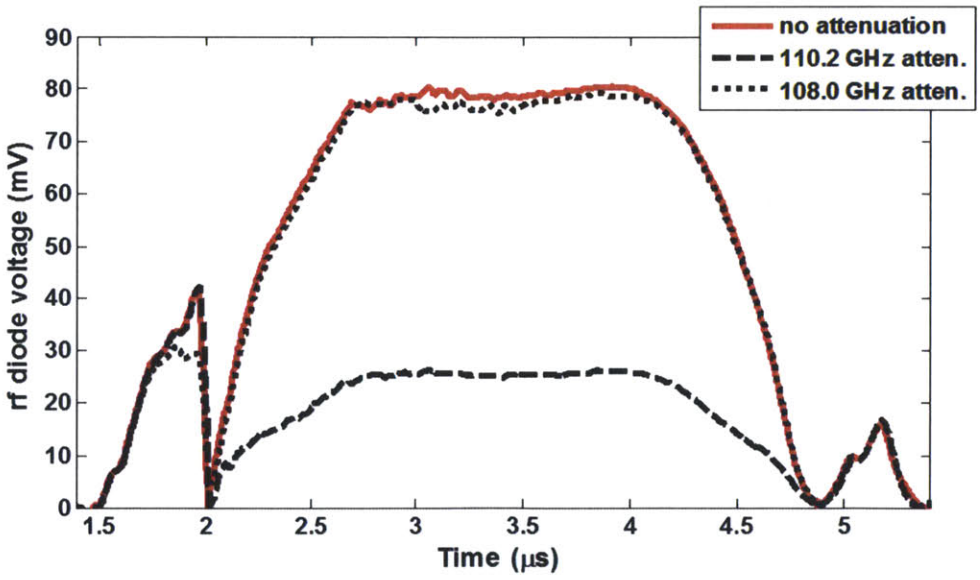

Figure 4-14: Time dependent output power for a 110.2 GHz flat-top frequency pulse for B_0 = 4.38 T, V_k = 78 kV, I_{beam} = 38 A. Traces for no wavemeter attenuation (solid red), attenuation of 110.2 GHz (long dash black), and attenuation of 108.0 GHz (short dash black) are shown.

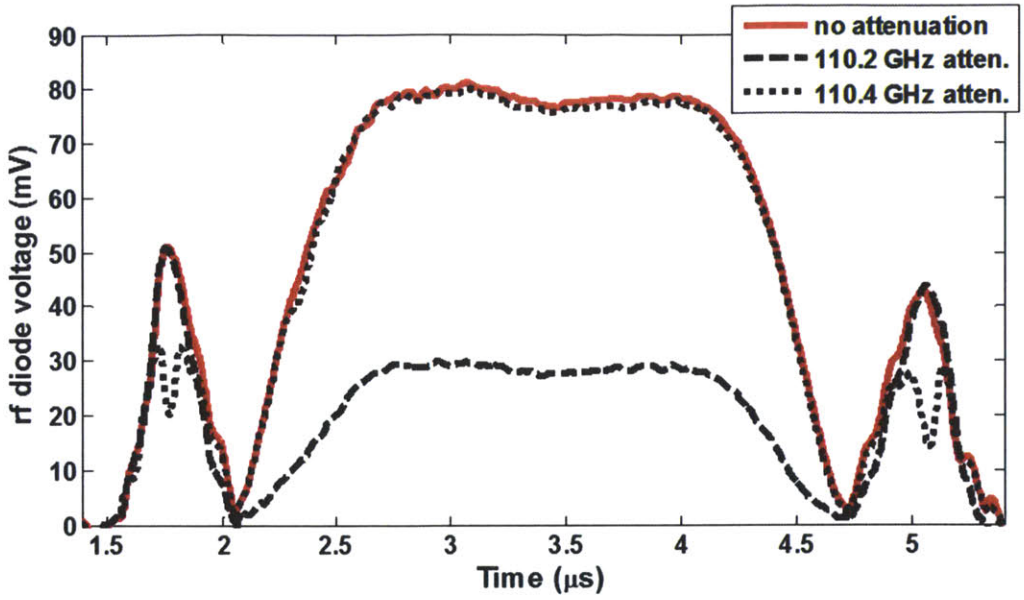

Figure 4-15: Time dependent output power for a 110.2 GHz flat-top frequency pulse for $B_0 = 4.45$ T, $V_k = 85$ kV, $I_{beam} = 39$ A. Traces for no wavemeter attenuation (solid red), attenuation of 110.2 GHz (long dash black), and attenuation of 110.4 GHz (short dash black) are shown.

4.3.2 Output Beam Pattern Measurement and Theory

While the set of output power and frequencies is at the core of this study, it does not present the whole of information required to extract the necessary scientific takeaways. In particular, the mode excitations at 108-109 GHz have not been previously predicted and do not represent frequencies commonly seen in such experiments. A variety of possibilities exist for seeing modes at such a frequency like higher-order axial cavity modes or mode excitations within the tapers, and in order to help distinguish the nature of the excitation, additional measurements are required.

Given the range of input parameters in the experiment, we have a reasonably good idea of the main competing modes for the $TE_{22,6,1}$ operating mode. These modes are those nearby in frequency with the same radial index $p = 6$ but different azimuthal indices, i.e. $TE_{20,6,q}$, $TE_{21,6,q}$, and $TE_{23,6,q}$, as well as counter-rotating modes with a different radial index

$p = 7$, i.e. $TE_{19,7,q}$ and $TE_{20,7,q}$ and $TE_{22,6,q}$ modes with higher order axial field structures, i.e. $q > 1$. One potential means of identifying these modes is by measuring the output beam spatial pattern. If the modes were indeed excited in the cavity, then the output beam should follow closely the theoretical prediction from numerical codes like Surf3d and LOT, which allow us to provide a seed mode and frequency at the input of the launcher of the gyrotron's IMC. After using these aforementioned codes to calculate the theoretical fields from the launcher, the solution can then be propagated through the system of mirrors and out to the measurement plane, using the code SCATTER, for comparison with the experimental patterns.

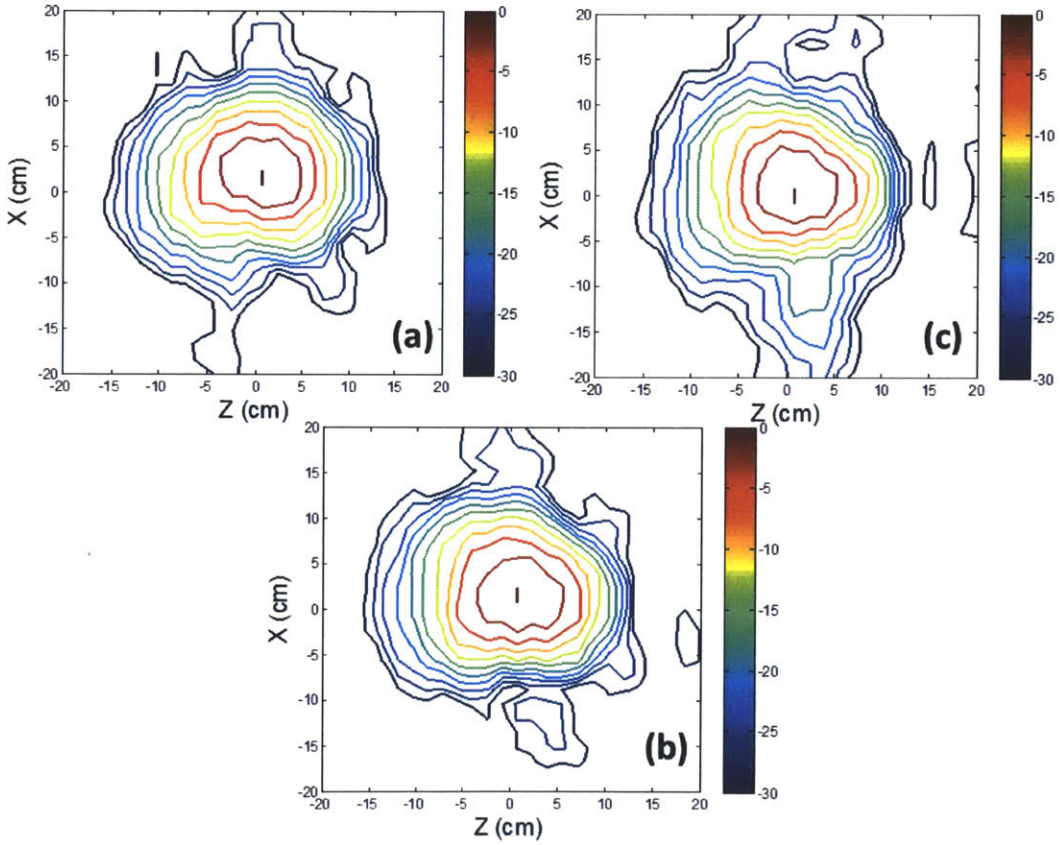

Figure 4-16: Measured beam patterns of various modes near their cutoff frequency. (a) $TE_{21,6}$ at $B_0 = 4.34$ T and $B_g = 0.185$ T, (b) $TE_{22,6}$ at $B_0 = 4.38$ T and $B_g = 0.184$ T, and (c) $TE_{23,6}$ at $B_0 = 4.58$ T and $B_g = 0.202$ T.

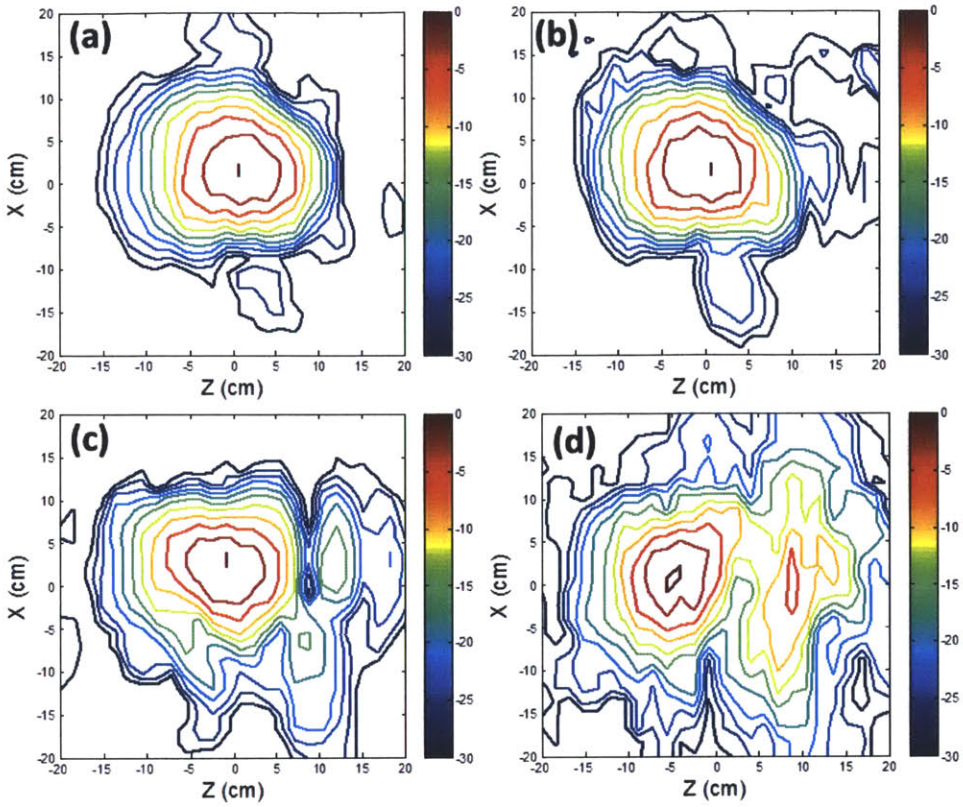

Figure 4-17: Output beam patterns measured 1 m from the window during the voltage rise for the high power operating point. With B_0 = 4.38 T and B_g = 0.184 T, beams were measured at (a) 96 kV, (b) 73 kV, (c) 65 kV, (d) 54 kV.

As a first step, we may consider an extension of the results of Chapter 3's discussion on mode converter performance. In those experiments, only the $TE_{22,6}$ design mode was of interest and measured, however the beam pattern may be measured for other mode excitations as well. To see how the IMC performs for each of the different modes, similar operating points should be selected such that a stable excitation with moderate output power is achieved in each case. The modes should then be excited close to their cutoff frequencies of 107.00 GHz, 109.94 GHz, and 112.88 GHz for the $TE_{21,6}$, $TE_{22,6}$, and $TE_{23,6}$ modes, respectively. The measured beam patterns were obtained by the methodology discussed in Chapter 3 and are shown in Figure 4-16. We see that for each mode, the output beam pattern is quite Gaussian. While the $TE_{23,6}$ mode pattern does show

some imperfections, this is a result of the fact that we cannot operate at its optimal parameters since the $TE_{20,7}$ mode is excited instead in that region, though the beam pattern is still quite good. While high quality beams for each mode is a positive characteristic for gyrotron operation, it does not provide an added means of directly distinguishing between the different mode excitations in this experiment.

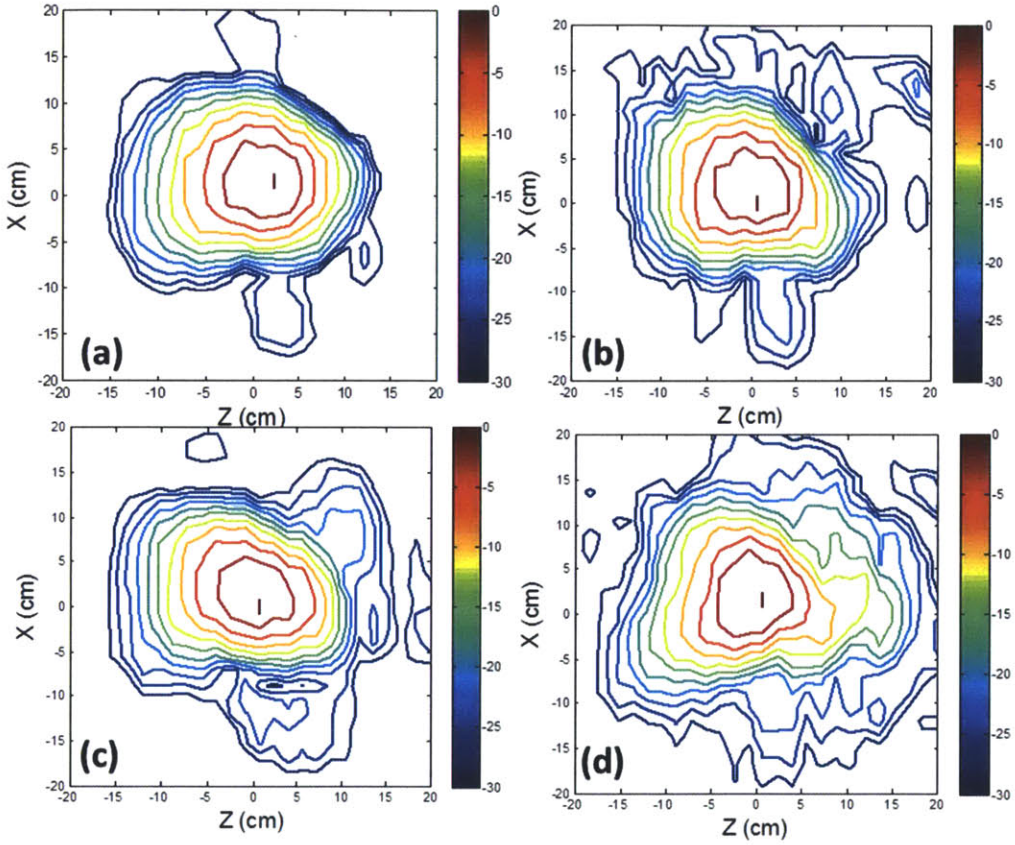

Figure 4-18: Output beam patterns measured 1 m from the window during the voltage rise for the highly stable operating point. With B_0 = 4.45 T and B_g = 0.193 T, beams were measured at (a) 96 kV, (b) 83 kV, (c) 72 kV, (d) 62 kV.

It is still worthwhile though to investigate the operation of the gyrotron via beam pattern measurements at different points during the start-up scenario. In Figure 4-17, the output beam is shown for several different voltages during start-up for the high power operating point. We see that there is a distinct change in the output beam pattern measured below 70 kV where the 108-109 GHz frequencies are observed before switching to ~110

GHz at higher voltage. The beam patterns may also be measured for the highly stable operating point as shown in Figure 4-18. Over the range of voltages, the mode frequencies ranged from 110.1 - 110.7 GHz and no significantly distorted pulse was observed as in the high power case. We also note that while, in each case, modes may be excited at even lower voltages, the rf pulse is not as stable and the beam patterns are highly noisy and thus omitted. Additionally, by means of this analysis and the power measurements in the previous section, we recognize that the counter-rotating modes with radial mode index p = 7 are not excited in experiment. If these modes were excited, we would see a region where no output power was being measured from the gyrotron since this power would not be radiated properly from the launcher and through the set of mirrors.

In order to properly identify the modes, the beam patterns should be compared to theoretical predictions as previously described. Let us first consider the excitations at and above 110 GHz. Because there is no sudden jump in frequency, it stands to reason that the mode excited over this range is the $TE_{22,6}$ mode. The output beams are all highly Gaussian, though somewhat less so at lower voltages, which is also seen in theoretical calculations. The interesting modes to investigate though are those seen in Figure 4-17 (c) and (d). At these operating points, not only does the beam quality degrade, but a clear sidelobe appears. We conjecture that these are $TE_{21,6,q}$ excitations with $q > 1$, and to ascertain this, the measurements are compared with theory. To simulate this in LOT, the transverse mode structure, i.e. $TE_{21,6}$, and frequency must be provided as inputs, where we use the measured frequency from experiment. Figure 4-19 shows a comparison between experimental results at 65 kV for the high power operating point and theory for a $TE_{21,6,q}$ mode excitation at 108.00 GHz. In both experiment and theory, a sidelobe appears on the collector end of the pattern (positive z) with similar amplitude: -15 dB in experiment and -18 dB in the calculation. By comparing multiple sets of measurement and simulation, we found both experiment and calculation agreed that the beam patterns were Gaussian at the

cutoff frequency, but, as the voltage was lowered, and the oscillation frequency increased, a sidelobe in the beam pattern appeared. In addition, the centroid position of the main power lobe began to shift in the axial direction in both measurement and simulation.

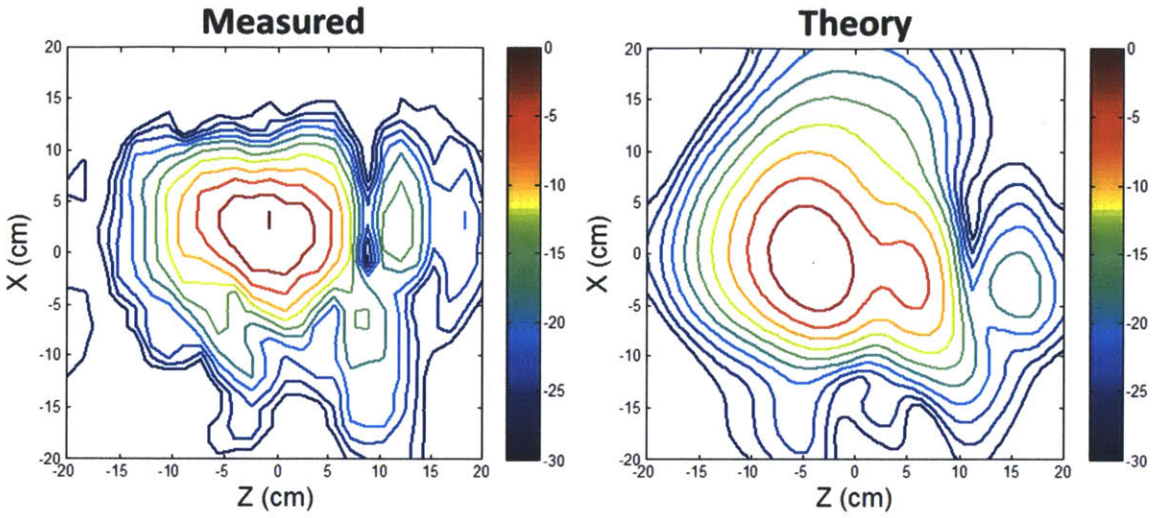

Figure 4-19: Comparison of the output beam pattern measured 167 cm from the gyrotron window with theoretical calculations. Beam pattern measured at $B_0 = 4.38$ T, $B_g = 0.184$ T, and $V_k = 65$ kV where the $TE_{21,6,q}$ mode is excited at 108.00 GHz.

Both aspects of this behavior may be explained through LOT simulations. Recall from Chapter 3 that the output of the launcher is determined by the field distribution along the wall within the final Brillouin zone before the launcher's helical cut. In Figure 4-20, we compare the wall field intensity for the launcher for the $TE_{21,6,q}$ mode given input frequencies of 107.2 GHz and 108.0 GHz. In Figure 4-20(a), at 107.2 GHz, the final Brillouin zone encloses a nice Gaussian beam with low field intensity along the cut. In Figure 4-20(b), at 108.0 GHz, the field pattern appears elongated along the z axis and there is now significant field along the cut. To see the consequence of this, we may calculate the radiated fields from the end of the launcher. Figure 4-21 shows radiated field patterns at the aperture for $TE_{21,6,q}$ mode excitations at frequencies of 107.2, 108.0, and 109.0 GHz. As the frequency increases, the main lobe shifts to larger z values and the amplitude of the sidelobe grows, just as seen in experiment. The effect is quite simply explained by a small

increase in the bounce angle of the mode resulting from increases in the difference between the excitation frequency and the cutoff frequency of the mode. This change in angle as the rays propagate through the mirror system results in a displacement of the beam position on the experimental measurement plane. Therefore, both the theoretical calculations and experimental measurements indicate that the low frequency modes observed near 108 GHz must be $TE_{21,6,q}$ mode excitations.

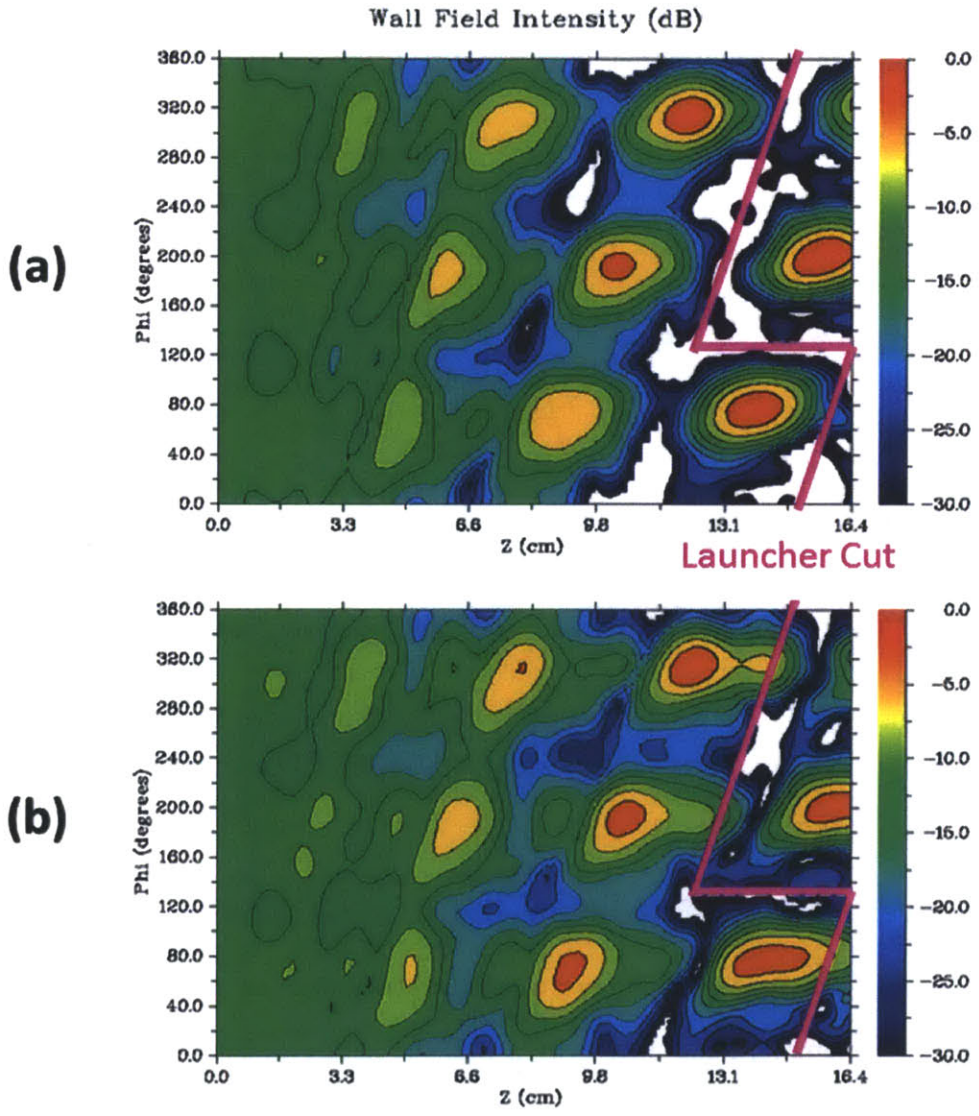

Figure 4-20: LOT simulation of the wall field intensity for $TE_{21,6,q}$ input modes at (a) 107.2 GHz, and (b) 108.0 GHz.

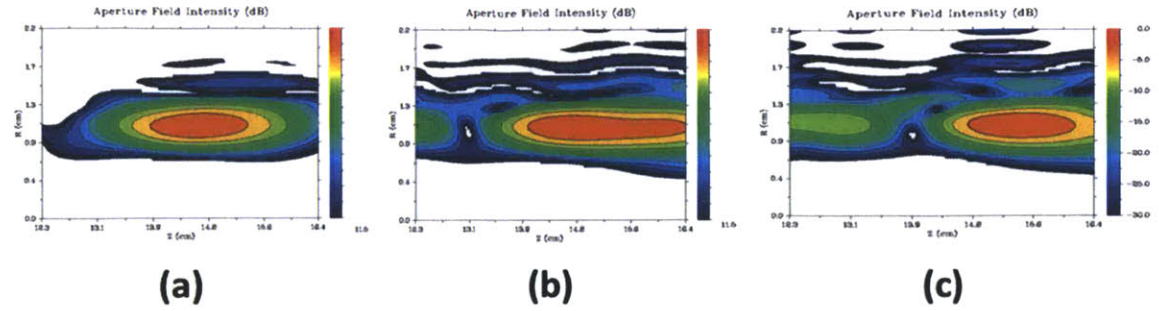

Figure 4-21: Comparison of the radiated field intensity at the aperture of the IMC launcher for a $TE_{21,6,q}$ mode input. Input mode frequency is: (a) 107.2 GHz, (b) 108.0 GHz, and (c) 109.0 GHz.

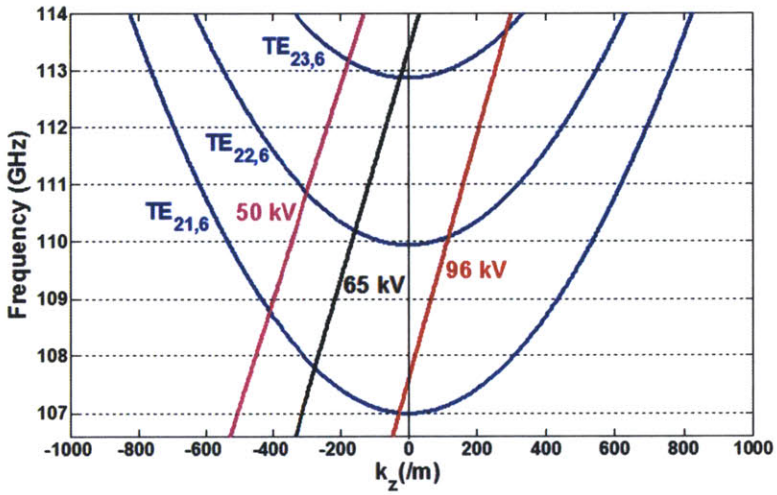

Figure 4-22: Uncoupled dispersion relation for a start-up scenario. The $TE_{21,6}$, $TE_{22,6}$, and $TE_{23,6}$ waveguide modes are shown along with Doppler shifted beam resonance for 50, 65, and 96 kV.

4.3.3 Analysis of Mode Excitation

To further study these modes, a number of other theory and simulation tools could be considered. For example, additional insight into the nature of the start-up modes was obtained by considering the uncoupled dispersion relation. Each waveguide mode is represented by a hyperbola relating the mode frequency to k_z defined by Eq. (2.19) and the Doppler shifted beam resonances are linear functions for a given voltage defined by:

$$\omega - k_z v_z = \omega_{c0} / \gamma \tag{4.3}$$

where v_z is the longitudinal electron velocity, $\omega_{c0} = eB_0/m_e$ is the non-relativistic cyclotron frequency, and $\gamma = 1 + (e/m_e c^2)V_k$ is the relativistic factor for electrons with energy $-V_k$, charge e, and mass m_e. As previously discussed, the intersection of a beam line and a mode's hyperbola denotes where a simple resonance condition is satisfied for a possible gyrotron beam-wave interaction to excite that mode. In Figure 4-22, we have plotted the uncoupled waveguide dispersion curve for the modes of particular interest, $TE_{21,6}$, $TE_{22,6}$, and $TE_{23,6}$, as well as the beam lines for three different voltages. For each voltage, we may identify possible beam-wave interactions with each mode. For example, at 65 kV, interactions may occur in the $TE_{21,6}$ mode at 107.8 GHz, in the $TE_{22,6}$ mode at 110.2 GHz, and in the $TE_{23,6}$ mode at 112.9 GHz; however additional analyses, typically using computer codes like MAGY, are required to determine which interaction may be preferred. At lower voltages, the relativistic cyclotron frequency, $\omega_c = \omega_{c0}/\gamma$, is larger thus shifting the beam line up in frequency. Also, while the values of the beam α and v_z are indeed dependent on voltage, the slope of the beam line does not change dramatically over the range of interest, therefore in order for the beam line to intersect a waveguide dispersion curve at lower voltages and at the observed frequencies, we require that $k_z < 0$. This means that we have a backward wave interaction, defined by the synchronism condition:

$$\omega + k_z v_z = \omega_{c0} / \gamma \tag{4.4}$$

where $\omega < \omega_{c0}/\gamma$, unlike the forward wave defined by Eq. (4.3) which has $\omega > \omega_{c0}/\gamma$. In addition, we can recognize that these intersection points, particularly for the modes excited at much lower voltages, are well away from the cutoff frequency. Due to the presence of a steep downtaper on the gun side of the cavity, any backward wave power would be fully reflected and transmitted through the window where it could still be observed.

In the broadband power measurements of Figure 4-11 and Figure 4-12, local minima are observed. Each of these minima represents a mode transition where the power drops sharply in the initially excited mode and begins to grow from a reduced level in the subsequent mode. By also considering the frequency measurements, two different types of mode transitions may be identified. In Figure 4-11 at ~70 kV, a local minimum in power is observed along with a sudden jump in frequency which indicates that the transverse structure of the mode is changing. In this case, the $TE_{21,6,q}$ mode at lower voltages transitions to the nominal $TE_{22,6,1}$ operating mode at higher voltages. The mode transition that occurs in Figure 4-12 at ~74-82 kV is not accompanied by a sudden shift in frequency, therefore the transverse field structure must remain constant, but there may be a change to the axial field structure within the cavity. In this case, the desired $TE_{22,6,1}$ operating mode is excited at higher voltage, while at lower voltage, a $TE_{22,6,2}$ backward wave mode is excited. The backward wave nature of the mode is confirmed by finding that the condition $k_z < 0$ applies. By calculating the approximate frequency for each axial mode, based on the approximation of $k_z \approx q\pi/L$, we can determine that the $TE_{21,6,3}$ backward wave mode is excited in the high power case from 52-69 kV, while, for both operating points, the $TE_{21,6,4}$ backward wave mode is excited first at a frequency near 109 GHz.

For a more elaborate theoretical interpretation of these results, we turn to the MAGY code. Recall that a study of the start-up scenario was previously performed using MAGY with the parameters of the MIT gyrotron whose results were shown in Figure 4-8. That study showed the higher frequency $TE_{23,6,1}$ mode near 113.0 GHz being excited during the voltage rise. In these latest experiments, it was instead the lower frequency modes that were observed during start-up and no evidence of the $TE_{23,6,1}$ mode was found with the frequency measurement system. In the theoretical work, the MAGY simulations were seeded with a triplet of modes, namely the $TE_{21,6,1}$ mode at 107.1 GHz, the $TE_{22,6,1}$ mode at 110.0 GHz, and the $TE_{23,6,1}$ mode at 112.9 GHz, i.e. near their respective cutoff frequencies.

These three modes form a set of modes with almost exactly equal spacing in frequency. Such a triplet of equally spaced modes is known to lead to parametric mode excitation, which can enhance mode competition [151]. Such MAGY runs are important as they do accurately predict the operating range for the design mode and give a clear picture of mode competition during the steady-state portion of the voltage pulse [159]. However, by seeding the three specific frequencies, modes at significantly different frequencies, such as the $TE_{21,6,3}$ and $TE_{21,6,4}$ modes in the 108-109 GHz range, are not excited by the code. That is, if the oscillation frequency is too far from the seeded frequency, the code is not capable of converging on the solution. Therefore, we must conclude that the previous MAGY simulations did not include the possibility of exciting the $TE_{21,6,3}$ or $TE_{21,6,4}$ modes as observed in the experiment. In addition, the backward wave modes excited during the voltage rise are not fixed in frequency but change very rapidly and continuously with time. This rapid variation presents a great challenge to the MAGY code or any simulation code for that matter.

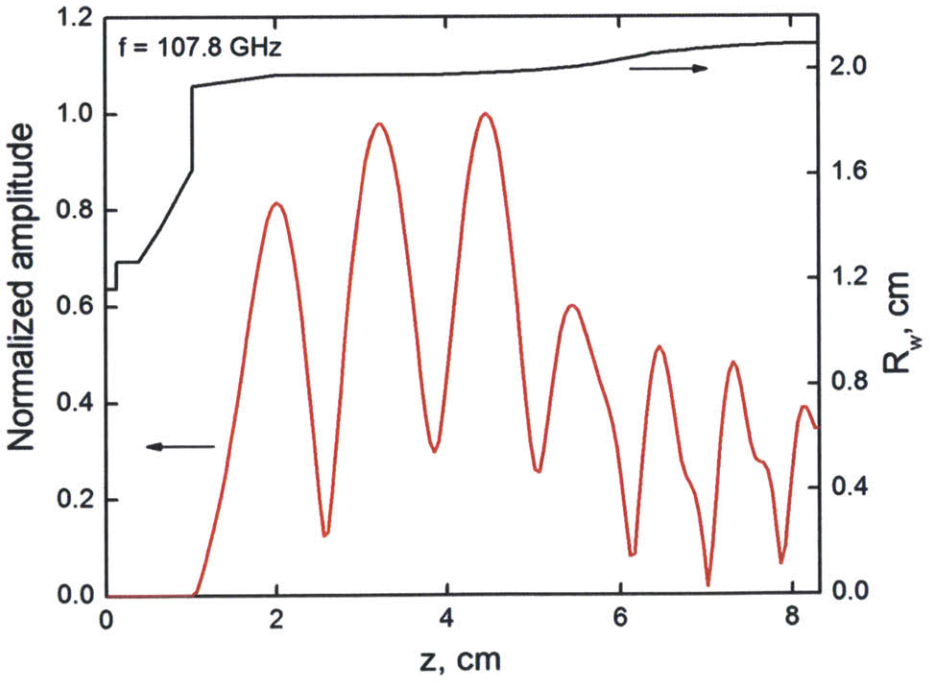

Figure 4-23: Axial field profile for the 107.8 GHz $TE_{21,6,3}$ mode from a MAGY simulation. The full cavity profile is shown alongside.

In order to explain the observed excitation of the $TE_{21,6,3}$ and $TE_{21,6,4}$ modes, we recruited the help of collaborators at the University of Maryland, Oleksandr Sinitsyn and Gregory Nusinovich, to carry out a limited set of MAGY simulations. A full treatment of the mode competition using the MAGY code would require a new, extensive set of code runs and is beyond the scope of this work. Instead we focused on using the MAGY code to help understand the nature of the excited $TE_{21,6,3}$ and $TE_{21,6,4}$ modes. We began by looking at simple single-mode simulations of these modes, with a constant voltage, and found that it was indeed possible to excite them in MAGY using the experimental input parameters. The resultant axial field profile for a sample MAGY calculation with a $TE_{21,6,q}$ mode excited at 107.8 GHz is shown in Figure 4-23. It is noted that only the transverse structure of the input mode and its frequency are input into MAGY and that the code solves for the axial field profile. We observe that the axial field structure calculated by MAGY is consistent with our previous conjecture that the $TE_{21,6,3}$ mode, the mode with 3 axial field peaks, is excited at 107.8 GHz. In addition, the strong axial field peaks are not well confined within the cavity straight section itself, i.e. the region from z = 2.0 to 3.8 cm which has a constant radius. It is possible that this field profile may play a role in preferentially bunching the beam for these modes thus resulting in their excitation over other anticipated modes. For example, let us again consider the starting current calculations that were presented in Section 4.2.2. By allowing for a slight variation in parameters, and taking a magnetic field value of 4.58 T, the starting current curves in Figure 4-24 are obtained. First, note that the starting current of the $TE_{21,6,2}$ mode is smaller than the beam current for a range of voltages meaning that it could possibly be excited, though the starting currents for the $TE_{22,6,1}$ mode and $TE_{23,6,1}$ are lower over the same range. Second, the starting current of the $TE_{22,6,2}$ mode, which was seen in experiment, is very close to the beam current, though slightly larger. In both of these modes, the approximate starting current curve comes close to explaining the experimental results. In reality, there are additional factors that can influence the starting current. One possible explanation is

reflections from the window. In Figure 4-25, we plot the transmission of the window as a function of frequency. We see that nearly perfect transmission is expected for the $TE_{22,6,1}$ mode at 110 GHz and for nearby frequencies, however the reflection jumps to ~5% at 109 GHz and over 10% at 108 GHz. Similar to how the the discontinuity in the cavity geometry at the uptaper contributes a small reflection to support the oscillation, reflections from the window may also affect mode excitation and stability [160]. It is therefore reasonable that a small increase in the Q factor can contribute more significantly to the excitation of low Q high order axial modes than it would for higher frequency mode near cutoff whose initial Q was much larger.

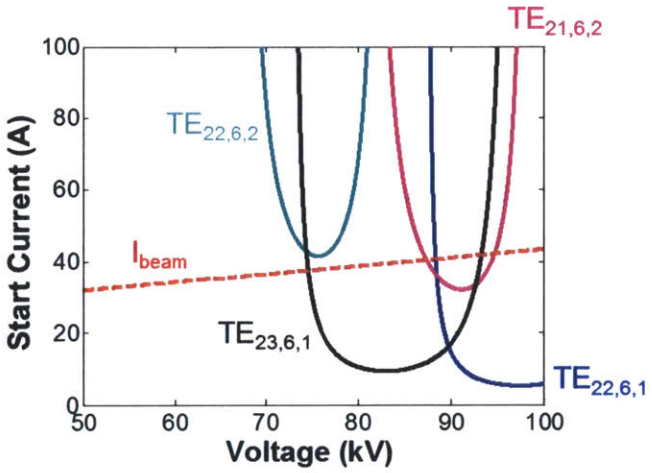

Figure 4-24: Calculation of the starting currents for the $TE_{21,6}$, $TE_{22,6}$ and $TE_{23,6}$ modes, including modes with higher order axial field profiles. Only those modes with sufficiently low starting currents appear in the figure.

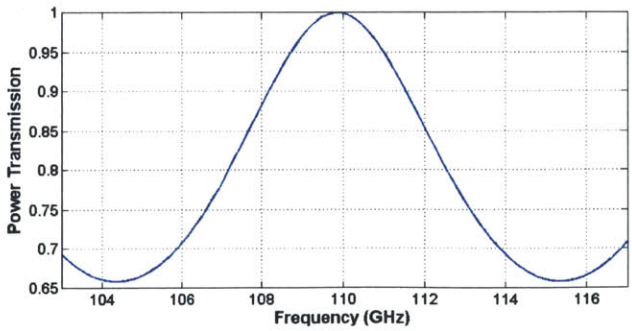

Figure 4-25: Power transmission for the 6.99 mm thick fused quartz window.

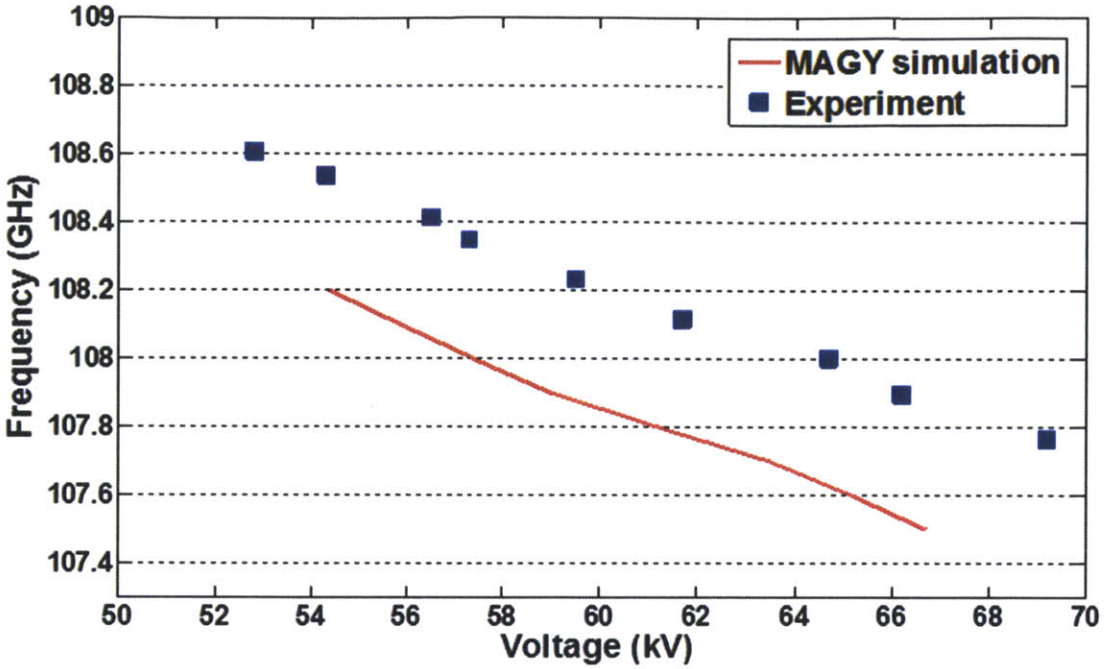

Figure 4-26: Comparison of experimental data for the high power operating point ($B_0 = 4.38$ T) and single-mode MAGY simulations of the $TE_{21,6,q}$ mode at several frequencies.

To gain more insight into this problem, we performed some more single-mode MAGY simulations for the $TE_{21,6,q}$ mode and introduced a time-varying voltage. In this case, the voltage was allowed to ramp up from 40 to 100 kV and the beam current and α values rose according to the experimental data recorded during the voltage rise, as shown earlier in Figure 4-10. By running simulations with different input frequencies, we observed resonant behavior in the phase of the fields at a particular time during the voltage rise which indicated that the oscillation frequency in the cavity at that particular voltage matched the input frequency. The time, and corresponding voltage, at which this resonance occurred varied depending on the input frequency. In Figure 4-26, we have plotted the simulated voltage and frequency points where this resonance occurred and compared it with the experimental data observed for the high power operating point. Since the magnetic field is only measured to about ± 1 % accuracy, the MAGY

calculations were carried out over a small range of magnetic field to find a best match with experiment. While there is a small offset in frequency between the two data sets, we see that the slope is the same, and MAGY is accurately predicting the kind of frequency tuning that we see in experiment during the voltage rise. This provides good evidence that the modes that we infer from the experiment can indeed be excited. We also looked at the predicted power levels by performing single-mode MAGY simulations with constant voltage for the voltage and frequency pairs of Figure 4-26. The power levels were in reasonable agreement with experiments, as MAGY calculated power levels of 200 W – 30 kW over the voltage range while power levels of 3 kW – 30 kW were observed in experiment over the same range.

4.4 Summary

Mode competition is a major issue facing the design and operation of MW gyrotrons due to operation in large, overmoded cavities. Mode selectivity is aided by a convenient choice of parameters like the beam radius and magnetic field. Analysis of parameters like the coupling coefficient and starting currents can help determine which modes may be preferentially excited, however full simulations with a multi-mode code like MAGY should be incorporated to make a proper determination.

The start-up scenario plays a particularly important role in MW gyrotrons. To achieve the highest possible device efficiency, the gyrotron should operate in the hard self-excitation regime, which can only be initiated in the presence of a strong enough initial electric field amplitude. Therefore, the gyrotron must first excite a mode in the soft self-excitation regime, where the beam current is greater than the starting current, to help seed the hard excitation oscillation, where the starting current exceeds the beam current.

An in depth experimental study of the start-up scenario has been carried out on the 1.5 MW, 110 GHz gyrotron at MIT. We discovered that a set of lower frequency modes with higher order axial field structures are excited during the rise of the voltage pulse

which contradicted previous MAGY simulations showing the excitation of higher frequency modes. A theoretical study of these lower frequency modes showed that they are possible to excite and can be roughly explained by linear theory. This is important because incorporating such modes as part of a multi-mode non-stationary MAGY study is currently beyond the capability of the code. A better understanding of the start-up scenario should aid in the design of future high power gyrotrons and provide additional means by which to diagnose their performance.

Chapter 5

A Two Frequency Gyrotron Experiment

In this chapter, we present a new experimental configuration for the MIT gyrotron. Previous gyrotron designs have only focused on a single frequency, namely 110 GHz for application to DIII-D's ECH system in our case. However, in recent years, the fusion scientists at General Atomics had expressed interest in a 105-120 GHz tunable gyrotron since it could allow for more efficient control of the current profile at different locations in the tokamak. Other benefits could include: simultaneous suppression of different neoclassical modes, fine control of magnetic shear, added flexibility in minimizing undesired trapping effects and third harmonic damping, and allowing ECCD to be deposited on the midplane at a different radius to optimize the efficiency. In order to provide these benefits, the gyrotron should exhibit stable, high power operation at the frequencies of interest.

Here we present a general discussion of the design of such a gyrotron followed by the specific design for the components of a 110/124.5 GHz gyrotron before reporting on the experimental results obtained in this new configuration.

5.1 General Design of a Multi-Frequency Gyrotron

Before discussing the additional design considerations for multi-frequency operation, let us first discuss general design practices. The first step in the design of a gyrotron involves

evaluating the fundamental parameters of the gyrotron. The requirements for the design will generally be the desired output power, and efficiency, and the operating frequency which will help determine the necessary magnetic field. The next step in the design involves a number of tradeoffs. Recall from Chapter 2 that the efficiency of the device can be stated in terms of a set of normalized parameters, meaning that an approximate operating point can be determined while the specific design still consists of many free parameters like voltage, current, etc. In MW gyrotrons, another strong constraint is imposed by the Ohmic losses, which must be limited. As previously discussed, at higher frequencies, this limit on Ohmic loss will generally require operating in a high order mode of a large, overmoded cavity, meaning that mode competition must also be balanced.

The selection of a design mode is typically done first. Like most things, all modes are not built equal. The mode selection will involve balancing of both Ohmic losses and mode competition which also relates to the diameter of the cavity. Once a guideline for the acceptable range of cavity radius and mode order is obtained, the modes may be studied parametrically. Such an analysis led to the selection of the $TE_{22,6}$ mode for 110 GHz MW gyrotrons as it experiences far less mode competition than other choices.

With a mode selected, focus then shifts to the design of the gun. Careful consideration of the interplay between the parameters is necessary as choices of voltage, current, and beam alpha and radius are all coupled to the efficiency, magnetic detuning, and cavity losses. Once a set of parameters is selected, the design can then turn to the interaction cavity as linear tapers are implemented to provide the necessary reflection to achieve the desired Q factors for optimized output power and low Ohmic loss.

In designing a gyrotron for multi-frequency operation, much of the design remains the same. The rough design and establishing of the basic parameters should focus on one operating mode, though the other mode should also be considered throughout the process to ensure feasibility. With basic parameters established, an optimization can be carried out for efficiency and mode competition with both operating points taken into account,

which requires further tradeoffs. Let us now consider the case of the two frequency gyrotron design as part of this thesis work.

Here, the design of a two frequency gyrotron must fit within an existing set of constraints, namely the electron gun and its operating voltage and current and beam attributes. Just as it was in a single-mode design, the first consideration is the mode excitation.

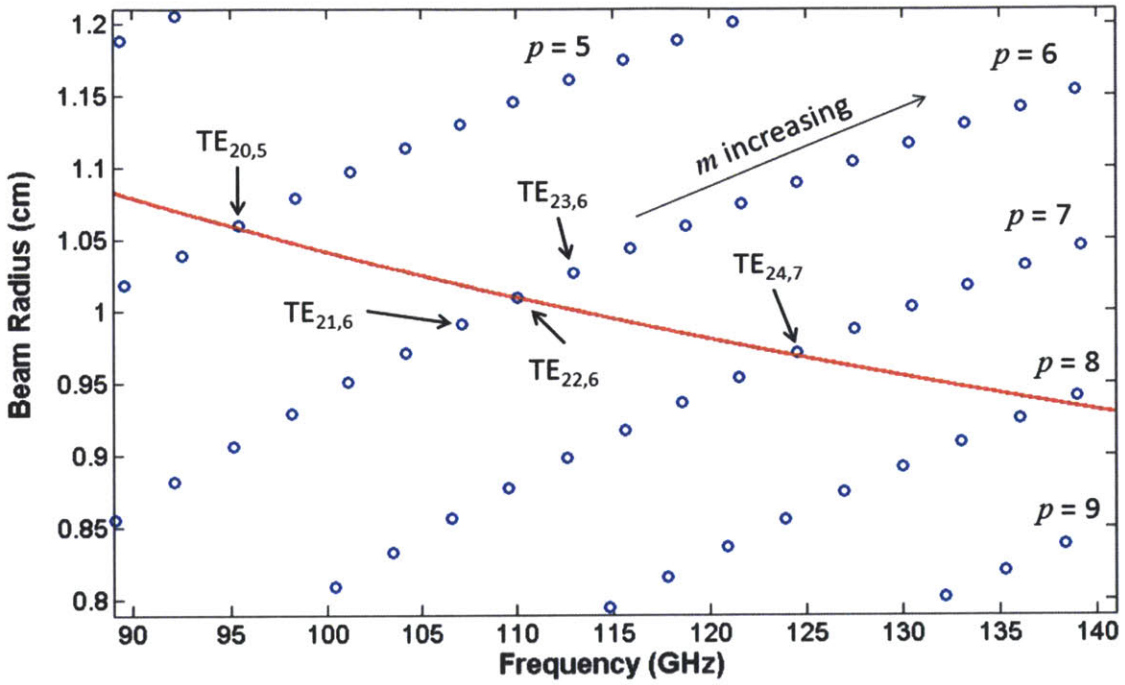

Figure 5-1: Plot of the optimal beam radius for various $TE_{m,p}$ cavity modes vs. the mode's cutoff frequency. The curve indicates the beam radius for constant compression as a function of the cyclotron frequency (magnetic field).

To this end, we assume operation at 96 kV and α of 1.4 where the base mode at 110 GHz is still $TE_{22,6}$ and thus the cavity radius should be the same. To determine which modes might be easily excited, we plot the optimal beam radius for coupling, i.e. the location of the first electric field peak going radially out from the axis of the cavity, against the cutoff frequency. As previously discussed, the operating modes of interest in high power gyrotrons are forward waves with only a single peak in their axial field profile

that are excited near the cutoff frequency. In Figure 5-1, we have plotted the position of many $TE_{m,p}$ modes with m = 16-32 and p = 5-9 in this rbeam-frequency parameter space. The curve represents the change in beam radius as the magnetic field is tuned assuming constant compression, which scales as approximately $f^{1/3}$ [161]. Therefore, points along this line, and those nearby which can be reached by tuning of the gun coil, represent the modes that could be excited by the beam provided by the existing electron gun. Based on the results of this study, parameters designed for operation in the $TE_{22,6}$ mode at 110 GHz should translate best to operation in the $TE_{24,7}$ mode at 124.5 GHz. According to Figure 5-1, operation is also possible in the $TE_{20,5}$ mode at 95.5 GHz and the $TE_{26,8}$ mode at 139.0 GHz. It would however be very difficult to keep all parameters within appropriate design bounds over such a wide band and therefore it was decided to focus on the two frequencies of interest. Operation at other frequencies would be an added bonus.

5.2 Design of 110/124.5 GHz Gyrotron Components

With the desired operating modes established, and an existing apparatus which includes the electron gun, collector, magnet systems, and vacuum envelope, we look to the design of the specific components to operate in this new configuration. The main component of the design is naturally the cavity, which now must be optimized over both modes. We therefore anticipate a reduced performance at either mode as neither can be optimized perfectly for power and mode competition as they would if that were the only mode under consideration. One difficult component to design is the mode converter. As such, this project developed as a collaboration between MIT and the University of Wisconsin (UW). Since UW has extensive experience in developing IMC design codes and designing launchers, the mode converter design would be provided by them, while we were responsible for building, testing, and incorporating that design within the gyrotron. The final component that needs to be redesigned is the window, which must ideally provide full transmission at both desired output frequencies.

5.2.1 IMC Design and Cold Test

We first consider the design of the gyrotron's mode converter. While typically a cavity would be designed first, due to the collaborative nature of this project, an IMC design was already in existence for this application and it was agreed upon that it would be implemented in our experiment. Therefore, the cavity should be constrained to fit the necessary IMC parameters, and we first introduce the IMC design.

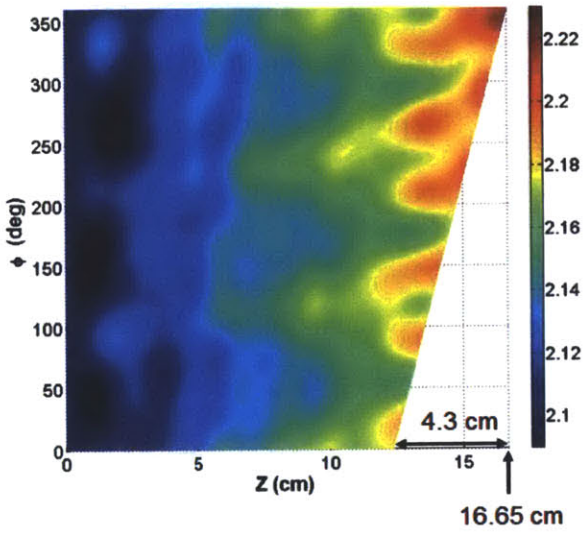

Figure 5-2: Wall profile for the dual frequency IMC launcher. The 16.65 cm launcher has a 0.35° degree uptaper from an initial radius of 2.0955 cm at z = 0. The launcher cut is 4.3 cm long.

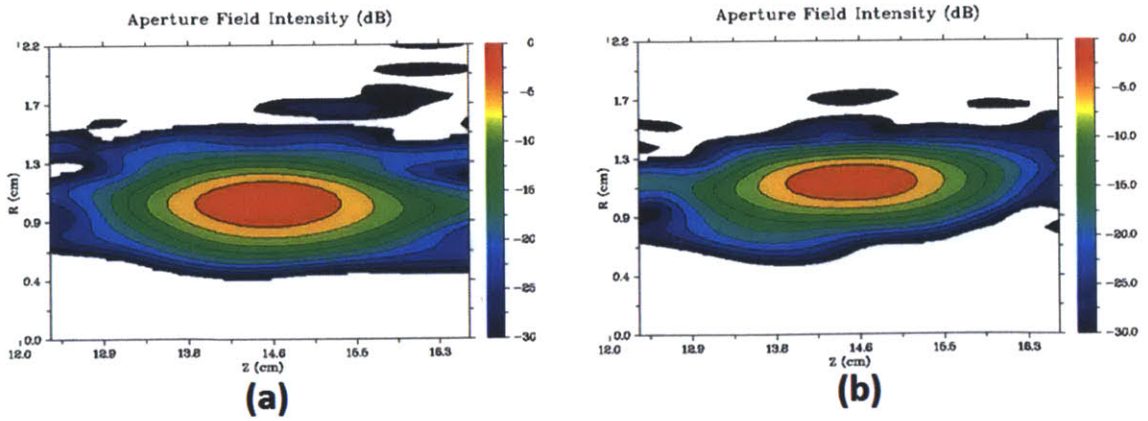

Figure 5-3: Radiated fields at the aperture of the launcher for (a) the $TE_{22,6}$ mode and (b) the $TE_{24,7}$ mode.

The design of IMC launchers has been covered extensively in Chapters 2 and 4 with this launcher being designed in much the same way. The launcher design came courtesy of collaborator Ben Rock of UW. The group at UW focuses on the design of gyrotron mode converters and the development of codes for their analysis [162]. The same design tools were used, that being Surf3D and LOT, however in this particular design, the additional consideration of the performance for the $TE_{24,7}$ mode was necessary. Therefore the optimization was based on 4 factors: maximizing the complex Gaussian content at the aperture for the $TE_{22,6}$ and $TE_{24,7}$ modes and minimizing the fields along the launcher cut for the $TE_{22,6}$ and $TE_{24,7}$ modes. The profile of the launcher is shown in Figure 5-2. The launcher is 16.65 cm long with an uptaper angle of 0.35° and features a launcher cut of 4.3 cm. The resulting field output at the aperture for each mode is shown in Figure 5-3, where high quality Gaussian beams are predicted for each mode. The calculated Gaussian content of these beams from the launcher is 98.4 % for the $TE_{22,6}$ mode and 98.0 % for the $TE_{24,7}$ mode.

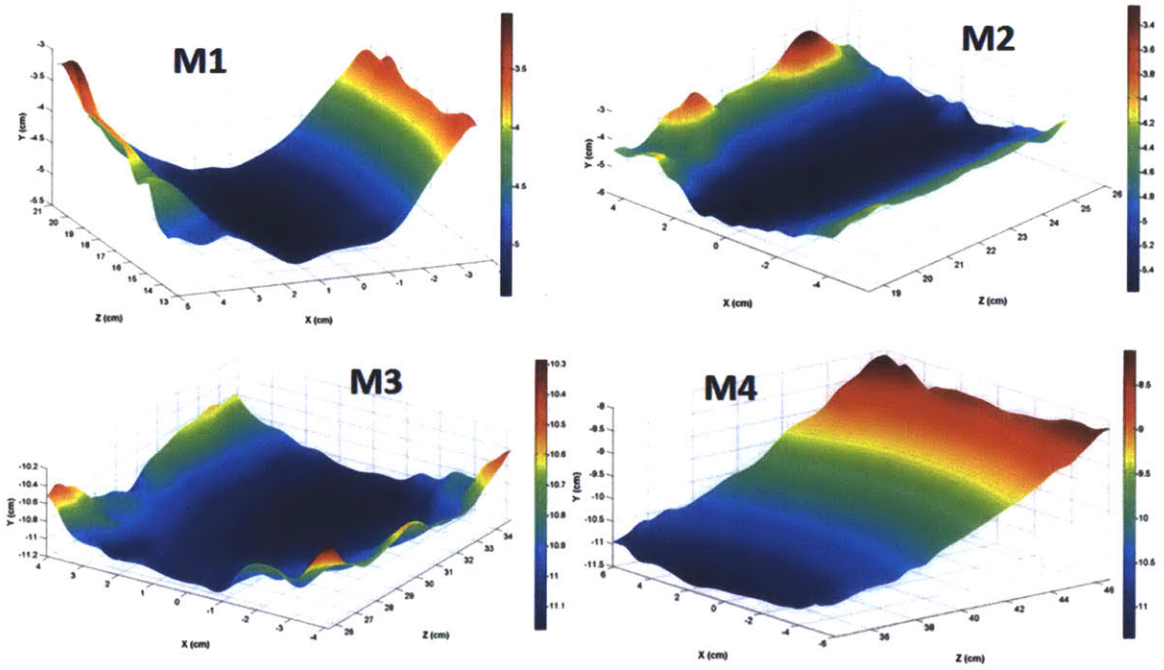

Figure 5-4: Profiles for the 4 phase-correcting mirrors of the dual frequency IMC design.

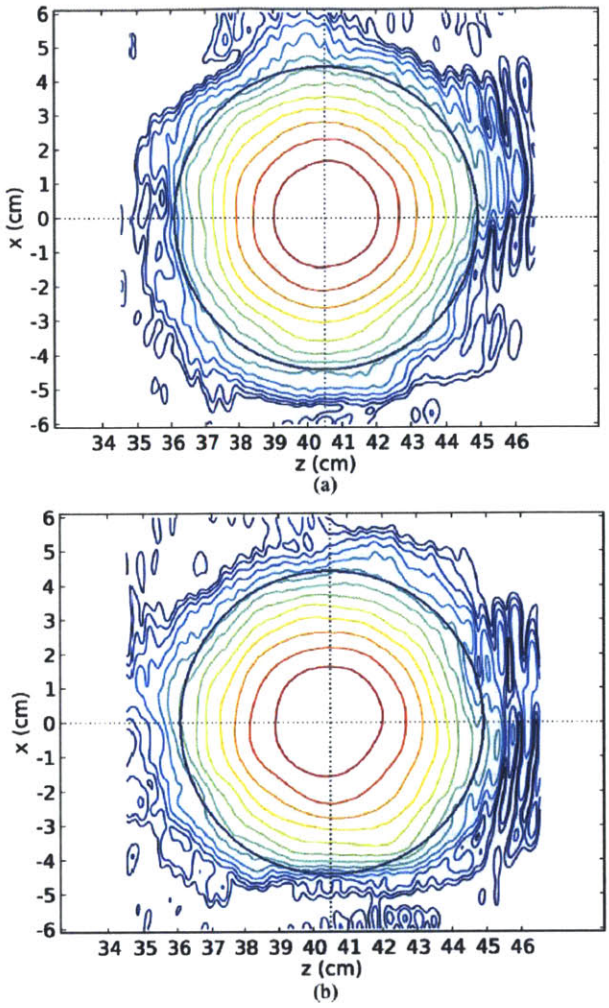

Figure 5-5: Electric field intensity distribution at the window plane for (a) the $TE_{22,6}$ mode at 110 GHz and (b) the $TE_{24,7}$ mode at 124.5 GHz. Adapted from [163].

To maximize the Gaussian content, it was decided that a set of phase-correcting mirrors needs to be implemented. The design of the mirror profiles was part of the contribution by Ben Rock at UW. The profiles of the mirrors are shown in Figure 5-4. The design of the mirrors in such a system is a two stage process as the mirrors are first optimized for maximum power transmission to the window and then optimized for Gaussian beam content. The results of this mode converter design have been published by the group at UW, with the predicted output beam profiles shown in Figure 5-5 [163]. Calculations show that the Gaussian beam content for both modes should be > 99 %, and

each beam is round with a waist of 2.63 cm. The Ohmic and diffractive losses from the launcher and system of mirrors should be on the order of ~3%, with another 1% loss from the window. One important note on the design of such a launcher is that unlike a single-mode launcher, consideration of two modes and their different bounce angles means that both modes are expected to come out with a small offset and tilt angle with respect to the axis of the window.

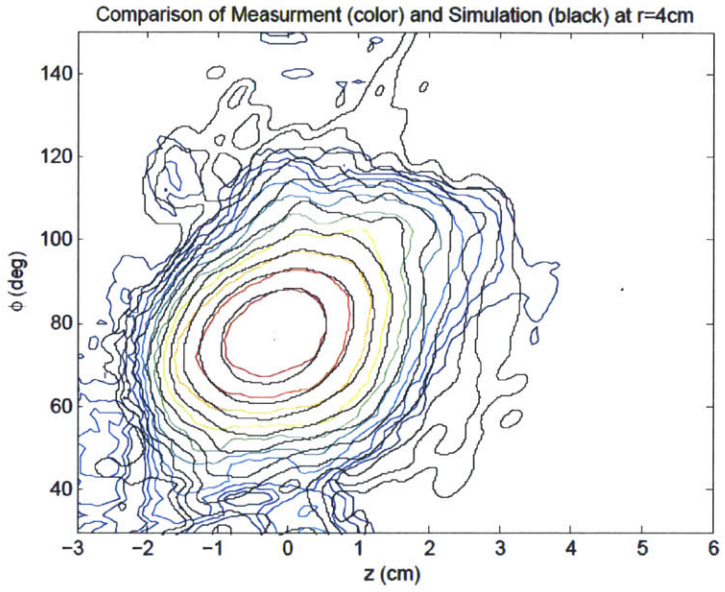

Figure 5-6: Cold test measurement at the launcher aperture (color) compared with theoretical calculation (black) at a cylindrical surface with R = 4 cm. Theoretical calculation was shifted by 1.5 mm along the axis and 1° to match up properly with measured pattern.

Bringing such a mode converter from the design world to a physical product proved to be a very challenging task which was to be completed as part of this thesis work. First, machining the parts to the necessary precision is very complicated and many machine shops do not have the capability due to the accuracy needed on the inner profile and the size, and aspect ratio, of the launcher. On the recommendation of CPI, we had the launcher machined to better than 1 mil (1/1000th of an inch) tolerance by Ron Witherspoon, Inc., who had successfully machined similar launchers for them in the past. With a

launcher built, it was important to first verify the machining of the launcher through cold test. Once again, our collaborators at UW did this measurement for us due to their available cylindrical-plane scanner. The result of this cold test is shown in Figure 5-6 where it is compared with the theoretical calculation from Surf3D at this location. While the agreement is quite good, a 1.5 mm offset and 1° rotation was necessary to line up both sets of data, which could be explained by experimental error in alignment, though they caution that such errors have historically been smaller in other launcher measurements.

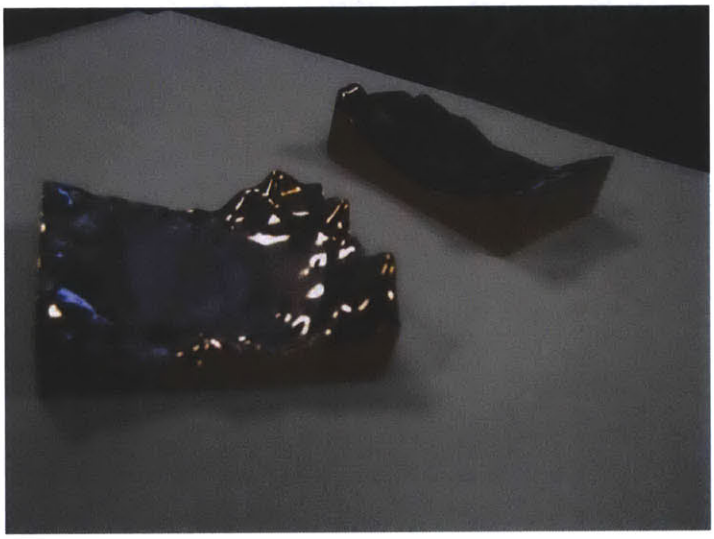

Figure 5-7: Photograph of copper mirror 1 (background) and mirror 2 (foreground). Mirrors were machined by Ramco Machine, LLC and the picture shows the interesting profiling of the phase correcting surface.

With a successfully demonstrated launcher, attention turned to the mirrors. Again, high precision machining was needed for the profiled mirror surfaces, though with the easier planar geometry, we were able to use a local machine shop, Ramco Machine, LLC to machine the 4 mirrors to better than 1 mil. A photograph of mirrors 1 and 2, showing their interesting surface profile and beautiful finish is shown in Figure 5-7. Not only did the mirror profiles require high precision, but the positioning of each mirror was just as critical, if not more so. The mirror assembly consisted of plates for each mirror and connecting joints that implemented dowel pin and bolted connections to preserve the

highest level of alignment. The mode converter was then assembled and ready for cold test.

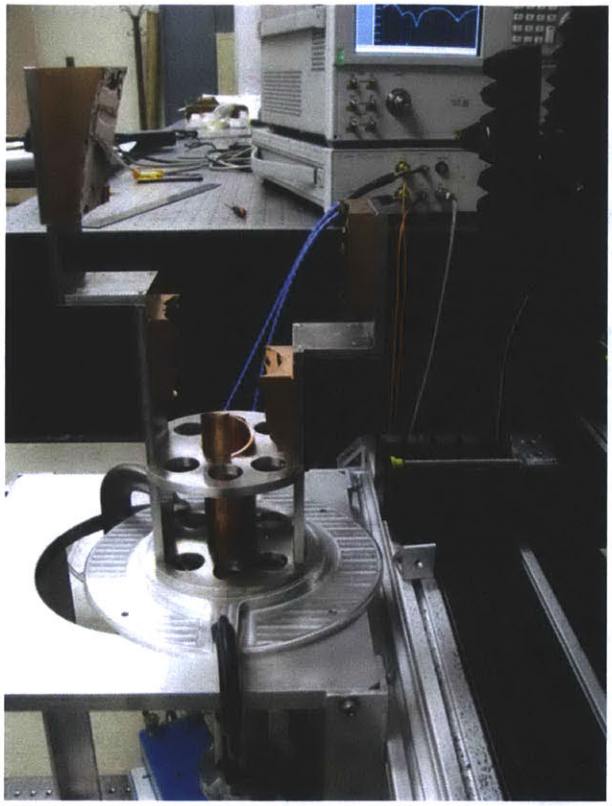

Figure 5-8: Experimental setup for the cold test measurement of the dual frequency IMC. The dimpled wall launcher and 4 profiled copper mirrors are assembled to a frame with the $TE_{22,6}$ mode generator connected to the input of the launcher. The receiving head of the VNA is mounted to a 3-axis scanner on the right where a cut waveguide antenna is used to detect the field intensity.

The experimental setup for the cold test measurement is shown in Figure 5-8. In this picture, we can see the 4 copper mirrors and the launcher with a helical cut all secured to the frame. In the background, the VNA, whose receiver is mounted to the three-axis scanner on the right, is seen. The cold test methodology has been thoroughly described in Chapter 3, though we also take note that this measurement was carried out at 109.95 GHz after a measurement of the $TE_{22,6}$ mode generator [142] showed that its narrowband

performance was optimal at this frequency. The amplitude and phase of the output beam were measured at the location of the window and are shown in Figure 5-9.

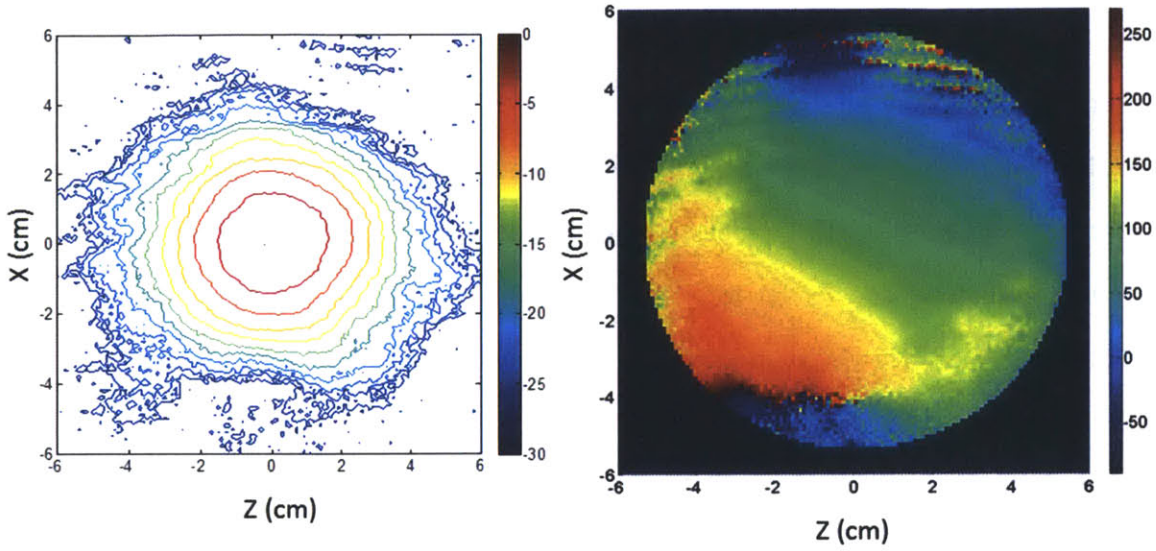

Figure 5-9: Cold test measurement of the amplitude (left) and phase (right) for the dual frequency mode converter given a $TE_{22,6}$ input at 109.95 GHz.

To assist with the characterization of the beam, many more measurements were taken in different planes to perform an additional phase retrieval analysis. The measured beam waists were W_z = 2.5 cm and W_x = 2.4 cm. We considered a few different ways of evaluating the Gaussian content. By simply using the amplitude data and assuming a flat phase, a scalar Gaussian content could be established which we found to be 99.0 % for a Gaussian beam with circular beam waist of 2.55 cm. By evaluating the phase in Figure 5-9, we can see an apparent tilt in both axes with approximate tilt angles $\alpha_z = 0.6°$ and $\alpha_x = 0.3°$. While this is on the order of the theoretical calculations [163] which predicted tilt angles of ~0.4° with respect to the axis of the window, the other likely source of this tilt error is misalignment. This misalignment could exist in the measurement system if the measurement axis differs from the window axis, and it could also result from mechanical misalignment of the mode converter itself. Regardless, while a tilted beam coupling into a

pipe could see as much as 5 % mode conversion into higher order modes at these angles [137], a matching optics unit (MOU) may be placed at the output of the gyrotron to optimize the external beam coupling, and therefore we can safely account for such tilts in our analysis. Therefore, by including the phase measurement into the analysis and allowing for a tilted Gaussian beam, we determine the Gaussian beam content to be 98.8 %. In the absence of tilt, the phase of the Gaussian beam is extremely flat, with a radius of curvature of ~6 m, meaning that the beam focus is indeed located at the window.

Unfortunately, due to the lack of an available source, the IMC cannot be cold tested at 124.5 GHz. However, the excellent result obtained at 110 GHz implies that the measurements match the theory well, and it should be expected to perform adequately at the higher frequency.

5.2.2 Cavity Design

The reason we introduced the mode converter first is that it imposes additional design constraints on the cavity design. While it would be ideal to have full control over the cavity parameters, a number of them are fixed, including the entrance coordinate and the exit coordinate. This means that every geometric factor that is considered involves a tradeoff with another.

To approach this multi-frequency design, it is difficult to obtain a true ideal optimization metric of power and mode competition across both modes simultaneously. Therefore, we divide the design process up into more manageable steps. The first step is to use general design guidelines to come up with a rough design, then that rough design may be refined by optimization of power and verification of mode competition through simulation work.

The primary cavity design components will be the straight section, the downtaper towards the gun, and the uptaper towards the IMC. To simplify the analysis, we note that Section 5.1 demonstrates that successful operation could be obtained for the same beam

radius and compression at the higher frequency mode, therefore the cavity radius will remain fixed at 1.98 cm. We can also refer to the design work on the V-2005 cavity which showed that a downtaper of 2.5° was necessary to ensure efficient operation across all uptaper angles [111], with both previous 110 GHz cavities using this value, therefore it will remain fixed. The parameter space of interest for this design will therefore be the uptaper angle and the length of the straight section of the cavity.

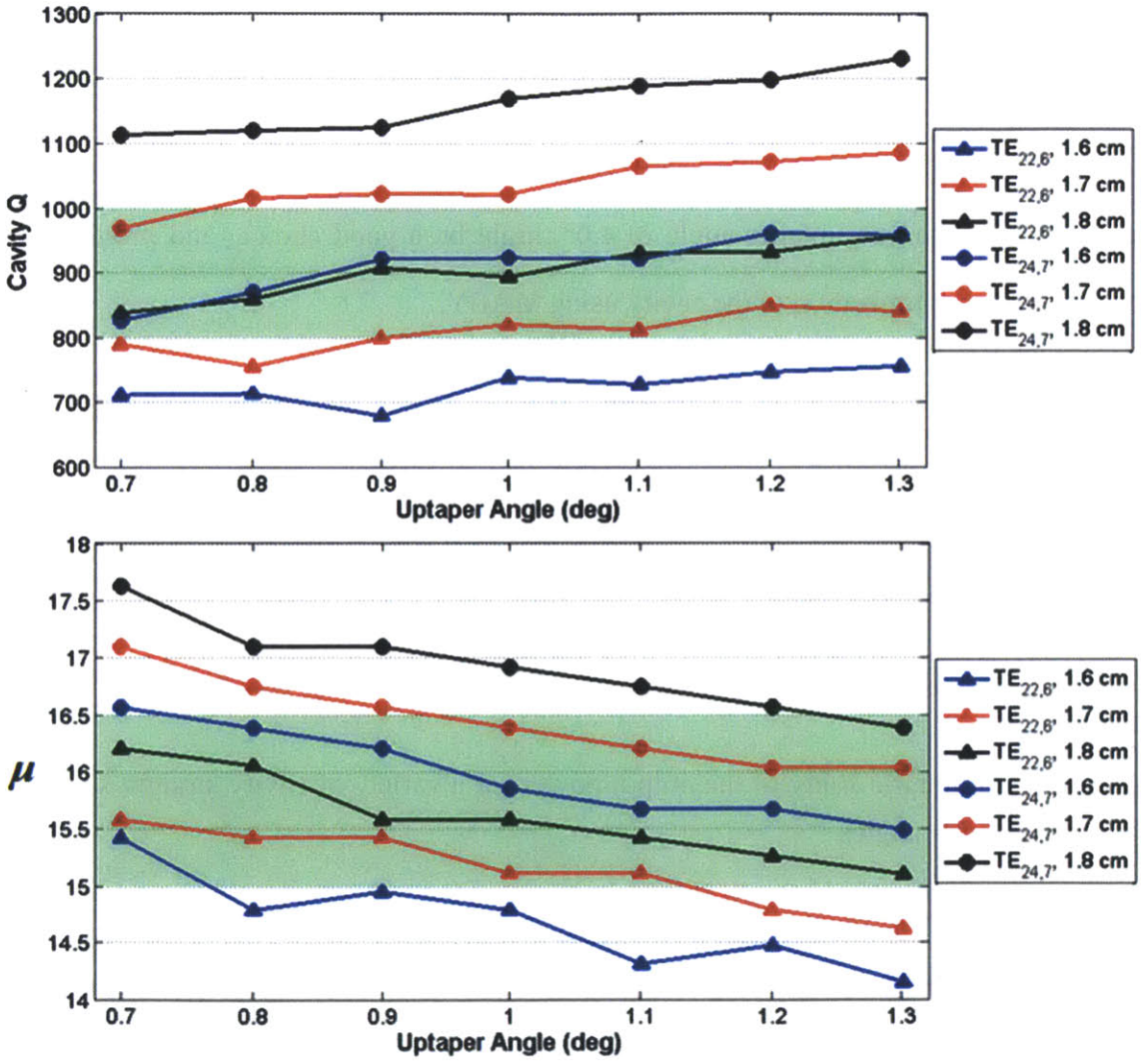

Figure 5-10: Parametric analysis of the cavity diffractive Q and the normalized length Π for a variety of cavity straight section lengths and uptaper angles. The cavity radius and downtaper angle remain fixed at 1.98 cm and 2.5°, respectively. The highlighted region indicates a desirable parameter range.

For a rough design, we may consider best design practices for a high power gyrotron. Inspection of the efficiency contour plot in Section 2.2 indicates that the peak efficiency regime is given for a normalized cavity radius with $\mu \approx$ 15-18, though ideally this should be limited to ~16. At the same time, in Section 2.3, the role of the cavity's diffractive Q was discussed, which determines the power coupling out of the cavity and the Ohmic losses. Q_D values of 800-1000 are typical in successful gyrotron designs, like those previously demonstrated at MIT. We now employ a cold-cavity code for a parametric analysis to determine μ and Q_D. In Figure 5-10, we compare these parameters for a variety of uptaper angles and cavity lengths. This analysis indicates that a cavity length of 1.7 cm and an uptaper angle of 1.0° might be a good choice, and provides a starting point for optimization of the cavity using MAGY.

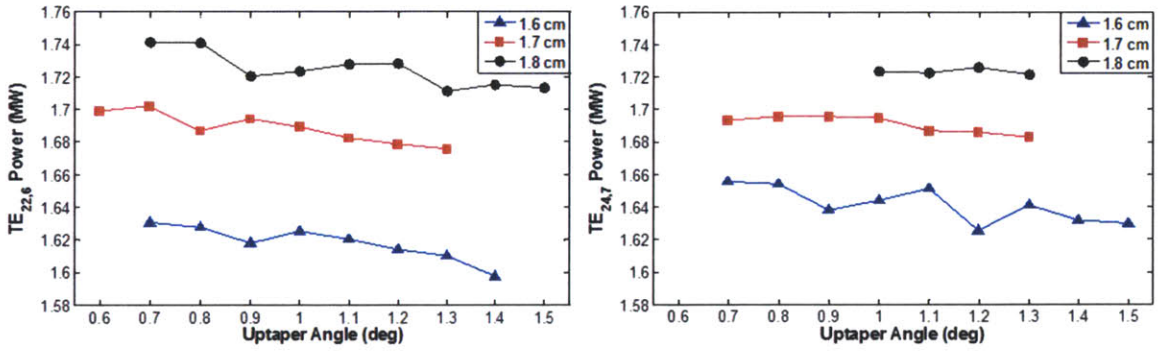

Figure 5-11: Parametric study of the output power for a variety of cavity straight section lengths and uptaper angles.

We begin MAGY analysis by looking at just the single mode excitation, thus looking at the interaction efficiency. Simulations are run by varying the geometry in a similar manner as before and use the real magnetic field profile and the 96 kV, 40 A beam with an alpha of 1.4. For a more extensive study, the peak magnetic field is varied to find the maximum power, and in each case the simulations must be run until the frequency converges to the nearest MHz. The result of this study is shown in Figure 5-11. We see

that there is only a very slight variation in output power over the range of taper angles while the drop in power is much more severe between the 1.7 cm and 1.6 cm straight sections than it is between the 1.8 cm and 1.7 cm straight sections. This result is easily explained by theory since the increase in uptaper angle increases the diffractive Q which means there is less power coupled out of the cavity and more Ohmic loss. Meanwhile for the shorter cavity, despite having a smaller diffractive Q, its normalized cavity length is too short and it no longer resides in the high efficiency zone of the F-μ contour plot.

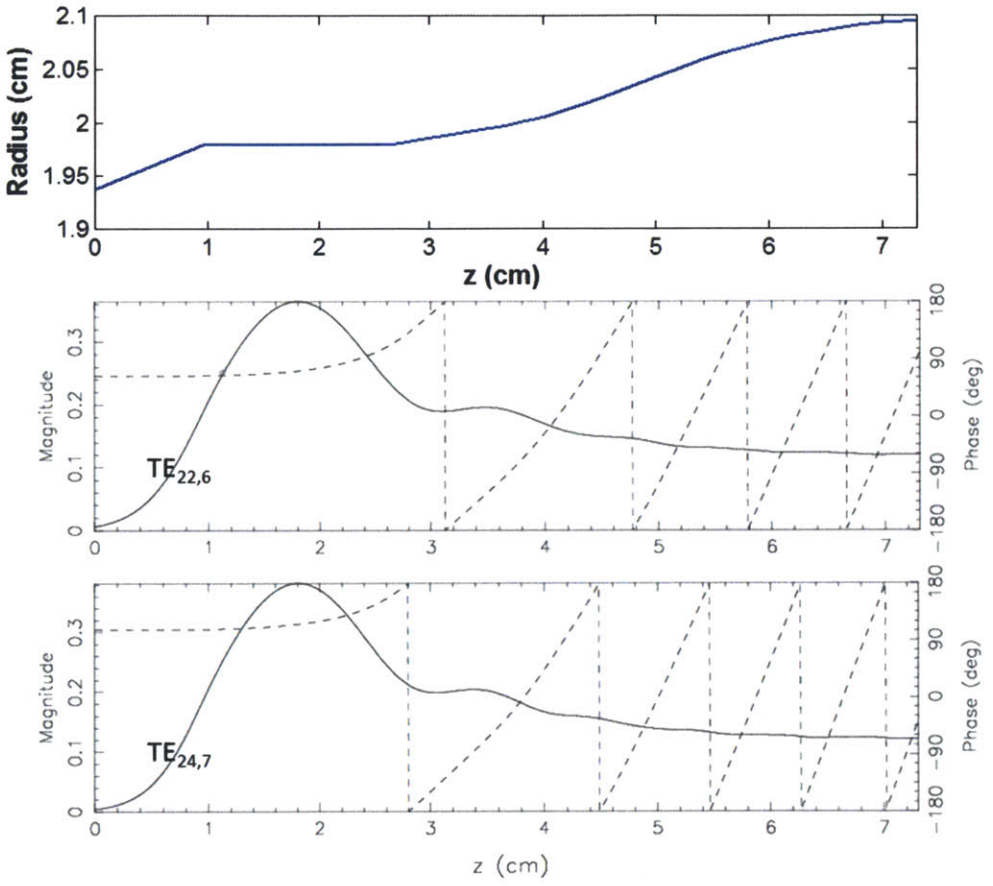

Figure 5-12: Cavity geometry and simulated axial electric field profile in MAGY for the $TE_{22,6}$ and $TE_{24,7}$ modes.

The final step involves evaluating the multi-mode case to investigate the mode competition. We found that at smaller uptaper angles, the output became unstable for the $TE_{24,7}$ mode at around 0.8°, particularly in the case of the 1.8 cm cavity, though it was seen

in the 1.7 cm cavity as well. Therefore, it was decided to go with the 1.7 cm length and 1.0° uptaper to provide an additional safety factor against this effect. To complete the design, the rest of the taper geometry had to be completed. Another parametric study was initiated to evaluate the optimal length of the linear uptaper section as well as the geometry for the final non-linear taper section. Given the constraints at either end, the possibilities were limited for this section, however optimal power was found when the linear uptaper was 1 cm long leading into the cubic spline non-linear section that joined this point with the entrance of the launcher. The cavity profile as well as the axial electric field amplitude and phase for both operating modes are shown in Figure 5-12. The design parameters for the cavity are shown in Table 5-1.

With the cavity designed, we again considered multiple machining options and went with Ramco Machine, LLC to direct machine it to a 1 mil tolerance.

Table 5-1: Design parameters of the new dual frequency cavity

Input taper	2.5 deg	
Straight section length	1.7 cm	
Straight section radius	1.98 cm	
Output taper	1.0 deg	
Mode	$TE_{22,6}$	$TE_{24,7}$
Frequency	110.09 GHz	124.57 GHz
Diffractive Q factor	830	1060
Normalized Length (μ)	15.1	16.4
Power (Singlet)	1.65 MW	1.68 MW

5.2.3 Window Design and Cold Test

The final component left to design is then the window. There are a number of options when it comes to extracting the microwaves from the tube, with the choice coming down

to the needs of the specific application. In this case, we only require nearly full transmission at 2 frequencies, therefore a single-disc window should suffice. While CW high power gyrotrons require diamond windows due to the heat loading, we can get away with a simple fused quartz window. An additional design consideration for the window is that it must hold vacuum without breaking. For a clamped disc, most manufacturers indicate that the minimum thickness, t_{min}, should be given by:

$$t_{min} = \sqrt{\frac{Pd_0^2}{4 * 1.333 * S_{max}}} \tag{5.1}$$

where P is the pressure differential across the window, d_0 is the unsupported disc diameter of the window, and S_{max} is the maximum stress for fused quartz. The value of S_{max} typically incorporates a ~7:1 safety factor, meaning a value of 1000 psi is used when the modulus of rupture for fused quartz is 7000 psi. For a 4.25" window like we have in the experiment, this leads to a 5.5 mm thickness.

Now we consider the desired thickness to ensure transmission at both frequencies. Following the treatment by Kong [107], we may define a variable $p_{01} = n$ representing the boundary between vacuum (medium 0) and medium 1 where we will assume normal incidence and n is its index of refraction. Relations for the amplitude reflection R and transmission T at the interface may therefore be defined as:

$$R_{01} = \frac{1 - p_{01}}{1 + p_{01}} \tag{5.2}$$

$$T_{01} = \frac{2}{1 + p_{01}} \tag{5.3}$$

and where the reflection/transmission in the opposite direction is a function of $p_{10} = 1/n$. Here, we have assumed that the medium has no loss, an adequate approximation for fused quartz at the frequencies of interest. The power transmission through a slab of medium 1 spanning d_0 to d_1 is therefore:

$$T^2 = \left(\frac{T_{01}T_{10}\exp(j(k_0 - k_1)d_0)\exp(j(k_1 - k_0)d_1)}{1 + R_{01}R_{10}\exp(2jk_1(d_1 - d_0))} \right)^2 . \tag{5.4}$$

Applying this theory, we can solve for solutions with total transmission at each frequency for fused quartz with n = 1.9562. There are of course multiple solutions depending on how many maxima will occur between the two frequencies. We opted for the solution that had only maxima at 110 and 124.5 GHz with a single minimum in between which was a thickness of 5.555 mm. This just barely meets the required thickness specification, however recall that the minimum thickness quoted does include a strong safety factor.

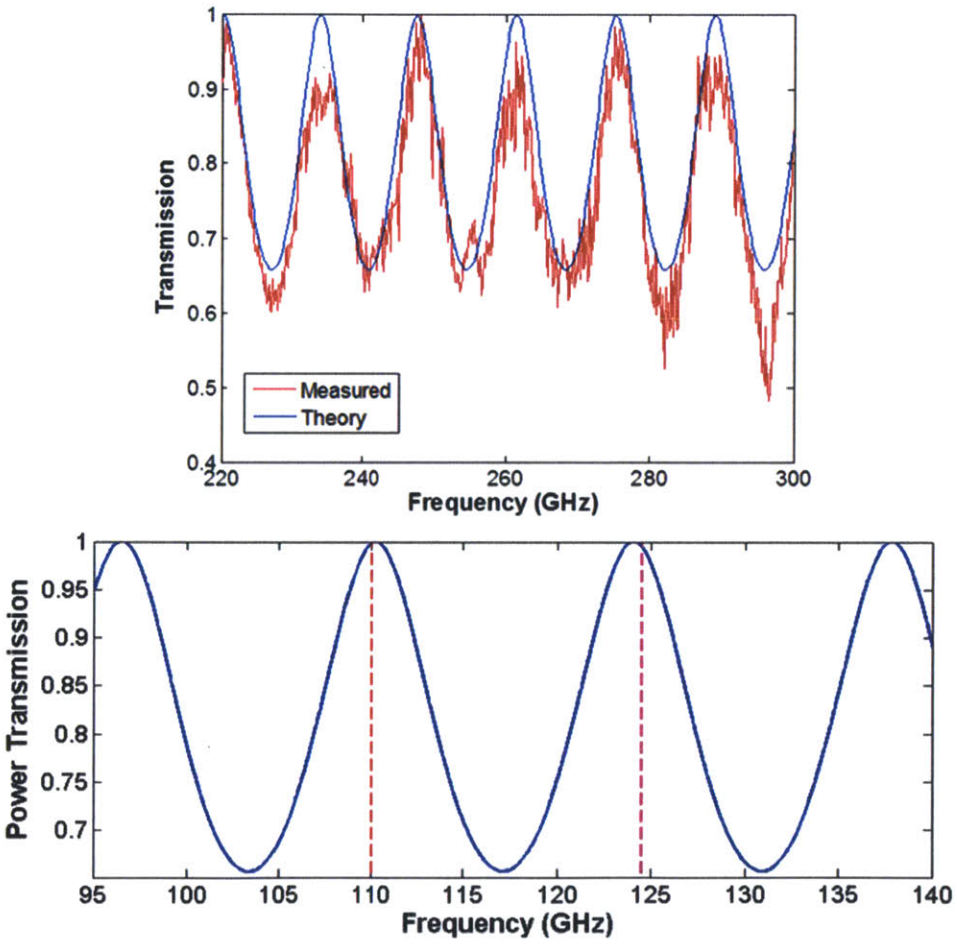

Figure 5-13: Cold test measurement and theoretical calculation of the window transmission. Vertical lines in lower figure indicate frequencies of the two operating modes where greater than 99.5 % transmission is obtained at each.

The polished quartz windows were obtained and cold tested on the VNA. Due to poor performance of the VNA at 110 GHz at the time of the measurements, we opted to cold test the windows with a WR-5 setup for 220-300 GHz. To determine the agreement, we find the thickness for which the theory fits best to the measurement since there was a finite tolerance when the windows were made. The best fit thickness was well within the 0.5 mil tolerance and was found to be 5.56 mm. In Figure 5-13, we plot the cold test data along with the theoretical fit at this thickness. Additional loss resulting from the loss tangent over this frequency range should be under 1 % for the given window thickness [164]. We also plot the theoretical transmission at the two output frequencies for the experiment where we see that the window should have over 99.5 % transmission at both 110 and 124.5 GHz.

5.3 Experimental Performance of the Two Frequency Gyrotron

With all the components designed and assembled, the new gyrotron configuration was installed in the vacuum tube. Once the pressure of the tube had recovered and the performance of components like the electron gun was restored, the tube was aligned. The alignment process begins with a physical alignment as the gyrotron is operated at low voltage and the tube is displaced until beam interception occurs. Once a central position is discovered, the input parameters may be increased and oscillations in the desired mode are sought. We begin by operating at 110 GHz in the $TE_{22,6}$ mode since this operation and the corresponding parameter space have been well studied. Once oscillations are obtained, a rigorous alignment process is undertaken. This involves moving the gyrotron along all possible axes and varying magnetic field parameters to find a region with maximum power and good stability.

5.3.1 $TE_{22,6}$ Power

We begin by examining the output power of the tube. After a lengthy alignment process, MW power levels were achieved. We first examine the output power as a function of the main magnetic field B_0 as shown in Figure 5-14. At each point, we vary the gun coil, and thus optimize alpha and the beam radius for maximum power operation at that value of magnetic field. We see that at 96 kV and 40 A operation, the tube was able to achieve over 1.1 MW of power. This was a pleasant surprise in fact since the previous configuration had stability issues at this voltage and current, and most previous results were obtained by operating at 42 A. In this case, when the gyrotron operates at 98 kV, 42 A, the output power of 1.25 MW is very close to the previous operation with the V-2005 cavity.

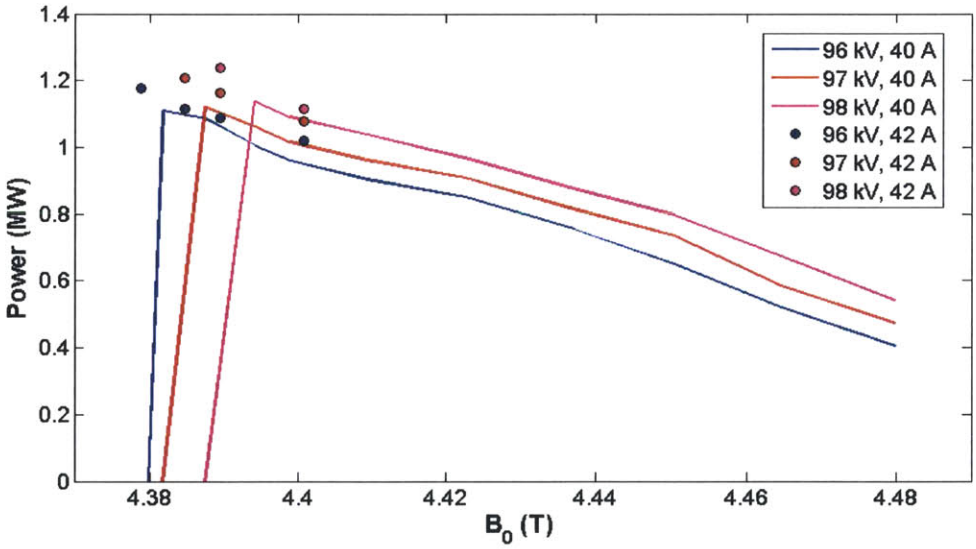

Figure 5-14: Measured power vs. main magnetic field B_0 for the $TE_{22,6}$ mode at 110 GHz.

We may additionally consider how the output varies with the beam current. The power and efficiency as a function of beam current are shown in Figure 5-15 for a fixed voltage of 98 kV. At each point, the magnetic field was tuned for maximum power, ranging from 4.38 T at 45 A to 4.41 T at 35 A, with minor adjustments to the gun field as well. We see that at 45 A, the output power reaches nearly 1.4 MW while the efficiency

has also increased by about 5 % compared to the 35 A operating point. The efficiency reaches the 30 % point at the design point of 40 A.

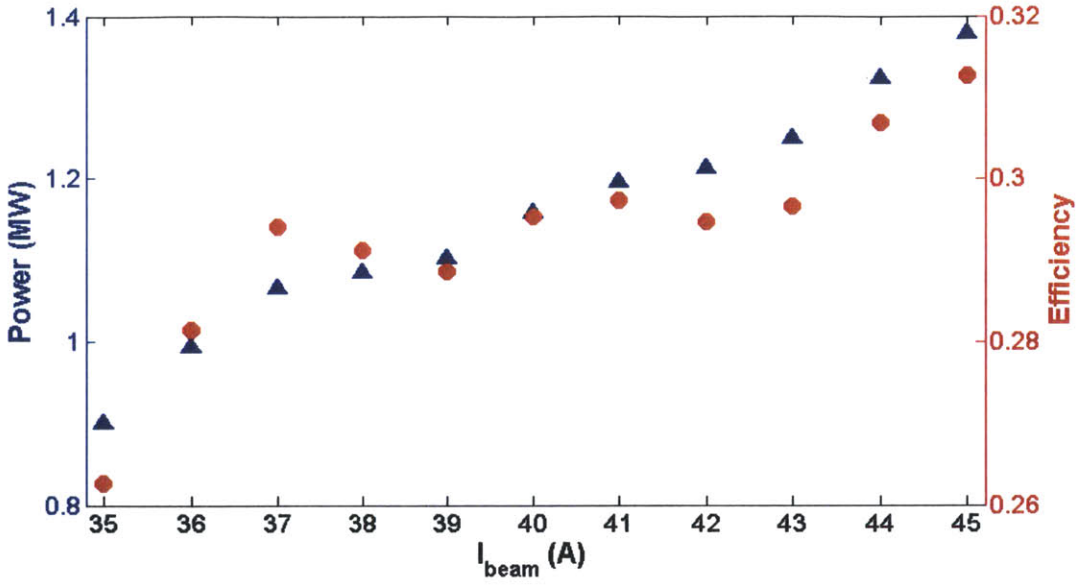

Figure 5-15: Output power and efficiency as a function of beam current for a fixed voltage of 98 kV. The main magnetic field is varied at each point for maximum power.

5.3.2 $TE_{22,6}$ Output Beam Pattern

With the desired output power coming from the device, it is a good indication that the gyrotron's mode converter is working well, though the question of course is how well. The methodology here is the same as that which was applied in Chapter 3 using the 2-axis scanner, rf diode and programmable variable attenuator. For beam pattern measuring, we back off slightly from the peak power point to ensure we have a perfectly stable operating point throughout the measurement, and select a field of $B_0 = 4.4$ T with a 96 kV, 40 A beam. We take 3 measurements far from the location of the window, as shown in Figure 5-16 where distances of 125, 148, and 182 cm from the window plane are used. The phase retrieval algorithm is then employed to determine the amplitude and phase of the fields at the window. The retrieved amplitude and phase are shown in Figure 5-17. The quality of this beam was excellent. The beam waist of Wz = Wx = 2.65 cm shows that a nice circular

beam is generated and agrees very well with the cold test measurement where a circular beam with W = 2.55 cm was predicted, and even better with the theoretical calculation where a W = 2.63 cm beam was predicted. The beam also has very high Gaussian content as we calculate it to be 97.7 % with the inclusion of the phase. The scalar Gaussian content again yields an even better 99.0 %, just as in the cold test.

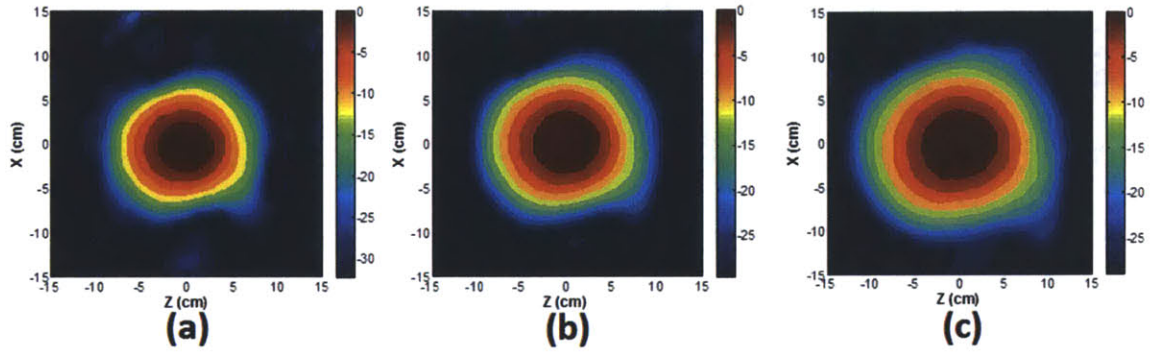

Figure 5-16: Output beam pattern measurements for the TE22,6 mode at 110 GHz taken at distances (a) 125 cm, (b) 148 cm, and (c) 182 cm.

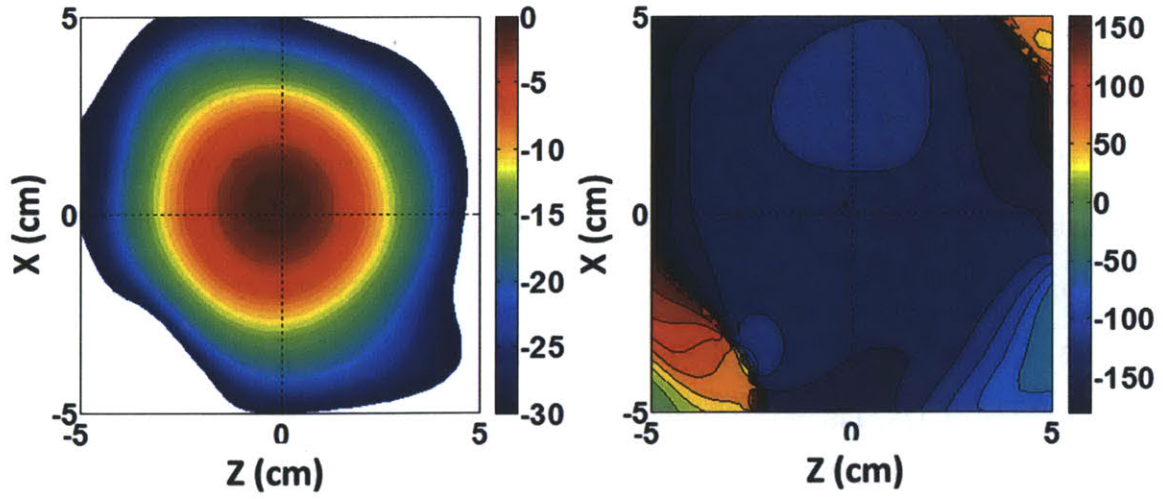

Figure 5-17: Retrieved amplitude and phase of the output beam for the $TE_{22,6}$ mode at 110 GHz.

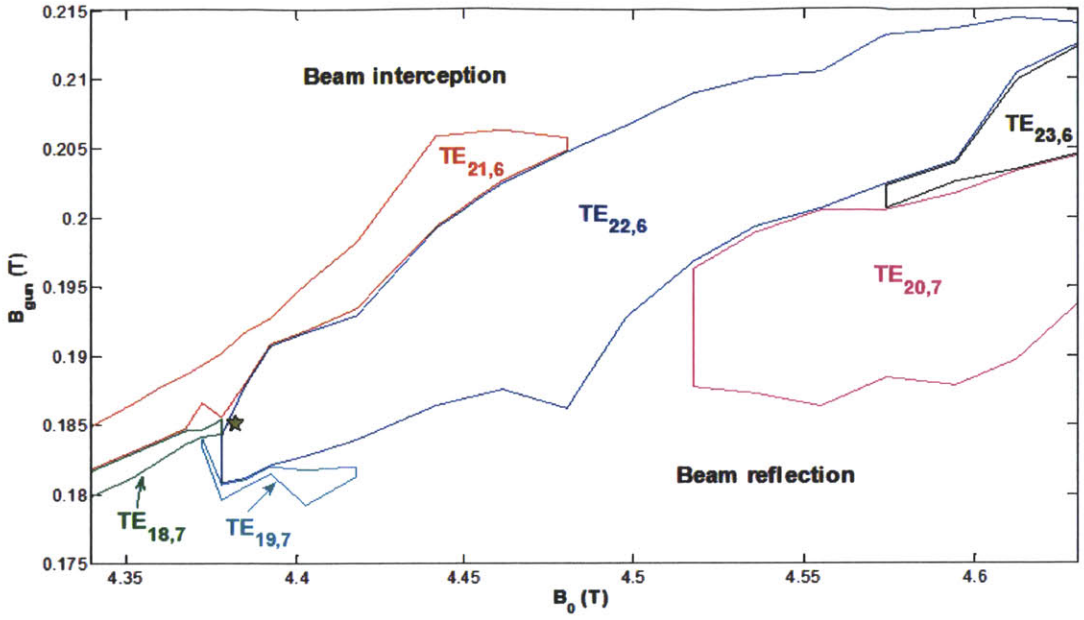

Figure 5-18: Mode map taken around 110 GHz at 96 kV, 40 A. Gold star marks the high power operating point.

5.3.3 Mode Competition at 110 GHz

Similar to previous experiments, we examine the issue of mode competition by taking a mode map, which is a mapping of the frequency excitation as a function of the magnetic field parameters. The mode map taken at 96 kV, 40 A is shown in Figure 5-18. This mode map is very similar to the result shown in Chapter 3 for the old high efficiency configuration. One thing to note is that the excitation region of the $TE_{-19,7}$ mode is reduced in this cavity, though we still do see the mode competing near the high power operating point. In fact, the minimum field at which the $TE_{22,6}$ mode can be excited is larger in this configuration, which could partly be attributed to mode competition with the $TE_{-19,7}$ mode. We also note that this configuration suffers from the same excitation of the $TE_{-20,7}$ mode at slightly larger magnetic field. While this excitation does not affect operation at 110 GHz, it limits operation at 113 GHz in the $TE_{23,6}$ mode. This does limit the tunability of the device if operating at +/- 3 GHz from the base operating mode, where performance of the IMC has previously been demonstrated, was desired. One final comment on the mode

map is that the region of excitation for the $TE_{21,6}$ mode is severely reduced. While a high power regime is still accessible in this mode, at higher gun field where the mode would typically be excited, an instability arises. This appears in the form of a modulation which can be seen during the flat top of operation at lower power in the $TE_{21,6}$ mode. Investigation into this modulation effect may be worthwhile at a later time.

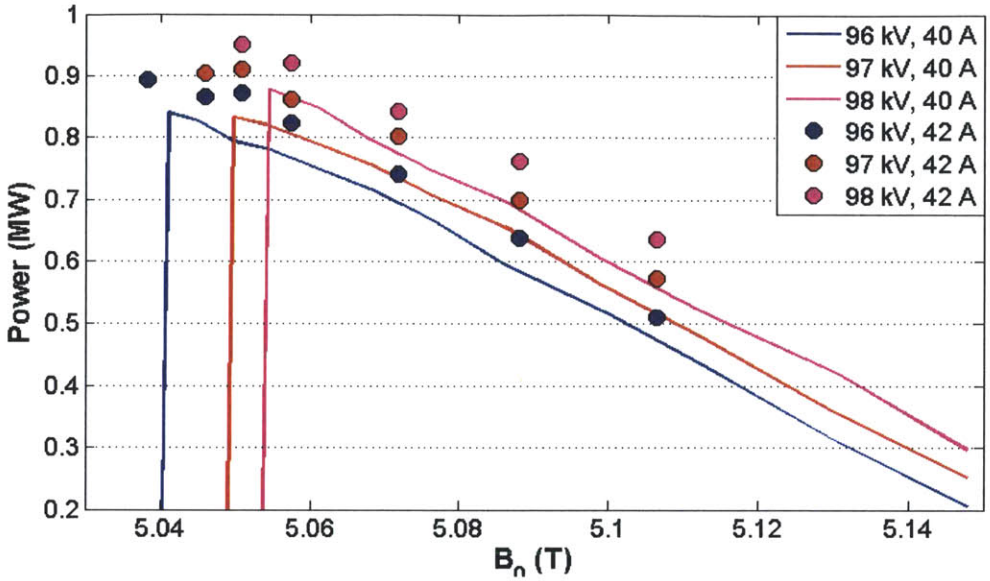

Figure 5-19: Power as a function of main magnetic field for the $TE_{24,7}$ mode at 124.5 GHz.

5.3.4 $TE_{24,7}$ Power

With successful operation measured across the board at 110 GHz, we tuned the magnetic field up to the estimated value for the $TE_{24,7}$ mode, around 5 T. Since there was some uncertainty about the operation of the gun and the stability of oscillations, we first explored the parameter space at lower voltages. Once we detected the desired oscillations and found the appropriate range of magnetic compression, we were able to push the voltage and current to their full value. The power measured as a function of the main magnetic field is shown in Figure 5-19. In this case, we do see that the power is somewhat limited from the goal of 1 MW, with ~850 kW of power measured at 96 kV and 40 A, and upwards of 950 kW measured at 98 kV, 42 A. The gyrotron though is capable of 1 MW

operation at this field point as seen in Figure 5-20 where 1 MW is achieved around 44 A beam current. It is worth noting though that operation in the $TE_{24,7}$ mode does exhibit some differences as compared with the typical $TE_{22,6}$ operation. It seems that there are some changes in the performance of the gun as the highest power is only achievable with the gun coil field set to a minimum value right on the verge of beam reflection. Just above this value though, the $TE_{24,7}$ mode experiences stable operation with high power. Generally for the $TE_{22,6}$ mode, there is a region of unstable, lower power oscillations in the mode when the gun coil is lowered and the compression, and alpha, is driven too high. The fact that we don't see this at 124.5 GHz may indicate that the operation of the gun is limiting both operation at the desired compression and higher alpha, as well as the possibility of operating at lower magnetic field where power would also be higher.

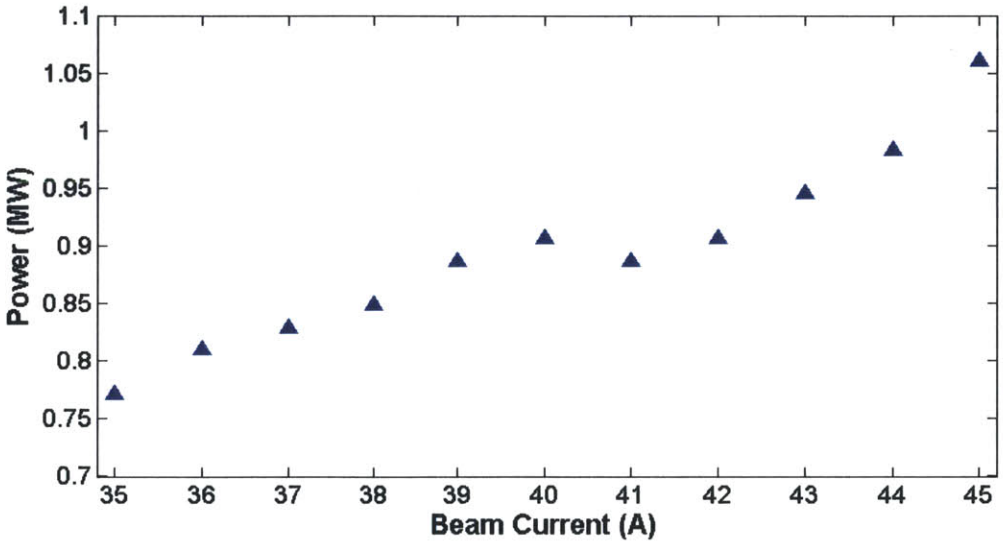

Figure 5-20: Power vs beam current at 98 kV for the $TE_{24,7}$ mode at 124.5 GHz. The main magnetic field is varied at each data point for maximum power.

5.3.5 $TE_{24,7}$ Output Beam Pattern

We again took several scans of the beam pattern, this time at 98 kV and 42 A where we see nearly 1 MW of output power. The measurement planes for these scans were 133, 154, and 167 cm from the window. The beam measurements are shown in Figure 5-21. Again, the

beam appears to be quite Gaussian upon first inspection. We next apply the phase retrieval process to these results to obtain the amplitude and phase of the output beam at the window as shown in Figure 5-22. We do notice right away that this beam is a fair bit smaller than the beam at 110 GHz, however this is an expected result that was predicted by the theoretical calculations [163]. The scalar Gaussian content is again excellent as we measure it to be 97.1 %. However, a quick inspection of Figure 5-22 shows a beam that is significantly off-center with a small tilt as well, therefore the complex Gaussian content will be limited. The calculated value is still quite reasonable as we found it to be 94.4 %. The effective beam waists of $W_z = W_x = 2.65$ cm shows again that the beam is highly circular and agrees very well with theory.

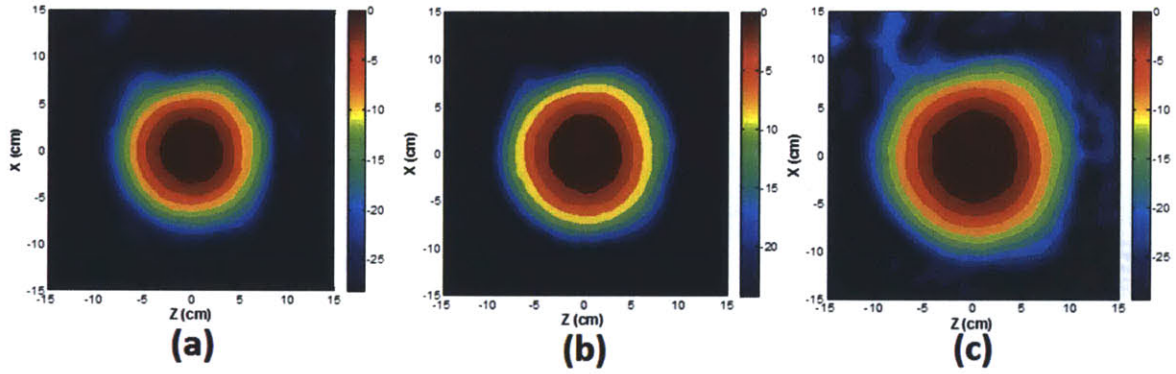

Figure 5-21: Beam pattern measurements at 98 kV, 42 A for the $TE_{24,7}$ mode at 124.5 GHz. Measured planes include: (a) 133 cm, (b) 154 cm, and (c) 167 cm from the gyrotron window.

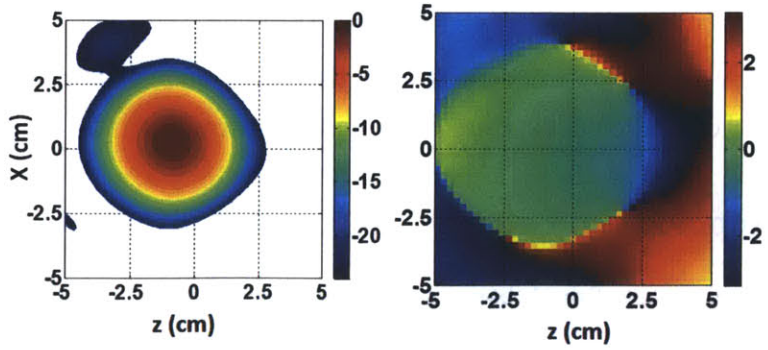

Figure 5-22: Retrieved amplitude and phase for the output beam measurements of the $TE_{24,7,1}$ mode at 124.5 GHz.

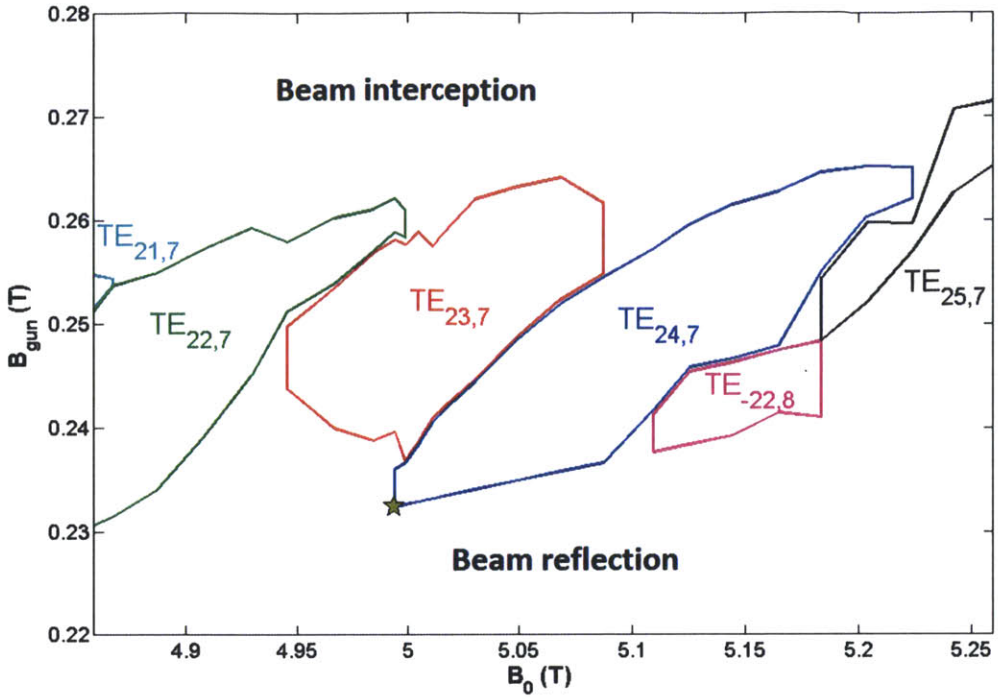

Figure 5-23: Mode Map taken around the 124.5 GHz operating point at 98 kV, 42 A. High power operating point shown by gold star.

5.3.6 Mode Competition around 124.5 GHz

We also examine the mode competition around this higher frequency point by means of a mode map The mode map at this new frequency is shown in Figure 5-23 and taken around the MW operating point of 98 kV, 42 A. First, it should be noted that there are some regions where no modes were identified as a result of unstable operation where frequencies could not be measured or regions where there was no apparent rf signal. Looking at the modes seen, just as in the case of the $TE_{22,6}$ mode, the modes with equal radial mode index are preferentially excited in general. The exception though is at higher magnetic field where the $TE_{-22,8}$ mode is excited, similar to how the $TE_{-20,7}$ mode is excited over the $TE_{23,6}$ at the lower frequency. We also note the peculiar location of the high power operating point which is at the absolute bottom corner of the $TE_{24,7}$ excitation region. This illustrates the point earlier about performance of the gun limiting the achievable

power. It seems that there should be a further parameter space to explore where higher power at 124.5 GHz could be achieved, but is instead limited by the beam reflection. The reason for this behavior is unclear at this time, though efforts are underway to simulate the gun performance to see if any limitations could be uncovered.

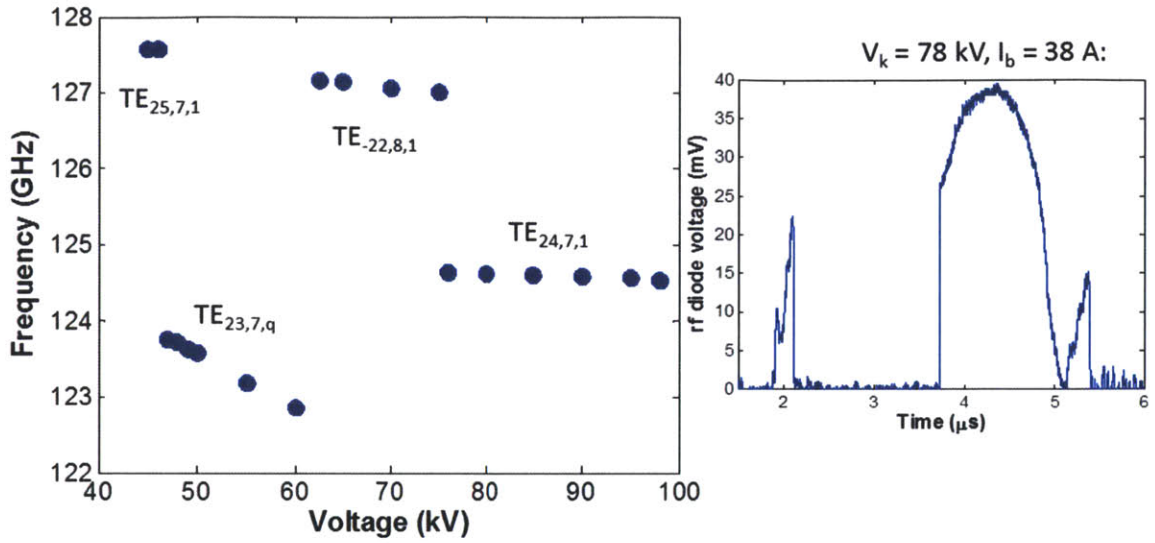

Figure 5-24: Measured start-up scenario for a $TE_{24,7}$ high power excitation. 950 kW of power was observed at 124.54 GHz for a 96 kV voltage with B_0 = 5.00 T and B_g = 0.233 T.

5.4 Investigation of Start-Up Scenarios

In Chapter 4, the issue of the start-up scenario was examined in great detail. In that chapter, we presented a thorough analysis of the mode frequencies and output powers during the voltage rise and offered a theory to explain the mode excitations that we observed. In this section, we need not discuss the phenomenon in such great detail, however the implementation of a new cavity and window, as well as the new operating frequency of 124.5 GHz, presents an excellent opportunity. As with any experimental study, particularly one where an unexpected result is obtained, there always remains a question of whether an observed effect is unique to an experiment or universal. By at least roughly examining some of these start-up scenarios in this new configuration and

observing a similar behavior, we could provide an additional means of validating the results of Chapter 4.

For these results here, we will show a complete sequence of frequencies observed during the start-up and measured over the flat-top of pulses of varying peak voltage. Obtaining proper calibrated power measurements is a lengthier process and, therefore, we will instead provide a characteristic rf diode trace, which essentially provides the power vs time (or voltage) characteristic to help diagnose the mode excitations.

We begin first with the start-up scenario observed for a high power point of the $TE_{24,7}$ mode excited at 124.54 GHz. The observed power at this point was about 950 kW with magnetic fields B_0 = 5.00 T, and B_g = 0.233 T. Figure 5-24 shows the interesting start-up scenario that we observe at this operating point, along with a power trace shown for a peak voltage of 78 kV where the beam current is 38 A. The most encouraging aspect of this measured result is that we do indeed observe the same lower frequency backward-wave mode as we did at 110 GHz. In this case, the $TE_{23,7,q}$ mode (where it is likely that q=3 or 4 as before) is excited at 123-124 GHz, which is around 2 GHz from its cutoff frequency of 121.56 GHz, for voltages of 45-60 kV. This mode shows the same characteristic steep frequency tuning as a function of voltage that we observed with the $TE_{21,6,3-4}$ modes which were also up to 2 GHz from the cutoff frequency. The situation at both operating points is quite analogous as the separation between the modes that differ by 1 in their azimuthal indexes is about 3 GHz in both cases. At this 124.5 GHz operating point, we interestingly also observe the higher frequency modes, like those that might be predicted in theory. We can determine, however, that it is not the $TE_{25,7,1}$ mode that is excited between 65 and 75 kV, but, rather, its main competing mode: the counter-rotating $TE_{-22,8,1}$ mode. The first indication of this is the frequency, which, at 127.00 GHz, is too low for the $TE_{25,7,1}$ mode whose cutoff frequency is 127.48 GHz. The second indication is the "power gap" observed in the rf diode trace. This is a result of the counter-rotating mode being excited, and due to the opposite rotation, it will not emit correctly from the IMC launcher. This provides an

important reminder when operating in an IMC configuration since an apparent lack of output power in the tube does not automatically signify a lack of power being excited within the cavity. Proper frequency analysis can diagnose such behavior.

A stable operating point with $B_0 = 5.06$ T and $B_g = 0.240$ T was also examined. The behavior at this operating point showed the same set of modes. In this case, the $TE_{24,7,1}$ mode was only excited at voltages above 88 kV. The counter-rotating $TE_{-22,8,1}$ mode was again excited, this time over a 72kV – 88 kV range, however at voltages around 70 kV, the $TE_{25,7,1}$ mode was also observed. Finally, we again saw the $TE_{23,7,q}$ backward-wave modes from about 54 to 68 kV at approximately the same frequency as for the high power point of Figure 5-24. Just as in the measurements of chapter 4, the voltage at which oscillations are first observed for the stable operating point was about 10 kV higher than the lowest voltage for which oscillations are seen at the high power point. In both cases, this was about 45 kV for high power operation and 55 kV at the highly stable operating points.

The start-up scenario for the 110 GHz operating point was also revisited for this new configuration. We examined a 1 MW operating point with $B_0 = 4.39$ T and $B_g = 0.185$ T. An interesting result was once again observed. At voltages above 68 kV, the $TE_{22,6,1}$ mode was again measured and the frequency tuning was consistent with the experiments in Chapter 4. However, below 68 kV, we did not observe higher frequency modes, nor did we observe the $TE_{21,6,q}$ backward wave modes as we did previously, instead observing an excitation that ranged in frequency from about 105.6 GHz to 106.3 GHz. Based on the measured frequencies, and the steep tuning, this mode should be a $TE_{20,6,q}$ backward-wave mode, essentially the same type of mode as the $TE_{21,6,q}$ mode we previously observed, but with a different azimuthal index and lower cutoff frequency. While it is not the only change made between the two experiments, it is interesting to note that the new, thinner window employed in this experiment has significant reflection at this frequency. The reflection around 105-106 GHz is in the range of 20-30%, which is quite significant. The fact that the reflection is so significant at these frequencies may further

substantiate that the window reflection could play a role in the excitation of these lower frequency backward-wave modes observed during start-up. In this case, the reflection at 106 GHz is so substantial as compared to the reflection at 108-109 GHz that the $TE_{20,6,q}$ mode is excited instead of the $TE_{21,6,q}$ mode observed previously, with any excitation of the $TE_{23,6,1}$ mode being suppressed in both experiments.

While further study of the start-up scenario in this new gyrotron configuration could be part of the future work, it is recommended that later studies also consider data taken on different gyrotrons to progress towards determining a universal phenomenon that could be related to the different parameters of each experiment, window reflections being one of them. The start-up scenario remains an important characteristic of the gyrotron to study, and should not be overlooked in future experiments.

5.5 Summary

High efficiency gyrotron operation at multiple frequencies represents a desirable characteristic for the scientists and engineers operating ECH systems on magnetic fusion experiments. In this chapter, we have presented a basic description of how a multi-frequency gyrotron can be designed and the range of modes that could possibly be excited without a significant change to the gyrotron's basic operating parameters. We investigated the particular case of a two frequency gyrotron designed to operate in the $TE_{22,6,1}$ mode at 110 GHz and the $TE_{24,7,1}$ mode at 124.5 GHz. A set of new components was designed for this new configuration, including a cavity and window designed as part of this thesis, and an internal mode converter that was built and tested as part of this work. The cavity was designed and optimized for efficient operation at both frequencies, using a shorter 1.7 cm length and steeper 1° uptaper than the previous high efficiency single-mode design. Based on simulations, this new design could be expected to produce 1.4 MW of power. A new, thinner 5.555 mm-thick window was also designed and implemented in this experiment and should provide over 99.5 % transmission at both frequencies.

The experiments were largely successful. At 110 GHz, 1.15 MW of power was observed at 96 kV and 40 A, while 1.25 MW of output power was produced for 98 kV and 42 A. Increasing the beam current to 45 A allowed for nearly 1.4 MW of output power at an efficiency of over 31 %. The output power at 124.5 GHz was more modest in comparison though it seemed clear that the device's potential in this operating range was being limited by the performance of the electron gun. Nonetheless, we were able to achieve 850 kW of output power at 96 kV and 40 A with 950 kW produced at 98 kV and 42 A. MW operation was achieved for a beam current of 42-44 A. In all cases, stable operation was achieved without severe mode competition at the high power operating points.

At both frequencies, we measured excellent beam quality. A cold test and gyrotron experiment both showed about 99% Gaussian beam content for the $TE_{22,6,1}$ mode, agreeing quite well with theory. The result was also quite good for the $TE_{24,7,1}$ mode where a Gaussian beam content of 97% was calculated, though consideration of the tilted phase resulted in a more modest 94.4%. In all cases, the beam waist measured in experiment and recovered via phase retrieval matched the predicted 2.63 cm circular beam very closely.

Finally, we considered some new measurements of the start-up scenario for this new configuration. At the 124.5 GHz operating point, we observed a mix of lower frequency backward-wave modes analogous to those observed in Chapter 4 that were accompanied, however, by higher frequency modes as expected by theory. Start-up scenario measurements at 110 GHz, showed an excitation of an even lower frequency $TE_{20,6,q}$ mode compared to the TE21,6,q modes seen in Chapter 4. A major difference between the two experiments is the window reflection, which reaches its peak around 105 GHz and is close to the frequency of the $TE_{20,6,q}$ modes. This may provide some further evidence that window reflections play a role in the excitations of these modes.

Chapter 6

Conclusions

A number of high power gyrotron experiments were successfully carried out and reported in this thesis. The gyrotron community is a particularly collaborative one with groups like MIT focusing on experimental physics, while groups at the University of Wisconsin and University of Maryland focus on theoretical device physics and design, and companies like CPI work on the development of industrial tubes for CW operation. By leveraging the experimental tools at MIT and working together with collaborators, the thorough body of work presented in this thesis will be of great value to the entire community. The contributions focused in 3 areas: analysis of gyrotron mode converters, experimental investigation of device physics including the start-up scenario, and demonstration of a new concept by operating at two different frequencies with a diode-type electron gun.

This work began by using an existing configuration of the 1.5 MW, 110 GHz gyrotron which incorporated a cavity optimized for high efficiency operation and an internal mode converter (IMC) with phase correcting mirrors. The phase-correcting mirror IMC was then replaced by a newly designed smooth-mirror mode converter. Most previous gyrotrons that implemented phase-correcting mirror designs had Gaussian output beams come out with far lower Gaussian content than predicted. This new smooth-mirror design would be much simpler to fabricate and should be far less susceptible to errors in machining and misalignment. A 3-axis scanning system was developed for the measurement of gyrotron output beams and a phase-retrieval method was applied to

analyze the data and obtain consistent measurements of the Gaussian beam content. The results of the smooth-mirror IMC experiment were successful. Theoretical calculations predicted a round output beam with a beam waist of 2.9 cm and a Gaussian beam content of 98 %. Cold test experiments agreed very well in size with measured beam waists of W_x = 2.7 cm and W_z = 2.9 cm being observed, though the Gaussian beam content was only 95.3 %. When installed on the gyrotron, the results were even better with measured beam waists of W_x = 2.9 cm and W_z = 3.0 cm with a Gaussian beam content of 96.3 %. The increased performance could be expected due to the improved mode quality at the launcher input in the gyrotron experiment. Such a beam output quality would meet the requirements for a gyrotron used in an electron cyclotron heating system for nuclear fusion experiments. The gyrotron operated at a power level of 1.3 MW, with a temporal width of the microwave pulse that was about 20 % larger than in previous operation.

The increased pulse width from initial experiments motivated the next study into the experimental investigation of device physics. The longer pulse width was an indication that modes were being excited on the leading edge of the microwave pulse, meaning during the voltage rise before the voltage pulse reached its flat-top steady-state level. The excitation of modes during the voltage rise is often referred to as the "start-up scenario". This is because it is actually a requirement for the gyrotron to operate in its most efficient regime known as hard self-excitation. While theoretically explored via simulation, the issue had not yet been thoroughly examined experimentally.

The issue of mode competition is closely tied to the startup scenario and is typically the main concern in the design of MW gyrotrons due to the extremely dense spectrum of modes that can be excited in the highly-overmoded cavity. Start-up scenario experiments examined two operation regimes in detail: a high power operating point close to unstable regions where other modes are excited, and a highly stable region where variations in parameters would still lead to the excitation of the desired $TE_{22,6}$ mode. Frequency measurements using a heterodyne receiver system showed the excitation of

lower frequency modes, in the range of 108-109 GHz excited at the lowest voltages. This was a surprising result as prior simulation and theory work had predicted that higher frequency modes should be excited instead. A theoretical analysis of these modes showed that they should be cavity modes with the transverse structure of the $TE_{21,6}$ mode but with a higher order axial field profile, i.e. multiple variations, as opposed to the nearly Gaussian axial field profile seen in high power mode excitations near their cutoff frequency. The discovery of these mode excitations also had implications on gyrotron simulation work as they were not previously considered in simulations. In collaboration with Oleksandr Sinitsyn at the University of Maryland, a new approach was developed that was able to show the experimental mode excitations during the voltage rise in the simulations. However, in order to properly take these effects into account in regular gyrotron design and analyses, modifications to the code should be introduced.

The final component of this thesis work involved the complete design and experimental demonstration of a new gyrotron configuration. Analysis showed that a two frequency gyrotron could be designed to excite the $TE_{22,6}$ mode at 110 GHz, and the $TE_{24,7}$ mode at 124.5 GHz. For two frequency operation, the design of a new cavity, IMC, and output window were necessary. The cavity was designed by supplementing the gyrotron non-linear theory with both cold-cavity simulations and multi-mode time-dependent simulations using the code MAGY. It was decided to use a shorter 1.7 cm cavity along with a larger 1.0° uptaper as compared to the previous single-mode high efficiency cavity design. These parameters correlate to a cavity Q factor of 830 and 1060 with normalized cavity lengths of 15.1 and 16.4 respectively for the $TE_{22,6}$ and $TE_{24,7}$ modes. MAGY predicted 1.65 MW of output power using simpler single-mode calculations, though the more realistic multi-mode case, which also incorporated the effects of a 5 % velocity spread, predicted a more modest 1.4 MW could be achieved in experiment. The design of the dual frequency IMC was done by Ben Rock at the University of Wisconsin (now with the Naval Research Laboratory). Theoretical calculations predicted that a Gaussian beam

content of over 99 % could be achieved during operation at either frequency. Cold test of the IMC at 110 GHz showed excellent results as a Gaussian beam content of ~99 % was measured. Finally, it was decided to use a simple single-disc window to couple the power out from the tube. The designed 5.555 mm fused quartz window should have over 99.5 % transmission at both frequencies. A quick cold test of the window showed that the manufactured window thickness was correct and transmission peaks were located at the right frequencies.

The new components were installed in the vacuum vessel and experiments were carried out at both frequencies. In operation at 96 kV and 40 A, 1.1 MW of output power was demonstrated. However, by raising the voltage and current to 98 kV and 42 A, similar to results reported on the previous configuration, it was shown that 1.25 MW of output power could be achieved. The output beam at this frequency was of the highest quality. A circular Gaussian beam was measured and had a waist size of 2.65 cm which is almost identical to the theoretical prediction of 2.63 cm. The amplitude and phase at the window were obtained using a phase retrieval algorithm and calculated Gaussian beam content was 97.7 %. The mode map which indicates the mode excitation as a function of magnetic field parameters was similar to those measured in the previous configurations of the MIT MW gyrotron. At 124.5 GHz, the output power of the gyrotron was limited to a more modest 850 kW of output power at 96 kV and 40 A, though 1 MW could be achieved by pushing the beam current to 42-44 A. The behavior at the gyrotron indicates that a higher efficiency regime might be seen at lower values of the gun magnetic field, though the performance of the electron gun limits operation in this regime. The output beam at this frequency is still of high quality though it is approximately 20 % smaller, where the predicted size should be the same as that at 110 GHz. By considering amplitude data only, a Gaussian beam content of 97 % is calculated for the beam, though due to measured tilts and offsets, the Gaussian beam content when including the retrieved phase is a more modest 94.4 %. The mode map for this configuration showed that the expected modes

with radial mode index $p = 7$ are excited throughout most of the parameter space, but, similar to 110 GHz operation, the counter-rotating mode is excited at higher values of magnetic field. A brief investigation of the start-up scenario for 124.5 GHz operating points, showed the excitations of both lower frequency modes, as seen in the experiments of Chapter 4, as well as higher frequency modes, as predicted by theory. This measurement is helpful in validating the previous experimental results observed in the original study of the start-up scenario.

The experiments herein have therefore demonstrated successful MW operation at two frequencies, successful operation using a mode converter with smooth mirrors, and have initiated an important discussion on the start-up scenario that has improved the understanding of gyrotron physics and should help in the design and modification of simulation codes for future gyrotron design and analysis. Future work could involve further characterization of this new gyrotron configuration, particularly operation with a depressed collector to investigate the after cavity interaction effect with this geometry. In addition, some instabilities were observed in various regions of the parameter space, though none coinciding with operation at 110 or 124.5 GHz. Investigation of these effects could yield some interesting insights into the physics of the gyrotron. Finally, a design modification could be considered to optimize operation for a smaller compression, i.e. higher gun magnetic field. This may help access the highest power operating regime at 124.5 GHz where the power was more limited in this current design.

References

[1] E. H. Armstrong, "Some recent developments in the audion receiver," *Proceedings of the Institute of Radio Engineers,* vol. 3, pp. 215, 1915.

[2] J. L. Hogan Jr., "Developments of the heterodyne receiver," *Proceedings of the Institute of Radio Engineers,* vol. 3, pp. 249, 1915.

[3] V. L. Granatstein, R. K. Parker and C. M. Armstrong, "Vacuum electronics at the dawn of the twenty-first century," *Proceedings of the IEEE,* vol. 87, pp. 702-716, 1999.

[4] A. W. Hull, "The Effect of A Uniform Magnetic Field on the Motion of Electrons Between Coaxial Cylinders." *Phys. Rev.,* vol. 18, pp. 31-57, Jul, 1921.

[5] J. B. Fisk, H. D. Hagstrum and P. L. Hartman, "The Magnetron as a Generator of Centimeter Waves," *The Bell System Technical Journal,* vol. XXV, pp. 167-348, 1946.

[6] H. A. H. Boot and J. T. Randall, "The cavity magnetron," *Electrical Engineers - Part IIIA: Radiolocation, Journal of the Institution Of,* vol. 93, pp. 928-938, 1946.

[7] H. Guerlac, *Radar in World War II.* Tomash Publishers, 1987.

[8] R. Buderi, *The Invention that Changed the World: How a Small Group of Radar Pioneers Won the Second World War and Launched a Technical Revolution.* New York, NY: Touchstone, 1996.

[9] D. A. Fleischer, "The MIT Radiation Laboratory: RLE's Microwave Heritage," *RLE Currents,* vol. 4, 1991.

[10] Communications & Power Industries LLC. (2013). *Magnetrons*. Available: http://www.cpii.com/product.cfm/8/2.

[11] A. D. Andreev and K. J. Hendricks, "Multicavity Magnetron With the "Rodded" Quasi-Metamaterial Cathode," *Plasma Science, IEEE Transactions On,* vol. 41, pp. 620-627, 2013.

[12] T. P. Fleming, M. R. Lambrecht, P. J. Mardahl and J. D. Keisling, "A High-Efficiency Megawatt-Class Nonrelativistic Magnetron," *Plasma Science, IEEE Transactions On,* vol. 40, pp. 2112-2118, 2012.

[13] R. M. Gilgenbach, Yue-Ying Lau, D. M. French, B. W. Hoff, M. Franzi and J. Luginsland, "Recirculating Planar Magnetrons for High-Power High-Frequency Radiation Generation," *Plasma Science, IEEE Transactions On,* vol. 39, pp. 980-987, 2011.

[14] T. P. Fleming and P. J. Mardahl, "Performance Improvements in the Relativistic Magnetron: The Effect of DC Field Perturbations," *Plasma Science, IEEE Transactions On,* vol. 37, pp. 2128-2138, 2009.

[15] G. Caryotakis, "Klystrons," in *Modern Microwave and Millimeter-Wave Power Electronics*, 1st ed., R. Barker, N. Luhmann, J. Booske and G. Nusinovich, Eds. Piscataway, NJ: Wiley-IEEE Press, 2005, pp. 107-170.

[16] R. H. Varian and S. F. Varian, "A High Frequency Oscillator and Amplifier," *J. Appl. Phys.,* vol. 10, pp. 321-327, 1939.

[17] J. W. Gewartowski and H. A. Watson, *Principles of Electron Tubes.* Princeton, NJ: D. Van Nostrand Company, Inc., 1965.

[18] M. Chodorow, E. L. Ginzton, I. R. Neilsen and S. Sonkin, "Design and Performance of a High-Power Pulsed Klystron," *Proceedings of the IRE,* vol. 41, pp. 1584-1602, 1953.

[19] M. I. Skolnik, "Fifty years of radar," *Proceedings of the IEEE,* vol. 73, pp. 182-197, 1985.

[20] A. Roitman, D. Berry and B. Steer, "State-of-the-art W-band extended interaction klystron for the CloudSat program," *Electron Devices, IEEE Transactions On,* vol. 52, pp. 895-898, 2005.

[21] J. R. Pierce and L. M. Field, "Traveling-Wave Tubes," *Proceedings of the IRE,* vol. 35, pp. 108-111, 1947.

[22] R. Kompfner, "The travelling wave valve," *Wireless World,* vol. 52, pp. 369-372, November 1946.

[23] N. H. Pond, *The Tube Guys.* West Plains, MO: Russ Cochran Publishing, 2008.

[24] B. G. James and P. Kolda, "A ladder circuit coupled-cavity TWT at 80-100 GHz," in *Electron Devices Meeting, 1986 International,* 1986, pp. 494-497.

[25] E. J. Kowalski, M. A. Shapiro and R. J. Temkin, "Over-moded W-band traveling wave tube design," in *Vacuum Electronics Conference (IVEC), 2012 IEEE Thirteenth International,* 2012, pp. 457-458.

[26] A. M. Cook, C. D. Joye, J. P. Calame, K. T. Nguyen, A. Vlasov, E. L. Wright, D. K. Abe and B. Levush, "Serpentine waveguide 220 GHz millimeter wave amplifier cold test," in *Vacuum Electronics Conference (IVEC), 2012 IEEE Thirteenth International,* 2012, pp. 547-548.

[27] J. C. Tucek, M. A. Basten, D. A. Gallagher, K. E. Kreischer, R. Lai, V. Radisic, K. Leong and R. Mihailovich, "A 100 mW, 0.670 THz power module," in *Vacuum Electronics Conference (IVEC), 2012 IEEE Thirteenth International,* 2012, pp. 31-32.

[28] R. Twiss, "Radiation Transfer and the Possibility of Negative Absorption in Radio Astronomy," *Aust. J. Phys.,* vol. 11, pp. 564-579, 1958.

[29] J. Schneider, "Stimulated Emission of Radiation by Relativistic Electrons in a Magnetic Field," *Phys. Rev. Lett.,* vol. 2, pp. 504-505, 1959.

[30] A. V. Gaponov, "Interaction between electron fluxes and electromagnetic waves in waveguides," *Izv. VUZov Radiofizika,* vol. 2, pp. 450-462, 1959, (in Russian).

[31] J. L. Hirshfield and V. L. Granatstein, "The Electron Cyclotron Maser--An Historical Survey," *Microwave Theory and Techniques, IEEE Transactions On,* vol. 25, pp. 522-527, 1977.

[32] R. H. Pantell, "Backward wave oscillations in an unloaded waveguide," *Proc. IRE,* vol. 47, pp. 1146, 1959.

[33] I. B. Bott, "Tunable source of millimeter and submillimeter electromagnetic radiation," *Proceedings of the IEEE,* vol. 52, pp. 330-332, 1964.

[34] J. L. Hirshfield and J. M. Wachtel, "Electron Cyclotron Maser," *Phys. Rev. Lett.,* vol. 12, pp. 533-536, May, 1964.

[35] K. L. Felch, B. G. Danly, H. R. Jory, K. E. Kreischer, W. Lawson, B. Levush and R. J. Temkin, "Characteristics and applications of fast-wave gyrodevices," *Proceedings of the IEEE,* vol. 87, pp. 752-781, 1999.

[36] A. V. Gaponov, M. I. Petelin and V. K. Yulpatov, "The induced radiation of excited classical oscillators and its use in high-frequency electronics," *Radiophysics and Quantum Electronics,* vol. 10, pp. 794-813, 1967.

[37] A. V. Gaponov, A. L. Gol'denberg, D. P. Grigor'ev, I. M. Orlova, T. B. Pankratova and M. I. Petelin, "Induced synchrotron radiation of electrons in cavity resonators," *JETP Letters,* vol. 2, pp. 267-269, 1965.

[38] Y. V. Bykov and A. L. Gol'denberg, "Influence of resonator profile on the maximum power of a cyclotron resonance maser," *Radiophysics and Quantum Electronics,* vol. 18, pp. 791-792, 1975.

[39] V. P. Taranenko, V. N. Glushenko, S. V. Koshevaya, K. Y. Lizhdvoy, V. A. Prus and V. A. Trapezon, "Influence of electron velocity dispersion upon start current and efficiency of gyrotrons," *Elektronnaya Tekhnika, Ser. 1 Elektronika SVCh,* vol. 12, pp. 47, 1974.

[40] D. V. Kisel, G. S. Korablev, V. G. Navel'yev, M. I. Petelin and S. Y. Tsimring, "An experimental study of a gyrotron, operating at the second harmonic of the cyclotron frequency, with optimized distribution of the high frequency field," *Radio Eng. Electron Phys.,* vol. 19, pp. 95-100, 1975.

[41] N. I. Zaytsev, T. B. Pankratova, M. I. Petelin and V. A. Flyagin, "Millimeter and submillimeter waveband gyrotrons," *Radiotekhnika i Elektronika,* vol. 19, pp. 1056-1060, 1974.

[42] V. A. Flyagin, A. V. Gaponov, M. I. Petelin and V. K. Yulpatov, "The Gyrotron," *Microwave Theory and Techniques, IEEE Transactions On,* vol. 25, pp. 514-521, 1977.

[43] H. R. Jory, F. Friedlander, S. J. Hegji, J. F. Shively and R. S. Symons, "Gyrotrons for high power millimeter wave generation," in *Electron Devices Meeting, 1977 International,* 1977, pp. 234-237.

[44] K. E. Kreischer and R. J. Temkin, "Linear theory of an electron cyclotron maser operating at the fundamental," *Int J Infrared Millim Waves,* vol. 1, pp. 195-223, 1980.

[45] K. E. Kreischer and R. J. Temkin, "Mode excitation in a gyrotron operating at the fundamental," *Int J Infrared Millim Waves,* vol. 2, pp. 175-196, 1981.

[46] B. G. Danly and R. J. Temkin, "Generalized nonlinear harmonic gyrotron theory," *Phys. Fluids,* vol. 29, pp. 561-567, 1986.

[47] K. E. Kreischer, B. G. Danly, J. B. Schutkeker and R. J. Temkin, "The Design of Megawatt Gyrotrons," *Plasma Science, IEEE Transactions On,* vol. 13, pp. 364-373, 1985.

[48] B. Levush and W. M. Manheim, "Generation of High-Frequency Radiation by Quasi-Optical Gyrotron at Harmonics of the Cyclotron Frequency," *Microwave Theory and Techniques, IEEE Transactions On,* vol. 32, pp. 1398-1401, 1984.

[49] R. J. Temkin, K. E. Kreischer, W. J. Mulligan, S. MacCabe and H. R. Fetterman, "A 100 kW, 140 GHz pulsed gyrotron," *Int J Infrared Millim Waves,* vol. 3, pp. 427-437, 1982.

[50] B. Arfin, Kwo Ray Chu, D. Dialetis and M. E. Read, "A high power gyrotron operating in the TE041mode," *Electron Devices, IEEE Transactions On,* vol. 29, pp. 1911-1916, 1982.

[51] H. Jory, R. Bier, S. Evans, K. Felch, L. Fox, H. Huey, J. Shively and S. Spang, "First 200 kW CW operation of a 60 GHz gyrotron," in *Electron Devices Meeting, 1983 International,* 1983, pp. 267-270.

[52] A. Bensimhon, G. Faillon, P. Garin, G. Mourier and A. Thevenot, "First Experimental Results on 100-Ghz 200-kW Gyrotrons," *Plasma Science, IEEE Transactions On,* vol. 13, pp. 389-392, 1985.

[53] E. A. Nanni, A. B. Barnes, R. G. Griffin and R. J. Temkin, "THz Dynamic Nuclear Polarization NMR," *Terahertz Science and Technology, IEEE Transactions On,* vol. 1, pp. 145-163, 2011.

[54] R. J. Temkin, K. Kreischer, S. M. Wolfe, D. R. Cohn and B. Lax, "High frequency gyrotrons and their application to tokamak plasma heating," *J Magn Magn Mater,* vol. 11, pp. 368-371, 4, 1979.

[55] K. Felch, H. Huey and H. Jory, "Gyrotrons for ECH applications," *J. Fusion Energy,* vol. 9, pp. 59-75, 1990.

[56] D. S. Clark, "Detailed implosion modeling of deuterium-tritium layered experiments on the National Ignition Facility," *Phys Plasmas,* vol. 20, pp. 056318, May 2013, 2013.

[57] C. Bellei, P. A. Amendt, S. C. Wilks, M. G. Haines, D. T. Casey, C. K. Li, R. Petrasso and D. R. Welch, "Species separation in inertial confinement fusion fuels," *Phys Plasmas,* vol. 20, pp. 012701, January 2013, 2013.

[58] P. B. Radha, "Polar-drive implosions on OMEGA and the National Ignition Facility," *Phys Plasmas,* vol. 20, pp. 056306, May 2013, 2013.

[59] D. G. Hicks, "Implosion dynamics measurements at the National Ignition Facility," *Phys Plasmas,* vol. 19, pp. 122702, December 2012, 2012.

[60] S. H. Glenzer, "Cryogenic thermonuclear fuel implosions on the National Ignition Facility," *Phys Plasmas,* vol. 19, pp. 056318, May 2012, 2012.

[61] J. Lohr, M. Cengher, J. Doane, Y. Gorelov, C. Moeller, D. Ponce and R. Prater, "The Multiple Gyrotron System on the DIII-D Tokamak," *Journal of Infrared, Millimeter, and Terahertz Waves,* vol. 32, pp. 253-273, 2011.

[62] D. Wagner, J. Stober, F. Leuterer, F. Monaco, M. Münich, D. Schmid-Lorch, H. Schütz, H. Zohm, M. Thumm, T. Scherer, A. Meier, G. Gantenbein, J. Flamm, W. Kasparek, H. Höhnle, C. Lechte, A. Litvak, G. Denisov, A. Chirkov, L. Popov, V. Nichiporenko, V. Myasnikov, E. Tai, E. Solyanova and S. Malygin, "Recent Upgrades and Extensions of the ASDEX Upgrade ECRH System," *Journal of Infrared, Millimeter, and Terahertz Waves,* vol. 32, pp. 274-282, 2011.

[63] S. Kubo, "Extension and characteristics of an ECRH plasma in LHD," *Plasma Phys. Controlled Fusion,* vol. 47, pp. A81, 2005.

[64] M. A. Henderson et al., "The ITER ECH&CD system," in *Electron Cyclotron Emission and Electron Cyclotron Resonance Heating (EC-16): Proceedings of the 16th Joint Workshop, Sanya, China, 12-15 April 2010*, R. Prater, Ed. World Scientific, 2011, pp. 353-363.

[65] T. Omori et al., "Overview of the ITER EC H&CD system and its capabilities," *Fusion Eng. Des.,* vol. 86, pp. 951-954, 2011.

[66] V. Erckmann et al., "Electron Cyclotron Heating for W7-X: Physics and Technology," *Fusion Science and Technology,* vol. 52, pp. 291, 2007.

[67] A. Kasugai, K. Sakamoto, K. Takahashi, K. Kajiwara and N. Kobayashi, "Steady-state operation of 170 GHz–1 MW gyrotron for ITER," *Nucl Fusion,* vol. 48, pp. 054009, 2008.

[68] K. Felch, M. Blank, P. Borchard, P. Cahalan and S. Cauffman, "Recent high-power gyrotron activities at 95, 110 and 170 GHz," in *Vacuum Electronics Conference (IVEC), 2012 IEEE Thirteenth International,* 2012, pp. 109-110.

[69] K. Felch, M. Blank, P. Borchard, P. Cahalan, S. Cauffman, T. S. Chu and H. Jory, "Recent ITER-Relevant Gyrotron Tests," *Journal of Physics: Conference Series,* vol. 25, 2005.

[70] A. G. Litvak, G. G. Denisov, M. V. Agapova, V. E. Myasnikov, L. G. Popov, E. M. Tai, S. V. Usachev, V. E. Zapevalov, A. V. Chirkov, V. I. Ilin, A. N. Kuftin, V. I. Malygin, E. V. Sokolov and E. A. Soluyanova, "Development in russia of 170 GHz gyrotron for ITER," in *Infrared, Millimeter and Terahertz Waves (IRMMW-THz), 2011 36th International Conference On,* 2011, pp. 1-3.

[71] J. Jelonnek, S. Alberti, K. Avramidis, H. Braune, V. Erckmann, G. Gantenbein, J. -. Hogge, S. Illy, Jianbo Jin, S. Kern, F. Noke, I. Pagonakis, B. Piosczyk, F. Purps, T. Rzesnicki, A. Samartsev, A. Schlaich, M. Schmid and M. Thumm, "High power gyrotron development at KIT for ECH&CD of fusion plasmas," in *Vacuum Electronics Conference (IVEC), 2012 IEEE Thirteenth International,* 2012, pp. 111-112.

[72] T. Rzesnicki, B. Piosczyk, S. Kern, S. Illy, Jianbo Jin, A. Samartsev, A. Schlaich and M. Thumm, "2.2-MW Record Power of the 170-GHz European Preprototype Coaxial-Cavity Gyrotron for ITER," *Plasma Science, IEEE Transactions On,* vol. 38, pp. 1141-1149, 2010.

[73] R. A. James, G. Giruzzi, B. de Gentile, L. Rodriguez, R. Harvey, J. Lohr, T. C. Luce, K. Matsuda, C. P. Moeller, R. Prater, R. Snider, A. Fyakhretdinov, Y. Gorelov, V. Trukhin and S. Janz, "Electron-cyclotron-current-drive experiments in the DIII-D tokamak," *Phys. Rev. A,* vol. 45, pp. 8783-8786, Jun, 1992.

[74] R. J. La Haye, "Neoclassical tearing modes and their control," *Phys Plasmas,* vol. 13, pp. 055501, May 2006, 2006.

[75] G. L. Jackson, D. A. Humphreys, A. W. Hyatt, J. M. Lohr, T. C. Luce and J. H. Yu, "Noninductive plasma initiation and startup in the DIII-D tokamak," *Nucl Fusion,* vol. 51 (8), 083015, 2011.

[76] I. T. Chapman, R. J. La Haye, R. J. Buttery, W. W. Heidbrink, G. L. Jackson, C. M. Muscatello, C. C. Petty, R. I. Pinsker, B. J. Tobias and F. Turco, "Sawtooth control using electron cyclotron current drive in ITER demonstration plasmas in DIII-D," *Nucl Fusion,* vol. 52 (6), 063006, 2012.

[77] J. R. Ferron, C. T. Holcomb, T. C. Luce, P. A. Politzer, F. Turco, J. C. DeBoo, E. J. Doyle, Y. In, R. J. La Haye, M. Murakami, O. Okabayashi, J. M. Park, T. W. Petrie, C. C. Petty and H. Reimerdes, "Balancing current drive and heating in DIII-D high noninductive current fraction discharges through choice of the toroidal field," *Nucl Fusion,* vol. 51 (11), 113007, 2011.

[78] J. X. Rossel, J. M. Moret, S. Coda, O. Sauter, T. P. Goodman, F. Felici, D. Testa, Y. Martin and the TCV Team, "Edge-localized mode control by electron cyclotron waves in a tokamak plasma," *Nucl Fusion,* vol. 52 (3), 032004, 2012.

[79] J. Stober et al., "ECRH-assisted plasma start-up with toroidally inclined launch: multi-machine comparison and perspectives for ITER," *Nucl Fusion,* vol. 51 (8), 083031, 2011.

[80] G. Gantenbein, H. Zohm, G. Giruzzi, S. Gunter, F. Leuterer, M. Maraschek, J. Meskat, Q. Yu, ASDEX Upgrade Team and ECRH-Group, "Complete Suppression of Neoclassical Tearing Modes with Current Drive at the Electron-Cyclotron-Resonance Frequency in ASDEX Upgrade Tokamak," *Phys. Rev. Lett.,* vol. 85, pp. 1242-1245, 2000.

[81] M. A. Shapiro, E. J. Kowalski, J. R. Sirigiri, D. S. Tax, R. J. Temkin, T. S. Bigelow, J. B. Caughman and D. A. Rasmussen, "Loss estimate for ITER ECH transmission line including multimode propagation," *Fusion Science and Technology,* vol. 57, pp. 196-207, 2010.

[82] D. Strauss, G. Aiello, R. Chavan, S. Cirant, M. deBaar, D. Farina, G. Gantenbein, T. P. Goodman, M. A. Henderson, W. Kasparek, K. Kleefeldt, J. -. Landis, A. Meier, A. Moro, P. Platania, B. Plaum, E. Poli, G. Ramponi, D. Ronden, G. Saibene, F. Sanchez, O. Sauter, T. Scherer, S. Schreck, A. Serikov, C. Sozzi, P. Spaeh, A. Vaccaro and H. Zohm, "Preliminary design of the ITER ECH Upper Launcher," *Fusion Eng. Des.,* In Press, 2013.

[83] Y. Bykov, A. Eremeev, V. Flyagin, V. Kaurov, A. Kutfin, A. Luchinin, O. Malygin, I. Plotnikov and V. Zapevalov, "The gyrotron system for ceramics sintering," *Microwaves: Theory Applicat. Materials Processing III, Ceramic Trans.,* vol. 59, pp. 133-140, 1995.

[84] Y. V. Bykov and V. E. Semenov, "Chapter 8," in *Applications of High-Power Microwaves*, A. V. Gaponov-Grekhov and V. L. Granatstein, Eds. Norwood, MA: Artech House, 1994, pp. 319-351.

[85] (2013). *ITER: the world's largest Tokamak.* Available: http://www.iter.org/mach.

[86] N. Kobayashi, T. Bigelow, T. Bonicelli, S. Cirant, G. Denisov, R. Heidinger, M. Henderson, J. -. Hogge, B. Piosczyk, G. Ramponi, S. L. Rao, D. Rasmussen, G. Saibene, K. Sakamoto, K. Takahashi, R. J. Temkin, M. Thumm, M. Q. Tran, A. G. A. Verhoeven and H. Zohm, "Design of Electron Cyclotron Heating and Current Drive System of ITER," *AIP Conf. Proc.,* vol. 933, pp. 413-416, September 28, 2007, 2007.

[87] W. M. Manheimer, G. Mesyats and M. I. Petelin, "Chapter 5: Applications of high power microwave sources to enchanced radar systems," in *Applications of High-Power Microwaves*, A. V. Gaponov-Grekhov and V. L. Granatstein, Eds. Norwood, MA: Artech House, 1994, pp. 169-207.

[88] V. L. Granatstein and W. Lawson, "Gyro-amplifiers as candidate RF drivers for TeV linear colliders," *Plasma Science, IEEE Transactions On,* vol. 24, pp. 648-665, 1996.

[89] A. Abragam and M. Goldman, "Principles of dynamic nuclear polarisation," *Reports on Progress in Physics,* vol. 41, pp. 395, 1978.

[90] A. B. Barnes, G. De Paëpe, P. C. A. van der Wel, K. -. Hu, C. -. Joo, V. S. Bajaj, M. L. Mak-Jurkauskas, J. R. Sirigiri, J. Herzfeld, R. J. Temkin and R. G. Griffin, "High-Field Dynamic Nuclear Polarization for Solid and Solution Biological NMR," *Applied Magnetic Resonance,* vol. 34, pp. 237-263, 2008.

[91] A. B. Barnes, E. A. Nanni, J. Herzfeld, R. G. Griffin and R. J. Temkin, "A 250 GHz gyrotron with a 3 GHz tuning bandwidth for dynamic nuclear polarization," *Journal of Magnetic Resonance,* vol. 221, pp. 147-153, 8, 2012.

[92] A. C. Torrezan, M. A. Shapiro, J. R. Sirigiri, R. J. Temkin and R. G. Griffin, "Operation of a Continuously Frequency-Tunable Second-Harmonic CW 330-GHz Gyrotron for Dynamic Nuclear Polarization," *Electron Devices, IEEE Transactions On,* vol. 58, pp. 2777-2783, 2011.

[93] M. Rosay, L. Tometich, S. Pawsey, R. Bader, R. Schauwecker, M. Blank, P. M. Borchard, S. R. Cauffman, K. L. Felch, R. T. Weber, R. J. Temkin, R. G. Griffin and W. E. Maas, "Solid-state dynamic nuclear polarization at 263 GHz: spectrometer design and experimental results," *Phys. Chem. Chem. Phys.,* vol. 12, pp. 5850-5860, 2010.

[94] T. Idehara, K. Kosuga, L. Agusu, R. Ikeda, I. Ogawa, T. Saito, Y. Matsuki, K. Ueda and T. Fujiwara, "Continuously Frequency Tunable High Power Sub-THz Radiation Source—Gyrotron FU CW VI for 600 MHz DNP-NMR Spectroscopy," *Journal of Infrared, Millimeter, and Terahertz Waves,* vol. 31, pp. 775-790, 2010.

[95] A. C. Torrezan, Seong-Tae Han, I. Mastovsky, M. A. Shapiro, J. R. Sirigiri, R. J. Temkin, A. B. Barnes and R. G. Griffin, "Continuous-Wave Operation of a Frequency-Tunable 460-GHz Second-Harmonic Gyrotron for Enhanced Nuclear Magnetic Resonance," *Plasma Science, IEEE Transactions On,* vol. 38, pp. 1150-1159, 2010.

[96] V. E. Zapevalov, V. V. Dubrov, A. S. Fix, E. A. Kopelovich, A. N. Kuftin, O. V. Malygin, V. N. Manuilov, M. A. Moiseev, A. S. Sedov, N. P. Venediktov and N. A. Zavolsky, "Development of 260 GHZ second harmonic CW gyrotron with high stability of output parameters for dnp spectroscopy," in *Infrared, Millimeter, and Terahertz Waves, 2009. IRMMW-THz 2009. 34th International Conference On,* 2009, pp. 1-2.

[97] K. Kreischer, C. Farrar, R. Griffin, R. Temkin and J. Vieregg, "A 250 GHz gyrotron for NMR spectroscopy," in *Plasma Science, 2000. ICOPS 2000. IEEE Conference Record - Abstracts. the 27th IEEE International Conference On,* 2000, pp. 198.

[98] T. Idehara, K. Yoshida, N. Nishida, I. Ogawa, M. L. Pereyaslavets and T. Tatsukawa, "CW Operation of a Submillimeter Wave Gyrotron (Gyrotron Fu IV) for High Stability of the Output Frequency," *Int J Infrared Millim Waves,* vol. 19, pp. 793-801, 1998.

[99] M. Y. Glyavin, A. G. Luchinin and G. Y. Golubiatnikov, "Generation of 1.5-kW, 1-THz Coherent Radiation from a Gyrotron with a Pulsed Magnetic Field," *Phys. Rev. Lett.,* vol. 100, pp. 015101, Jan, 2008.

[100] A. B. Barnes, E. Markhasin, E. Daviso, V. K. Michaelis, E. A. Nanni, S. K. Jawla, E. L. Mena, R. DeRocher, A. Thakkar, P. P. Woskov, J. Herzfeld, R. J. Temkin and R. G. Griffin, "Dynamic nuclear polarization at 700 MHz/460 GHz," *Journal of Magnetic Resonance,* vol. 224, pp. 1-7, 11, 2012.

[101] E. J. Koers, E. A. W. van de Cruijsen, M. Rosay, J. van de Zwan, W. E. Maas and M. Baldus, "Dynamic nuclear polarization at 527 GHz / 800 MHz," in *54th ENC Conference,* Pacific Grove, CA, 2013, pp. 61.

[102] A. C. Torrezan, "Frequency-tunable second-harmonic submillimeter-wave gyrotron oscillators," *PhD Thesis, Massachusetts Institute of Technology,* 2010.

[103] C. R. Crowell, "The Richardson constant for thermionic emission in Schottky barrier diodes," *Solid-State Electronics,* vol. 8, pp. 395-399, 4, 1965.

[104] A. S. Gilmour Jr., *Principles of Traveling Wave Tubes.* Norwood, MA: Artech House, 1994.

[105] J. P. Anderson, S. E. Korbly, R. J. Temkin, M. A. Shapiro, K. L. Felch and S. Cauffman, "Design and emission uniformity studies of a 1.5-MW gyrotron electron gun," *Plasma Science, IEEE Transactions On,* vol. 30, pp. 2117-2123, 2002.

[106] B. Piosczyk, "Electron guns for gyrotron applications," in *Gyrotron Oscillators: Their Principles and Practice*, C. J. Edgecombe, Ed. London, England: Taylor & Francis, 1993, pp. 123-146.

[107] J. A. Kong, *Electromagnetic Wave Theory.* Cambridge, MA: EMW Publishing, 2005.

[108] G. S. Nusinovich, *Introduction to the Physics of Gyrotrons.* Baltimore, MD: Johns Hopkins, 2004.

[109] A. W. Fliflet, M. E. Read, K. R. Chu and R. Seeley, "A self-consistent field theory for gyrotron oscillators: application to a low Q gyromonotron," *International Journal of Electronics,* vol. 53, pp. 505-521, 1982.

[110] V. A. Flyagin and G. S. Nusinovich, "Gyrotron oscillators," *Proceedings of the IEEE,* vol. 76, pp. 644-656, 1988.

[111] E. M. Choi, "Experimental Study of a High Efficiency Gyrotron Oscillator," *Ph. D. Thesis, Massachusetts Institute of Technology,* 2007.

[112] S. N. Vlasov, L. I. Zagryadskaya and M. I. Petelin, "Transformation of a whispering gallery mode, propagating in a circular waveguide, into a beam of waves," *Radio Eng. Electron. Phys.,* vol. 12, pp. 14-17, 1975.

[113] G. G. Denisov, A. N. Kuftin, V. I. Malygin, N. P. Venediktov, D. V. Vinogradov and V. E. Zapevalov, "110 GHz gyrotron with built-in high-efficiency converter," *Int. J. Electron.,* vol. 72, pp. 1079-1091, 1992.

[114] A. V. Gaponov, V. A. Flyagin, A. L. Gol'denberg, G. S. Nusinovich, S. E. Tsimring, V. G. Usov and S. N. Vlasov, "Powerful millimetre-wave gyrotrons," *International Journal of Electronics,* vol. 51, pp. 277-302, 1981.

[115] M. K. Hornstein, V. S. Bajaj, R. G. Griffin, K. E. Kreischer, I. Mastovsky, M. A. Shapiro, J. R. Sirigiri and R. J. Temkin, "Second harmonic operation at 460 GHz and broadband continuous frequency tuning of a gyrotron oscillator," *Electron Devices, IEEE Transactions On,* vol. 52, pp. 798-807, 2005.

[116] A. T. Drobot and K. Kim, "Space charge effects on the equilibrium of guided electron flow with gyromotion," *International Journal of Electronics,* vol. 51, pp. 351-367, 1981.

[117] A. K. Ganguly and K. R. Chu, "Limiting current in gyrotrons," *Int J Infrared Millim Waves,* vol. 5, pp. 103-121, 1984.

[118] M. V. Kartikeyan, E. Borie and M. K. Thumm, *Gyrotrons: High-Power Microwave and Millimeter Wave Technology.* Berlin-Heidelberg: Springer-Verlag, 2004.

[119] A. W. Fliflet, R. C. Lee, S. H. Gold, W. M. Manheimer and E. Ott, "Time-dependent multimode simulation of gyrotron oscillators," *Phys. Rev. , A,* vol. 43, pp. 6166-6176, Jun, 1991.

[120] G. S. Nusinovich, "Review of the theory of mode interaction in gyrodevices," *Plasma Science, IEEE Transactions On,* vol. 27, pp. 313-326, 1999.

[121] D. R. Whaley, M. Q. Tran, S. Alberti, T. M. Tran, J. Antonsen T.M. and C. Tran, "Startup Methods for Single-Mode Gyrotron Operation," *Phys. Rev. Lett.,* vol. 75, pp. 1304-1307, 1995.

[122] M. Botton, T. M. Antonsen, B. Levush, K. T. Nguyen and A. N. Vlasov, "MAGY: a time-dependent code for simulation of slow and fast microwave sources," *Plasma Science, IEEE Transactions On,* vol. 26, pp. 882-892, 1998.

[123] K. E. Kreischer, T. Kimura, B. G. Danly and R. J. Temkin, "High-power operation of a 170 GHz megawatt gyrotron," *Phys Plasmas,* vol. 4, pp. 1907-1914, 1997.

[124] J. P. Anderson, M. A. Shapiro, R. J. Temkin, I. Mastovsky and S. R. Cauffman, "Studies of the 1.5-MW 110-GHz gyrotron experiment," *Plasma Science, IEEE Transactions On,* vol. 32, pp. 877-883, 2004.

[125] E. M. Choi, A. J. Cerfon, I. Mastovsky, M. A. Shapiro, J. R. Sirigiri and R. J. Temkin, "Efficiency enhancement of a 1.5-MW, 110-GHz gyrotron with a single-stage depressed collector," *Fusion Sci Tech,* vol. 52, pp. 334-339, 2007.

[126] O. Dumbrajs and J. P. T. Koponen, "Generalized gyrotron theory with inclusion of electron velocity and energy spreads," *Phys Plasmas,* vol. 6, pp. 2618-2621, 1999.

[127] J. P. Anderson, "Experimental Study of a 1.5-MW, 110-GHz Gyrotron Oscillator," *Ph. D. Thesis, Massachusetts Institute of Technology,* 2005.

[128] K. Kreischer, S. Korbly, M. Shapiro, R. Temkin, S. Cauffman and K. Felch, "The development of a 1.5 MW, 110 GHz gyrotron for plasma heating," in *Vacuum Electronics Conference, 2000. Abstracts. International,* 2000, pp. 2 pp.

[129] C. R. K. Marrian and A. Shih, "The operation of coated tungsten-based dispenser cathodes in nonideal vacuum," *Electron Devices, IEEE Transactions On,* vol. 36, pp. 173-179, 1989.

[130] J. M. Neilson, "Optimal synthesis of quasi-optical launchers for high-power gyrotrons," *Plasma Science, IEEE Transactions On,* vol. 34, pp. 635-641, 2006.

[131] K. E. Kreischer, J. B. Schutkeker, B. G. Danly, W. J. Mulligan and R. J. Temkin, "High efficiency operation of a 140 GHz pulsed gyrotron," *International Journal of Electronics,* vol. 57, pp. 835-850, 1984.

[132] W. C. Guss, T. L. Grimm, K. E. Kreischer, J. T. Polevoy and R. J. Temkin, "Velocity ratio measurements of a gyrotron electron beam," *J. Appl. Phys.,* vol. 69, pp. 3789-3795, April 1, 1991, 1991.

[133] A. J. Cerfon, Eunmi Choi, C. D. Marchewka, I. Mastovsky, M. A. Shapiro, J. R. Sirigiri and R. J. Temkin, "Observation and Study of Low-Frequency Oscillations in a 1.5-MW 110-GHz Gyrotron," *Plasma Science, IEEE Transactions On,* vol. 37, pp. 1219-1224, 2009.

[134] E. M. Choi, M. A. Shapiro, J. R. Sirigiri and R. J. Temkin, "Experimental observation of the effect of aftercavity interaction in a depressed collector gyrotron oscillator," *Phys Plasmas,* vol. 14, pp. 093302, 2007.

[135] V. E. Zapevalov and M. A. Moiseev, "Influence of Aftercavity Interaction on Gyrotron Efficiency," *Radiophysics and Quantum Electronics,* vol. 47, pp. 520-527, 2004.

[136] E. J. Kowalski, D. S. Tax, M. A. Shapiro, J. R. Sirigiri, R. J. Temkin, T. S. Bigelow and D. A. Rasmussen, "Linearly Polarized Modes of a Corrugated Metallic Waveguide," *Microwave Theory and Techniques, IEEE Transactions On,* vol. 58, pp. 2772-2780, 2010.

[137] K. Ohkubo, S. Kubo, H. Idei, M. Sato, T. Shimozuma and Y. Takita, "Coupling of tilting Gaussian beam with hybrid mode in the corrugated waveguide," *Int J Infrared Millim Waves,* vol. 18, pp. 23-41, 1997.

[138] D. S. Tax, E. M. Choi, I. Mastovsky, J. M. Neilson, M. A. Shapiro, J. R. Sirigiri, R. J. Temkin and A. C. Torrezan, "Experimental Results on a 1.5 MW, 110 GHz Gyrotron with a Smooth Mirror Mode Converter," *Journal of Infrared, Millimeter, and Terahertz Waves,* vol. 32, pp. 358-370, 2011.

[139] M. Blank, "High Efficiency Quasi-Optical Mode Converters for Overmoded Gyrotrons," *Ph. D. Thesis, Massachusetts Institute of Technology,* 1994.

[140] M. Blank, K. Kreischer and R. J. Temkin, "Theoretical and experimental investigation of a quasi-optical mode converter for a 110-GHz gyrotron," *Plasma Science, IEEE Transactions On,* vol. 24, pp. 1058-1066, 1996.

[141] J. M. Neilson and R. Bunger, "Surface integral equation analysis of quasi-optical launchers," *Plasma Science, IEEE Transactions On,* vol. 30, pp. 794-799, 2002.

[142] C. Moeller, "A coupled cavity whispering gallery mode transducer," in *Conf. Digest on 17th Int. Conf. on Infrared and Millimeter Waves,* Pasadena, CA, 1992, pp. M3.7.

[143] M. P. Perkins, R. Cao, J. M. Neilson and R. J. Vernon, "A High Efficiency Launcher and Mirror System for Use in a 110 GHZ TE22,6 Mode Gyrotron," *Int J Infrared Millim Waves,* vol. 28, pp. 207-218, 2007.

[144] A. V. Chirkov, G. G. Denisov and N. L. Aleksandrov, "3D wavebeam field reconstruction from intensity measurements in a few cross sections," *Optics Communications,* vol. 115, pp. 449-452, 1995.

[145] D. R. Denison, Tak Sum Chu, M. A. Shapiro and R. J. Temkin, "Gyrotron internal mode converter reflector shaping from measured field intensity," *Plasma Science, IEEE Transactions On,* vol. 27, pp. 512-519, 1999.

[146] S. K. Jawla, E. A. Nanni, M. A. Shapiro, P. P. Woskov and R. J. Temkin, "Mode Content Determination of Terahertz Corrugated Waveguides Using Experimentally Measured Radiated Field Patterns," *Plasma Science, IEEE Transactions On,* vol. 40, pp. 1530-1537, 2012.

[147] D. R. Denison, "Gyrotron Mode Converter Mirror Shaping Based on Phase Retrieval from Intensity Measurement," *Ph. D. Thesis, Massachusetts Institute of Technology,* 1999.

[148] D. S. Tax, O. V. Sinitsyn, W. C. Guss, G. S. Nusinovich, M. A. Shapiro and R. J. Temkin, "Experimental Study of the Start-Up Scenario of a 1.5-MW, 110-GHz Gyrotron," *Plasma Science, IEEE Transactions On,* vol. 41, pp. 862-871, 2013.

[149] G. S. Nusinovich, O. V. Sinitsyn, L. Velikovich, M. Yeddulla, T. M. Antonsen, A. N. Vlasov, S. R. Cauffman and K. Felch, "Startup scenarios in high-power gyrotrons," *Plasma Science, IEEE Transactions On,* vol. 32, pp. 841-852, 2004.

[150] M. Yeddulla, G. S. Nusinovich and T. M. Antonsen Jr., "Start currents in an overmoded gyrotron," *Phys Plasmas,* vol. 10, pp. 4513-4520, 2003.

[151] B. Levush and T. M. Antonsen, "Mode competition and control in higher-power gyrotron oscillators," *Plasma Science, IEEE Transactions On,* vol. 18, pp. 260-272, 1990.

[152] G. S. Nusinovich, A. N. Vlasov, T. M. Antonsen Jr., J. Lohr, B. G. Danly and J. P. Hogge, "Excitation of parasitic modes in gyrotrons with fast voltage rise," *Phys Plasmas,* vol. 15, pp. 103101, 2008.

[153] G. S. Nusinovich, M. Yeddulla, T. M. Antonsen and A. N. Vlasov, "Start-Up Scenario in Gyrotrons with a Nonstationary Microwave-Field Structure," *Phys. Rev. Lett.,* vol. 96, pp. 125101, 2006.

[154] K. E. Kreischer, R. J. Temkin, H. R. Fetterman and W. J. Mulligan, "Multimode Oscillation and Mode Competition in High-Frequency Gyrotrons," *Microwave Theory and Techniques, IEEE Transactions On,* vol. 32, pp. 481-490, 1984.

[155] W. C. Guss, M. A. Basten, K. E. Kreischer, R. J. Temkin, T. M. Antonsen Jr., S. Y. Cai, G. Saraph and B. Levush, "Influence of sideband oscillations on gyrotron efficiency," *Plasma Science, IEEE Transactions On,* vol. 22, pp. 871-877, 1994.

[156] A. Litvak, G. Denisov, V. Myasnikov, E. Tai, E. Azizov and V. Ilin, "Development in Russia of Megawatt Power Gyrotrons for Fusion," *Journal of Infrared, Millimeter and Terahertz Waves,* vol. 32, pp. 337-342, 2011.

[157] K. E. Kreischer, B. G. Danly, P. Woskoboinikow, W. J. Mulligan and R. J. Temkin, "Frequency pulling and bandwidth measurements of a 140 GHz pulsed gyrotron," *International Journal of Electronics,* vol. 57, pp. 851-862, 1984.

[158] Y. V. Zasypkin, "Electronic Frequency Tuning in Gyrotrons," *Sov. J. Comm. Tech. & Electron.,* vol. 33 (5), pp. 7-13, 1988.

[159] G. S. Nusinovich, O. V. Sinitsyn, L. Velikovich, M. Yeddulla, T. M. Antonsen Jr., A. N. Vlasov, S. R. Cauffman and K. Felch, "Startup scenarios in high-power gyrotrons," *Plasma Science, IEEE Transactions On,* vol. 32, pp. 841-852, 2004.

[160] T. M. Antonsen Jr., S. Y. Cai and G. S. Nusinovich, "Effect of window reflection on gyrotron operation," *Physics of Fluids B: Plasma Physics,* vol. 4, pp. 4131-4139, 1992.

[161] V. E. Zapevalov, A. A. Bogdashov, G. G. Denisov, A. N. Kuftin, V. K. Lygin, M. A. Moiseev and A. V. Chirkov, "Development of a Prototype of a 1-MW 105-156-GHz Multifrequency Gyrotron," *Radiophysics and Quantum Electronics,* vol. 47, pp. 396-404, 2004.

[162] B. Y. Rock and R. J. Vernon, "A New Method for the Analysis of Perturbed-Wall Waveguide Mode Converters," *Plasma Science, IEEE Transactions On,* vol. 40, pp. 1502-1511, 2012.

[163] B. Y. Rock, J. M. Neilson and R. J. Vernon, "A Power-Optimizing Integrated Design of a Dual-Frequency Gyrotron Quasi-Optical Mode Converter," *Plasma Science, IEEE Transactions On,* vol. 40, pp. 1522-1529, 2012.

[164] J. M. Dutta, C. R. Jones and H. Dave, "Complex Dielectric Constants for Selected Near-Millimeter-Wave Materials at 245 GHz," *Microwave Theory and Techniques, IEEE Transactions On,* vol. 34, pp. 932-936, 1986.